


2011

Steady and Transient Heat Transfer for Jet Impingement on Patterned Surfaces

Mark Michael Dobbertean

University of South Florida, mark.dobbertean@gmail.com

Follow this and additional works at: <http://scholarcommons.usf.edu/etd>

 Part of the [American Studies Commons](#), and the [Mechanical Engineering Commons](#)

Scholar Commons Citation

Dobbertean, Mark Michael, "Steady and Transient Heat Transfer for Jet Impingement on Patterned Surfaces" (2011). *Graduate Theses and Dissertations*.

<http://scholarcommons.usf.edu/etd/3076>

This Thesis is brought to you for free and open access by the Graduate School at Scholar Commons. It has been accepted for inclusion in Graduate Theses and Dissertations by an authorized administrator of Scholar Commons. For more information, please contact scholarcommons@usf.edu.

Steady and Transient Heat Transfer for Jet Impingement on Patterned Surfaces

by

Mark Michael Dobbertean

A thesis submitted in partial fulfillment
of the requirements for the degree of
Master of Science
Department of Mechanical Engineering
College of Engineering
University of South Florida

Major Professor: Muhammad M. Rahman, Ph.D.
Craig Lusk, Ph.D.
Frank Pyrtle III, Ph.D.

Date of Approval:
October 18, 2011

Keywords: Slot Jet, Conjugate Heat Transfer, Ribbed, Curved, Water

Copyright © 2011, Mark Michael Dobbertean

Table of Contents

List of Figures	iii
List of Symbols	xiii
Abstract	xvi
Chapter 1 Introduction and Literature Review	1
1.1 Introduction	1
1.2 Literature Review	2
1.2.1 Steady State Jet Impingement on a Heated Flat Plate	2
1.2.2 Steady State Jet Impingement on Patterned Surfaces	6
1.2.3 Transient Jet Impingement	7
1.3 Objectives of the Present Investigation	9
Chapter 2 Modeling and Computation	10
2.1 Jet Impingement on Patterned Surfaces: Steady State	10
2.2 Jet Impingement on Patterned Surfaces: Transient Analysis	14
2.3 Computational Procedure	15
2.3.1 Steady State Procedure	15
2.3.2 Transient Procedure	16
2.4 Optimization of Grid Size	17
2.5 Comparison with Previous Experimental Results	19
Chapter 3 Discussion of Results: Steady State	21
3.1 Slot Jet Impinging on a Uniformly Heated Plate with Rectangular Ridges: Steady State Heating	21
3.2 Slot Jet Impinging on a Uniformly Heated Plate with Triangular Ridges: Steady State Heating	54
3.3 Slot Jet Impinging on a Uniformly Heated Plate with Sinusoidal Ridges: Steady State Heating	69
Chapter 4 Discussion of Results: Transient Heating	83
4.1 Slot Jet Impinging on a Uniformly Heated Plate with Rectangular Ridges: Transient Heating	83
4.2 Slot Jet Impinging on a Uniformly Heated Plate with Triangular Ridges: Transient Heating	104
4.3 Slot Jet Impinging on a Uniformly Heated Plate with Sinusoidal Ridges: Transient Heating	120

Chapter 5 Conclusions and Recommendations for Future Research	135
5.1 Steady State Conclusions.....	135
5.2 Transient Conclusions	137
5.3 Recommendations for Future Research	137
List of References.....	138
Appendices.....	141
Appendix A: Rectangular Ridge FIDAP Code.....	142
Appendix B: Triangular Rib FIDAP Code.....	156
Appendix C: Sine Shaped Surface FIDAP Code.....	178

List of Figures

Figure 2.1	Schematic of a free slot jet impinging on a uniformly heated plate with a patterned surface.....	11
Figure 2.2	Grid independence study results for different numbers of elements in the horizontal and vertical directions (Steady state) ($Re = 1500$, $T_j = 313.15$ K, $b = 0.00125$ m, $H_n = 0.0055$ m, Silicon plate base case, $q = 63$ kW/m ² , $W=0.0017$ m)	18
Figure 2.3	Comparison with previous experimental work ($Re = 2200$, $T_j = 294.15$ K, $b = 0.0003$ m, $H_n = 0.01$ m, Inconel plate, $W = 0.00162$ m).....	20
Figure 3.1	Comparison of different rectangular step cases investigated.....	22
Figure 3.2	Velocity vector map ($Re = 750$, base rectangular case, $a = 0.00025$ m, $H_n = 0.0055$ m, $W = 0.0017$ m)	25
Figure 3.3	Free surface height distribution for different Reynolds number ($H_n = 0.0055$ m, $W = 0.0017$ m)	26
Figure 3.4	Interface temperatures for varying Reynolds number ($T_j = 313.15$ K, $b = 0.00125$ m, $H_n = 0.0055$ m, Silicon plate base case, $q = 63$ kW/m ² , $W=0.0017$ m)	27
Figure 3.5	Local heat transfer coefficient for various Reynolds numbers ($T_j = 313.15$ K, $b = 0.00125$ m, $H_n = 0.0055$ m, Silicon plate base case, $q = 63$ kW/m ² , $W=0.0017$ m)	28
Figure 3.6	Local Nusselt number for different Reynolds number ($T_j = 313.15$ K, $b = 0.00125$ m, $H_n = 0.0055$ m, Silicon plate base case, $q = 63$ kW/m ² , $W=0.0017$ m)	31
Figure 3.7	Local heat transfer coefficient for various indentation sizes ($Re = 750$, $T_j = 313.15$ K, $b = 0.00125$ m, $H_n = 0.0055$ m, Silicon plate base case, $q = 63$ kW/m ² , $W=0.0017$ m)	32

Figure 3.8	Local Nusselt number for various indentation sizes ($Re = 750$, $T_j = 313.15$ K, $b = 0.00125$ m, $H_n = 0.0055$ m, Silicon plate base case, $q = 63$ kW/m ² , $W=0.0017$ m).....	33
Figure 3.9	Local heat transfer coefficient for different surface geometry configurations ($Re = 750$, $T_j = 313.15$ K, $b = 0.00125$ m, $H_n = 0.0055$ m, Silicon plate, $q = 63$ kW/m ² , $W=0.0017$ m, $a = 0.00025$ m)	36
Figure 3.10	Local Nusselt number for different surface geometry configurations ($Re = 750$, $T_j = 313.15$ K, $b = 0.00125$ m, $H_n = 0.0055$ m, Silicon plate, $q = 63$ kW/m ² , $W=0.0017$ m, $a = 0.00025$ m)	37
Figure 3.11	Local Nusselt number for varying indentation depths Case A ($Re = 750$, $T_j = 313.15$ K, $b = 0.00125$ m, $H_n = 0.0055$ m, Silicon plate, $q = 63$ kW/m ² , $W=0.0017$ m)	39
Figure 3.12	Local Nusselt number for varying indentation depths Case B ($Re = 750$, $T_j = 313.15$ K, $b = 0.00125$ m, $H_n = 0.0055$ m, Silicon plate, $q = 63$ kW/m ² , $W=0.0017$ m)	40
Figure 3.13	Interface temperature variation for different plate materials ($Re = 750$, $T_j = 313.15$ K, $b = 0.00125$ m, $H_n = 0.0055$ m, $q = 63$ kW/m ² , $W=0.0017$ m).....	42
Figure 3.14	Variation in local Nusselt number for different plate materials ($Re = 750$, $T_j = 313.15$ K, $b = 0.00125$ m, $H_n = 0.0055$ m, $q = 63$ kW/m ² , $W=0.0017$ m).....	43
Figure 3.15	Interface temperature variation for different materials (R134a) ($Re = 1500$, $T_j = 253.15$ K, $b = 0.00125$ m, $H_n = 0.0055$ m, $q = 63$ kW/m ² , $W=0.0017$ m).....	45
Figure 3.16	Local heat transfer coefficient variation for different materials (R134a) ($Re = 1500$, $T_j = 253.15$ K, $b = 0.00125$ m, $H_n = 0.0055$ m, $q = 63$ kW/m ² , $W=0.0017$ m).....	46
Figure 3.17	Local Nusselt number variation for different materials (R134a) ($Re = 1500$, $T_j = 253.15$ K, $b = 0.00125$ m, $H_n = 0.0055$ m, $q = 63$ kW/m ² , $W=0.0017$ m).....	47
Figure 3.18	Isothermal lines (in degrees Celsius) within the plate for different Reynolds number ($T_j = 313.15$ K, $b = 0.00125$ m, $H_n = 0.0055$ m, Silicon plate, $q = 63$ kW/m ² , $W=0.0017$ m).....	49

Figure 3.19	Isothermal lines (in degrees Celsius) within the plate for different surface configurations ($Re = 750$, $T_j = 313.15$ K, $b = 0.00125$ m, $H_n = 0.0055$ m, Silicon plate, $q = 63$ kW/m ² , $W=0.0017$ m)	50
Figure 3.20	Isothermal lines (in degrees Celsius) within the plate for different materials ($Re = 750$, $T_j = 313.15$ K, $b = 0.00125$ m, $H_n = 0.0055$ m, $q = 63$ kW/m ² , $W=0.0017$ m).....	51
Figure 3.21	Isothermal lines (in degrees Celsius) for various materials (R134a) ($Re = 1500$, $T_j = 253.15$ K, $b = 0.00125$ m, $H_n = 0.0055$ m, $q = 63$ kW/m ² , $W=0.0017$ m).....	53
Figure 3.22	Comparison of different triangular ribbed geometries investigated.....	55
Figure 3.23	Velocity vector distribution for triangle ribs ($Re = 750$, $T_j = 313.15$ K, $b = 0.00125$ m, $H_n = 0.0055$ m, Silicon plate, $q = 63$ kW/m ² , $W=0.0017$ m)	56
Figure 3.24	Free surface height distribution for triangle ribs ($Re = 750$, $T_j = 313.15$ K, $b = 0.00125$ m, $H_n = 0.0055$ m, Silicon plate, base case, $q = 63$ kW/m ² , $W=0.0017$ m)	57
Figure 3.25	Interface temperature for varying Reynolds number ($Re = 750$, $T_j = 313.15$ K, $b = 0.00125$ m, $H_n = 0.0055$ m, Silicon plate, base case, $q = 63$ kW/m ² , $W=0.0017$ m)	58
Figure 3.26	Local heat transfer coefficient for varying Reynolds number ($Re = 750$, $T_j = 313.15$ K, $b = 0.00125$ m, $H_n = 0.0055$ m, Silicon plate, base case, $q = 63$ kW/m ² , $W=0.0017$ m)	59
Figure 3.27	Local Nusselt number for varying Reynolds number ($Re = 750$, $T_j = 313.15$ K, $b = 0.00125$ m, $H_n = 0.0055$ m, Silicon plate, base case, $q = 63$ kW/m ² , $W=0.0017$ m)	61
Figure 3.28	Local Nusselt number for varying plate geometries ($Re = 750$, $T_j = 313.15$ K, $b = 0.00125$ m, $H_n = 0.0055$ m, Silicon plate, $q = 63$ kW/m ² , $W=0.0017$ m)	62
Figure 3.29	Local Nusselt number for varying indentation depths ($Re = 750$, $T_j = 313.15$ K, $b = 0.00125$ m, $H_n = 0.0055$ m, Silicon plate, base case, $q = 63$ kW/m ² , $W=0.0017$ m)	65

Figure 3.30	Local Nusselt number for varying indentation depths ($Re = 750$, $T_j = 313.15$ K, $b = 0.00125$ m, $H_n = 0.0055$ m, Silicon plate, Case B, $q = 63$ kW/m ² , $W=0.0017$ m)	66
Figure 3.31	Isothermal lines (in degrees Celsius) within the plate for different Reynolds number ($T_j = 313.15$ K, $a=0.00025$ b = 0.00125 m, $H_n = 0.0055$ m, Silicon plate, $q = 63$ kW/m ² , $W=0.0017$ m)	67
Figure 3.32	Isothermal lines (in degrees Celsius) within the plate for different surface configurations ($Re = 750$, $T_j = 313.15$ K, $a = 0.00025$, $b = 0.00125$ m, $H_n = 0.0055$ m, Silicon plate, $q = 63$ kW/m ² , $W=0.0017$ m)	68
Figure 3.33	Comparison of the different sinusoidal geometries studied.....	69
Figure 3.34	Typical velocity vectors for the sinusoidal case ($Re = 750$, $T_j = 313.15$ K, $b = 0.00125$ m, $H_n = 0.0055$ m, Silicon plate, $q = 63$ kW/m ² , $W=0.0017$ m)	70
Figure 3.35	Free surface height distribution for different Reynolds number ($T_j = 313.15$ K, $b = 0.00125$ m, $H_n = 0.0055$ m, Silicon plate, $q = 63$ kW/m ² , $W=0.0017$ m)	72
Figure 3.36	Interface temperature for various Reynolds number ($T_j = 313.15$ K, $b = 0.00125$ m, $H_n = 0.0055$ m, Silicon plate, $q = 63$ kW/m ² , $W=0.0017$ m)	73
Figure 3.37	Local heat transfer coefficient for varying Reynolds number ($T_j = 313.15$ K, $b = 0.00125$ m, $H_n = 0.0055$ m, Silicon plate, $q = 63$ kW/m ² , $W=0.0017$ m)	74
Figure 3.38	Local Nusselt number for varying Reynolds number ($T_j = 313.15$ K, $b = 0.00125$ m, $H_n = 0.0055$ m, Silicon plate, $q = 63$ kW/m ² , $W=0.0017$ m)	76
Figure 3.39	Interface temperature variation for different indentation depths ($T_j = 313.15$ K, $b = 0.00125$ m, $H_n = 0.0055$ m, Silicon plate, $q = 63$ kW/m ² , $W=0.0017$ m)	77
Figure 3.40	Local Nusselt number variation for different indentation depths ($T_j = 313.15$ K, $b = 0.00125$ m, $H_n = 0.0055$ m, Silicon plate, $q = 63$ kW/m ² , $W=0.0017$ m)	78

Figure 3.41	Local Nusselt number variation for different surface geometries ($T_j = 313.15$ K, $b = 0.00125$ m, $H_n = 0.0055$ m, Silicon plate, $q = 63$ kW/m ² , $W=0.0017$ m)	80
Figure 3.42	Isothermal lines (in degrees Celsius) for different Reynolds number ($T_j = 313.15$ K, $b = 0.00125$ m, $H_n = 0.0055$ m, Silicon plate, $q = 63$ kW/m ² , $W=0.0017$ m)	81
Figure 3.43	Isothermal lines (in degrees Celsius) for different plate configurations ($Re = 750$, $T_j = 313.15$ K, $b = 0.00125$ m, $H_n = 0.0055$ m, Silicon plate, $q = 63$ kW/m ² , $W=0.0017$ m)	82
Figure 4.1	Interface temperature for different times ($Re = 750$, $T_j = 313.15$ K, $b = 0.00125$ m, $H_n = 0.0055$ m, Silicon plate base case, $q = 63$ kW/m ² , $W=0.0017$ m)	85
Figure 4.2	Local heat transfer coefficient for different times ($Re = 750$, $T_j = 313.15$ K, $b = 0.00125$ m, $H_n = 0.0055$ m, Silicon plate base case, $q = 63$ kW/m ² , $W=0.0017$ m)	86
Figure 4.3	Local Nusselt number for different Fourier values ($Re = 750$, $T_j = 313.15$ K, $b = 0.00125$ m, $H_n = 0.0055$ m, Silicon plate base case, $q = 63$ kW/m ² , $W=0.0017$ m)	88
Figure 4.4	Variation in maximum non-dimensional temperature at the interface, maximum non-dimensional temperature within the solid, and the maximum-to-minimum non-dimensional temperature difference at the interface for different Reynolds number ($T_j = 313.15$ K, $b = 0.00125$ m, $H_n = 0.0055$ m, Silicon plate base case, $q = 63$ kW/m ² , $W=0.0017$ m)	89
Figure 4.5	Variation of average heat transfer coefficient and average Nusselt number with Fourier number ($T_j = 313.15$ K, $b = 0.00125$ m, $H_n = 0.0055$ m, Silicon plate base case, $q = 63$ kW/m ² , $W=0.0017$ m)	90
Figure 4.6	Variation in maximum non-dimensional temperature at the interface, maximum non-dimensional temperature within the solid, and the maximum-to-minimum non-dimensional temperature difference at the interface for different indentation depths ($Re = 750$, $T_j = 313.15$ K, $b = 0.00125$ m, $H_n = 0.0055$ m, Silicon plate base case, $q = 63$ kW/m ² , $W=0.0017$ m)	92

Figure 4.7	Variation of average heat transfer coefficient and average Nusselt number with Fourier number for different indentation depths ($Re = 750$, $T_j = 313.15$ K, $b = 0.00125$ m, $H_n = 0.0055$ m, Silicon plate base case, $q = 63$ kW/m ² , $W=0.0017$ m)93
Figure 4.8	Variation in maximum non-dimensional temperature at the interface, maximum non-dimensional temperature within the solid, and the maximum-to-minimum non-dimensional temperature difference at the interface for different indentation depths ($Re = 750$, $T_j = 313.15$ K, $b = 0.00125$ m, $H_n = 0.0055$ m, Silicon plate, Case A, $q = 63$ kW/m ² , $W=0.0017$ m)94
Figure 4.9	Variation of average heat transfer coefficient and average Nusselt number with Fourier number for different indentation depths ($Re = 750$, $T_j = 313.15$ K, $b = 0.00125$ m, $H_n = 0.0055$ m, Silicon plate, Case A, $q = 63$ kW/m ² , $W=0.0017$ m)95
Figure 4.10	Variation in maximum non-dimensional temperature at the interface, maximum non-dimensional temperature within the solid, and the maximum-to-minimum non-dimensional temperature difference at the interface for different indentation depths ($Re = 750$, $T_j = 313.15$ K, $b = 0.00125$ m, $H_n = 0.0055$ m, Silicon plate, Case B, $q = 63$ kW/m ² , $W=0.0017$ m)97
Figure 4.11	Variation of average heat transfer coefficient and average Nusselt number with Fourier number for different indentation depths ($Re = 750$, $T_j = 313.15$ K, $b = 0.00125$ m, $H_n = 0.0055$ m, Silicon plate, Case B, $q = 63$ kW/m ² , $W=0.0017$ m)98
Figure 4.12	Variation in maximum non-dimensional temperature at the interface, maximum non-dimensional temperature within the solid, and the maximum-to-minimum non-dimensional temperature difference at the interface for different materials ($Re = 750$, $T_j = 313.15$ K, $b = 0.00125$ m, $H_n = 0.0055$ m, base case, $q = 63$ kW/m ² , $W=0.0017$ m)99
Figure 4.13	Variation of average heat transfer coefficient and average Nusselt number with Fourier number for different materials ($Re = 750$, $T_j = 313.15$ K, $b = 0.00125$ m, $H_n = 0.0055$ m, base case, $q = 63$ kW/m ² , $W=0.0017$ m) 100

Figure 4.14	Variation in maximum non-dimensional temperature at the interface, maximum non-dimensional temperature within the solid, and the maximum-to-minimum non-dimensional temperature difference at the interface for different materials (R134a) ($Re = 1500$, $T_j = 313.15$ K, $b = 0.00125$ m, $H_n = 0.0055$ m, base case, $q = 63$ kW/m ² , $W=0.0017$ m)	102
Figure 4.15	Variation of average heat transfer coefficient and average Nusselt number with Fourier number for different materials (R134a) ($Re = 1500$, $T_j = 313.15$ K, $b = 0.00125$ m, $H_n = 0.0055$ m, base case, $q = 63$ kW/m ² , $W=0.0017$ m)	103
Figure 4.16	Interface temperature for different times ($Re = 750$, $T_j = 313.15$ K, $b = 0.00125$ m, $H_n = 0.0055$ m, Silicon plate base case, $q = 63$ kW/m ² , $W=0.0017$ m)	105
Figure 4.17	Local heat transfer coefficient for different times ($Re = 750$, $T_j = 313.15$ K, $b = 0.00125$ m, $H_n = 0.0055$ m, Silicon plate base case, $q = 63$ kW/m ² , $W=0.0017$ m)	108
Figure 4.18	Local Nusselt number for different Fourier values ($Re = 750$, $T_j = 313.15$ K, $b = 0.00125$ m, $H_n = 0.0055$ m, Silicon plate base case, $q = 63$ kW/m ² , $W=0.0017$ m)	109
Figure 4.19	Variation in maximum non-dimensional temperature at the interface, maximum non-dimensional temperature within the solid, and the maximum-to-minimum non-dimensional temperature difference at the interface for different Reynolds number ($T_j = 313.15$ K, $b = 0.00125$ m, $H_n = 0.0055$ m, Silicon plate base case, $q = 63$ kW/m ² , $W=0.0017$ m)	111
Figure 4.20	Variation of average heat transfer coefficient and average Nusselt number with Fourier number ($T_j = 313.15$ K, $b = 0.00125$ m, $H_n = 0.0055$ m, Silicon plate base case, $q = 63$ kW/m ² , $W=0.0017$ m)	112
Figure 4.21	Variation in maximum non-dimensional temperature at the interface, maximum non-dimensional temperature within the solid, and the maximum-to-minimum non-dimensional temperature difference at the interface for different indentation depths ($Re = 750$, $T_j = 313.15$ K, $b = 0.00125$ m, $H_n = 0.0055$ m, Silicon plate base case, $q = 63$ kW/m ² , $W=0.0017$ m)	113

Figure 4.22	Variation of average heat transfer coefficient and average Nusselt number for different indentation depths ($Re = 750$, $T_j = 313.15$ K, $b = 0.00125$ m, $H_n = 0.0055$ m, Silicon plate base case, $q = 63$ kW/m ² , $W=0.0017$ m)	114
Figure 4.23	Variation in maximum non-dimensional temperature at the interface, maximum non-dimensional temperature within the solid, and the maximum-to-minimum non-dimensional temperature difference at the interface for different indentation depths ($Re = 750$, $T_j = 313.15$ K, $b = 0.00125$ m, $H_n = 0.0055$ m, Silicon plate, Case A, $q = 63$ kW/m ² , $W=0.0017$ m)	116
Figure 4.24	Variation of average heat transfer coefficient and average Nusselt number for different indentation depths ($T_j = 313.15$ K, $b = 0.00125$ m, $H_n = 0.0055$ m, Silicon plate, Case A, $q = 63$ kW/m ² , $W=0.0017$ m)	117
Figure 4.25	Variation in maximum non-dimensional temperature at the interface, maximum non-dimensional temperature within the solid, and the maximum-to-minimum non-dimensional temperature difference at the interface for different indentation depths ($Re = 750$, $T_j = 313.15$ K, $b = 0.00125$ m, $H_n = 0.0055$ m, Silicon plate, Case B, $q = 63$ kW/m ² , $W=0.0017$ m)	118
Figure 4.26	Variation of average heat transfer coefficient and average Nusselt number for different indentation depths ($T_j = 313.15$ K, $b = 0.00125$ m, $H_n = 0.0055$ m, Silicon plate, Case B, $q = 63$ kW/m ² , $W=0.0017$ m).....	119
Figure 4.27	Interface temperature for different times ($Re = 750$, $T_j = 313.15$ K, $b = 0.00125$ m, $H_n = 0.0055$ m, Silicon plate, sine base case, $q = 63$ kW/m ² , $W=0.0017$ m).....	121
Figure 4.28	Local heat transfer coefficient for different times ($Re = 750$, $T_j = 313.15$ K, $b = 0.00125$ m, $H_n = 0.0055$ m, Silicon plate base case, $q = 63$ kW/m ² , $W=0.0017$ m).....	122
Figure 4.29	Local Nusselt number for different Fourier values ($Re = 750$, $T_j = 313.15$ K, $b = 0.00125$ m, $H_n = 0.0055$ m, Silicon plate base case, $q = 63$ kW/m ² , $W=0.0017$ m)	124

Figure 4.30	Variation in maximum non-dimensional temperature at the interface, maximum non-dimensional temperature within the solid, and the maximum-to-minimum non-dimensional temperature difference at the interface for different Reynolds number ($T_j = 313.15$ K, $b = 0.00125$ m, $H_n = 0.0055$ m, Silicon plate, sine base case, $q = 63$ kW/m ² , $W=0.0017$ m) 125
Figure 4.31	Variation of average heat transfer coefficient and average Nusselt number with Fourier number ($T_j = 313.15$ K, $b = 0.00125$ m, $H_n = 0.0055$ m, Silicon plate, sine base case, $q = 63$ kW/m ² , $W=0.0017$ m) 126
Figure 4.32	Variation in maximum non-dimensional temperature at the interface, maximum non-dimensional temperature within the solid, and the maximum-to-minimum non-dimensional temperature difference at the interface for different indentation depths ($Re = 750$, $T_j = 313.15$ K, $b = 0.00125$ m, $H_n = 0.0055$ m, Silicon plate, sine base case, $q = 63$ kW/m ² , $W=0.0017$ m) 128
Figure 4.33	Variation of average heat transfer coefficient and average Nusselt number with Fourier number for different indentation depths ($T_j = 313.15$ K, $b = 0.00125$ m, $H_n = 0.0055$ m, Silicon plate, sine base case, $q = 63$ kW/m ² , $W=0.0017$ m) 129
Figure 4.34	Variation in maximum non-dimensional temperature at the interface, maximum non-dimensional temperature within the solid, and the maximum-to-minimum non-dimensional temperature difference at the interface for different indentation depths ($Re = 750$, $T_j = 313.15$ K, $b = 0.00125$ m, $H_n = 0.0055$ m, Silicon plate, sine case A, $q = 63$ kW/m ² , $W=0.0017$ m) 130
Figure 4.35	Variation of average heat transfer coefficient and average Nusselt number for different indentation depths ($T_j = 313.15$ K, $b = 0.00125$ m, $H_n = 0.0055$ m, Silicon plate, sine case A, $q = 63$ kW/m ² , $W=0.0017$ m) 131
Figure 4.36	Variation in maximum non-dimensional temperature at the interface, maximum non-dimensional temperature within the solid, and the maximum-to-minimum non-dimensional temperature difference at the interface for different indentation depths ($Re = 750$, $T_j = 313.15$ K, $b = 0.00125$ m, $H_n = 0.0055$ m, Silicon plate, sine case B, $q = 63$ kW/m ² , $W=0.0017$ m) 133

Figure 4.37 Variation of average heat transfer coefficient and average Nusselt number for different indentation depths ($T_j = 313.15$ K, $b = 0.00125$ m, $H_n = 0.0055$ m, Silicon plate, sine case B, $q = 63$ kW/m², $W=0.0017$ m) 134

List of Symbols

a	indentation depth [m]
b	thickness of the disk [m]
c_p	Specific heat at constant pressure [kJ / kg K]
Fo	Fourier number, $\alpha_f t / W^2$
g	Acceleration due to gravity [m / s^2]
h	Heat-transfer coefficient [$W / m^2 K$]
hav	Average heat-transfer coefficient [$W / m^2 K$]
H_n	Height of nozzle from impingement surface [m]
k	Thermal conductivity [$W / m K$]
n	Coordinate normal to the free surface [m]
Nu	Nusselt number
Nu_{av}	Average Nusselt number
p	Pressure [Pa]
q	Heat flux [W / m^2]
\bar{q}	Average heat flux [W / m^2]
q_o	Total heat transfer rate [W]
Re	Reynolds number, $W v_j / \nu_f$
t	Time [s]
T	Temperature [K]

\bar{T}	Average temperature [K]
T_j	Temperature of Jet [K]
v_i	Initial velocity [m / s]
v_j	Jet velocity [m / s]
v_r	Radial velocity [m / s]
v_t	Velocity tangential to the free surface [m / s]
v_z	Axial velocity [m / s]
W	Width of nozzle [m]
x	Horizontal coordinate [m]
y	Vertical coordinate [m]
z	Axial coordinate [m]

Greek Symbols

α	Thermal diffusivity [m ² / s]
δ	Height of free surface from impinging surface [m]
η	Coordinate perpendicular to the solid-fluid interface [m]
μ	Dynamic viscosity [kg / m s]
ξ	Coordinate along solid-fluid interface [m]
ν	Kinematic viscosity [m ² / s]
ρ	Density [kg / m ³]
σ	Surface tension coefficient [N / m]

Subscripts

atm	Atmospheric
f	Fluid
int	Interface
j	Jet
r	Radial direction
s	Solid
w	Bottom surface of disk
x	Horizontal direction
y	Vertical direction
z	Axial direction

Abstract

Free liquid-jet impingement is well researched due to its high heat transfer ability and ease of implementation. This study considers both the steady state and transient heating of a patterned plate under slot-free-liquid jet impingement. The primary working fluid was water (H₂O) and the plate material considered was silicon. Calculations were done for Reynolds number (Re) ranging from 500 to 1000 and indentation depths from 0.000125 to 0.0005 m for three different surface configurations. The effect of using different plate materials and R-134a as the working fluid were explored for the rectangular step case. The distributions of the local and average heat-transfer coefficient and the local and average Nusselt number were calculated for each case. A numerical model based in the FIDAP computer code was created to solve the conjugate heat transfer problem. The model used was developed for Cartesian coordinates for both steady state and transient conditions.

Results show that the addition of surface geometry alters the fluid flow and heat transfer values. The highest heat-transfer coefficients occur at points where the fluid flow interacts with the surface geometry. The lowest heat-transfer coefficients are found in the indentations between the changes in geometry. The jet velocity has a large impact on the heat transfer values for all cases, with increasing jet velocity showing increased local heat-transfer coefficients and Nusselt number. It is observed that increasing the indentation depth for the rectangular and sinusoidal surfaces leads to a decrease in local

heat transfer whereas for triangular patterns, a higher depth results in higher heat-transfer coefficient. The transient analysis showed that changing surface geometry had little effect on the time required to reach steady state. The selection of plate material has an impact on both the final maximum temperatures and the time required to reach steady state, with both traits being tied to the thermal diffusivity (α) of the material.

Chapter 1

Introduction and Literature Review

1.1 Introduction

Impinging liquid and gaseous jets have been used widely due to their ease of implementation and high heat-transfer coefficients. Jet impingement is used for cooling, heating and drying in situations where high heat-transfer coefficients are desired. Typical applications include cooling turbine blades and electrical equipment, drying of textiles and other wetted surfaces, and heating or cooling of metal plates. As these applications require heating and cooling to be at the maximum speed possible to maintain efficiency, it follows that the use of a process such as jet impingement is a viable option. There are several flow configurations for jet impingement. In submerged jet impingement, the jet discharges into a fluid that is often the same as the jet itself. As the jet impinges on the surface a region where the jet velocity is unaffected by the ambient fluid forms, this zone is called the potential core. As the potential core ends, the centerline velocity decreases and vortices may exist. In submerged jet impingement, it may also be beneficial to the transfer process to confine the jet flow. In submerged jet impingement, the gravitational forces are often negligible. Free jet impingement is the process in which a fluid jet discharges into a gaseous environment. The jet free surface forms from the nozzle exit and continues in the direction of the outflow. Fluid flow in a free jet is dependent on surface tension, pressure, and gravitational forces. As the jet impinges on the surface, a

region called the stagnation zone forms. The region outside of this zone is referred to as the wall jet or parallel flow zone. At some distance downstream, a hydraulic jump may form due to deceleration of the fluid velocity.

Jet impingement is also dependent on the geometry of the jet that is employed. In instances where the fluid discharges from a tube or circular nozzle along the axis, it is referred to as an axial jet. If the jet discharges from the radial direction, it is called a radial jet. A slot or planar jet is one that discharges from a rectangular nozzle and does not radially spread. Liquid jets can also be arrayed to provide the high level heat transport qualities present in the stagnation zone over a larger area. Planar jets are often arranged in rows while axisymmetric jets can be arranged in square or triangle formations. Ultimately, jet impingement may be most useful in the cooling of high end computer components. As microprocessors and other high heat producing electronics evolve, it becomes evident that using air cooling alone will not provide adequate performance. Jet impingement has the ability to remove large amounts of heat effectively from these high heat-flux environments.

1.2 Literature Review

1.2.1 Steady State Jet Impingement on a Heated Flat Plate

There has been considerable research into the heat transfer onto flat plates over the past 60 years. Glauert [1] studied both planar and axisymmetric jets impinging upon a plate surface. Results were found explicitly for the laminar case. Inada et al. [2] compared experimental and numerical results from a two-dimensional water jet impinging on a flat plate. In this example, a uniform heat flux was present at the bottom

of the plate. The primary aim was to determine how the height of the nozzle affected the heat-transfer coefficients. It was determined that the maximum heat-transfer coefficient was present near 0.7 for the ratio of nozzle height to nozzle width. Interestingly, the maximum heat-transfer coefficient was located in nearly the same place for both the uniform heat flux and uniform temperature boundary conditions at the bottom of the plate.

Wang et al. [3] performed experimental work with a free jet impinging upon a disk. It was found that increasing the ratio of conductivity of the fluid to that of the solid increased the local heat-transfer coefficient, assuming all other variables remained constant. Vader et al. [4] studied a water jet impinging on a flat plate with heat fluxes between 0.25 and 1.00 $MW m^{-2}$. The speed of the jet allowed for a free stream turbulence to develop, allowing for the increase in heat-transfer coefficient. It was also found that the Prandtl number had a large impact on the heat transfer enhancement.

Webb and Ma [5] conducted a lengthy literature review of jet impingement that included several examples of free jet impingement. Sezai and Mohamad [6] performed a numerical investigation of laminar slot jet arrays impinging onto a flat plate. It was found that the jet to jet spacing had little effect on the Nusselt number. Bula and Rahman [7] did extensive work into both uniform and discretely heated flat plates. The cooling fluid in these cases was the lubricant MIL 7808, primarily because of its uses in the aeronautic industry. The use of a high Prandtl number fluid necessitated the use of varied fluid parameters because the temperature had a large effect on the viscosity and conductivity of the fluid. It was found that increasing the jet velocity and the Reynolds numbers increased the Nusselt number. Increasing the thickness of the plate had an

inverse effect on the Nusselt number, though at a point it became almost entirely one-dimensional conduction. The thermal conductivity of the solid also had a large impact on the maximum temperature and Nusselt number. If used, the position of discrete heat sources greatly impacts the temperature of the disk.

Park et al. [8] performed numerical work to determine the best method for numerically solving the velocity field in jet impingement. The Galerkin method was found to be suitable when compared against experimental results. Sarghini and Ruocco [9] studied the use of discrete heating elements and buoyancy to determine their effects on conjugate heat transfer. There was an effort made to determine the impact of natural convection in the presence of low volumetric flow rate jet impingement. In this work air and water were the working fluids and the solids were alumina and epoxy-fiberglass. Lee et al. [10] investigated the effect of nozzle size on the heat transfer on a constant heat flux plate. In this work, a fully developed turbulent jet was used with a Reynolds number of 23,000. The experimental system was based on a dimensionless distance between nozzle and plate surface between 2 to 14 and a diameter between 1.36 and 3.40 *cm*. It was found that increasing the nozzle diameter increased the Nusselt number. Narayanan et al [11] ran an experiment with a submerged slot jet impinging on a flat plate. It was found that increased turbulence occurred before the jet impinged upon the plate, resulting in vortices around the stagnation zone. It was assumed this helped increase heat transfer values in the stagnation zone. Gao and Ewing [12] looked at the effect of a confining plate on the heat transfer of a jet impinging upon a flat plate. It was found that confinement plate had little effect on the heat transfer values when the ratio of the height of the nozzle to the diameter of the nozzle was over one. Chen et al. [13] performed a theoretical analysis of

free slot jet impingement on a flat plate. The study examined laminar flow and developed several equations to describe the local heat-transfer coefficients. The equations matched well with experimental and computational data. Baonga et al. [14] conducted an experimental study into a free jet impinging upon a flat disk. Results included the measurement of the hydraulic jump, Nusselt number, and temperatures along the length of the disk. Ibuki et al. [15] ran a series of experiments impinging a slot water jet onto a flat surface both normally and obliquely. The surface angles studied were 90° (normal), 70° , 60° , and 50° with Reynolds number values from 2200 to 8800. During the oblique impingement the highest Nusselt numbers are not symmetric about the axis. Aldabbagh and Mohamad [16] studied the effect of mixed convection of a laminar slot jet impinging on a plate. It was determined that while forced convection lead to higher heat transfer values when compared to jets with mixed convection, the Reynolds number of the jet had more of an effect than the mode of the jet.

Additionally, Zuckerman and Lior [17] did a large survey of the numerical modeling of jet impingement. The effect of nozzle type on initial turbulence, free jet shearing force, pressure drop, and ultimately the velocity profile of the jet are discussed. A comparison of the various turbulence models is described using the computational requirement and accuracy as measures of value. Various experimental and computational techniques from other authors are also described. Ebadian and Lewis [18] performed a review of high-heat-flux removal techniques, including Jet Impingement.

1.2.2 Steady State Jet Impingement on Patterned Surfaces

Compared to flat plates, the research into patterned surfaces is not as extensive. While there is a wide assortment of research available concerning rectangular and triangle fins and hemispherical dimples, nearly all of this research was conducted using air as the working fluid. Gau and Lee [19] used triangular ribs on a flat plate to determine the effect of a patterned surface on heat transfer during jet impingement. The working fluid considered was air from Reynolds number values of 2500 to 11000. Other variables that were changed included the rib height to width ratio and the nozzle height. It was found that once the jet became turbulent, the heat-transfer coefficient increased. Ekkad and Kontrovitz [20] did a similar study investigating a dimpled surface. It was assumed that the dimpled surface would increase heat-transfer coefficients, but it was found in this case that the surface reduced heat-transfer coefficients. The dimple case was also done using air. Lou et al [21] examined the effect of differing geometric surfaces on confined jet impingement using HFE8401. In this study the jet velocities were kept low enough to only consider laminar flow over several surface roughening shapes. It was found that under these low speeds the surface geometries tended to lower the heat transfer because the fluid became trapped in between the surface effects. Sagot et al. [22] performed experiments involving air jets impinging upon a circular plate with rectangular and triangular grooves. The grooves of the plate were 1 *cm* in depth and had a pitch of 2 *cm*. It was shown that the grooves increased heat transfer by 81% when compared to the flat disk studied. Guo et al. [23] conducted jet impingement experiments on micro-pin-finned surfaces using FC-72 as the working fluid. For this boiling problem the parameters modified included fin size, cross flow velocity, and jet velocity. It was

found that the pin-fins greatly enhanced heat transfer but increasing cross-flow reduced the heat transfer experienced by the surface. Xing et al [24] studied a micro ribbed patterned plate with cross flow for the cooling of microchips. In this case the maximum heat transfer enhancement due to micro ribs was found to be 9.6% at the maximum cross flow.

1.2.3 Transient Jet Impingement

Kumagai et al. [25] investigated a transient two-dimensional water jet impinging upon a flat plate with boiling conditions. It was found that the jet began to boil as soon as it struck the plate, leading to vapor being present at the impingement zone. Fujimoto et al. [26] numerically solved a transient circular free jet impinging on a hot surface. Finite element results included the flow solution and temperature distribution within the solid. Saniei and Yan [27] investigated the effect of air jets impinging onto a rotating disk in open space. The system parameters changed included the jet Reynolds numbers from 6800 to 48000, different jet heights, and different rotation speeds. A transient technique was used to measure the heat transfer. Hsieh et al. [28] studied the transient effect of surface roughness for a confined air jet impinging upon a rotating surface. For several surface patterns it was demonstrated that heat transfer enhancement occurred with the patterned surface. The presence of rotation decreased the heat-transfer coefficient when compared to a non-rotating example.

Rahman et al. [29] investigated the transient conjugate heat transfer of a free jet impinging on a flat plate. In this investigation the working fluid was MIL-7808 and the solid materials simulated included copper, constantan, and silicon. Computed results

included the heat-transfer coefficient and Nusselt number. Sarghini and Ruocco [30] investigated the transient effect of buoyancy and natural convection in the case of an air jet impinging on a plate. It was demonstrated that the effect of conjugate heat transfer could not be ignored when considering the early part of the transient process. Yan et al [31] studied the transient heat transfer of an air jet impinging on rib-roughened walls. By changing the surface geometry, jet Reynolds number, and nozzle to plate spacing it was observed that the best heat transfer enhancement occurred when the ribs were at a 45 degree angle.

Lin et al. [32] performed steady state and transient experimental work with horizontal heat sinks under confined slot jet impingement. Their results indicated that transient heating is strongly dependent on the jet Reynolds number and the ratio of nozzle height to nozzle width. Narayanan et al. [33] studied the thermal structures present during slot jet impingement on a flat plate. It was shown that during the transient process there were slight variances in the temperature profile at the surface. These variances were more pronounced when the nozzle-to-plate spacing is small. Lallave and Rahman [34] used numerical simulation to determine the effect of a rotating circular plate under partially confined liquid jet impingement. Calculations were completed with varying Reynolds number (225-900), confinement ratios, disk thickness, and different materials. It was determined that increasing the jet Reynolds number decreased the time to steady state, while increasing disk thickness caused an increase in transient times.

1.3 Objectives of the Present Investigation

Even with the large amount of available data on free jet impingement, there remains a need for more information on the effect of surface geometry on heat transfer values. The effect of using a fluid such as water is considered important due to its superior heat capacity and thermal performance. There is also little available information for the transient case, making it difficult to determine the effect of the geometry on the transient heating of these systems.

The present work will determine the effect of surface geometry on the transient and steady state heating of a plate being cooled by free jet impingement. The numerical simulations presented were run with three geometries: rectangular steps, triangular ribs, and sinusoidal wave shaped surfaces. The results presented for the steady state will include the temperature at the solid-liquid interface, local and average heat-transfer coefficient, and the local and average Nusselt number. For the transient case the development of the interface temperature, local heat-transfer coefficients, and Nusselt number with time are presented.

The following parameters are considered for the steady and transient heat transfer processes:

1. Jet Reynolds number.
2. Solid and fluid properties.
3. Plate geometry.
4. Depth of plate geometry.

Chapter 2

Modeling and Computation

2.1 Jet Impingement on Patterned Surfaces: Steady State

In this work, a two-dimensional jet discharging from a slot nozzle impinging normally onto a solid plate heated by a uniform source as shown in Figure 2.1 was investigated. Considering that only the plate geometry is changed, the governing equations and boundary conditions remain unchanged from geometry to geometry. If the fluid considered is incompressible with density dependent only on temperature, the equations for conservation of mass, momentum, and energy in the Cartesian coordinate system are written as [25]:

$$\nabla \cdot \vec{V} = 0 \quad (2.1)$$

$$(\vec{V} \cdot \nabla) \cdot V_y = -g - \frac{1}{\rho_f} \frac{\partial p}{\partial y} + \mu \nabla^2 V_y \quad (2.2)$$

$$(\vec{V} \cdot \nabla) \cdot V_x = -\frac{1}{\rho_f} \frac{\partial p}{\partial x} + \mu \nabla^2 V_x \quad (2.3)$$

$$(\vec{V} \cdot \nabla) T_f = \alpha_f \nabla^2 T_f \quad (2.4)$$

The heat transfer inside the solid can be expressed using the following equation for conduction:

$$\nabla^2 T_s = 0 \quad (2.5)$$

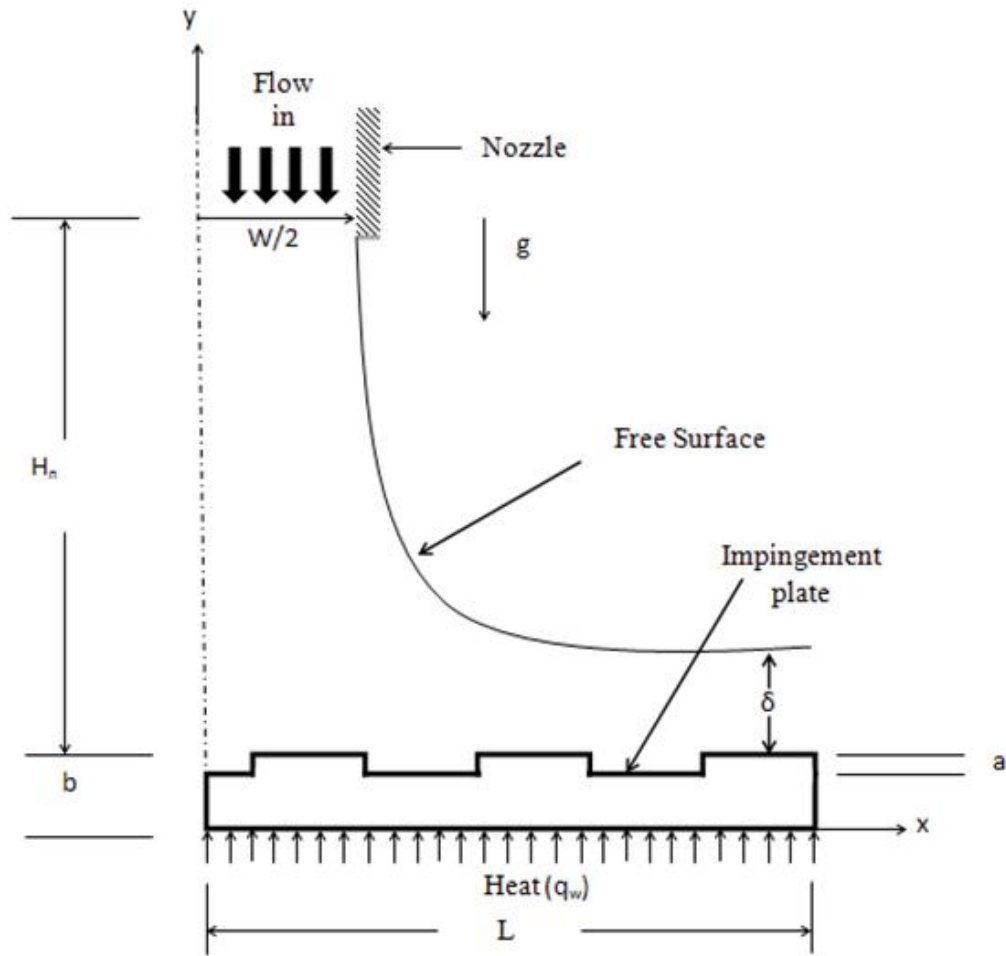


Figure 2.1 Schematic of a free slot jet impinging on a uniformly heated plate with a patterned surface

These equations are subject to the following boundary conditions:

$$\text{At } x = 0, 0 \leq y \leq b: \frac{\partial T_s}{\partial x} = 0 \quad (2.6)$$

$$\text{At } x = 0, b \leq y \leq H_n: \nu_x = 0, \frac{\partial T_f}{\partial x} = 0 \quad (2.7)$$

$$\text{At } x = L, 0 \leq y \leq b, \frac{\partial T_s}{\partial x} = 0 \quad (2.8)$$

$$\text{At } x = L, b \leq y \leq \delta: p = p_{atm}, \frac{\partial T_f}{\partial x} = 0 \quad (2.9)$$

$$\text{At solid-fluid interface: } T_s = T_f, \nu_x = 0, \nu_y = 0, k_s \frac{\partial T_s}{\partial \eta} = k_f \frac{\partial T_f}{\partial \eta} \quad (2.10)$$

$$\text{At } y = b + H_m, 0 \leq x \leq W/2: \nu_y = 0, \nu_x = -\nu_j, T_f = T_j \quad (2.11)$$

At the free surface the boundary conditions can be expressed by:

At $y = \delta, W/2 < x < L$:

$$\frac{dy}{dx} = \frac{\nu_y}{\nu_x}, p = p_{atm} - \frac{\sigma \frac{d^2 \delta}{dx^2}}{\left[1 + \left(\frac{d\delta}{dx}\right)^2\right]^{3/2}}, \frac{\partial \nu_t}{\partial n} = 0, \frac{\partial T_f}{\partial n} = 0 \quad (2.12)$$

The local heat-transfer coefficient and the average heat-transfer coefficient are described as:

$$h = \frac{q}{(T_{int} - T_j)} \quad (2.13)$$

$$h_{av} = \frac{1}{L(T_{int} - T_j)} \int_0^L h(T_{int} - T_j) dx \quad (2.14)$$

where \bar{T}_{int} is defined as the average temperature along the interface. The local and average Nusselt number can be calculated according to the following:

$$Nu = \frac{hW}{k_f} \quad (2.15)$$

$$Nu_{av} = \frac{h_{av}W}{k_f} \quad (2.16)$$

2.2 Jet Impingement on Patterned Surfaces: Transient Analysis

In this work, a two-dimensional jet discharging from a slot nozzle impinging normally onto a solid plate heated by a uniform source as shown in Figure 2.1 was investigated. Considering that only the plate geometry is changed, the governing equations and boundary conditions remain unchanged from geometry to geometry. The power is turned on to the heat source at $t = 0$ and heat is supplied to the system. If the fluid considered is incompressible with density dependent only on temperature, the equations for conservation of mass, momentum, and energy in the Cartesian coordinate system are written as [25]:

$$\nabla \cdot \vec{V} = 0 \quad (2.17)$$

$$(\vec{V} \cdot \nabla) \cdot V_y = -g - \frac{1}{\rho_f} \frac{\partial p}{\partial y} + \mu \nabla^2 V_y \quad (2.18)$$

$$(\vec{V} \cdot \nabla) \cdot V_x = -\frac{1}{\rho_f} \frac{\partial p}{\partial x} + \mu \nabla^2 V_x \quad (2.19)$$

$$\frac{\partial T_f}{\partial t} + (\vec{V} \cdot \nabla) T_f = \alpha_f \nabla^2 T_f \quad (2.20)$$

The conduction inside the equation can be described as:

$$\frac{\partial T_s}{\partial t} = \alpha_s \nabla^2 T_s \quad (2.21)$$

The equations above are subject to the boundary conditions specified in equations (2.6-2.12).

The plate and fluid are assumed to be in equilibrium isothermal conditions until the heat source is turned on at the start of the transient heating process. This is expressed as:

$$\text{At } t = 0: T_s = T_f = T_j, v = v_i(x, z) \quad (2.22)$$

To complete the model, the local heat-transfer coefficient, average heat-transfer coefficient, local Nusselt number, and average Nusselt number are defined above as equations (2.13-2.16).

2.3 Computational Procedure

2.3.1 Steady State Procedure

A finite element method was used to solve the governing transport equations with the boundary conditions presented in the previous section. The computational software suite FIDAP was used in this work. The purpose of finite element analysis is to break down the domain of the problem into a finite number of elements to be solved. The dependent variables are then interpolated into a set of nodal points that are used to define each element. Four node quadrilateral elements were used for this purpose. The velocity, pressure and temperature fields were solved at these finite elements that defined the continuum of the problem. Due to both the large variation in temperature near the interface and the complex fluid flow between geometries in this work, it was necessary to employ a scaled grid that became more dense near the interface. To solve for the free surface, a new degree of freedom is introduced along the nodes at the free surface. This new degree of freedom is introduced as an unknown into the global system of equations and is used to define the position of the free surface. The Galerkin formulation was used

to carry out the discretization of the governing equations and boundary conditions. The resulting coupled algebraic equations are then solved by using the Newton-Raphson method. This method was selected because it is useful for solving highly coupled 2-D free surface problems and allows for a simultaneous solution of the discretized equations with a relatively fast convergence time if a good initial free surface is guessed. As only two of the three momentum boundary conditions are required at the free surface, the third was used to upgrade the position of the free surface at the end of each iteration step. The Newton-Raphson solver uses splines to track the position of the free surface and to modify the mesh grid as the free surface moves. These splines are straight lines that pass through the nodes under the free surface. Free surface movement only affected the nodes connected by the splines and only to the depth specified during the formulation of the FIDAP code. The computation domain of this problem included both the fluid and solid and the governing equations for mass, momentum and energy. These equations were solved simultaneously as a conjugate problem using constant properties. The solution was assumed to be converged when the sum of the residuals for each degree of freedom is found to be 1E-6.

2.3.2 Transient Procedure

The transient case was simulated in the same fashion as the steady state case, by simultaneously solving the equations for the conservation of mass, momentum, and energy. The computational domain covered both the solid and fluid regions. Using the steady state velocity field and free surface, the heat source at the bottom of the plate is turned on at $t = 0$. The solution at each time step was considered converged when the

sum of the residual was less than 1E-06. Due to the difficulty in obtaining a solution in free surface problems and to adequately describe the velocity field once the jet flow began, a small initial time step of 0.0001 is required. Once the solution begins to converge towards steady state the variation in temperature and velocity becomes much smaller. To account for the large changes at the beginning of the transient process and the very small changes as it approaches steady state, a variable time step was used.

2.4 Optimization of Grid Size

In order to determine the number of elements in each direction for an accurate solution, a number of different grid configurations were tested. The results of these simulations are found in Figure 2.2. To determine the accuracy of the grid required, the solid-liquid interface temperature at steady state was plotted against the distance along the solid-fluid interface (ξ). To find the number of nodes for grid independence the base rectangular step geometry was used. Increasing the number of elements in the horizontal direction had a larger impact than increasing the nodes in the vertical direction, especially after 49 vertical elements. Due to the complex nature of the geometries tested, it was necessary to use a much finer mesh in and around the interface. Results indicate that the problem becomes grid independent when 70 elements are used in the y-direction and 136 elements are used in the x-direction. Numerical results from the 70x136, 80x136, and 70x114 grids were nearly identical. The average difference in interface temperature between these three cases was calculated at 0.0289%. All of the following computations were done using the 70x136 grid.

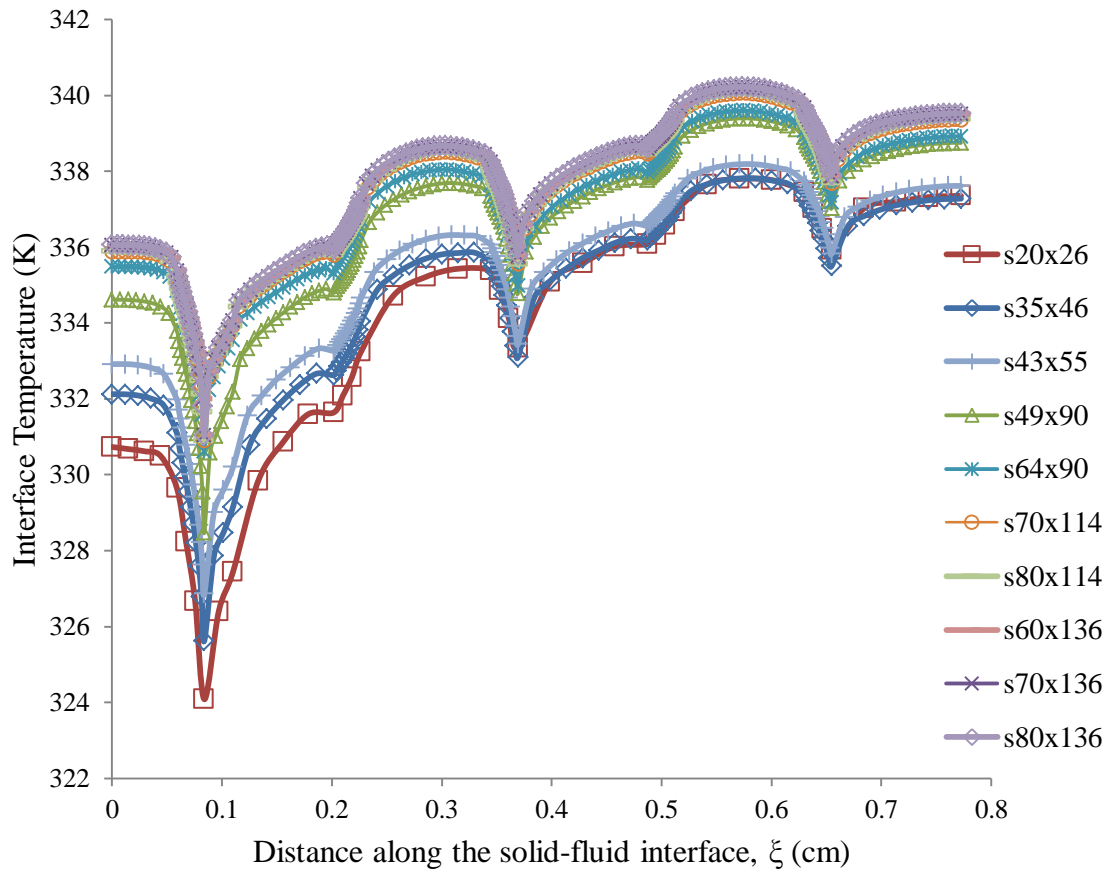


Figure 2.2 Grid independence study results for different numbers of elements in the horizontal and vertical directions (Steady state)
 ($Re = 1500$, $T_j = 313.15$ K, $b = 0.00125$ m, $H_n = 0.0055$ m, Silicon plate base case, $q = 63$ kW/m², $W=0.0017$ m)

2.5 Comparison with Previous Experimental Results

In order to validate the model used in this investigation it was necessary to compare it to an experimental work. A run was performed to compare this numerical model to the experimental results of Ibuki et al. [12]. In this case the impinging plate was flat, a consequence of the lack of available experimental data concerning liquids impinging on patterned plates. The numerical model was setup to mimic the experimental setup. The material used was an alloy of Inconel and the cooling fluid considered was water at 21°C. The results of this setup are displayed in Figure 3. It can be seen that the present model is in agreement with the experimental results, especially in the area close to where the jet impinges upon the plate. The largest difference between the numerical and experimental results is 25% at the end of the plate. However, this difference was expected as the experimental setup is three-dimensional and the inherent uncertainty of the experiment. Further error is introduced by the rounding that occurs throughout the computational procedure and furthered by the assumptions and approximations present.

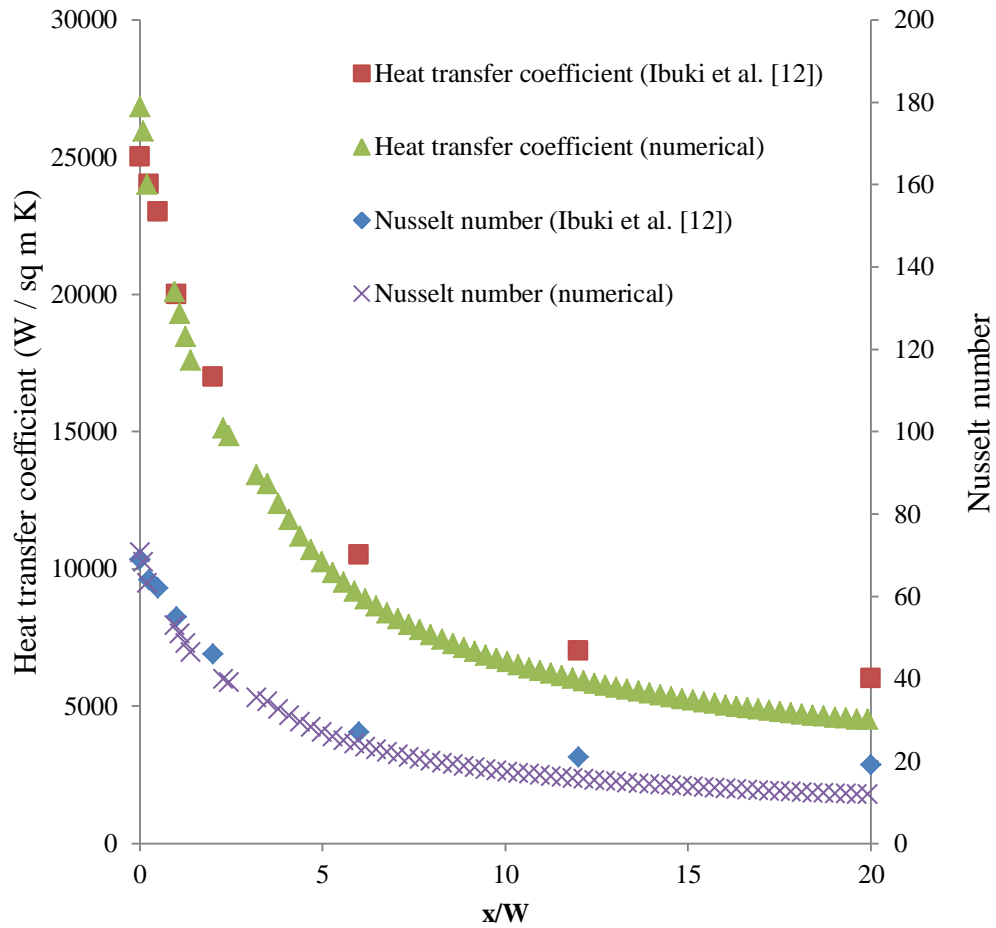


Figure 2.3 Comparison with previous experimental work
 ($Re = 2200$, $T_j = 294.15 K$, $b = 0.0003 m$, $H_n = 0.01 m$, Inconel plate, $W = 0.00162 m$)

Chapter 3

Discussion of Results: Steady State

3.1 Slot Jet Impinging on a Uniformly Heated Plate with Rectangular Ridges: Steady State Heating

The simulation was performed using three solid substrate materials: silicon, copper, and constantan. The fluids used were water and the refrigerant R134a.

For this investigation a surface with rectangular steps and indentations was considered. Figure 3.1 shows the three cases that were studied. Each case considered 6 steps with the end of the last step coinciding with the outlet. Since the slot jet is positioned exactly half way above the heated plate, the location of $x = 0$ coincided with the mid-point of an indentation. The base case considered the length of the step and the length of the indentations as equal. Case A is defined as the length of the step being twice the indentation. Case B is defined as the indentation length being twice the step. A typical distribution of the velocity vectors for the base case is presented in Figure 3.2. It can be seen that in the potential jet core region the velocity profile remains nearly uniform. As the jet comes closer to the stagnation zone the velocity drops and the jet diameter increases. As the first rectangular indentation is at the center of the stagnation zone, it was expected that there would be a recirculation zone similar to what would occur on a flat plate. This recirculation zone within the rectangular indentation was observed at the stagnation zone and in each subsequent indentation. After this zone the

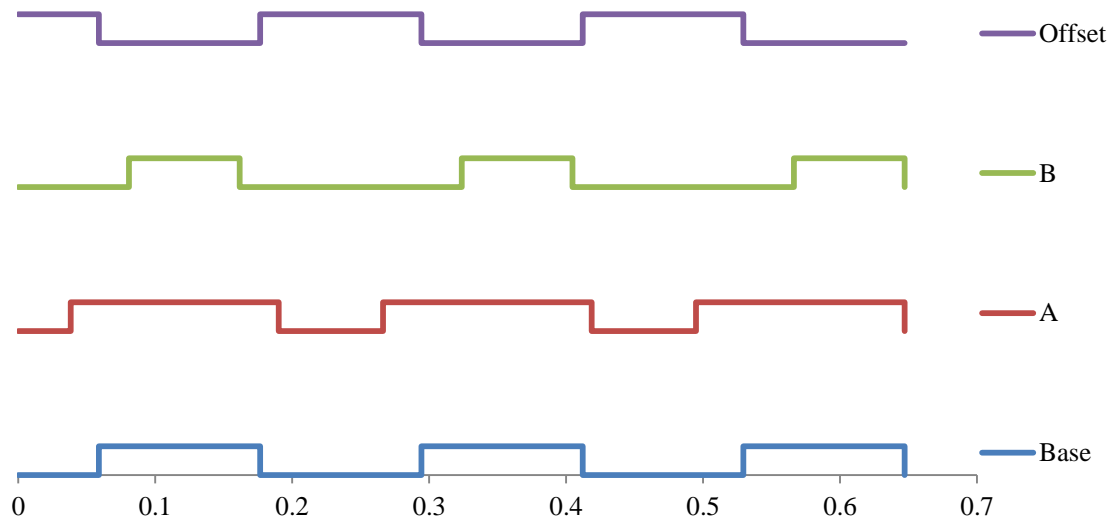


Figure 3.1 Comparison of different rectangular step cases investigated

plate returns to its full thickness allowing the fluid to accelerate as it would on a flat plate. However, due to the next indentation, the velocity of the film does not dramatically decrease as it progresses along the length of plate. It can be seen that as the fluid enters each of the rectangular indentations it recirculates back into the sheet, causing a slight turbulent flow to develop. As the fluid continues towards the end of the plate, fluid friction builds up along the flat surfaces and the slower moving fluid in the indentations causing the velocity close to the wall to drop. However, the overall velocity profile remains relatively high due to the turbulent recirculation caused by the changes in geometry. The velocity profile at the area where flow is fully developed is parabolic in nature, with the velocity being zero at the surface and increasing to the center of the flow.

Figure 3.3 shows the free surface height distribution for varying Reynolds number when the jet impinges upon the center of the patterned surface for the base case. As the

fluid strikes the surface it spreads out in the x-direction along the surface of the plate. Due to the fluid speeds used in this investigation and the geometries considered, there is no hydraulic jump present within the domain tested. The minimum film height occurs at a distance that is larger than the width of the nozzle and the film height increases slightly as the flow continues along the plate. This is due to the deceleration of the fluid as it moves downstream due to frictional resistance offered by the plate as well as the steps. It may be noticed that the film height increases with increasing Reynolds number. This is due to the increase of fluid flow rate with the increase of Reynolds number. A higher flow rate results in higher local fluid velocity above the heated plate as well as higher thickness of the liquid film above the plate. As the step height was much smaller compared to the liquid film thickness, the free surface appears to be fairly smooth and its curvature is not significantly affected by the presence of patterns at the solid-fluid interface.

Figure 3.4 shows the interface temperature across the length of the solid-fluid interface for varying Reynolds number. It is noted that the highest temperatures occur at the lowest depth for each indented rectangular step that occurs along the interface surface. As expected the temperature increases along the length of the plate. The lowest temperature is present at the top corner of the plate where it returns to full thickness after the first indentation, a point where the fluid is changing direction from fully vertical to nearly fully horizontal. The three low temperature spikes along each curve coincide with the points where the plate returns to full thickness. These lower temperatures occur due to the increased velocity that is experienced by these locations and is further reinforced by the observation that the edges below these tips are also lower in temperature,

indicating that thermal boundary layer is disturbed by the sharp edge present. A new thermal boundary layer is initialized at the tip of each step, resulting in a large rate of heat transfer at these locations. The high temperatures present in the indentations are caused by the close proximity to the heat flux source at the bottom of the plate and by the reduced circulation compared to the rest of the plate surface. Interface temperatures fall with increasing Reynolds number due to the higher velocity of the fluid that causes greater circulation along the length of the plate.

Figure 3.5 shows the variation of the local heat-transfer coefficient along the liquid-solid interface for varying Reynolds numbers. The maximum heat-transfer coefficient is present inside the stagnation zone at the tip of the first step along the interface at $\xi / L = 0.13$. This coincides with the lowest temperature along the interface as seen in Figure 3.4. From the peak value the heat-transfer coefficient decreases along the length of the plate due to an increase in the thermal resistance between the fluid and the patterned plate with the increase of thermal boundary layer thickness. However, there are further peaks in the heat-transfer coefficient at locations where the flow must enter and exit the indented steps in the plate surface. These high points are dramatically lower than the heat-transfer coefficient in the stagnation zone due to the loss of velocity and increase in temperature as the fluid moves downstream. It can be observed that at the heat-transfer coefficient at the final step near the end of the plate is not decreasing as dramatically as the previous two steps. Along the length of the plate, the thermal boundary layer does not penetrate the full thickness of the film layer. As expected, increasing the Reynolds number increases the heat-transfer coefficient due to the increased fluid velocity along the surface of the plate.

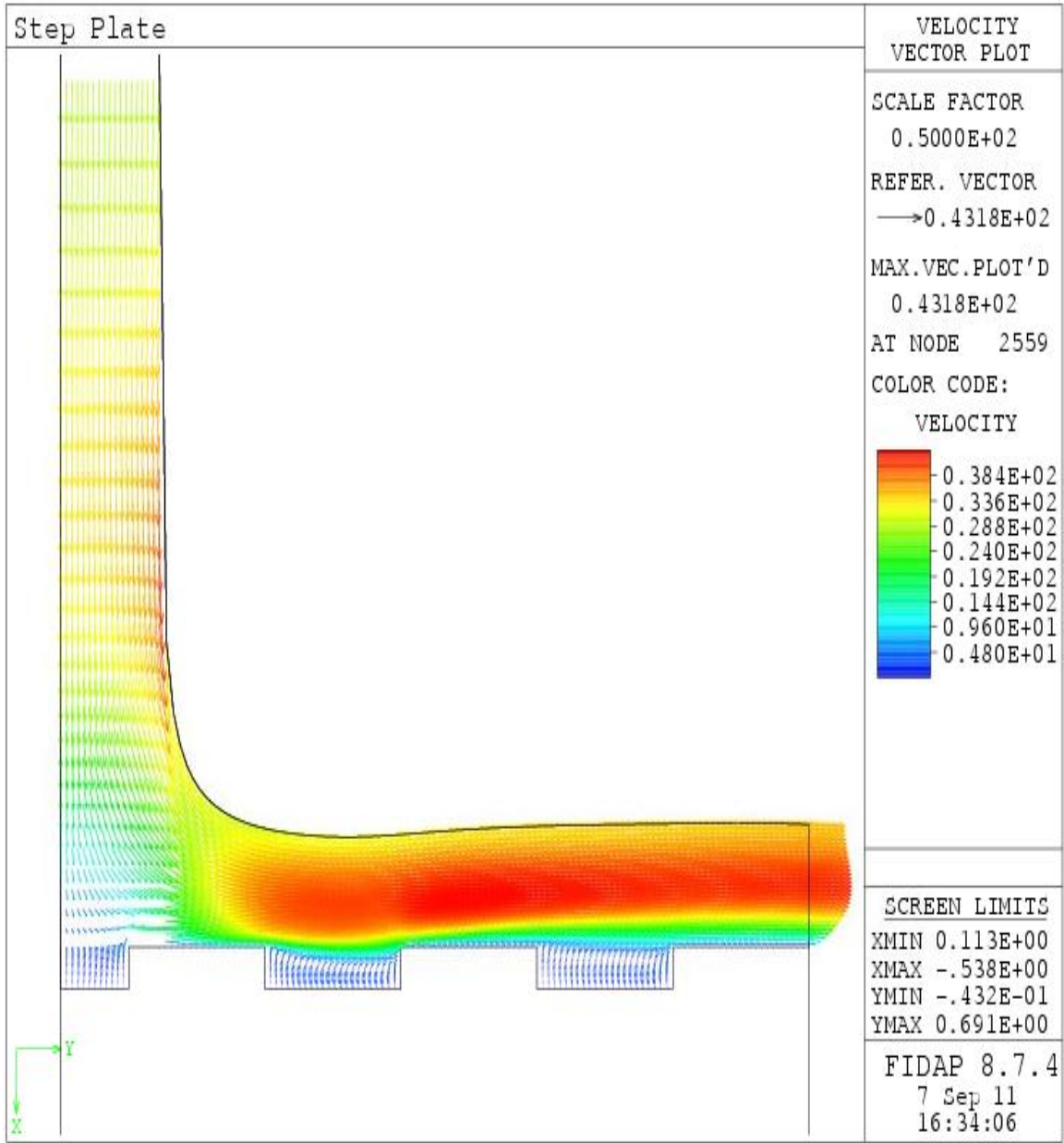


Figure 3.2 Velocity vector map
 (Re = 750, base rectangular case, $a = 0.00025$ m, $H_n = 0.0055$ m, $W = 0.0017$ m)

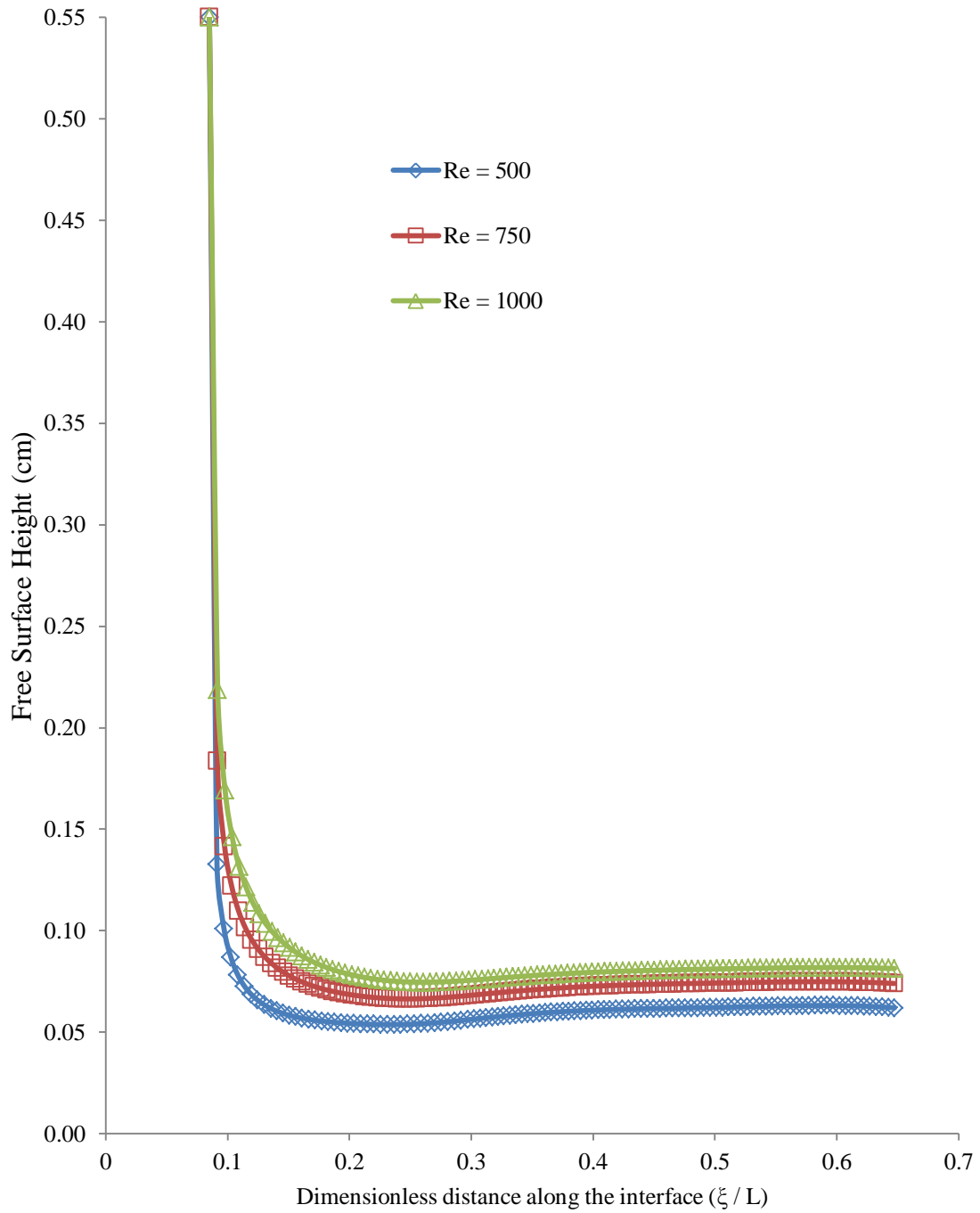


Figure 3.3 Free surface height distribution for different Reynolds number ($H_n = 0.0055$ m, $W = 0.0017$ m)

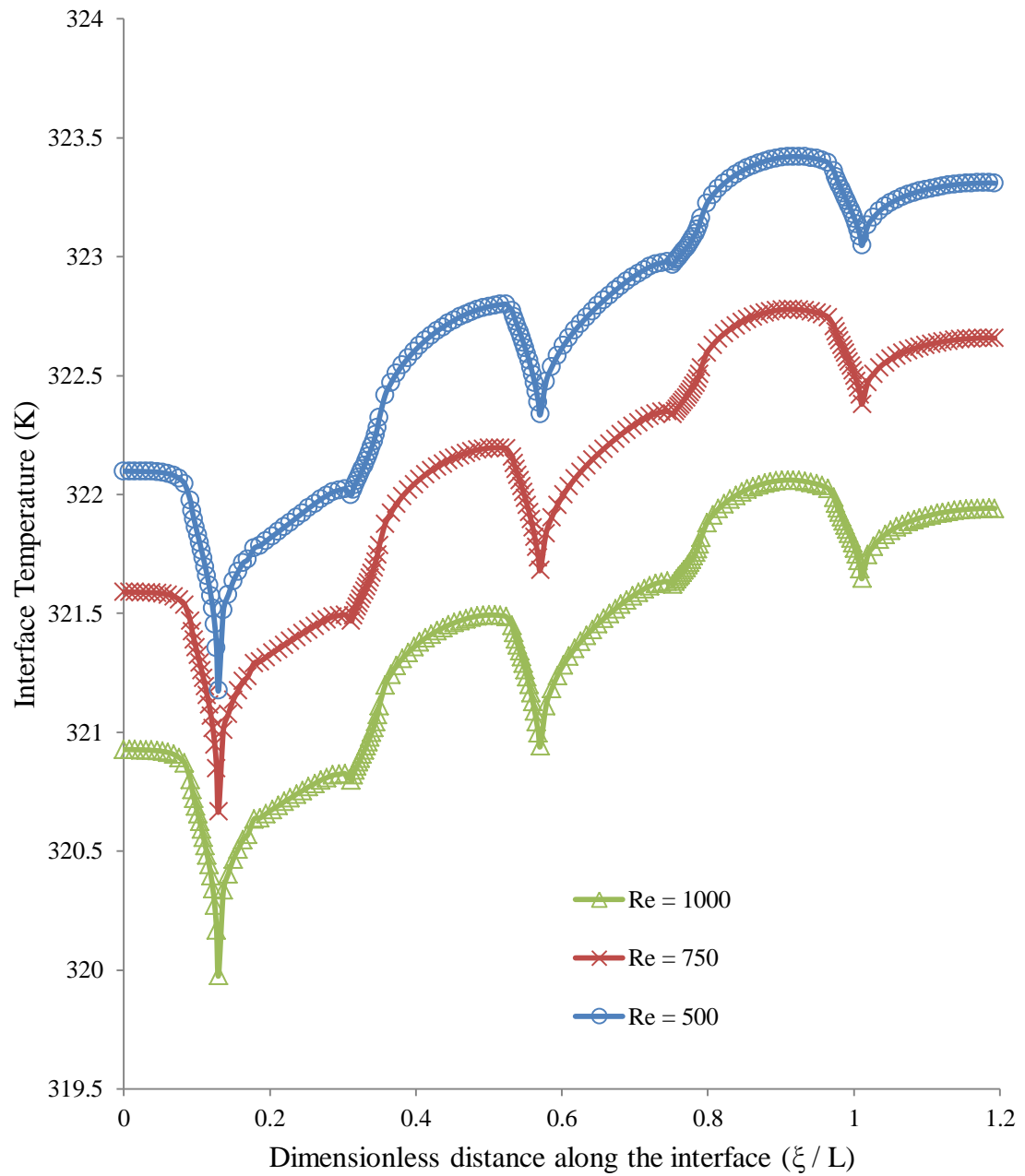


Figure 3.4 Interface temperatures for varying Reynolds number ($T_j = 313.15$ K, $b = 0.00125$ m, $H_n = 0.0055$ m, Silicon plate base case, $q = 63$ kW/m², $W=0.0017$ m)

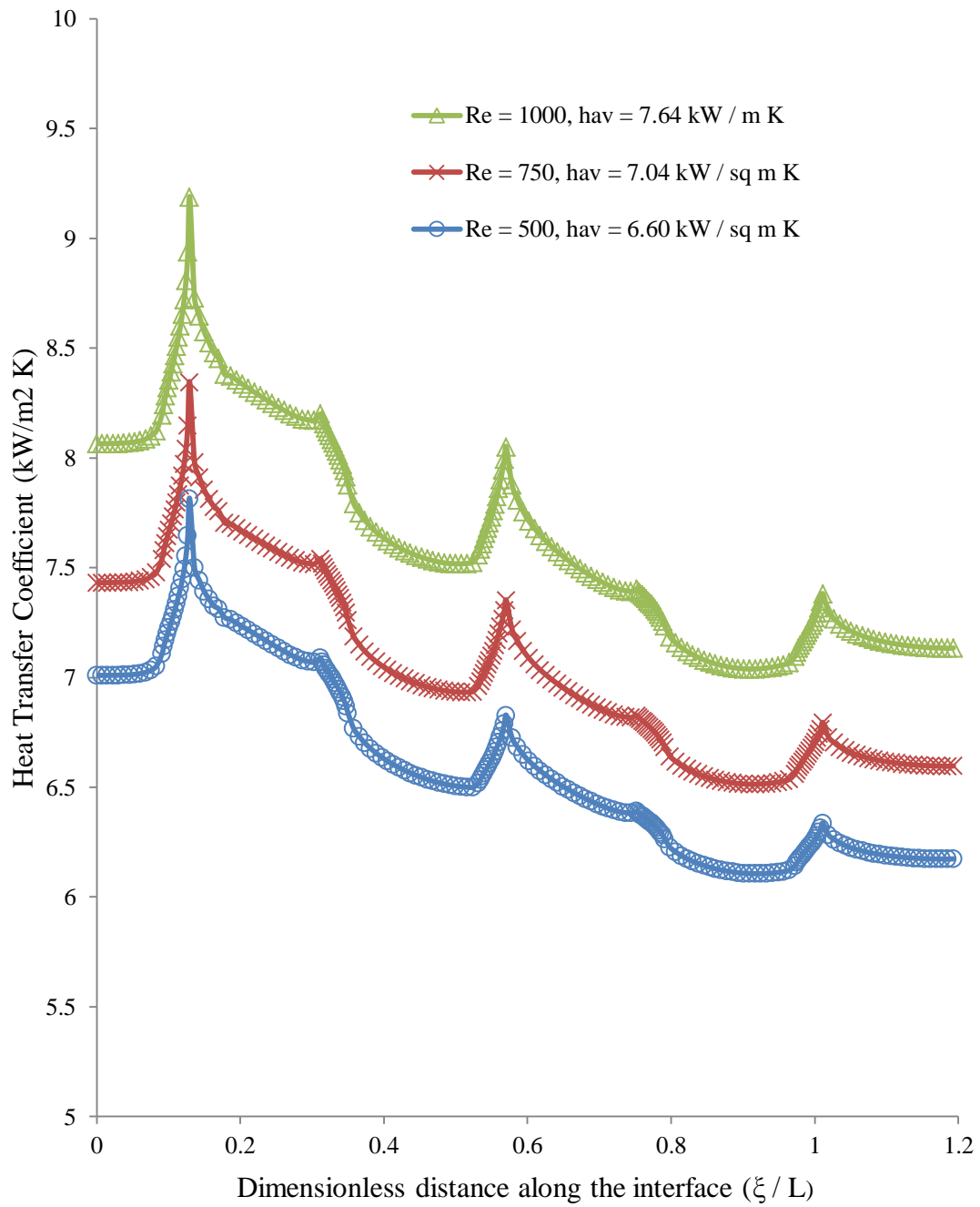


Figure 3.5 Local heat transfer coefficient for various Reynolds numbers
 ($T_j = 313.15$ K, $b = 0.00125$ m, $H_n = 0.0055$ m, Silicon plate base case, $q = 63$ kW/m²,
 $W = 0.0017$ m)

The variation of the local Nusselt number for different Reynolds numbers is displayed in Figure 3.6. It is observed that the behavior of the Nusselt number is very similar to that of the local heat-transfer coefficient. It can be observed that the highest Nusselt number occurs at $x/W = 0.5$, then rapidly decreases until again peaking at $x/W = 2.15$. These peaks coincide with the top corners of each rectangular step. It should also be noted that increasing the Reynolds number increases the Nusselt number.

Figure 3.7 displays the local heat-transfer coefficient for different indentation depths for the base case. The length of the interface varies in each of these cases due to the change in the depth of the step geometry. It can be observed that increasing the indentation depth to $a = 0.0005 \text{ m}$ results in a drop of the local heat-transfer coefficient due to the decrease in velocity at the center of the impingement zone. Increasing the depth of the indentations decreases the fluid speed attained at the bottom of each indentation and leads to less recirculation at the interface surface. However, there is an increase in the maximum heat-transfer coefficient when $a = 0.0005 \text{ m}$ at the beginning of the first step on the plate and each subsequent step along the plate. This phenomenon is due to the thermal boundary layer being disrupted at the edge of each step, causing slightly higher heat transfer when compared to the 0.00025 and 0.000125 m cases. When $a = 0.000125 \text{ m}$, the local heat-transfer coefficient at the center of the stagnation zone is higher than either $a = 0.00025$ or $a = 0.0005 \text{ m}$. This is due to the increased fluid velocity and recirculation in the bottom of the first indentation that allows for greater convective heat transfer. An important observation to make is a comparison between each step depth on the last heat transfer peak. The difference between the 0.0005 and 0.00025 m step is far smaller than the difference between the 0.00025 and 0.000125 m

step. This is largely due to a smaller difference in fluid speed for the $a = 0.000125 \text{ m}$ case between the developing flow within the film thickness and the speed of the fluid leaving the indentation. The average heat-transfer coefficient in the $a = 0.00025$ and $a = 0.0005 \text{ m}$ cases is the same due largely to the heat-transfer coefficients being similar over a large part of the plate. Figure 3.8 displays the Nusselt number for differing indentation depths in the base case. It is observed that the Nusselt for the smallest step of $a = 0.000125 \text{ m}$ is lower when compared to the larger step depths. The difference in average Nusselt number for the two larger depths is found to be the same. For the case of $a = 0.0005 \text{ m}$, the Nusselt number at the stagnation zone is lower when compared to the other two cases. This is largely due to a reduced velocity profile in the deepest part of the indentation, causing a reduction in convective heat transfer that was previously noted. However, the peak Nusselt number for this case is higher than in the base case. This indicates that the difference in indentation depth between these two cases merely changes the circulation inside the indentations, thus slightly altering the peaks and valleys in Nusselt number but leaving the average the same. This effect is almost completely negated by the final indentation and step.

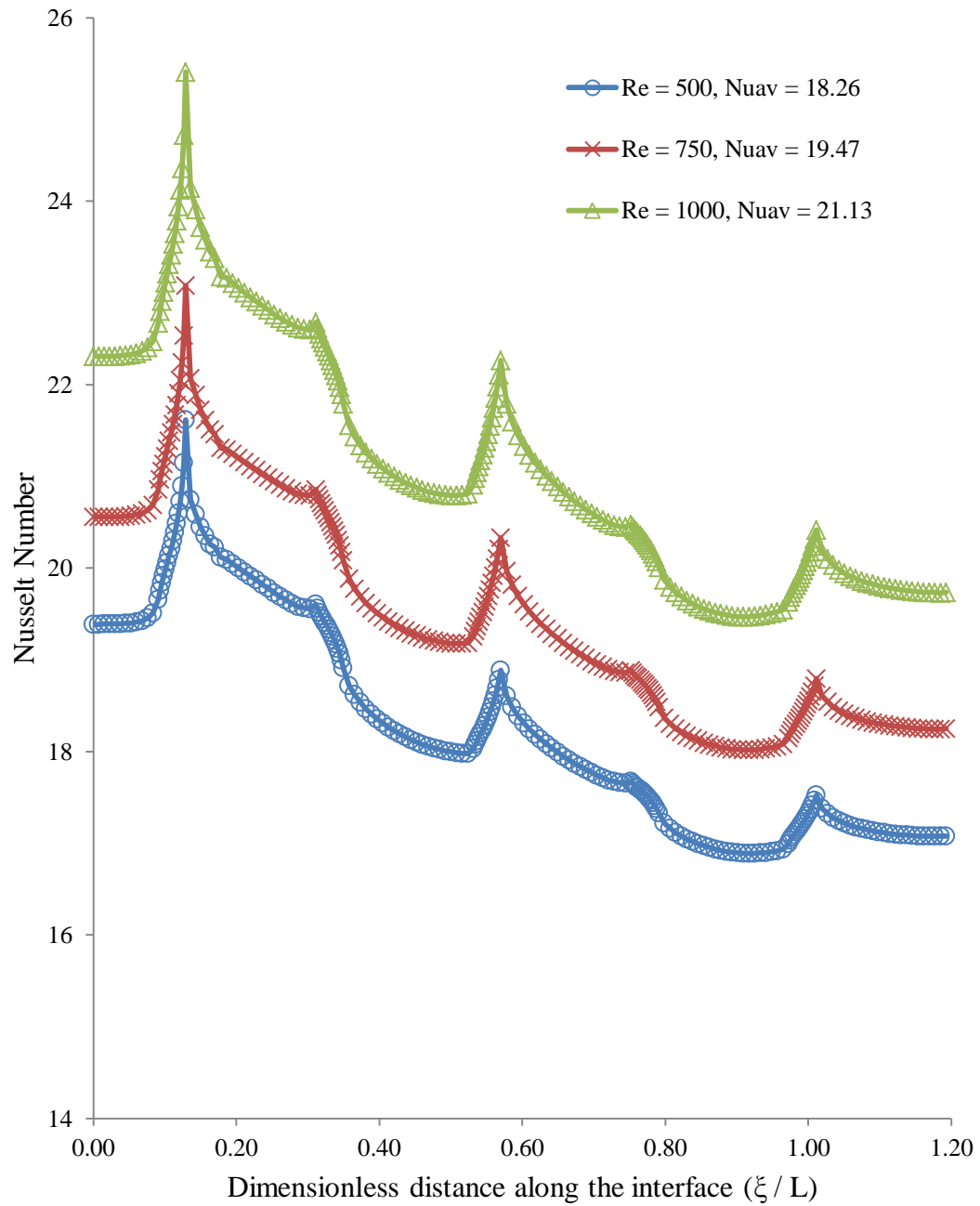


Figure 3.6 Local Nusselt number for different Reynolds number
 ($T_j = 313.15$ K, $b = 0.00125$ m, $H_n = 0.0055$ m, Silicon plate base case, $q = 63$ kW/m²,
 $W=0.0017$ m)

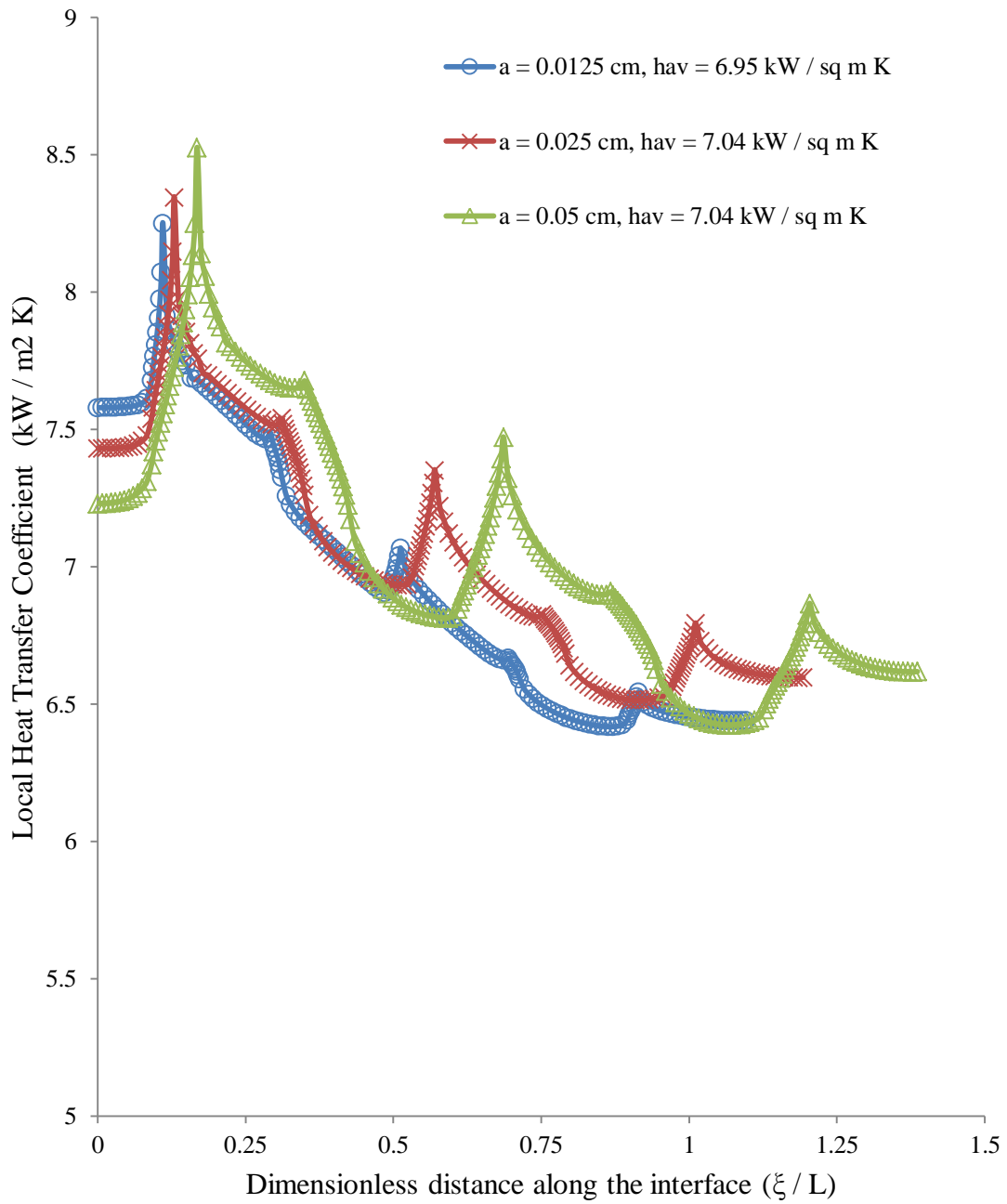


Figure 3.7 Local heat transfer coefficient for various indentation sizes
 ($Re = 750$, $T_j = 313.15$ K, $b = 0.00125$ m, $H_n = 0.0055$ m, Silicon plate base case,
 $q = 63$ kW/m², $W = 0.0017$ m)

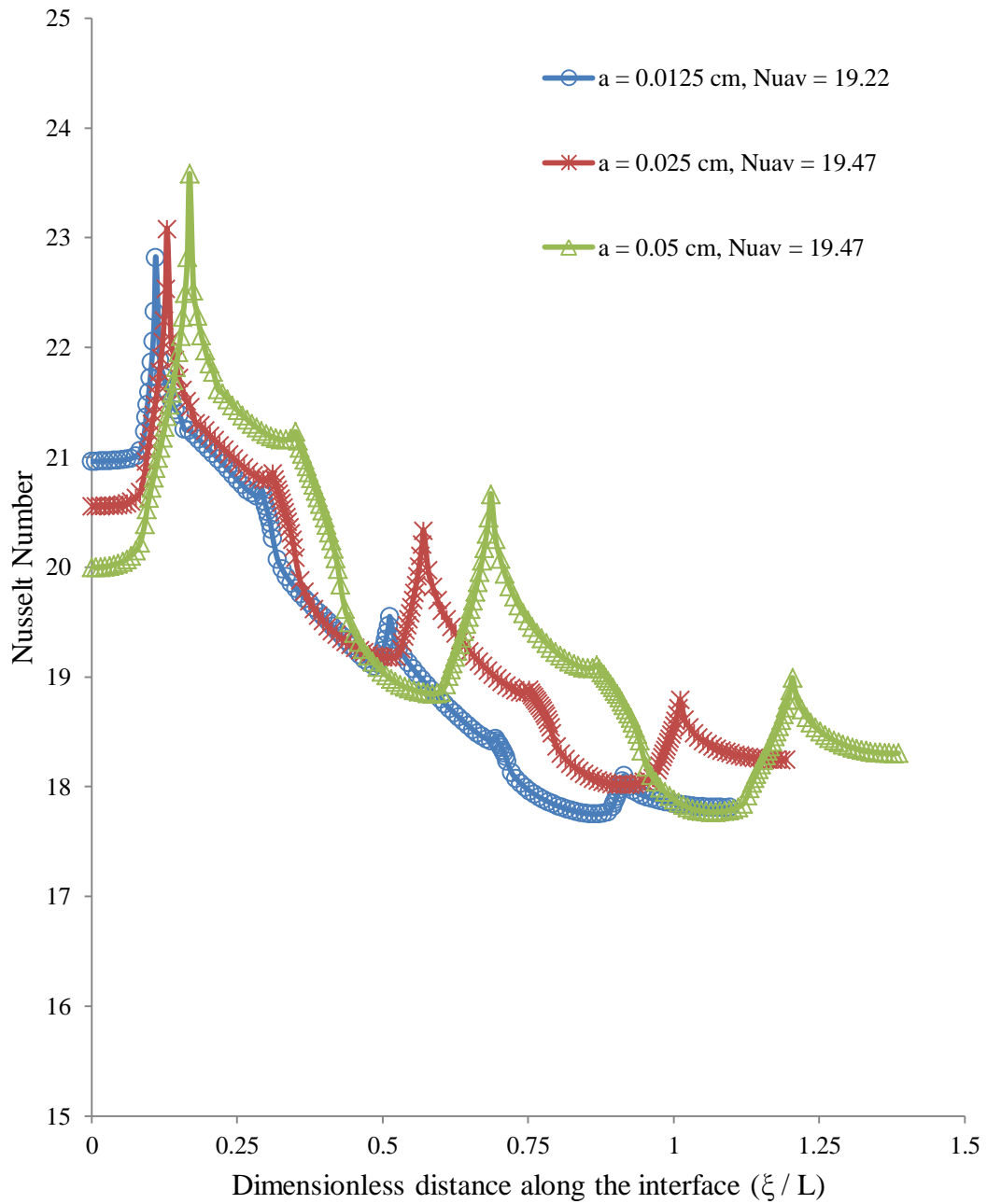


Figure 3.8 Local Nusselt number for various indentation sizes
 (Re = 750, $T_j = 313.15$ K, $b = 0.00125$ m, $H_n = 0.0055$ m, Silicon plate base case, $q = 63$ kW/m², $W = 0.0017$ m)

Figure 3.9 shows the effect of the different geometry configurations on the local heat-transfer coefficient. The smaller indentations of case A allow for more fluid recirculation, greatly increasing the local heat-transfer coefficient in these critical areas. When compared against each other, all three cases show the same general heat transfer characteristics, including loss of heat-transfer coefficient as the plate progresses towards its end. Case B has a very large spike in local heat-transfer coefficient in the same location as the other cases. This is due to the edge of the first step being outside the nozzle width, allowing it to be exposed to higher fluid speeds. Past this point the fluid speed inside each indentation is reduced and has a negative effect on the local heat-transfer coefficient. This is evident due to the observation that even with the large spike in local heat-transfer coefficient in case B, the average heat-transfer coefficient is lower than the optimum case by over 15%. When the position of the first step is moved, as in the offset case, it is noted that the local heat-transfer coefficient drops in the stagnation zone and exhibits slightly different peak values due to the change in position of the geometry. In this case it is advantageous to have the jet impinge into an indentation. The only clear advantage of any of these geometries over the flat plate is that of case A, which has higher heat transfer coefficients in the stagnation zone and an overall higher average heat-transfer coefficient. The large spikes in heat-transfer coefficient just outside the stagnation zone could be useful if required for certain applications. Figure 3.10 shows the impact of the surface geometry on the Nusselt number. The results for case A demonstrate the effect of increased fluid flow due to the smaller indentations on the heat transfer characteristics of the problem. Increased fluid flow in and around the interface due to smaller surface features leads to an increased amount of convective heat transfer,

which in turn raises the value of the Nusselt number. The results of this investigation suggest that use of indentations that are half the length of the solid steps is the optimal configuration for this system. Increased surface area in the indentations for the base case and case B causes a larger amount of friction and a reduction of speed inside the indentations, causing a negative impact upon the heat transfer. Case A is clearly the best for instances where Nusslet number is required in the stagnation zone and across the entirety of the plate. The flat plate shows higher average Nusslet number than the case B, the offset case, and the base case. In these instances, the addition of surface geometries only modifies the behavior of the local Nusselt number across the length of the plate. There are possible advantages to include the changes in geometry, including addition of increased surface area to allow for more contact area between the working fluid and the plate.

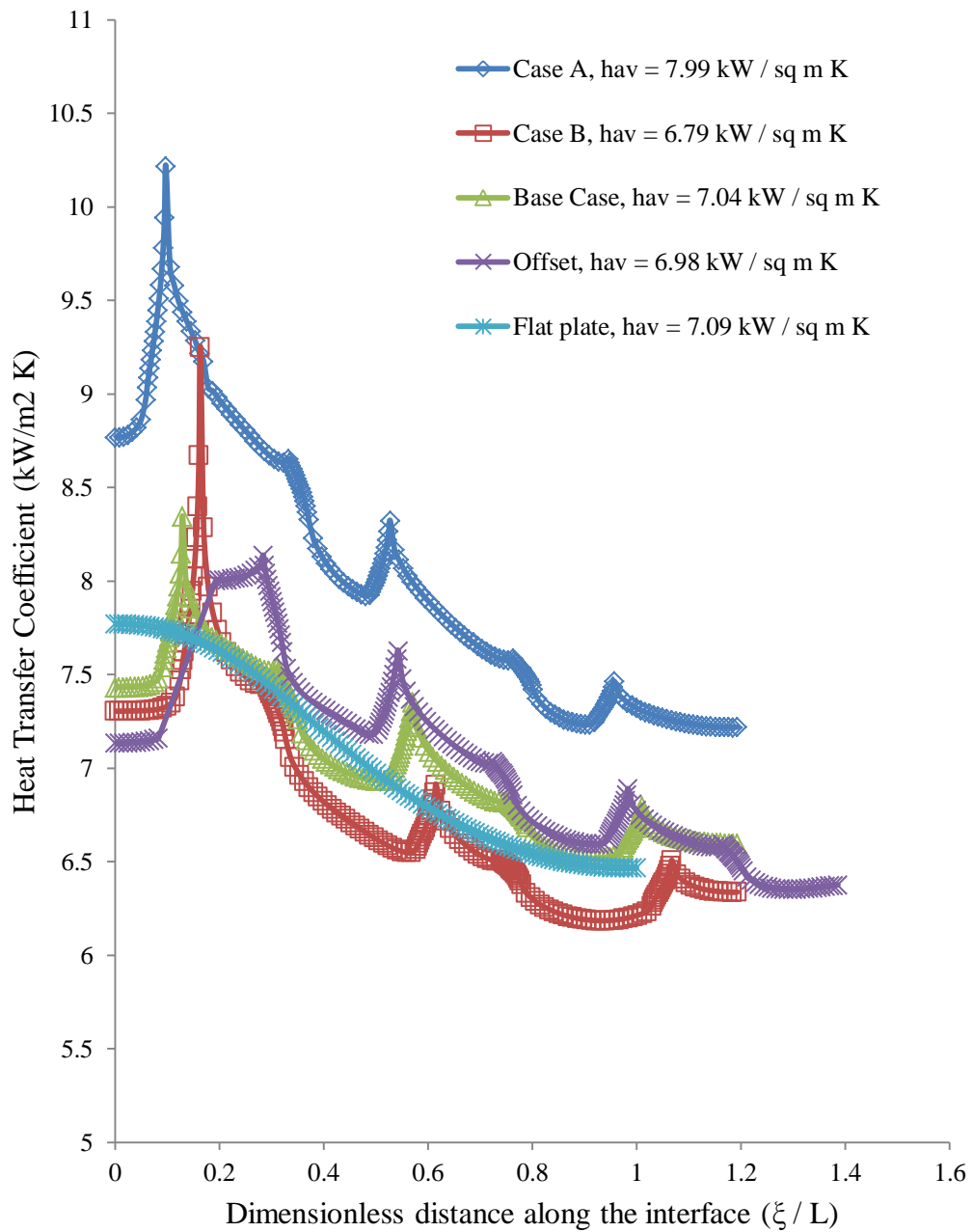


Figure 3.9 Local heat transfer coefficient for different surface geometry configurations (Re = 750, $T_j = 313.15$ K, $b = 0.00125$ m, $H_n = 0.0055$ m, Silicon plate, $q = 63$ kW/m², $W = 0.0017$ m, $a = 0.00025$ m)

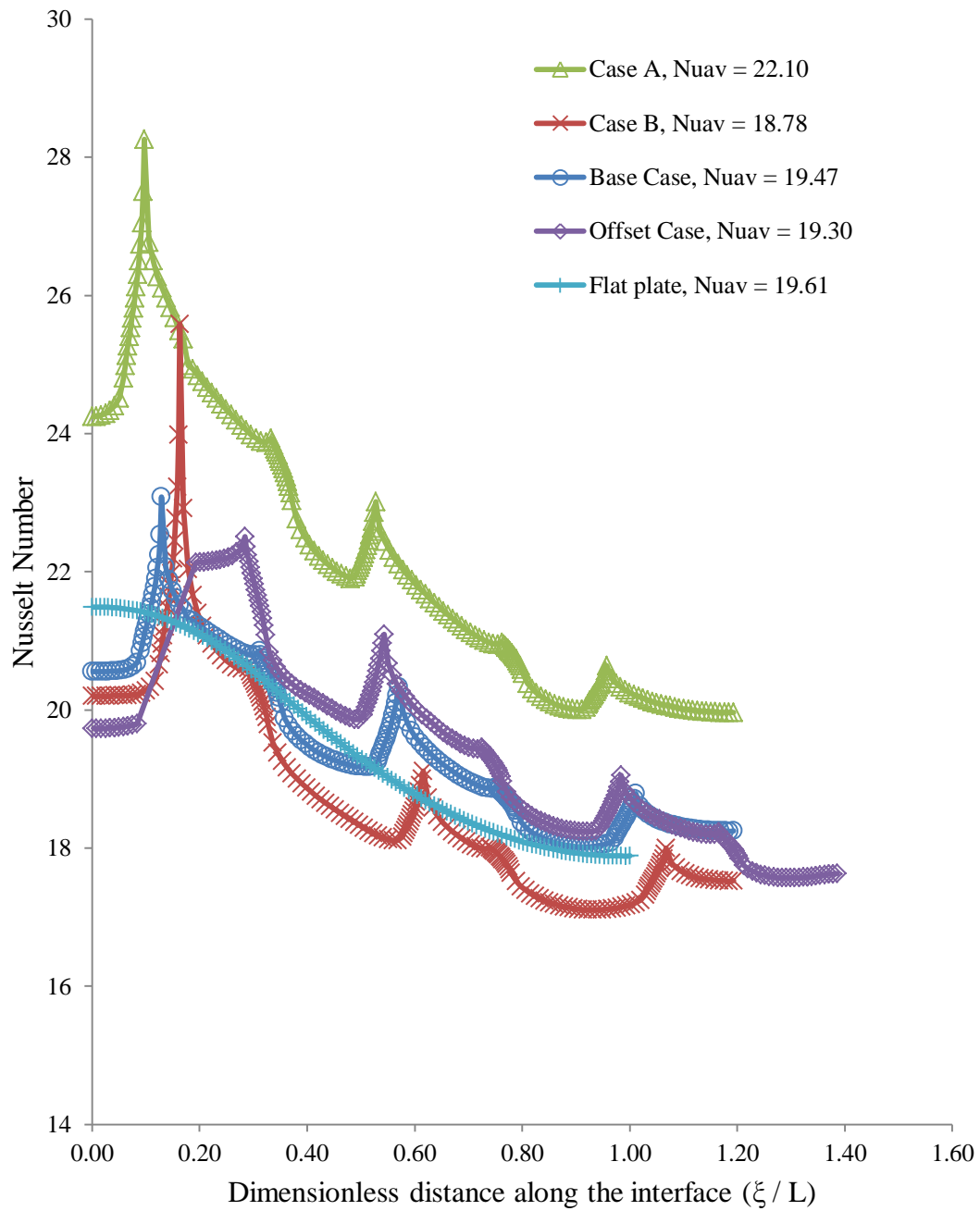


Figure 3.10 Local Nusselt number for different surface geometry configurations ($Re = 750$, $T_j = 313.15$ K, $b = 0.00125$ m, $H_n = 0.0055$ m, Silicon plate, $q = 63$ kW/m², $W = 0.0017$ m, $a = 0.00025$ m)

Figures 3.11 and 3.12 show the Nusselt number for varying indentation depths in case A and case B. As with the base case, increasing the depth of the indentation leads to higher peaks in the Nusselt number while keeping the average Nusselt numbers nearly equal. Further observation confirms that case A does have the highest Nusselt numbers of all the three cases, leading to the conclusion that it must be the optimal configuration for indentation geometry. Case B has the lowest average heat transfer values. However, in Case B for both $a = 0.0005 \text{ m}$ and $a = 0.000125 \text{ m}$ there a sharp peak of the Nusselt number at the edge of the first solid step. This is the only case where a smaller indentation depth increases the Nusselt number. There is an increase of nearly 10% when using the 0.000125 m indentation instead of the 0.0005 m indentation.

This numerical simulation was carried out on three materials: Silicon, copper, and Constantan. The base rectangular case was used for each of these simulations with $a = 0.00025 \text{ m}$ and $Re = 750$. Two working fluids were considered: water and the refrigerant R-134a. The properties of water are assumed to be constant over the temperature range used in this work. However, variable properties were used in the investigation of R-134a due to the possibility of a larger temperature swing in the development of the problem. Selecting the appropriate material for electronics packages relies heavily on the heat that must be dissipated within these systems. Therefore it is imperative to illustrate the thermal conditions for each of these materials under similar thermal loading conditions.

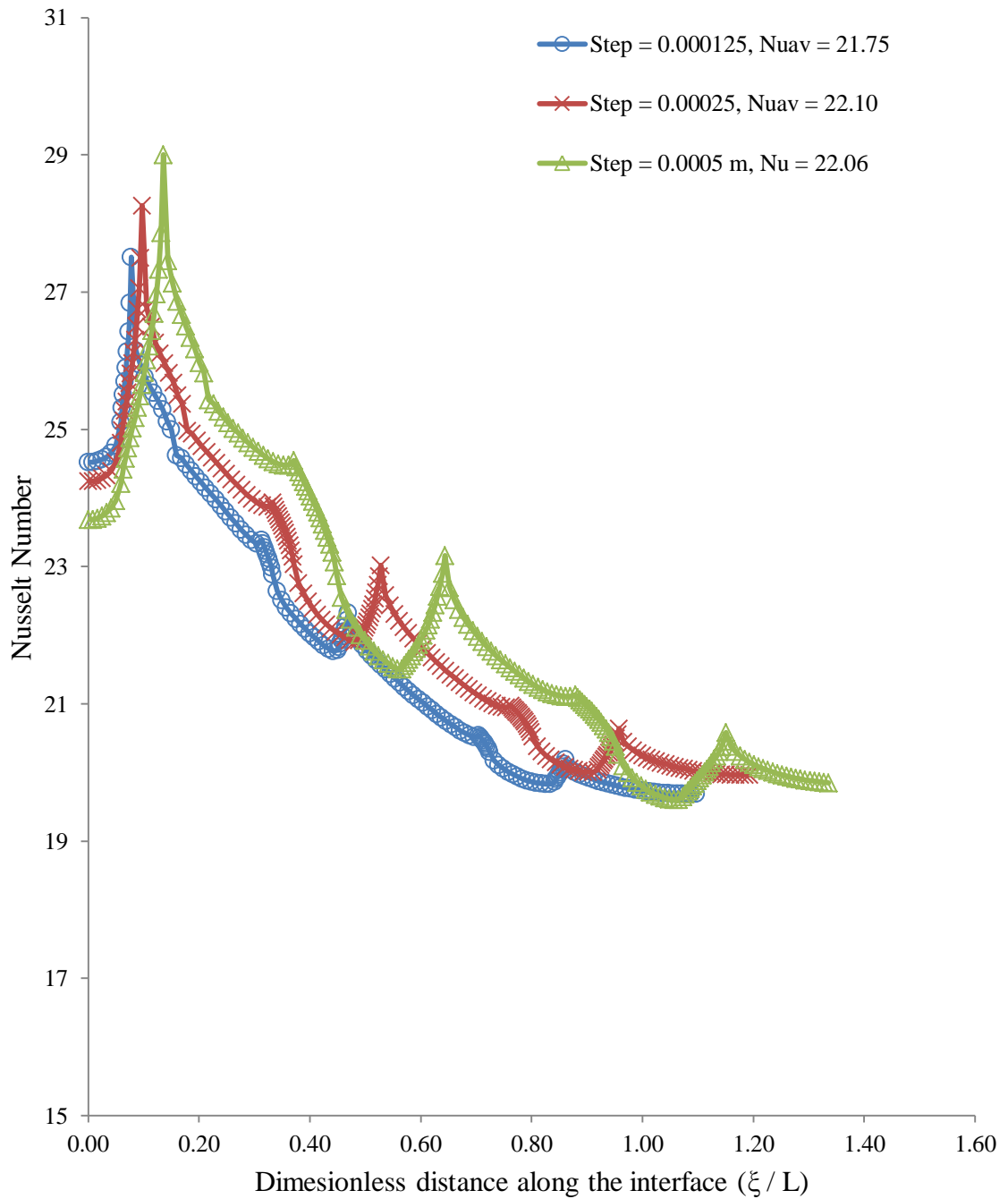


Figure 3.11 Local Nusselt number for varying indentation depths Case A
 ($Re = 750$, $T_j = 313.15$ K, $b = 0.00125$ m, $H_n = 0.0055$ m, Silicon plate, $q = 63$ kW/m²,
 $W = 0.0017$ m)

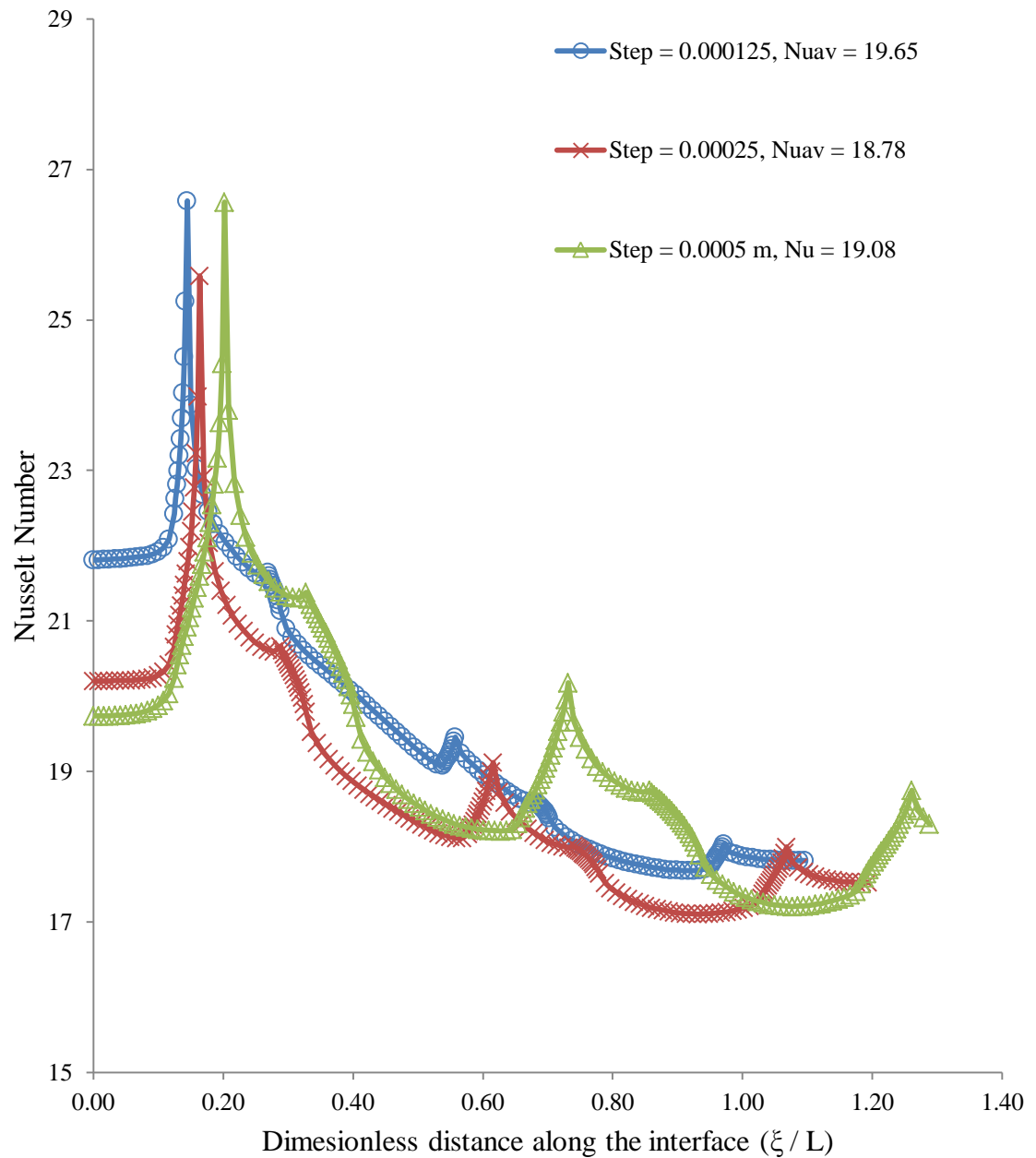


Figure 3.12 Local Nusselt number for varying indentation depths Case B
 ($Re = 750$, $T_j = 313.15$ K, $b = 0.00125$ m, $H_n = 0.0055$ m, Silicon plate, $q = 63$ kW/m²,
 $W = 0.0017$ m)

Figure 3.13 shows the variation in interface temperature for silicon, copper, and constantan with water as the working fluid. Copper and silicon have relatively high thermal conductivities ($k = 386$ and $135 \text{ W / m}\cdot\text{K}$) when compared to constantan ($22.7 \text{ W / m}\cdot\text{K}$). As a result the variation in minimum and maximum interface for copper and silicon is very low, with the difference being less than 3 degrees Kelvin for both materials. The interface temperature for copper is nearly constant throughout the plate due to its high thermal conductivity. High thermal conductivity paired with the plate thinness allows for the heat flux at the bottom of the plate to exert a strong influence upon the interface temperatures. Constantan is an insulator and prevents strong conduction through the plate thickness. This allows the interface temperatures to be more influenced by the fluid flow. This effect is very apparent at the first rectangular step, where the lowest temperature occurs at 318 K. This effect is only present for the first two peaks, coinciding with the leading edge of the first two steps. In the indentations the interface temperatures are actually higher than both silicon and copper; this is due to the loss of the insulating material that was present in the solid steps.

Figure 3.14 shows the variation in Nusselt number for all three materials using water as the working fluid. Copper and silicon experience less variation in their Nusselt number as the thermal conductivities of these materials allow for the heat flux to more evenly penetrate the plate. Constantan shows a larger variation in Nusselt number due to the larger temperature swing present at the interface. The high peak of all materials at $x/W = 0.5$ and $x/W = 2.17$ again relate to the leading corners of each solid step. The heat-transfer coefficient and Nusselt number at these spots clearly show a strong dependence on the interface temperatures present.

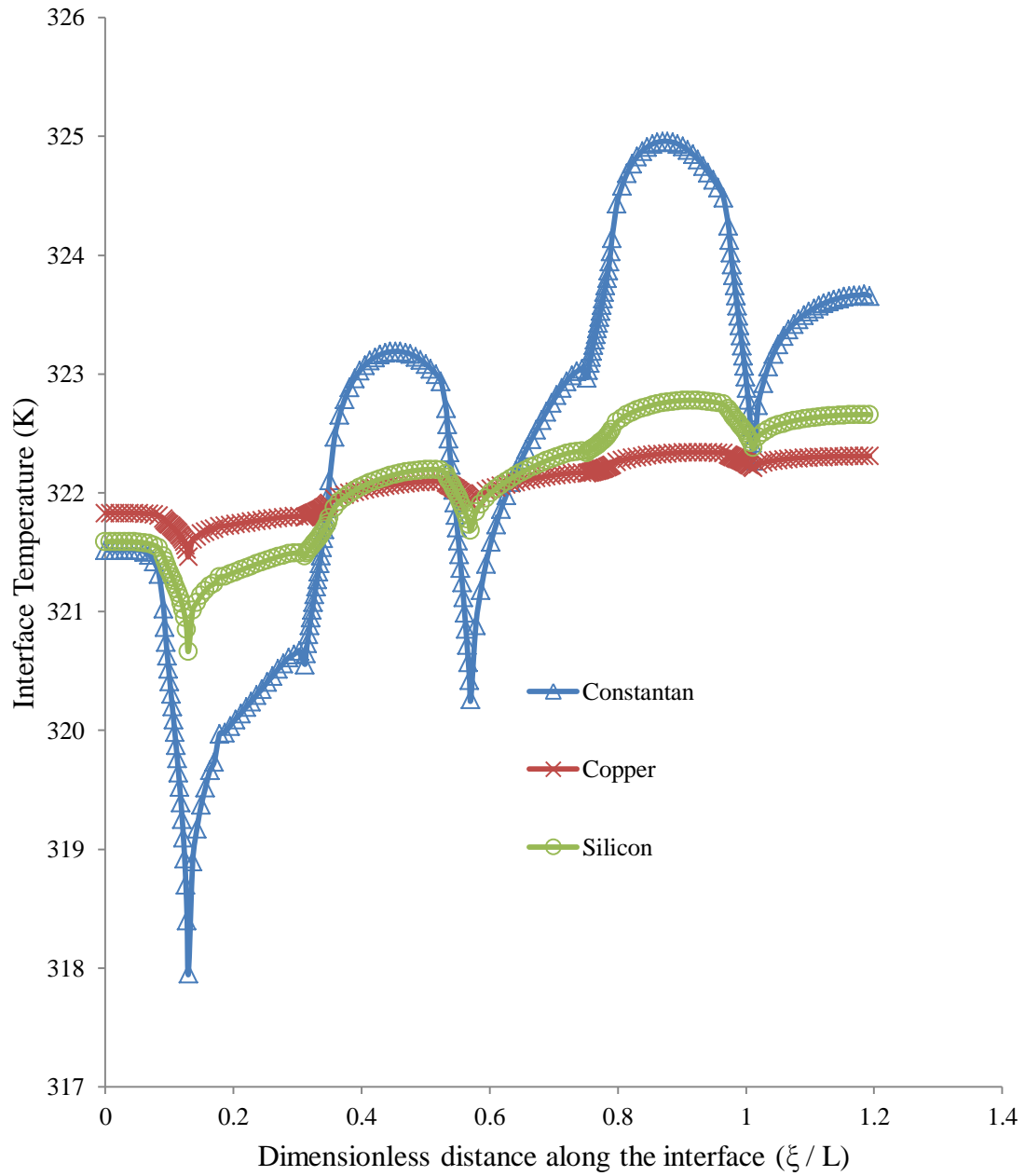


Figure 3.13 Interface temperature variation for different plate materials
 ($Re = 750$, $T_j = 313.15$ K, $b = 0.00125$ m, $H_n = 0.0055$ m, $q = 63$ kW/m², $W=0.0017$ m)

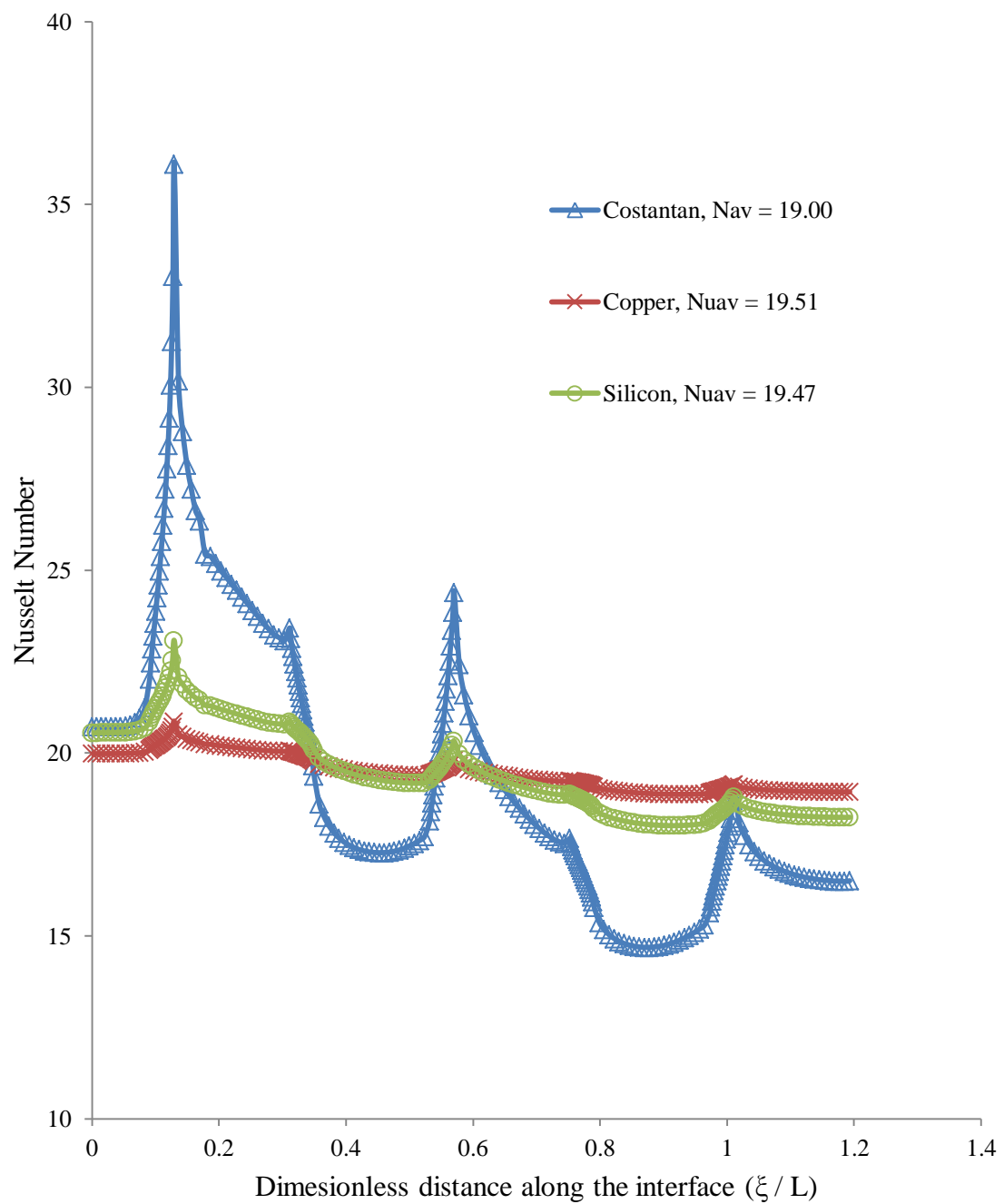


Figure 3.14 Variation in local Nusselt number for different plate materials
 (Re = 750, $T_j = 313.15$ K, $b = 0.00125$ m, $H_n = 0.0055$ m, $q = 63$ kW/m², $W = 0.0017$ m)

Figure 3.15 shows the variation in interface temperature for silicon, copper, and constantan using R134a as the working fluid. As the fluid temperature used for R134a was 253 K and the heat flux from the plate was quite low, the temperature values at the interface for all three materials are low. The high thermal conductivity of silicon and copper allow for the heat from the bottom of the plate to penetrate into the solid-liquid interface. Constantan's low thermal conductivity allows for the plate to resist the temperature change due to the heat flux near the stagnation zone. At this zone the temperature drops dramatically at the edge of the first step. However by $x/W = 1.33$ this effect reverses as the material stays warm in part due to lower heat transfer rates. Figure 3.16 shows the variation of local heat-transfer coefficient for copper, silicon, and constantan. It is observed that the local heat-transfer coefficients for all three cases are below those of the similar cases above using water. This is due to the reduced difference in temperature between the jet and the interface. This is accounted for by the fact that R134a has a higher heat capacity compared to water and the higher speed that the simulation was run. Silicon and copper have nearly the same profile for local heat-transfer coefficients, with a peak at the first step. Silicon and copper's average local heat-transfer coefficient is essentially equal and constantan is slightly lower (~4%).

Figure 3.17 displays the variation of Nusselt number against all three materials using R134a as the working fluid. The behavior of the Nusselt number is similar to the local heat-transfer coefficients. The values of the Nusselt number are higher due to the low thermal conductivity of the fluid, leading to a dominance of convective heat transfer.

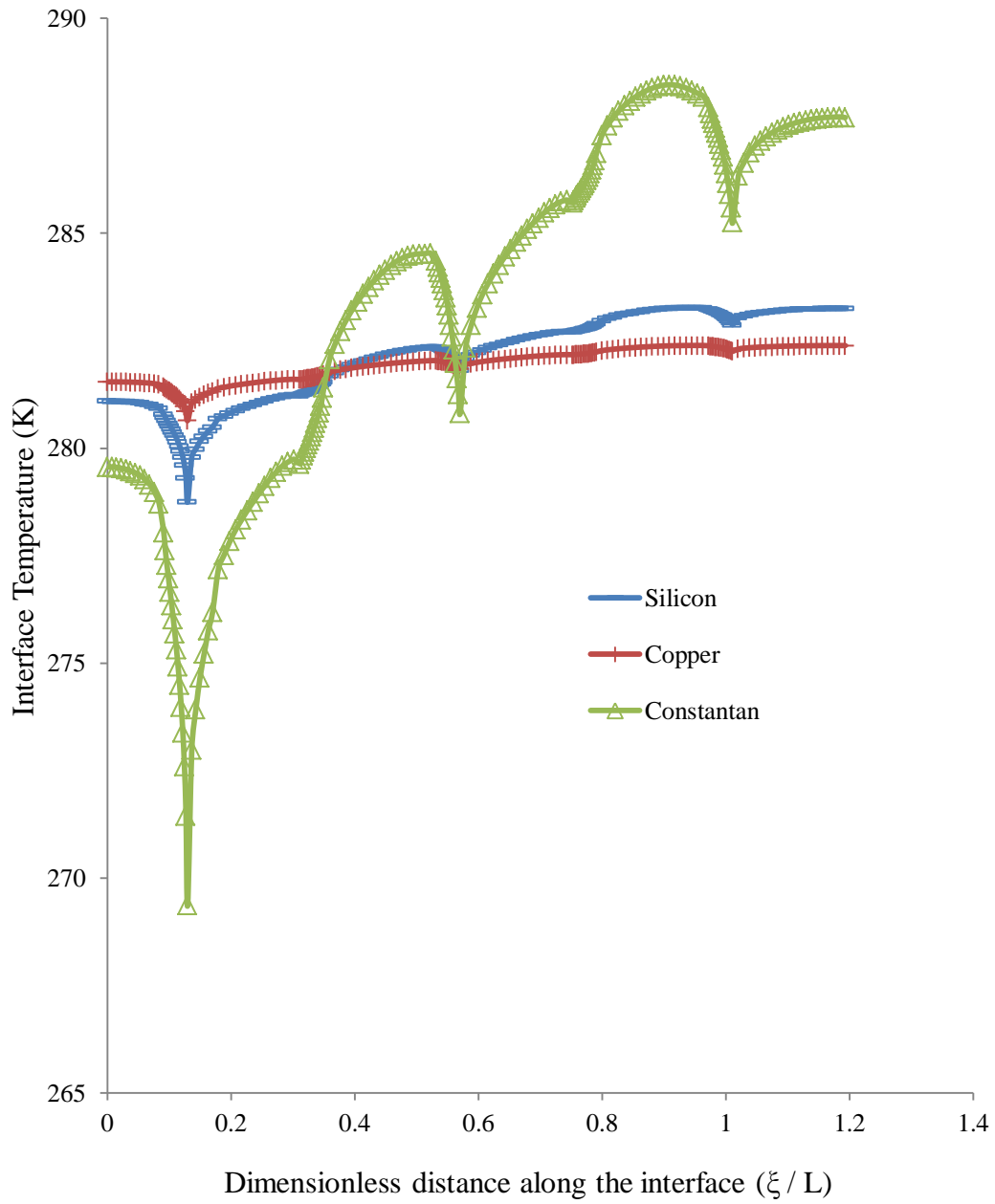


Figure 3.15 Interface temperature variation for different materials (R134a) ($Re = 1500$, $T_j = 253.15$ K, $b = 0.00125$ m, $H_n = 0.0055$ m, $q = 63$ kW/m², $W = 0.0017$ m)

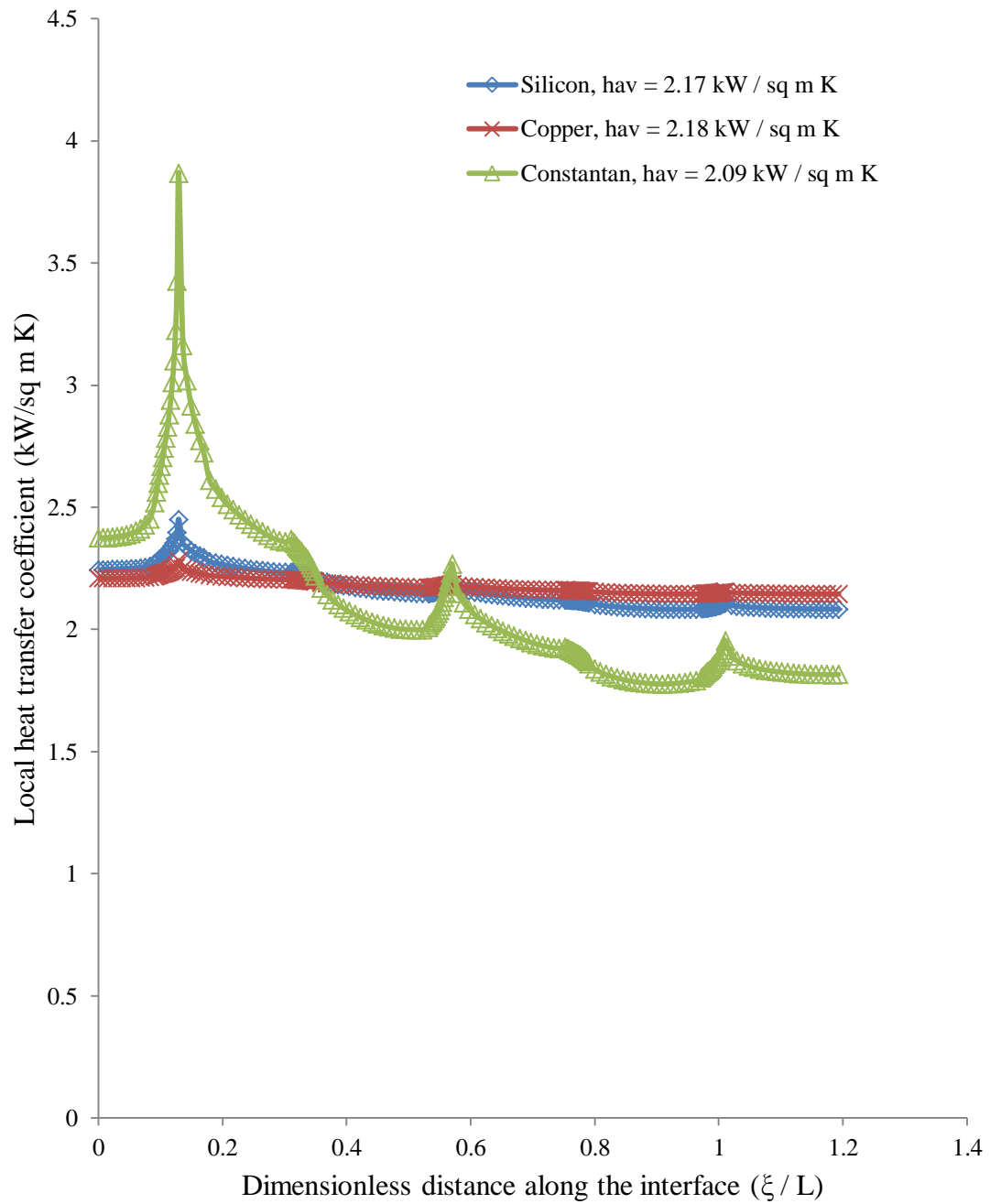


Figure 3.16 Local heat transfer coefficient variation for different materials (R134a)
 ($Re = 1500$, $T_j = 253.15$ K, $b = 0.00125$ m, $H_n = 0.0055$ m, $q = 63$ kW/m²,
 $W = 0.0017$ m)

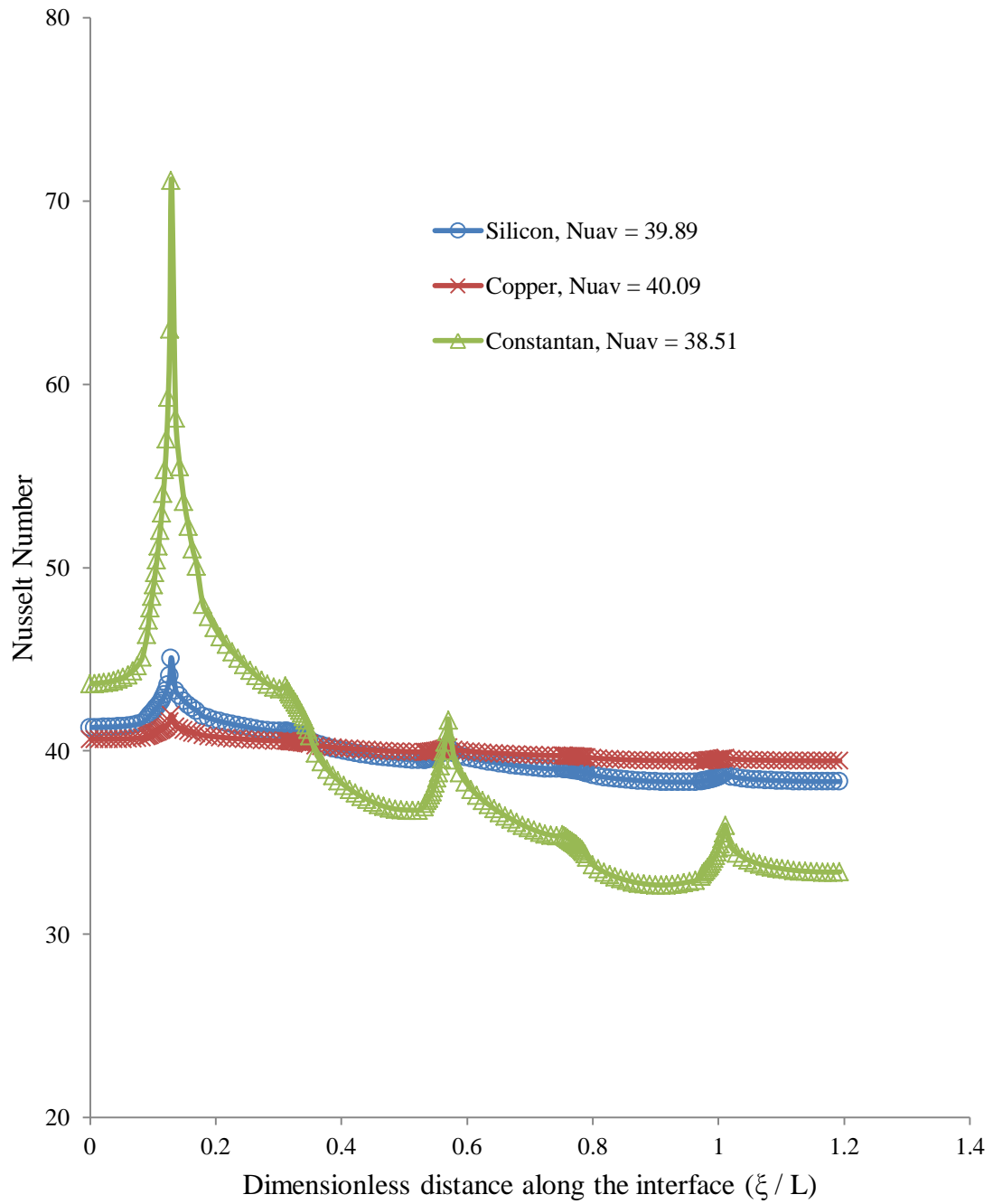
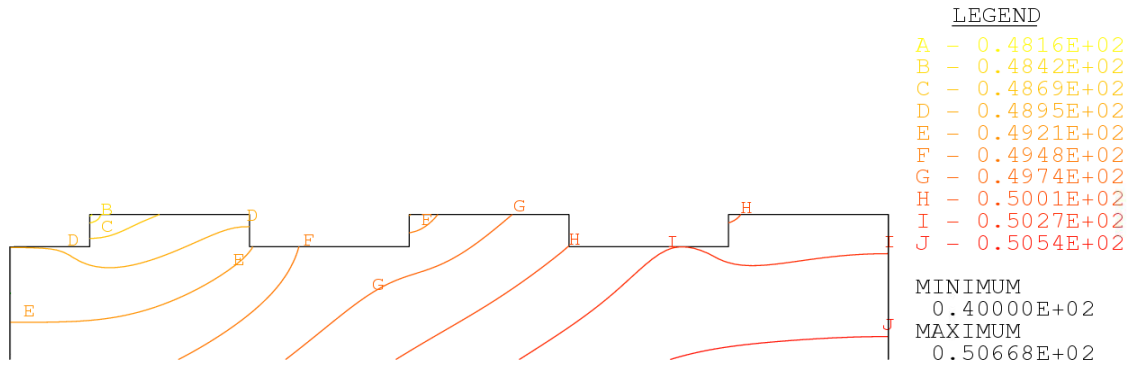
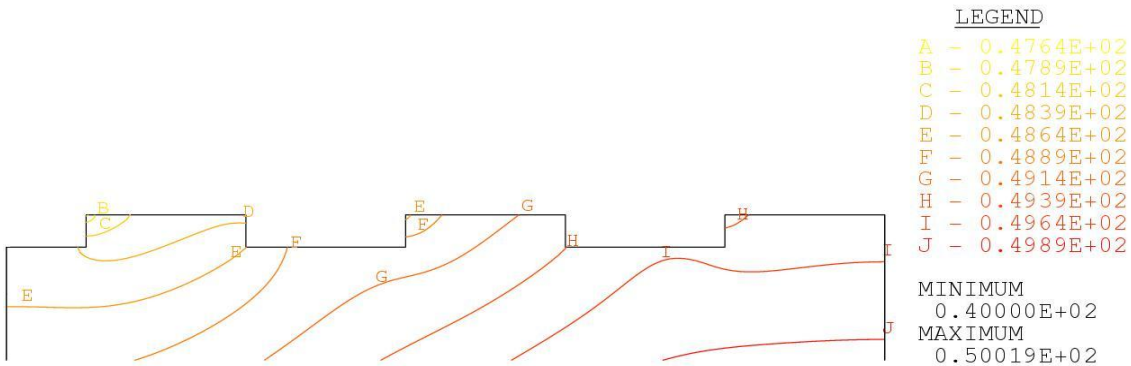


Figure 3.17 Local Nusselt number variation for different materials (R134a)
 ($Re = 1500$, $T_j = 253.15$ K, $b = 0.00125$ m, $H_n = 0.0055$ m, $q = 63$ kW/m²,
 $W=0.0017$ m)

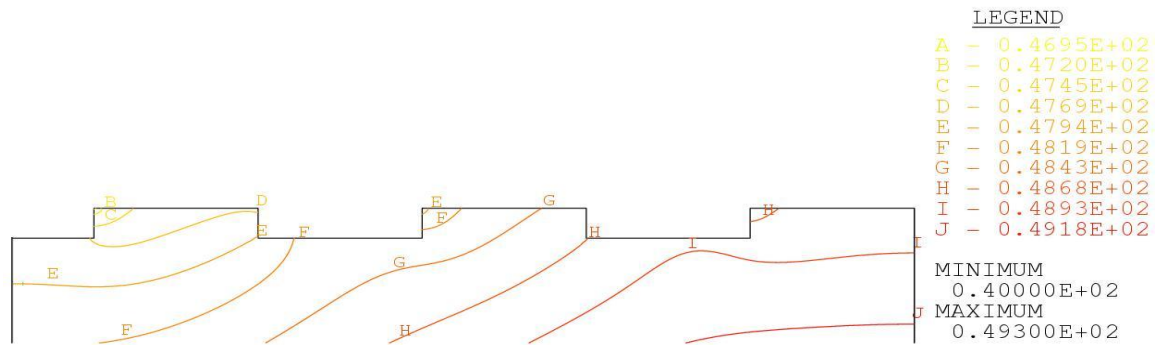
The temperature contour plot of the solid plate for differing Reynolds number is presented in Figure 3.18. The temperature within the plate is affected quite strongly by the Reynolds number of the impinging jet. There is, however, little change in the position of the isotherms with changing Reynolds number for the presented case. In the area immediately surrounding the stagnation zone, the contour lines are concentric around the impinging zone. Past this area the contours become parallel to the plate edge, implying that radial conduction is prevalent. Towards the end of the plate one-dimensional conduction appears to be taking hold of the plate as the contour lines become more parallel to the bottom of the plate. Figure 3.19 displays the isothermal lines for differing plate configurations. Case A has more obvious radial conduction within the solid, primarily due to the smaller indentations that contain the cooling fluid. Case B is about a degree K warmer than case A through the entire plate, but this effect is concentrated towards the end of the plate where one-dimensional conduction from the bottom of the plate is dominant. Figure 3.20 shows the isothermal lines for copper and constantan plates. As discussed above, the copper material and its high conductivity causes the plate to be largely the same temperature throughout, varying under a degree Kelvin throughout the entire solid. The constantan plate has a very large variation in temperature that is more evenly spread throughout the solid. The isothermal lines are much more parallel to the bottom of the plate when compared to the previous cases. Suppression of the radial conduction was expected given the low thermal conductivity of the material.



a) Re = 500



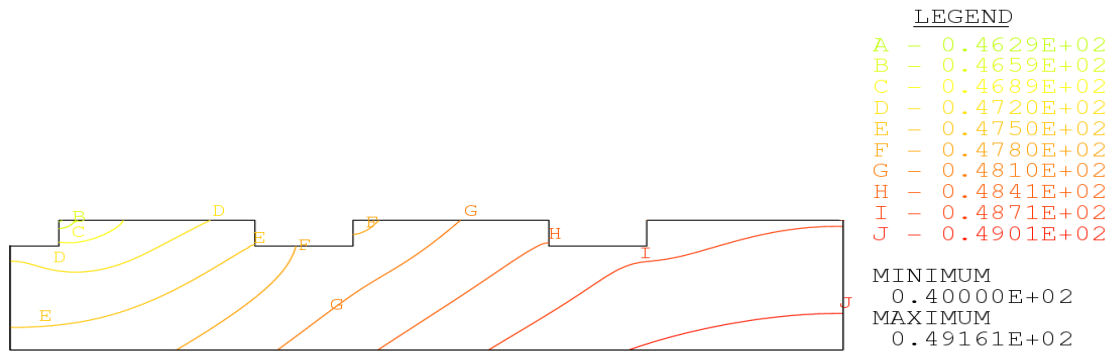
b) Re = 750



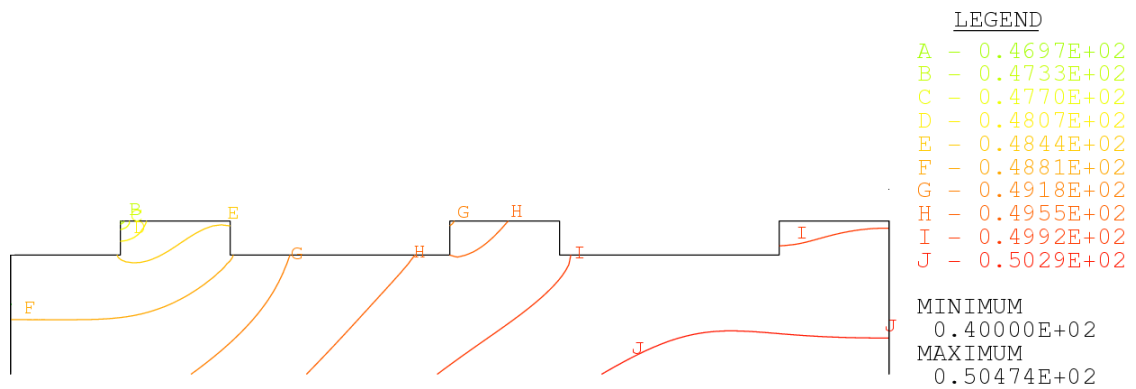
c) Re = 1000

Figure 3.18 Isothermal lines (in degrees Celsius) within the plate for different Reynolds number

($T_j = 313.15$ K, $b = 0.00125$ m, $H_n = 0.0055$ m, Silicon plate, $q = 63$ kW/m², $W=0.0017$ m)

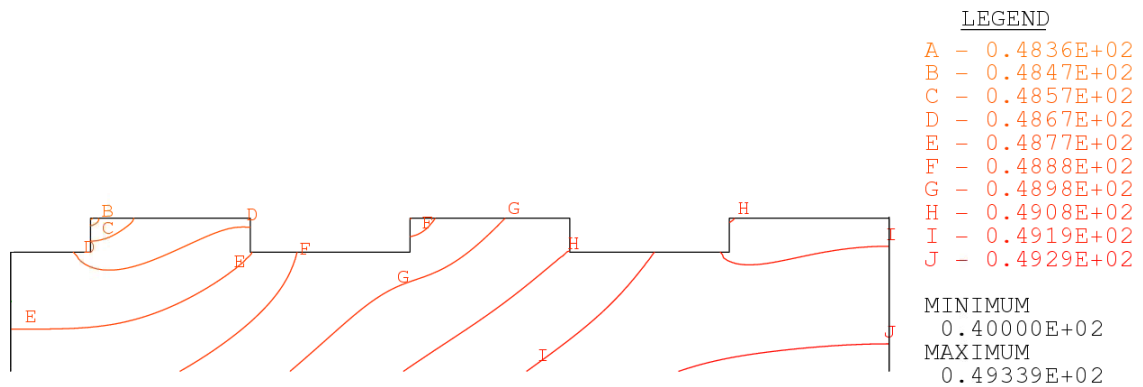


a) Case A

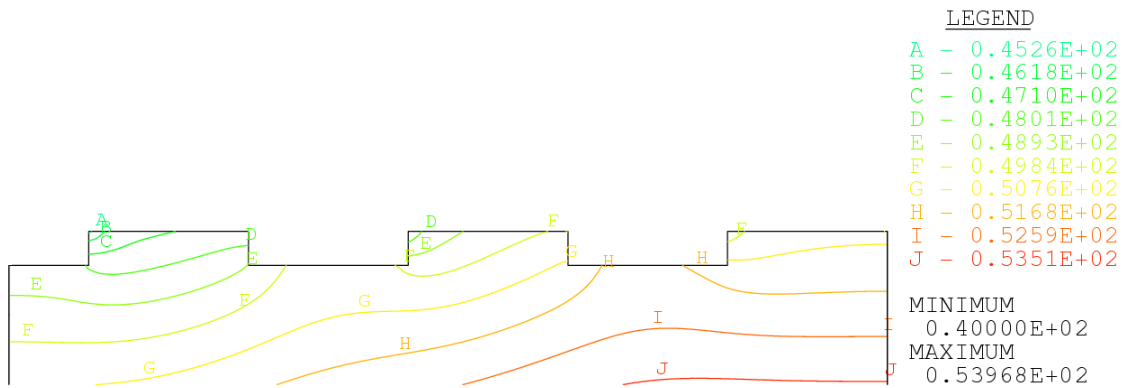


b) Case B

Figure 3.19 Isothermal lines (in degrees Celsius) within the plate for different surface configurations
 (Re = 750, $T_j = 313.15$ K, $b = 0.00125$ m, $H_n = 0.0055$ m, Silicon plate, $q = 63$ kW/m², $W = 0.0017$ m)



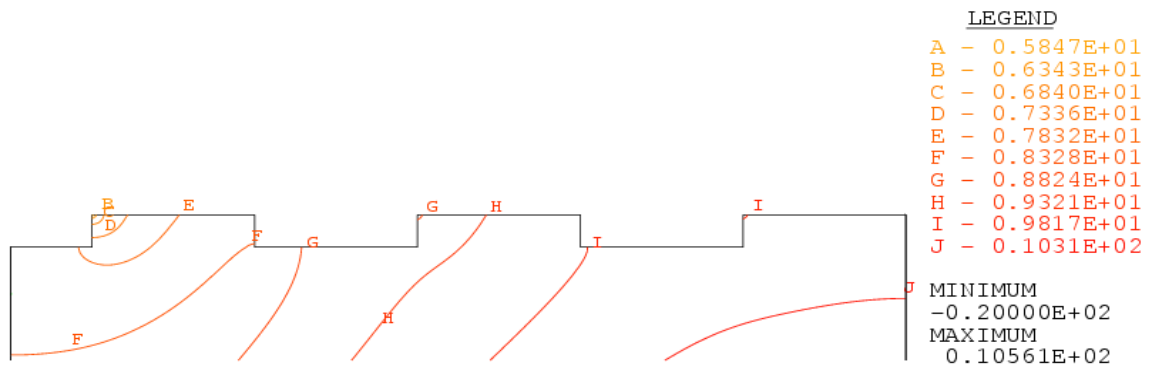
a) Copper



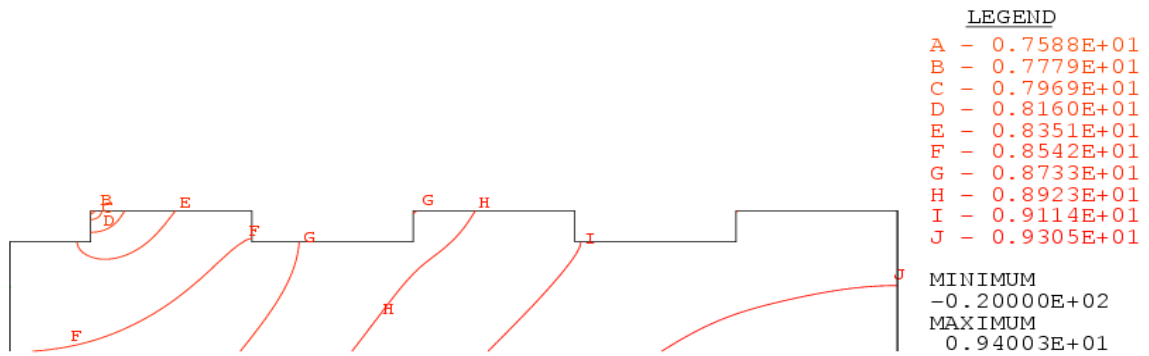
b) Constantan

Figure 3.20 Isothermal lines (in degrees Celsius) within the plate for different materials
 ($Re = 750$, $T_j = 313.15$ K, $b = 0.00125$ m, $H_n = 0.0055$ m, $q = 63$ kW/m²,
 $W=0.0017$ m)

The isothermal lines for silicon, copper, and constantan plates with R134a as the working fluid are shown in Figure 3.21. It is observed that silicon and copper have nearly the same temperature distribution, with the only major difference being in highest and lowest temperature. This is explained by their similar thermal conductivities that allow for a large amount of radial conduction. The coolest area of the plate is present in the stagnation zone, with the temperature difference between the two materials being ~2 K. The isotherms for constantan are indicative of its lower thermal conductivity. This results in a much larger variation in temperature along the x-axis. The lowest temperatures are once again in the stagnation zone, with the lowest being ~5 K lower than that of copper.



a) Silicon



b) Copper

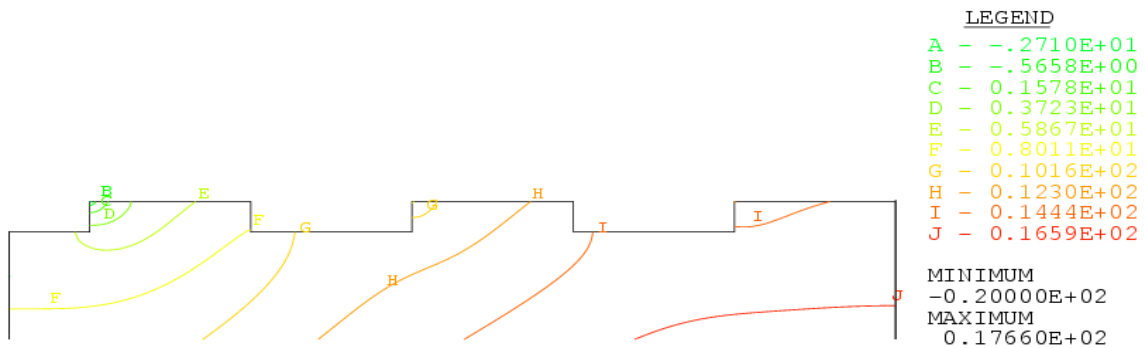


Figure 3.21 Isothermal lines (in degrees Celsius) for various materials (R134a)
 $(Re = 1500, T_j = 253.15 \text{ K}, b = 0.00125 \text{ m}, H_n = 0.0055 \text{ m}, q = 63 \text{ kW/m}^2,$
 $W=0.0017 \text{ m})$

3.2 Slot Jet Impinging on a Uniformly Heated Plate with Triangular Ridges: Steady State Heating

For this investigation water was used as the working fluid and silicon was used as the solid plate material. Figure 3.22 illustrates the three rib configurations studied in this series of simulations. The base case has a pitch angle of 60 degrees, case A has 90 degree angles, and case B has 30 degree angles. Each case considered 14 triangular ridges with the final half indentation being at the outlet. Since the slot jet is positioned at the midpoint of the plate, the $x = 0$ coincided with the midpoint of an indentation. A typical distribution of the velocity vectors can be seen in Figure 3.23. As the jet moves towards the plate surface, the potential jet core region of the velocity profile remains nearly uniform. As the jet comes closer to the stagnation zone the velocity drops and the jet diameter increases. Upon entering the stagnation zone the velocity reaches its lowest point, as the fluid changes direction nearly 90 degrees. Recirculation is present in each of the spaces between the ribs, resulting in accelerated fluid flow in film past the area of minimum sheet thickness. As the fluid progresses down the plate, friction builds up causing the velocity profile near the end of the plate to become parabolic, going from zero at the solid-liquid interface to a maximum in the center of the flow. Figure 3.24 presents the variation in free surface height with changing Reynolds number. It can be observed that with increasing Reynolds number the free surface height increases. This is a result of the recirculation that occurs within the space between each triangular rib. The length of the plate and velocities present do not allow for the formation of a hydraulic jump. At the end of the plate the free surface drops due to the gap between the final triangular rib and the end of the plate.

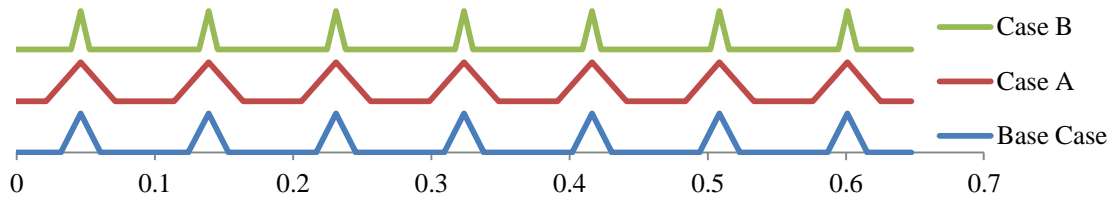


Figure 3.22 Comparison of different triangular ribbed geometries investigated

Figure 3.25 shows the variation of the solid-fluid interface temperature for different Reynolds number using the triangular base case. The point of minimum temperature is inside the stagnation zone, at approximately $\xi/L = 0.09$. This point coincides with the tip of the first triangular rib. After this low temperature the interface temperature then quickly rises ~ 2 K. This point is the center of the channel between the first and second triangular rib. The temperature then falls again to the next peak across nearly the same distance. This pattern continues until the end of the plate, with the average temperature rising as the fluid goes downstream. The drops in temperature are explained by the thermal boundary layer being disrupted by each abrupt change in geometry.

The distribution of the local heat-transfer coefficient for different Reynolds numbers in the base case is shown in Figure 3.26. It can be seen that inside the first channel, where the jet impinges, the local heat-transfer coefficient stays nearly constant

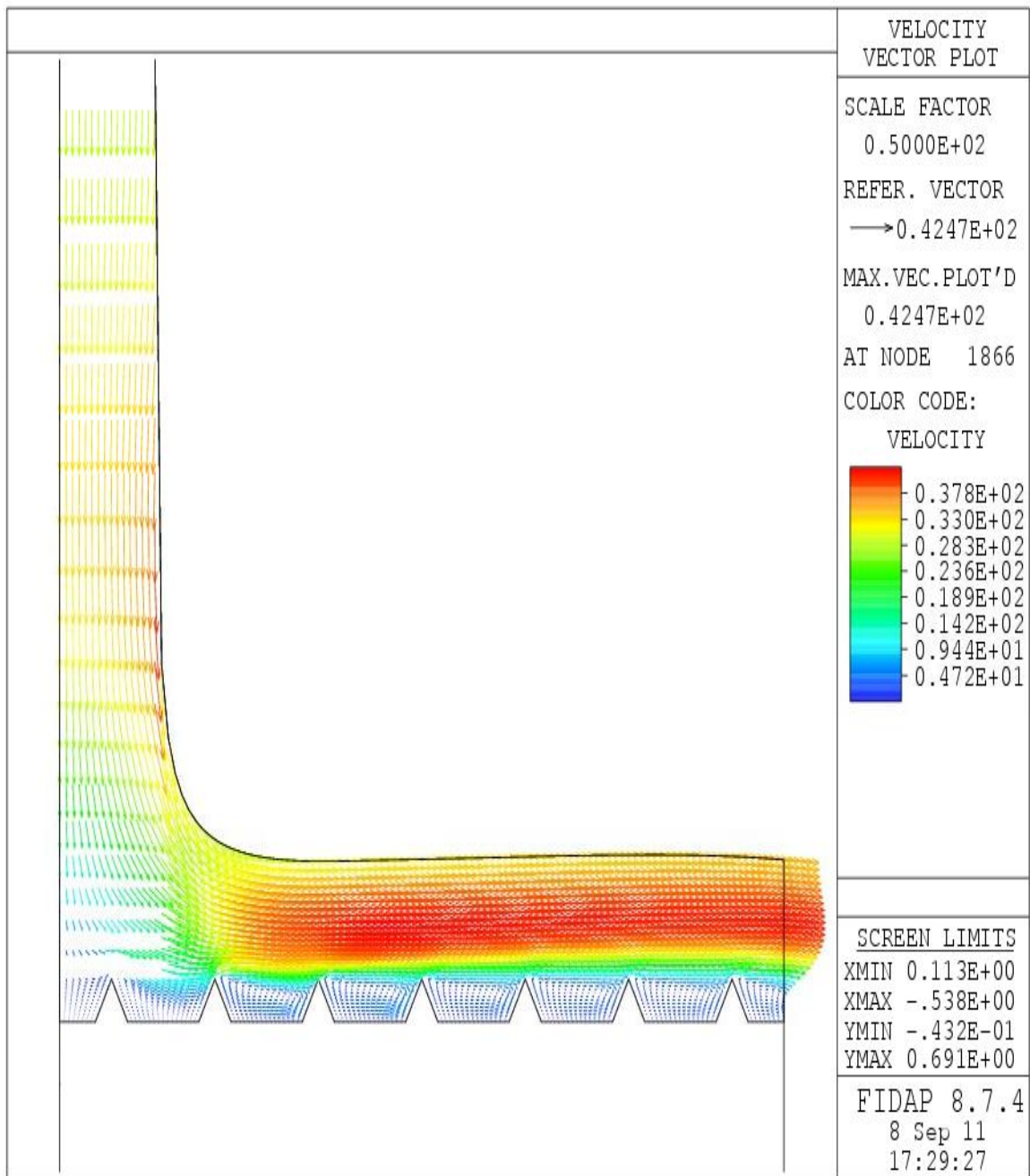


Figure 3.23 Velocity vector distribution for triangle ribs
($Re = 750$, $T_j = 313.15$ K, $b = 0.00125$ m, $H_n = 0.0055$ m, Silicon plate,
 $q = 63$ kW/m², $W=0.0017$ m)

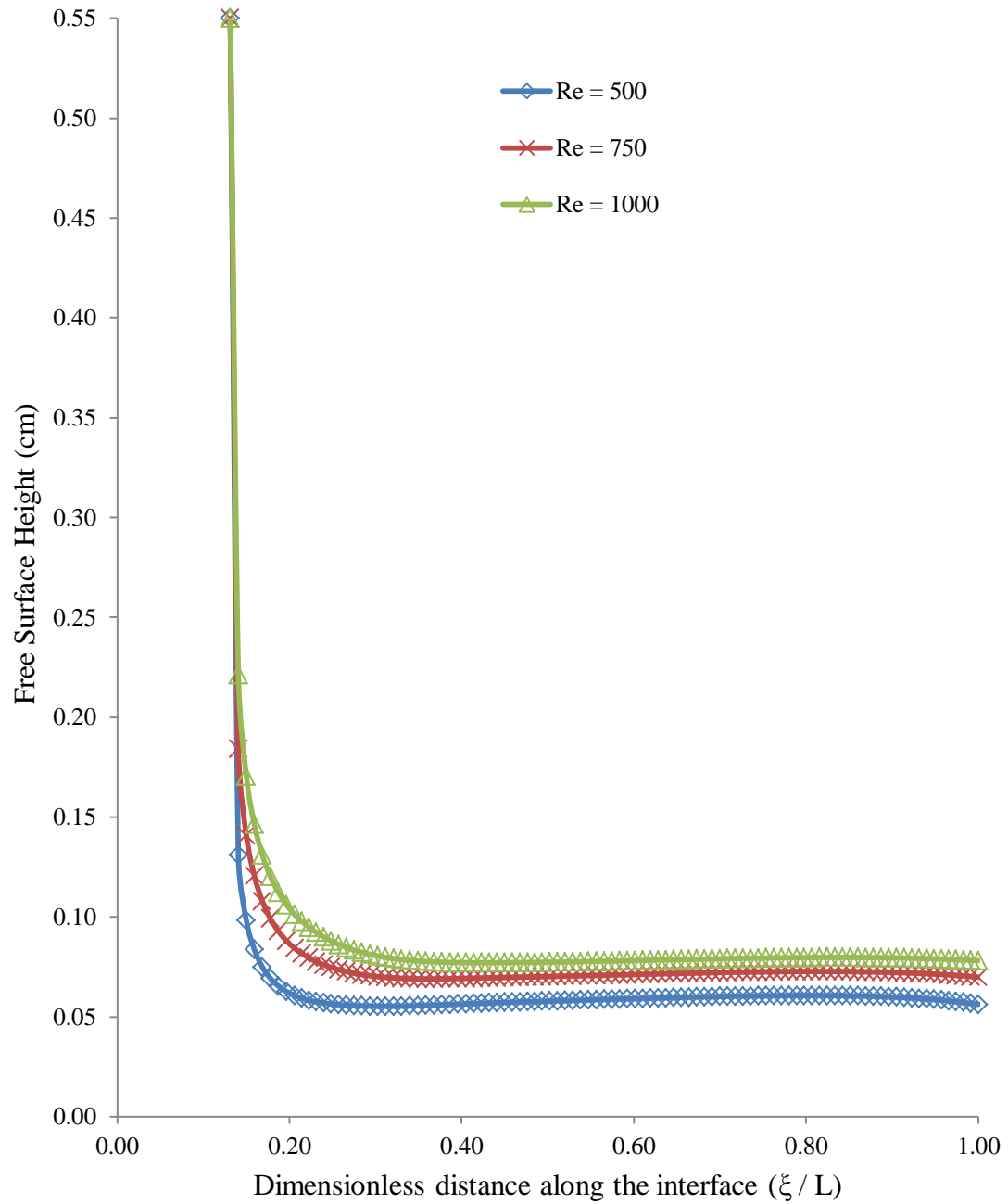


Figure 3.24 Free surface height distribution for triangle ribs
 (Re = 750, $T_j = 313.15$ K, $b = 0.00125$ m, $H_n = 0.0055$ m, Silicon plate, base case,
 $q = 63$ kW/m², $W = 0.0017$ m)

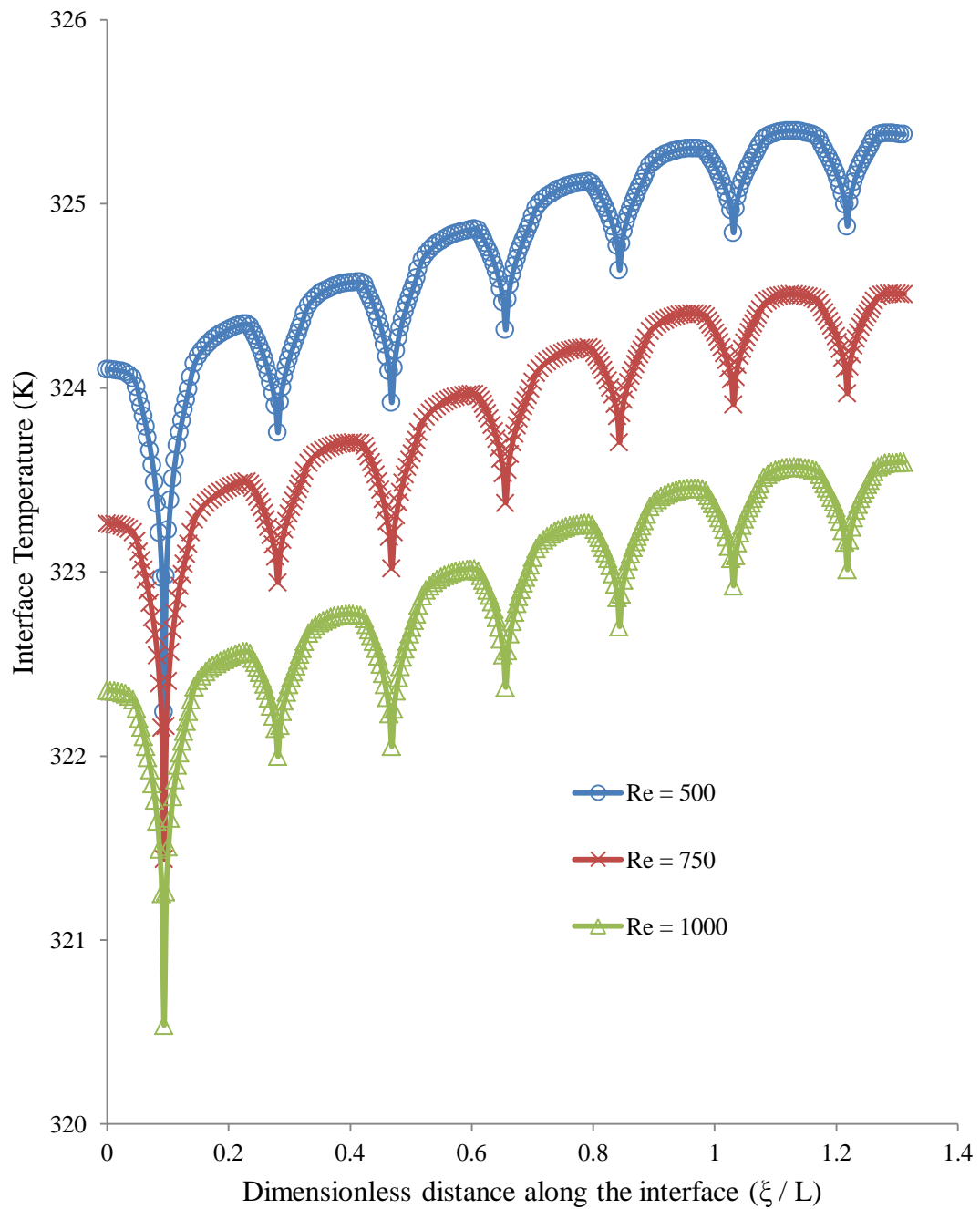


Figure 3.25 Interface temperature for varying Reynolds number
 (Re = 750, $T_j = 313.15$ K, $b = 0.00125$ m, $H_n = 0.0055$ m, Silicon plate, base case,
 $q = 63$ kW/m², $W = 0.0017$ m)

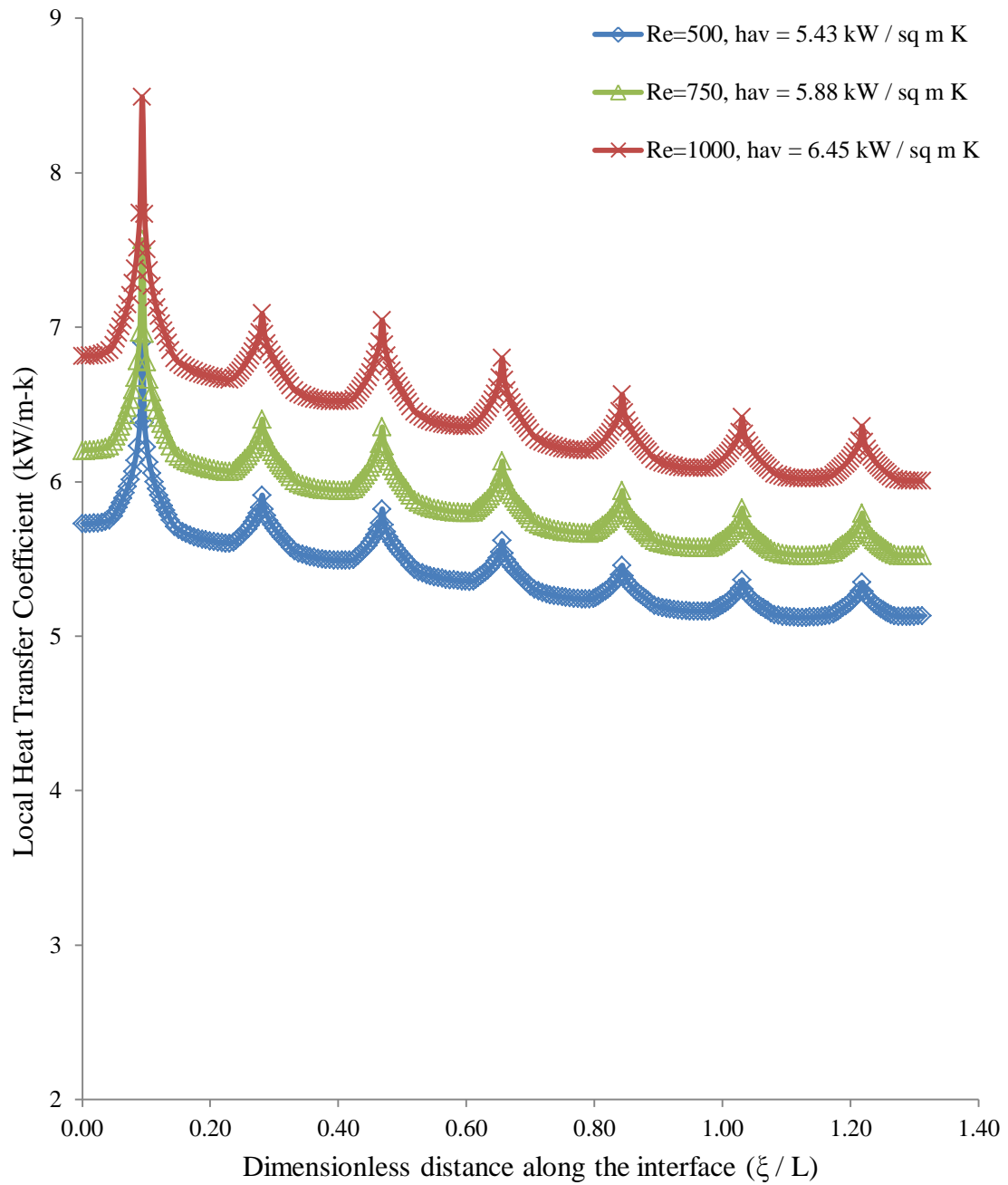


Figure 3.26 Local heat transfer coefficient for varying Reynolds number (Re = 750, $T_j = 313.15 \text{ K}$, $b = 0.00125 \text{ m}$, $H_n = 0.0055 \text{ m}$, Silicon plate, base case, $q = 63 \text{ kW/m}^2$, $W=0.0017 \text{ m}$)

until reaching a peak near $\xi/L = 0.09$, which coincides to the point where the interface temperature is lowest. Similar points occur along the length of the plate at locations where fluid strikes each rib before recirculating into the channel and back into the film above. This recirculation disrupts the thermal boundary layer, thus allowing for the increase in local heat-transfer coefficient along the path. This increase does not affect the entire channel due to the relative slow speed of the fluid contained between the ribs. Increasing the Reynolds number increased the local heat-transfer coefficient over the length of the plate. Doubling the Reynolds number from 500 to 1000 increased the average local heat-transfer coefficient by 15.8%. Figure 3.27 displays the local Nusselt number variation for different Reynolds numbers. Due to the definition of the local Nusselt number, the primary difference between each case is entirely due to the increase in heat-transfer coefficient as the fluid's velocity increases. Both the local Nusselt number and the average Nusselt number increase with Reynolds number.

Figure 3.28 shows the variation of Nusselt number with changes in plate configuration. Case B has the highest peak in Nusselt number due to the radical change in direction the fluid must undergo when it encounters the first extremely thin triangular rib. The channels between ribs show markedly lower heat transfer due to reduced fluid flow. In this instance the base case, which would be the middle case in terms of pitch angle, has the most favorable heat transfer characteristics. Even with the large spikes in Nusselt number in case B, the average Nusselt number for the base case is only slightly higher than the other two cases (by 0.7%). Unlike the rectangular case, the addition of surface geometry has a dramatic negative effect on the Nusselt number across the length of the plate. In this case keeping a flat plate for impingement is clearly superior.

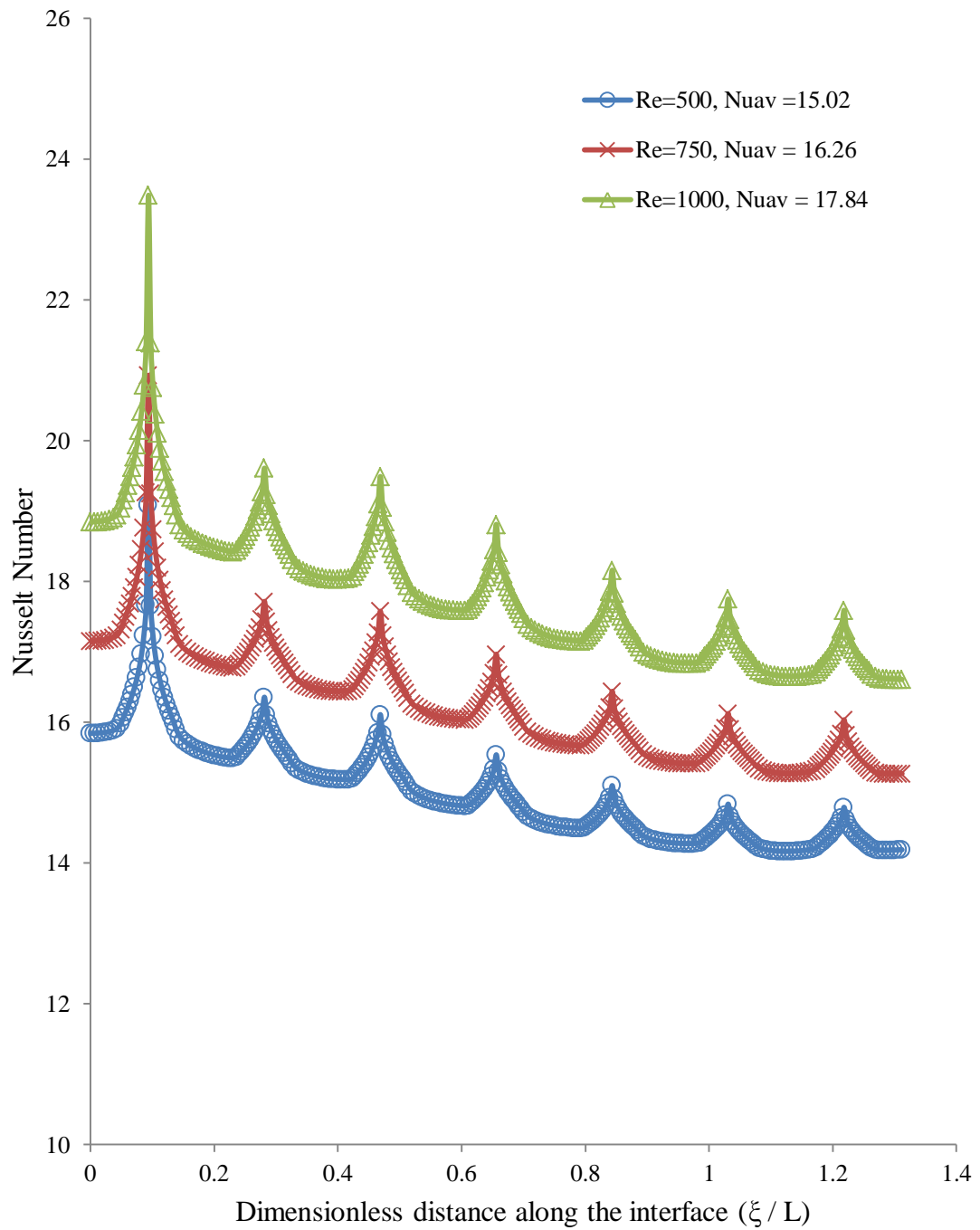


Figure 3.27 Local Nusselt number for varying Reynolds number
 (Re = 750, $T_j = 313.15$ K, $b = 0.00125$ m, $H_n = 0.0055$ m, Silicon plate, base case,
 $q = 63$ kW/m², $W = 0.0017$ m)

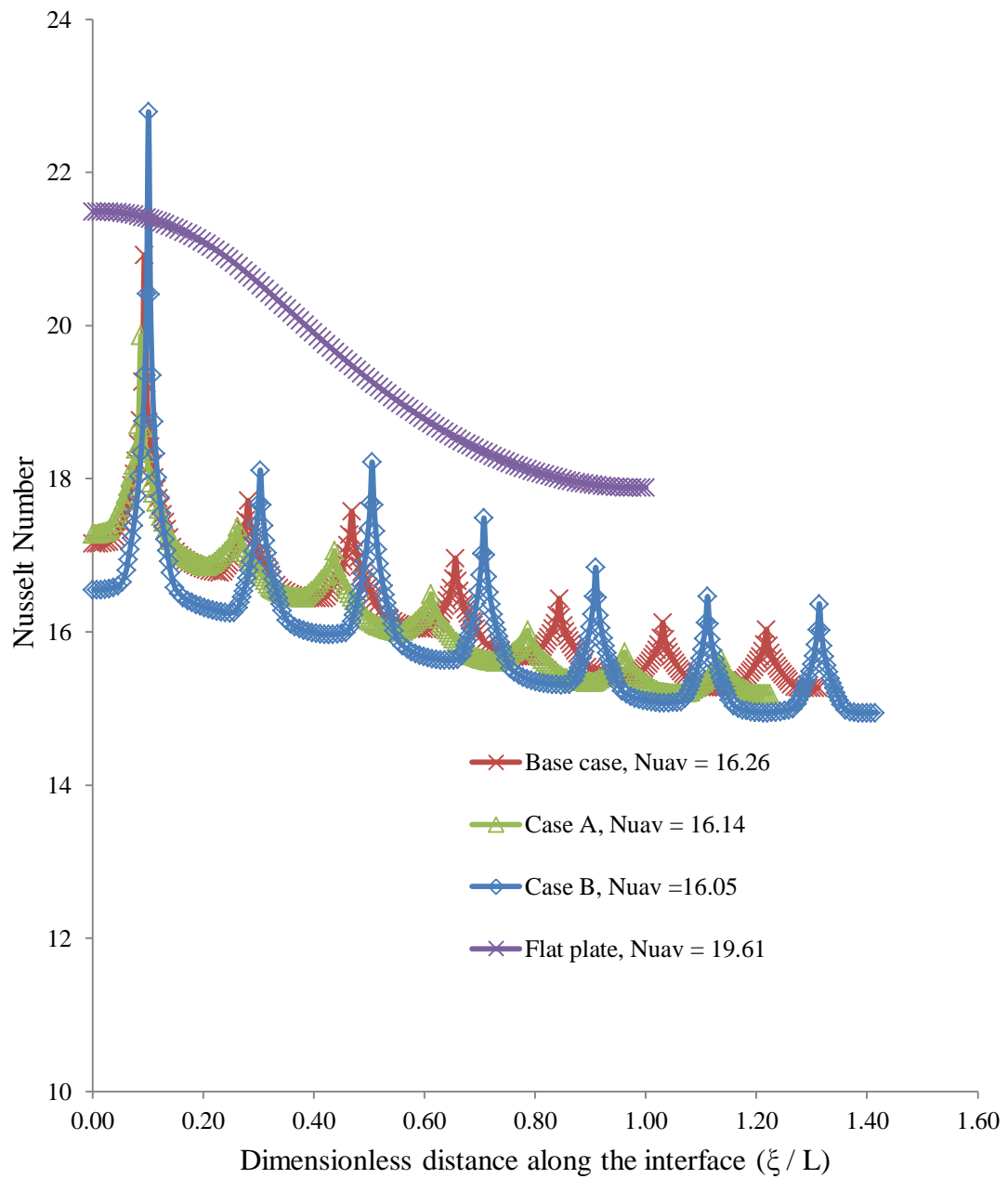


Figure 3.28 Local Nusselt number for varying plate geometries
 ($Re = 750$, $T_j = 313.15$ K, $b = 0.00125$ m, $H_n = 0.0055$ m, Silicon plate,
 $q = 63$ kW/m², $W = 0.0017$ m)

Figures 3.29 and 3.30 display the variation of Nusselt number with indentation depth for the base case and case B. Both cases illustrate that increasing the indentation depth increases the Nusselt number, a result that is not similar to the rectangular step cases. This is due to high rate of heat conduction through the thin ribs, allowing the fluid to cool more of the solid along the interface. The use of larger indentation depths also stabilizes the Nusselt number across the length of the plate, resulting in a much more consistent heat transfer profile. When $a = 0.000125 \text{ m}$, the fluid does not have to change direction in a drastic way, preventing the fluid disturbance that helps to cause the dramatic spikes in local Nusselt number in the other depths. The results here also show that the base case possesses higher average Nusselt number for all indentation depths. However, the difference in average values when $a = 0.0005 \text{ m}$ in the base case and case B is only 1.18%, showing that the Nusselt number and heat transfer values depend more on the indentation depth of the geometry as opposed to the configuration.

Figure 3.31 shows the isothermal lines for the base case with varying Reynolds numbers. Raising the Reynolds number affects the overall temperature of the plate but has little effect on the distribution of the temperatures from case to case. The isotherms are concentric around the stagnation zone and have the lowest temperature near the area where the jet initially interacts with the plate. This effect is negated as the cooling fluid is warmed moving downstream from the impingement zone. The conduction in the plate is initially radial in nature outside the stagnation zone. When the isothermal lines begin to become parallel to the bottom of the plate, one-dimensional conduction has become dominant. Outside of the stagnation zone the coolest temperatures are found at the very top of each triangular rib. These points coincide with the areas where convective heat

transfer is at its highest. Figure 3.32 displays the isothermal lines for the different surface configurations. The thinner more fin-like ribs in case B show a much larger variation in temperature compared to the base case and case A. This was expected as fins are some of the best geometric shapes for heat transfer due to their thinness and high surface area.

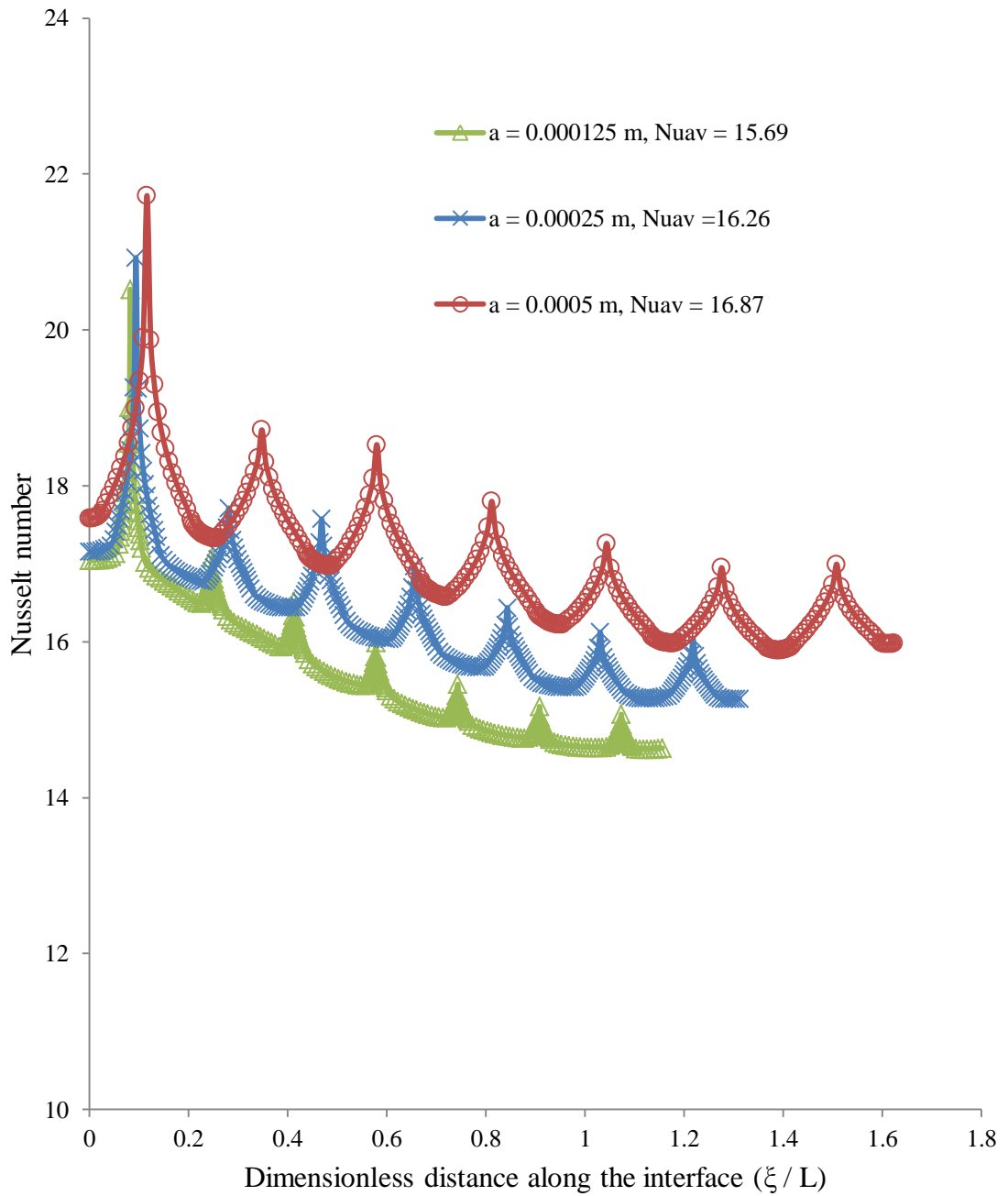


Figure 3.29 Local Nusselt number for varying indentation depths (Re = 750, $T_j = 313.15$ K, $b = 0.00125$ m, $H_n = 0.0055$ m, Silicon plate, base case, $q = 63$ kW/m², $W = 0.0017$ m)

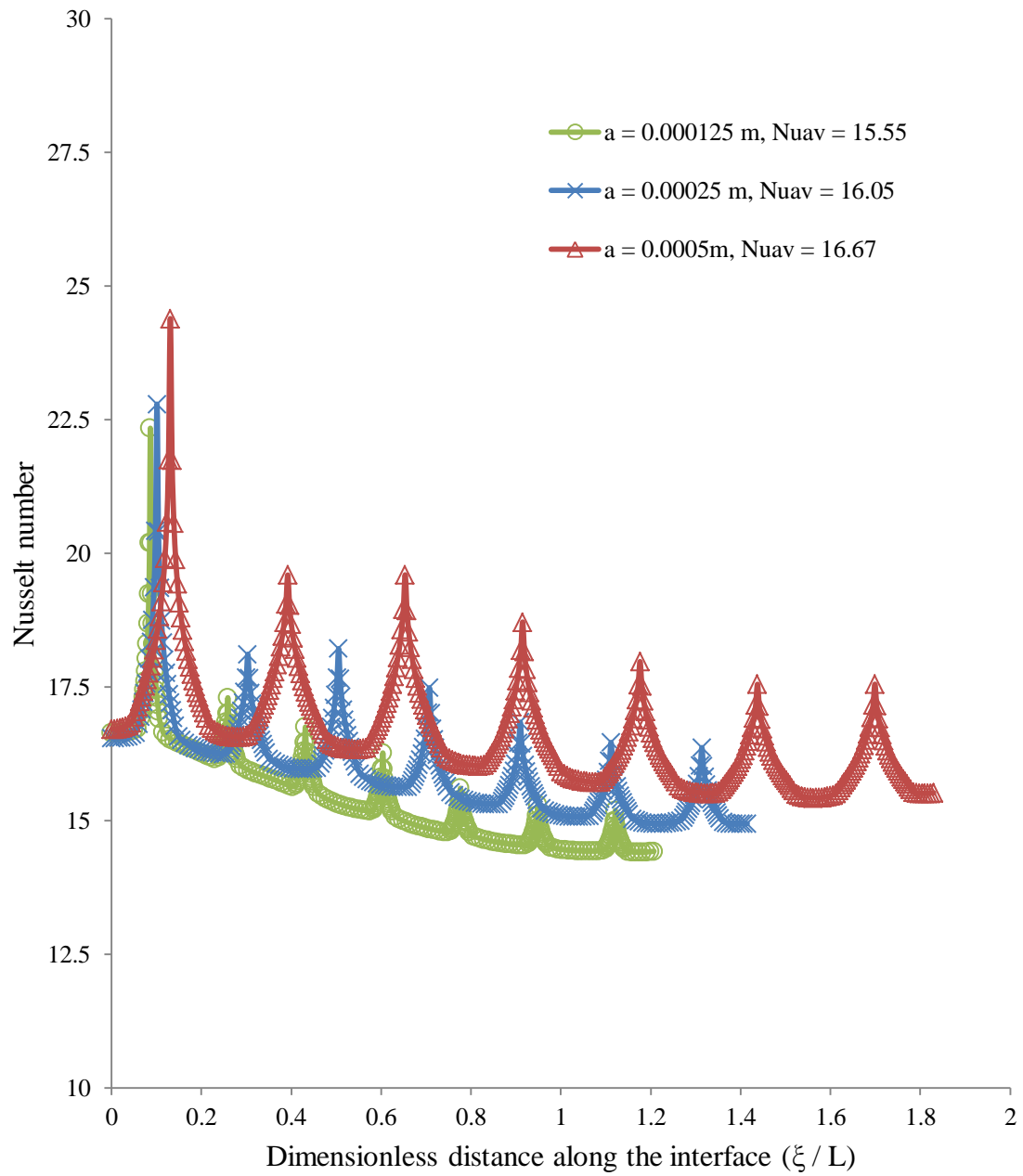
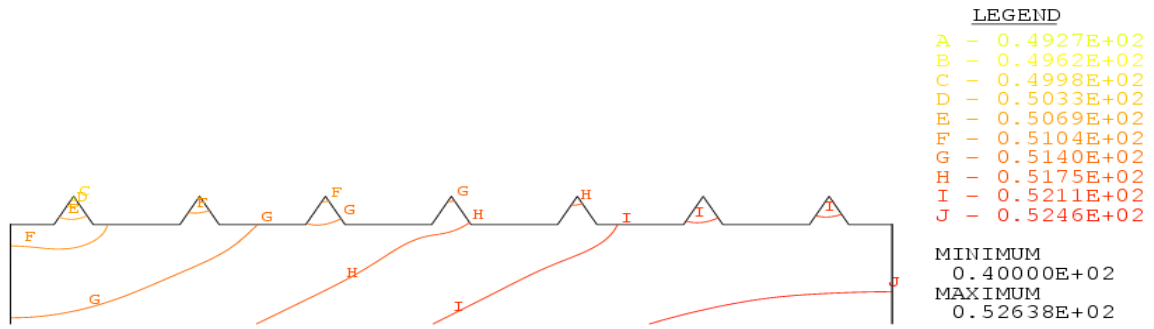
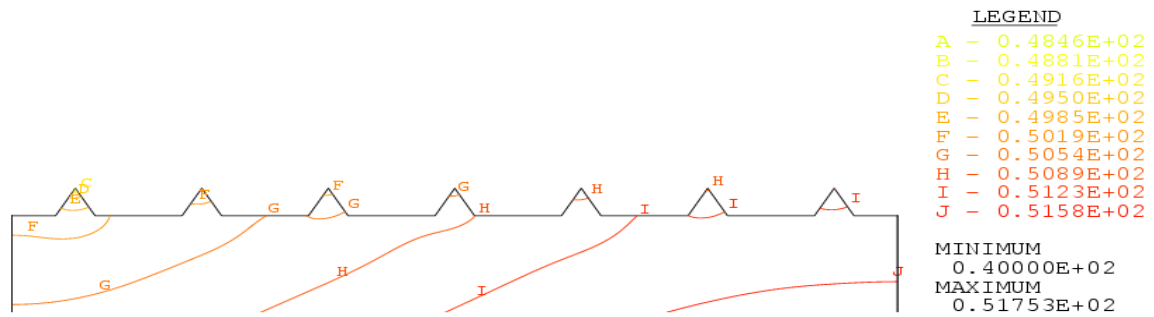


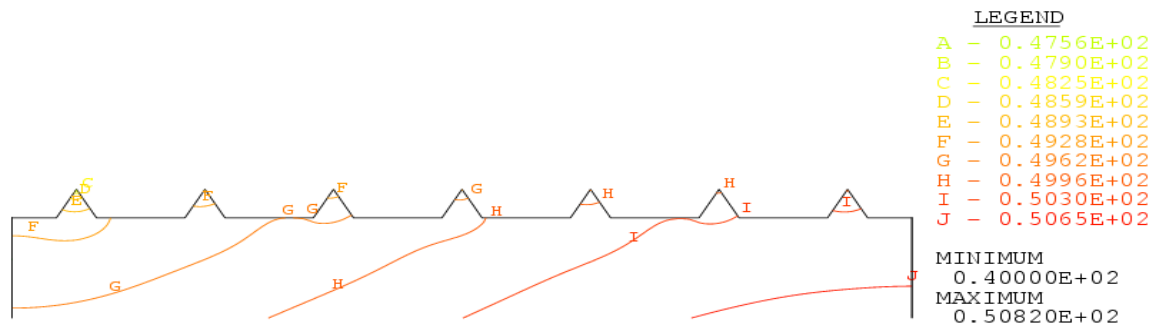
Figure 3.30 Local Nusselt number for varying indentation depths
 (Re = 750, $T_j = 313.15$ K, $b = 0.00125$ m, $H_n = 0.0055$ m, Silicon plate, Case B,
 $q = 63$ kW/m², $W = 0.0017$ m)



a) Re = 500

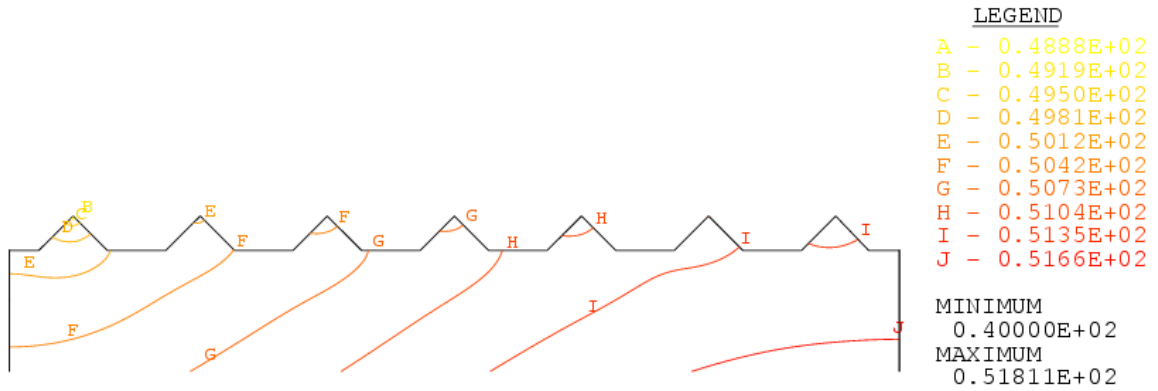


b) Re = 750

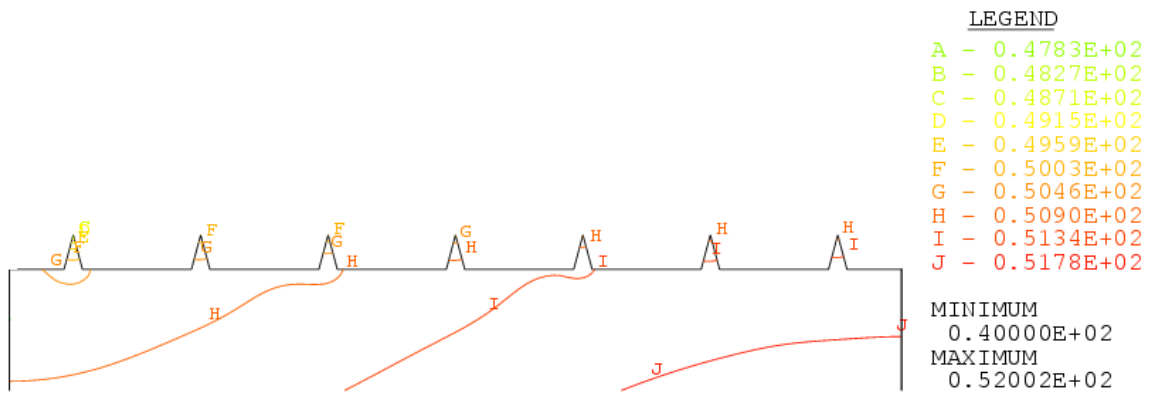


c) Re = 1000

Figure 3.31 Isothermal lines (in degrees Celsius) within the plate for different Reynolds number
 $(T_j = 313.15 \text{ K}, a=0.00025 \text{ m}, b = 0.00125 \text{ m}, H_n = 0.0055 \text{ m}, \text{Silicon plate}, q = 63 \text{ kW/m}^2, W=0.0017 \text{ m})$



a) Case A



b) Case B

Figure 3.32 Isothermal lines (in degrees Celsius) within the plate for different surface configurations
 (Re = 750, $T_j = 313.15$ K, $a = 0.00025$, $b = 0.00125$ m, $H_n = 0.0055$ m, Silicon plate, $q = 63$ kW/m², $W=0.0017$ m)

3.3 Slot Jet Impinging on a Uniformly Heated Plate with Sinusoidal Ridges: Steady State Heating

For this investigation water was used as the working fluid and silicon was used as the solid plate material. Figure 3.33 displays the configurations simulated in this case. The indentations and steps in case A are twice the length of those in base case. The steps and indentations in case B are the same radius as the step height. Each case considered 4 sinusoidal shaped surface effects. Unlike the previous geometries, the slot jet impinged in-between two indentations at $x = 0$.

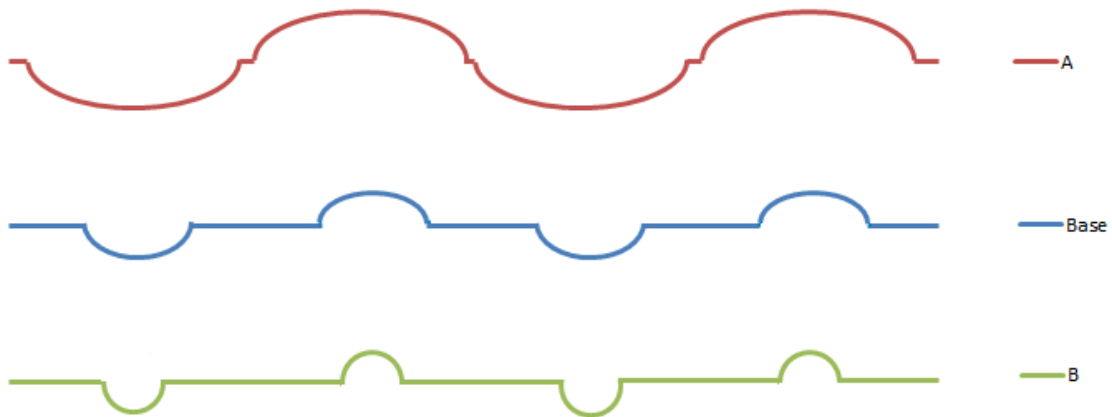


Figure 3.33 Comparison of the different sinusoidal geometries studied

The velocity vectors of a typical case are shown in Figure 3.34. The velocity profile of the free jet remains mostly constant as it progresses towards the impinging plate. As the jet comes closer to the stagnation zone the velocity drops and the jet diameter increases. As the jet enters the stagnation zone the velocity reaches its lowest point. Recirculation is present in each of the spaces between the ribs, this results in the

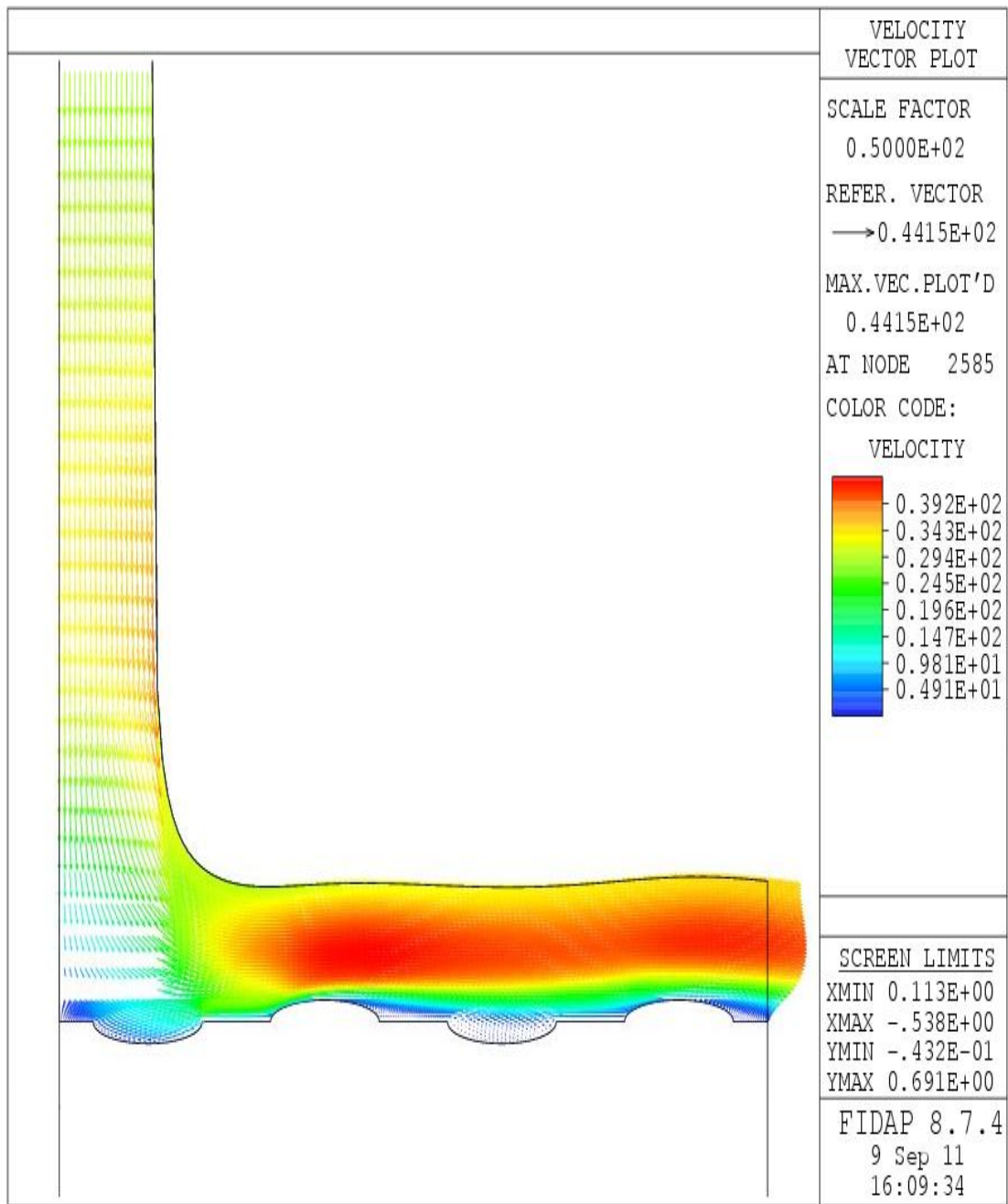


Figure 3.34 Typical velocity vectors for the sinusoidal case
 ($Re = 750$, $T_j = 313.15$ K, $b = 0.00125$ m, $H_n = 0.0055$ m, Silicon plate, $q = 63$ kW/m²,
 $W=0.0017$ m)

accelerated fluid flow past the area of minimum sheet thickness. As the fluid progresses down the plate, friction builds up causing the velocity profile near the end of the plate to become parabolic, going from zero at the solid-liquid interface to a maximum in the center of the flow. Compared to the previous cases discussed, the sinusoidal surface exhibits less of an effect on the velocity on the fluid. This is due to the reduced number of surface effects, the increased distance between each change in geometry, and the smoother surface shape.

The change in free surface height for differing Reynolds number is displayed in Figure 3.35. The free surface height increases in the two places along the plate where the curved surfaces protrude. This effect is more apparent with the lower Reynolds number jet. The increased height of the free surface with Reynolds number is due to the same effect described above in both the rectangular step and triangular ribs. Figure 3.36 The lowest temperatures are present in the stagnation zone where the fluid jet impinges upon the plate. The next low peak occurs at $\xi/L = 0.28$, a point where the first indentation ends and the plate becomes flat before the first curved step. Over the length of the plate the interface temperature steadily increases. Increasing Reynolds number results in the interface temperature decreasing. The behavior of the local heat-transfer coefficient for varying Reynolds number is displayed in figure 3.37. The highest heat-transfer coefficient is in the stagnation zone where the fluid changes direction by 90 degrees. As it progresses down the length of the plate a sheet of minimum thickness forms that leads to the fluid accelerating. In a flat plate this would eventually give way to a fully developed flow, in this case the surface features do not allow for this flow to develop. Peaks in the local heat-transfer coefficient occur due to the boundary layer being

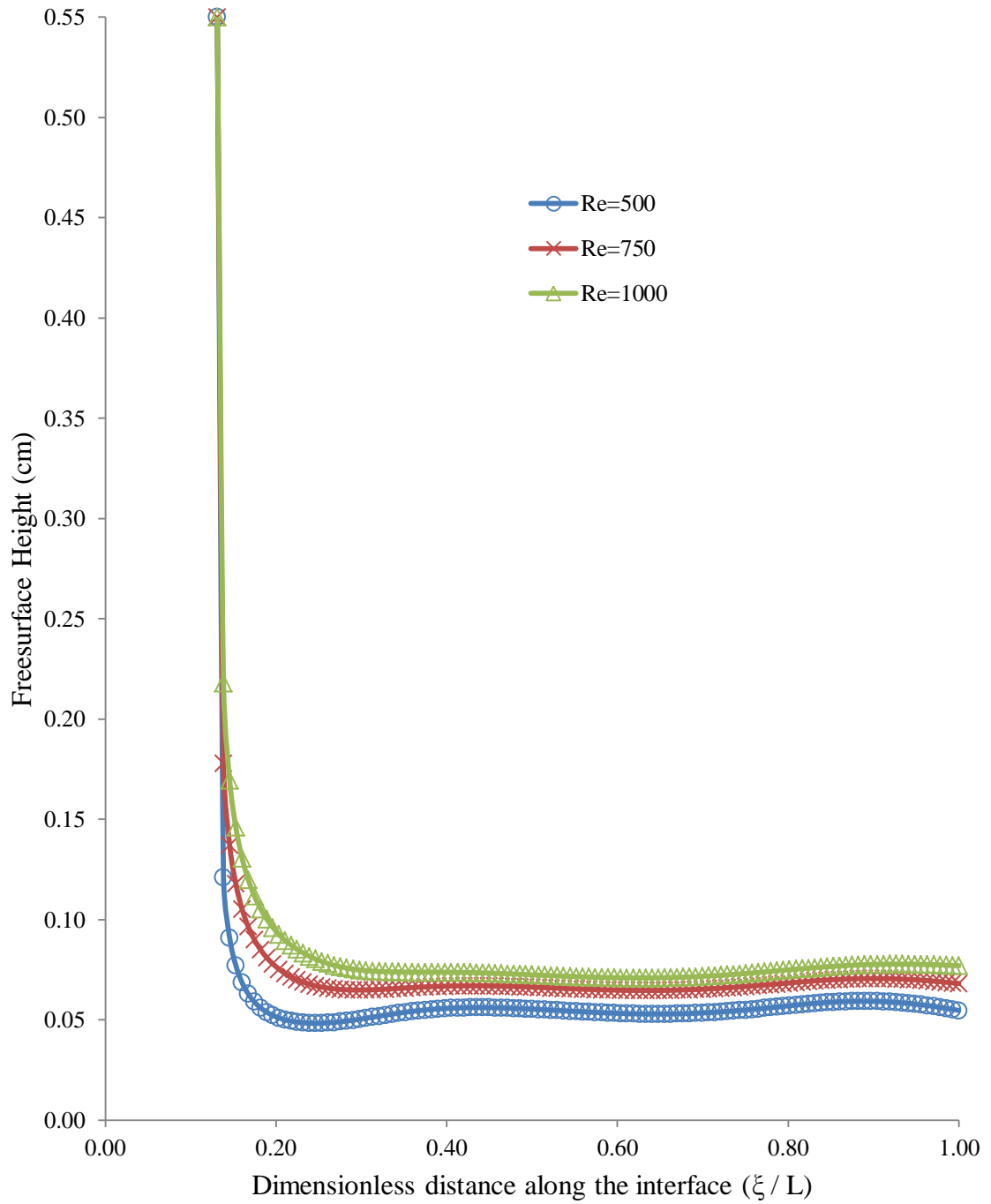


Figure 3.35 Free surface height distribution for different Reynolds number ($T_j = 313.15$ K, $b = 0.00125$ m, $H_n = 0.0055$ m, Silicon plate, $q = 63$ kW/m², $W=0.0017$ m)

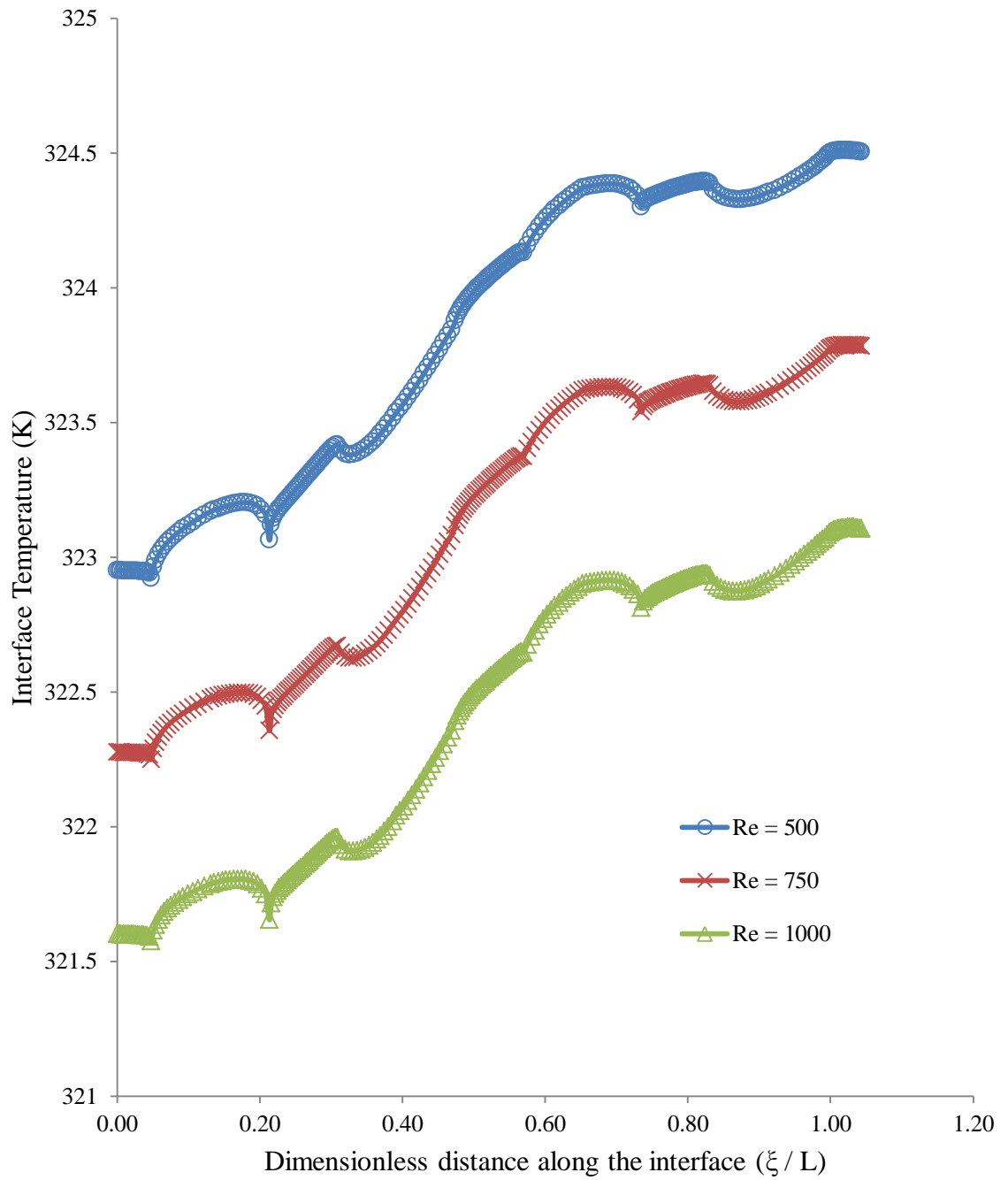


Figure 3.36 Interface temperature for various Reynolds number ($T_j = 313.15$ K, $b = 0.00125$ m, $H_n = 0.0055$ m, Silicon plate, $q = 63$ kW/m², $W = 0.0017$ m)

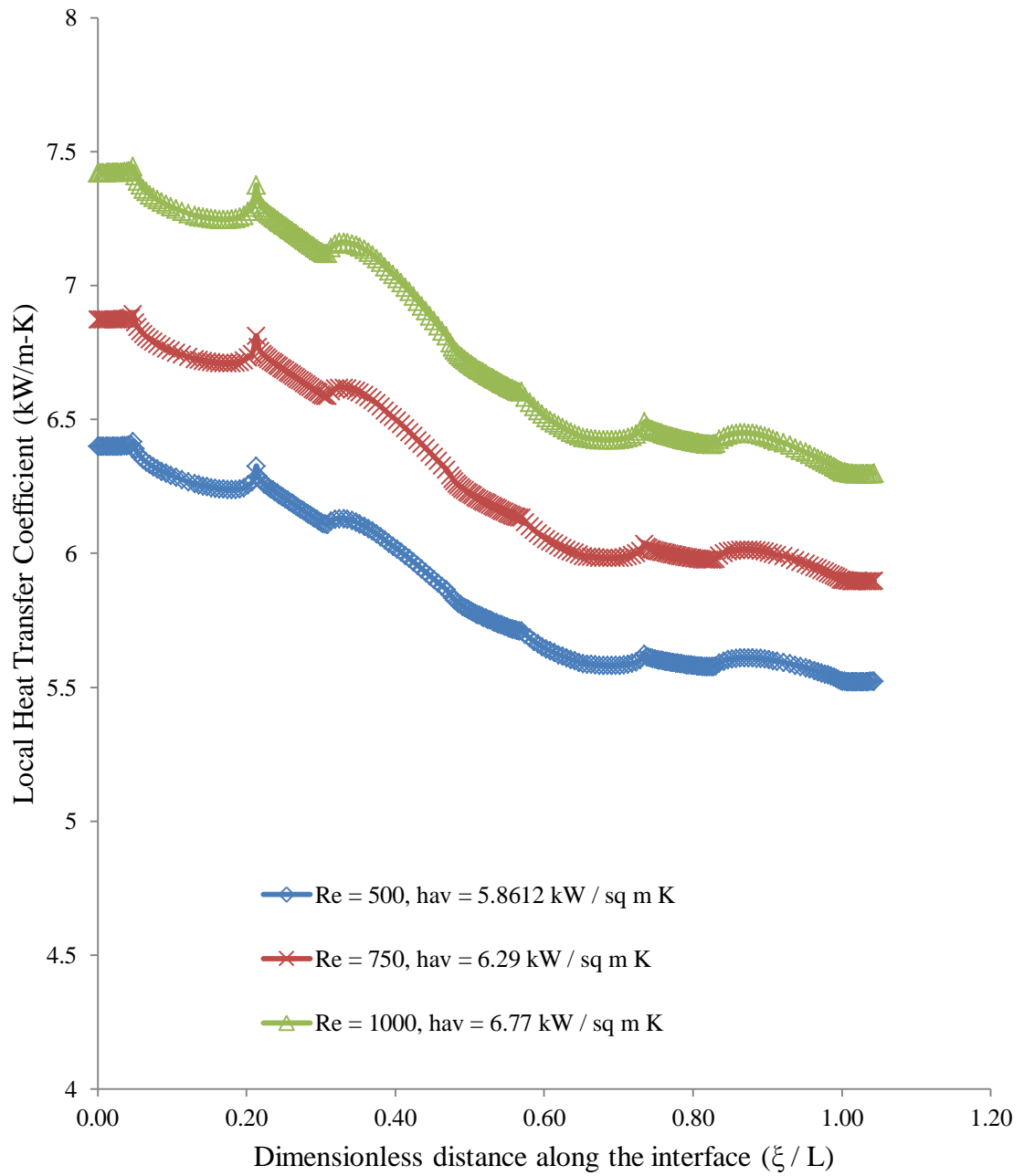


Figure 3.37 Local heat transfer coefficient for varying Reynolds number ($T_j = 313.15 \text{ K}$, $b = 0.00125 \text{ m}$, $H_n = 0.0055 \text{ m}$, Silicon plate, $q = 63 \text{ kW/m}^2$, $W=0.0017 \text{ m}$)

disrupted by changes in surface geometry. However, the disruption in this case is much lower than the rectangular and triangular shaped surface geometry. This is due to the curved surfaces being less sharp when compared to the others. It should be observed that increasing the Reynolds number leads to an increase in both the local heat-transfer coefficients and their averages. Figure 3.38 shows the behavior of the Nusselt number with changing Reynolds number. It is shown that the Nusselt number varies in a fashion similar to the local heat-transfer coefficient. The stagnation zone has the highest heat transfer values due to the change in fluid direction. The spikes present along the length of the plate are at locations where the thermal boundary layer is disturbed and allowed to mix with the free stream.

Figure 3.39 displays the effect of changing the indentation depth for the base case. Increasing the depth has the noticeable impact of increasing the interface temperature. The effect of increasing the depth causes the shape of the indentations to change which also brings different flow characteristics to the surface. Increasing the depth of the indentations results in less favorable recirculation, this in turn causes the fluid inside each indentation to transfer less heat back into the fluid by convection. Clearly the best option for this case is to use reduced indentation depths. The Nusselt number variation with indentation depth is plotted in Figure 3.40. As expected from the interface temperatures, increasing the depth of the indentations decreases the Nusselt number. The smaller indentation size of $a = 0.000125 \text{ m}$ results in less disturbance in the thermal boundary layer, allowing for the continued buildup of thermal resistance between the wall and the fluid. The larger indentation of $a = 0.0005 \text{ m}$ results in a more uneven surface for the fluid to move along. This causes slight fluid disturbance, resulting in the mixture of the

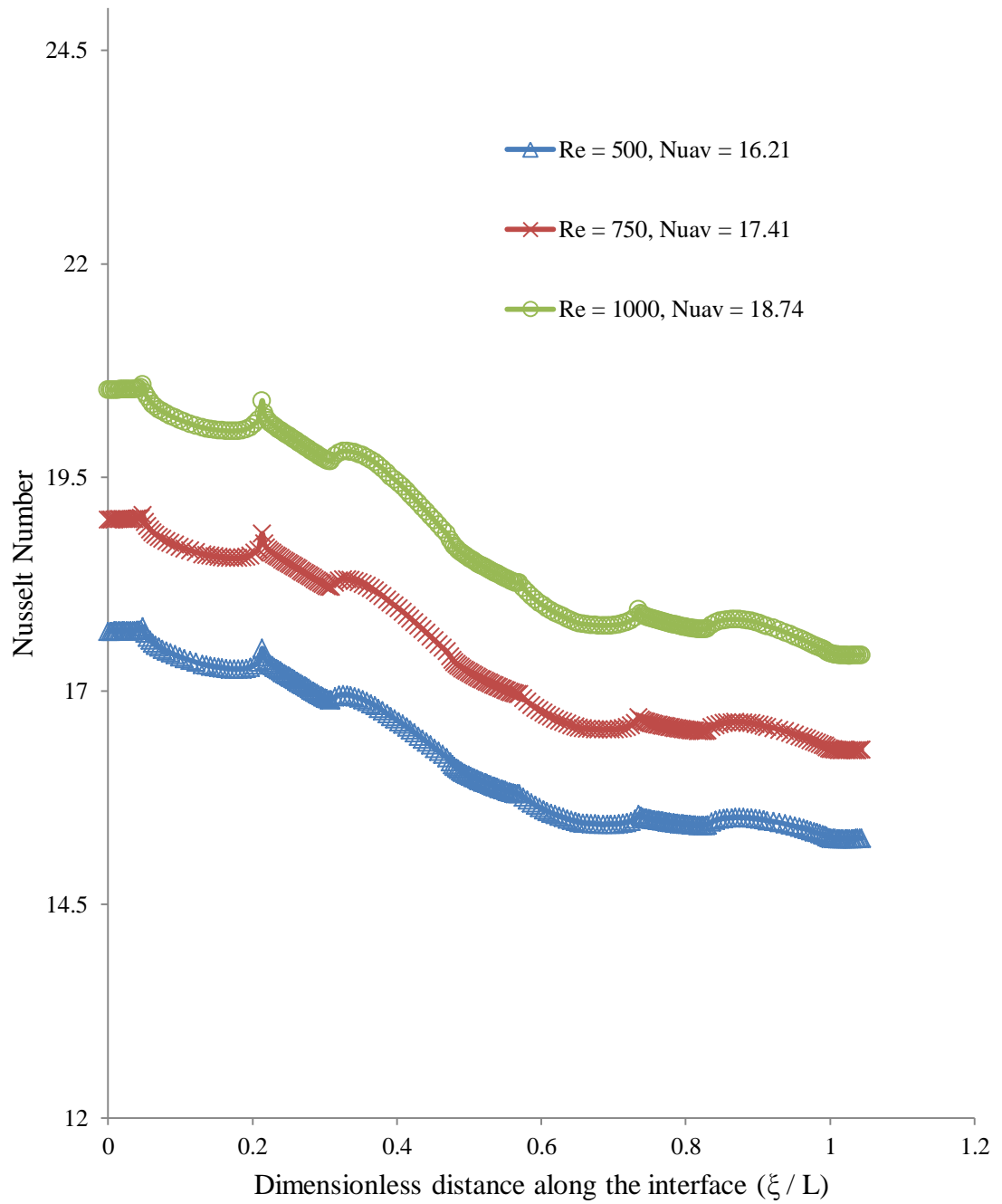


Figure 3.38 Local Nusselt number for varying Reynolds number
 ($T_j = 313.15$ K, $b = 0.00125$ m, $H_n = 0.0055$ m, Silicon plate, $q = 63$ kW/m²,
 $W=0.0017$ m)

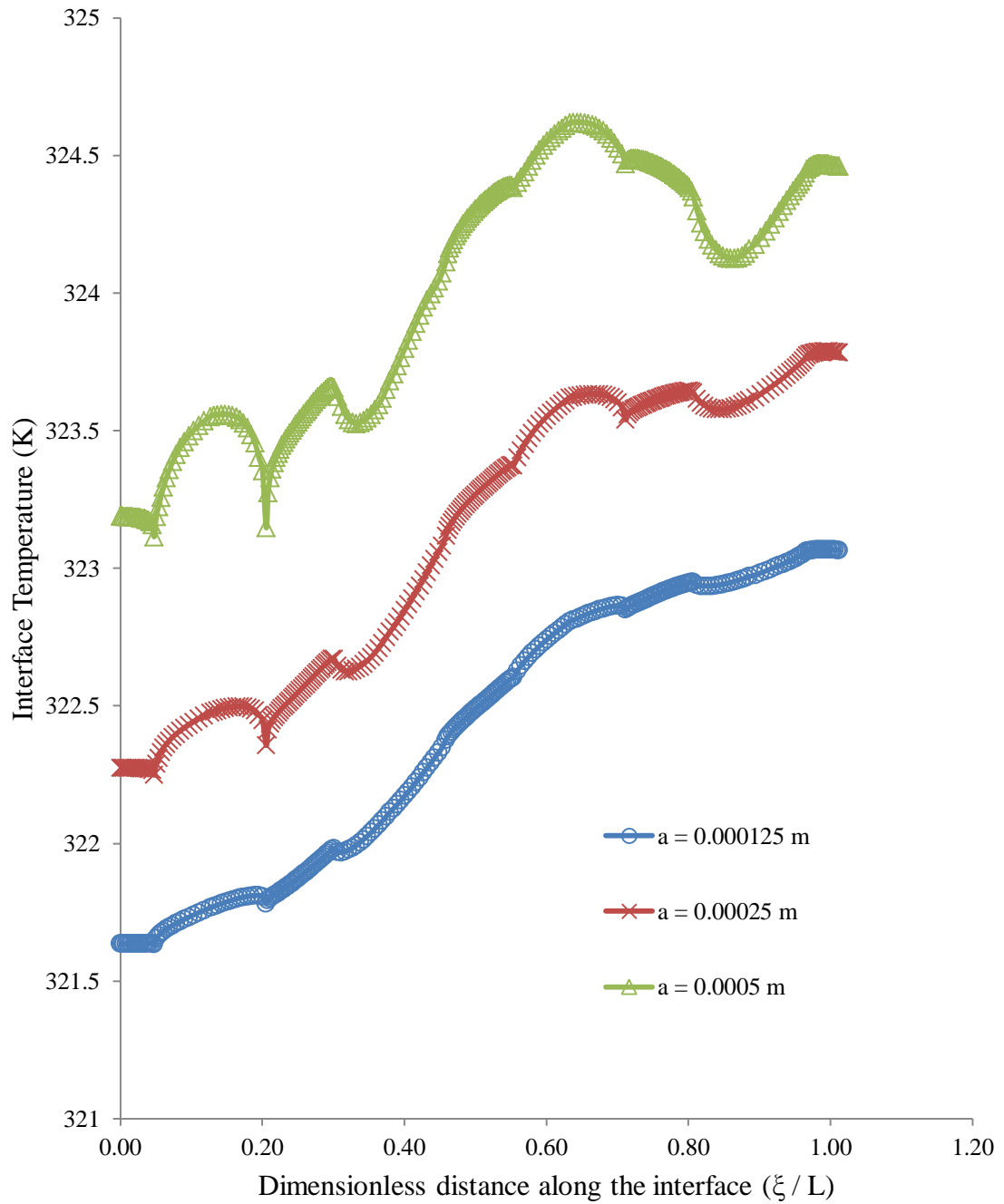


Figure 3.39 Interface temperature variation for different indentation depths ($T_j = 313.15$ K, $b = 0.00125$ m, $H_n = 0.0055$ m, Silicon plate, $q = 63$ kW/m², $W = 0.0017$ m)

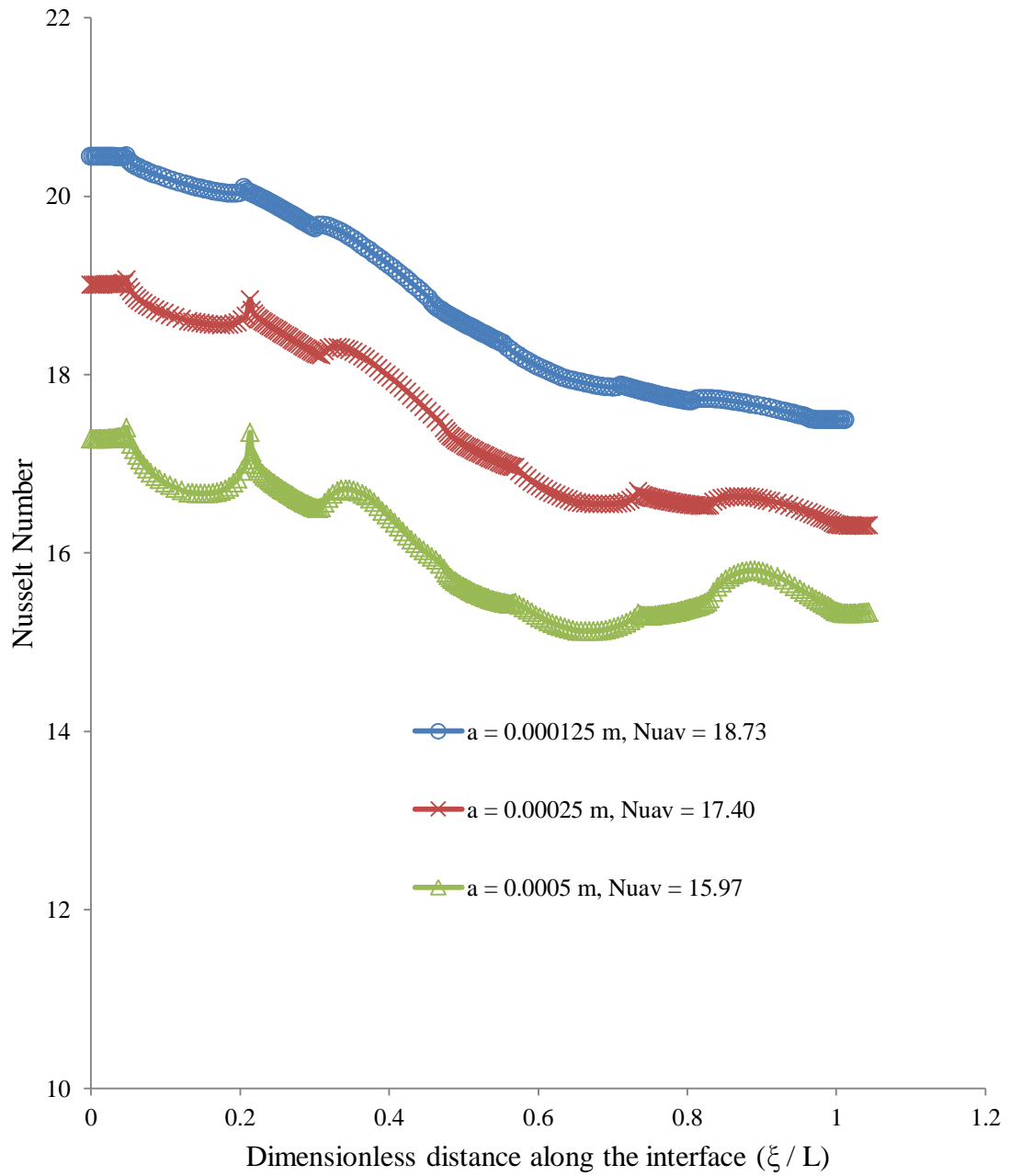


Figure 3.40 Local Nusselt number variation for different indentation depths ($T_j = 313.15$ K, $b = 0.00125$ m, $H_n = 0.0055$ m, Silicon plate, $q = 63$ kW/m², $W = 0.0017$ m)

thermal boundary layer and the surrounding fluid. However, this increased mixing does not lead to a marked increase in Nusselt number. The difference in average Nusselt number between the $a = 0.000125 \text{ m}$ and $a = 0.0005 \text{ m}$ cases is 14.7% in favor of the smaller step. Figure 3.39 displays the variation in Nusselt number for the three different sinusoidal configurations. Case A has larger channels and steps compared to the Base case, this results in a more wavy fluid flow that causes a more stable change in the Nusselt number. The larger peaks in Case B are due to the increased distance between the changes in geometry that occurs in that configuration. The space in between each indentation and curved step allows the fluid to develop more than in the other geometries. As the fluid strikes the next curved surface there is a spike in Nusselt number and heat transfer due to the thermal boundary layering being upset. Like the triangular rib case, the inclusion of surface geometry reduces the Nusselt number along the length of the plate. This is due to the fluid not becoming trapped in the indentations along the length of the plate.

Figure 3.42 displays the isothermal lines in the solid plate for the base case under different Reynolds number. Increasing Reynolds number leads to reduced temperature throughout the plate without changing the overall temperature distribution. This is due to pronounced radial conduction through the first half of the plate. Past this point the heat flux from the bottom of the plate exerts a higher influence than the cooling from the fluid can overcome. Figure 3.43 displays the isothermal lines for the solid silicon plate under differing surface configurations. The lowest temperatures again occur in the stagnation zone. The larger surface features clearly lead to slightly lower temperatures until the midpoint in the plate.

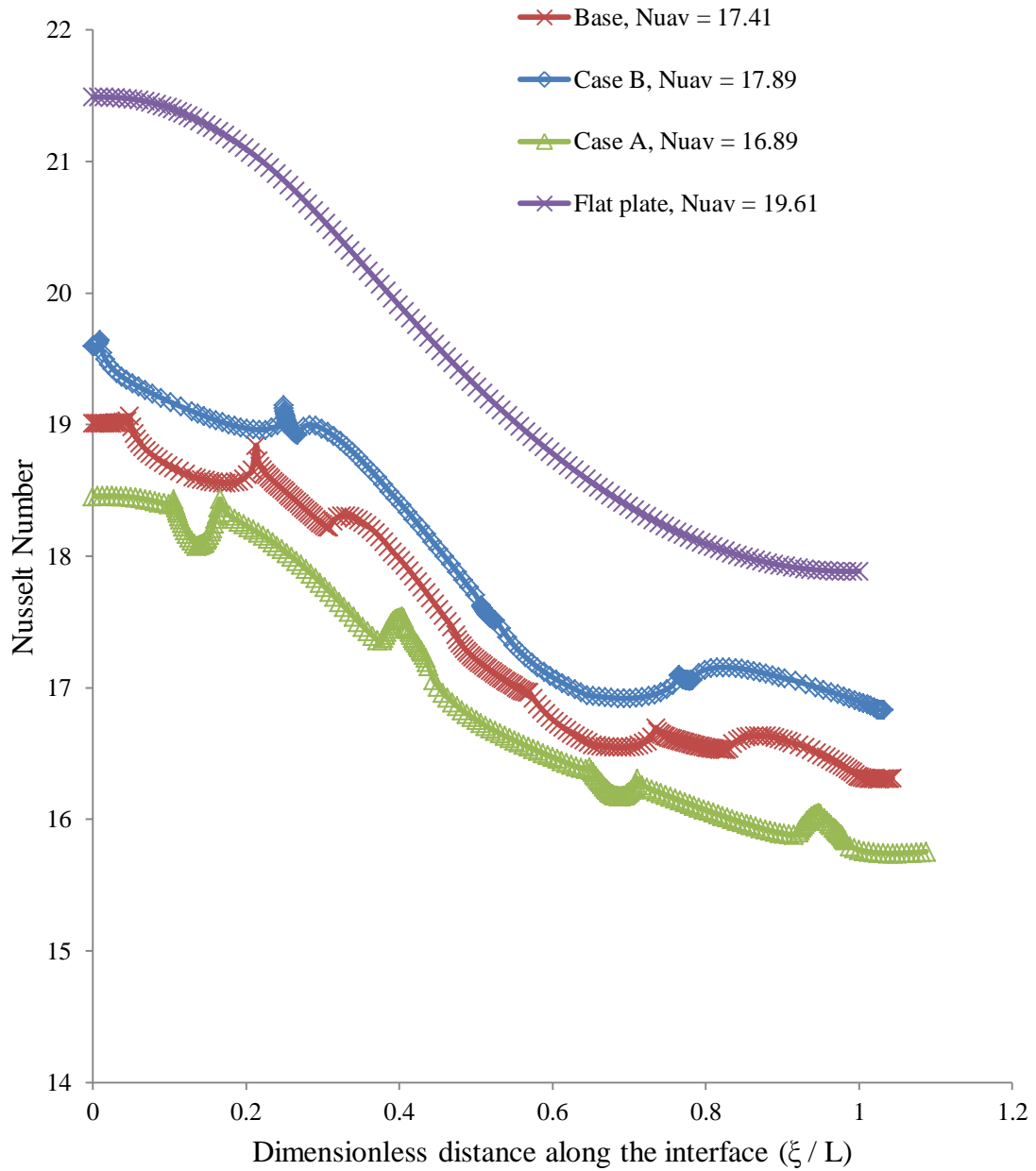
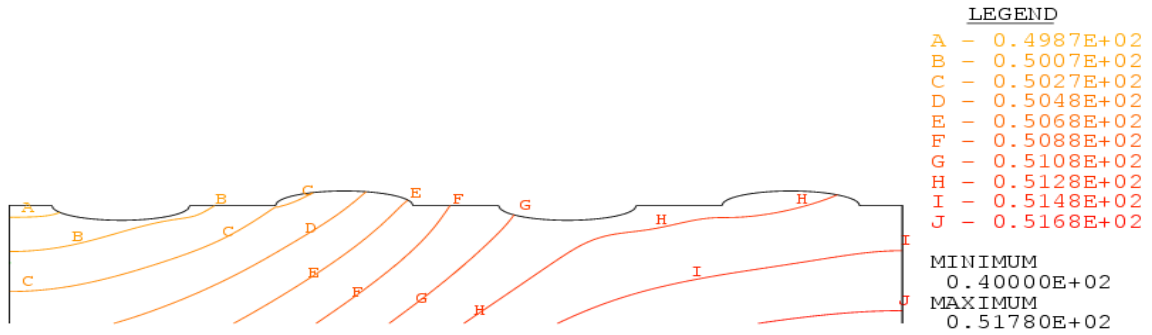
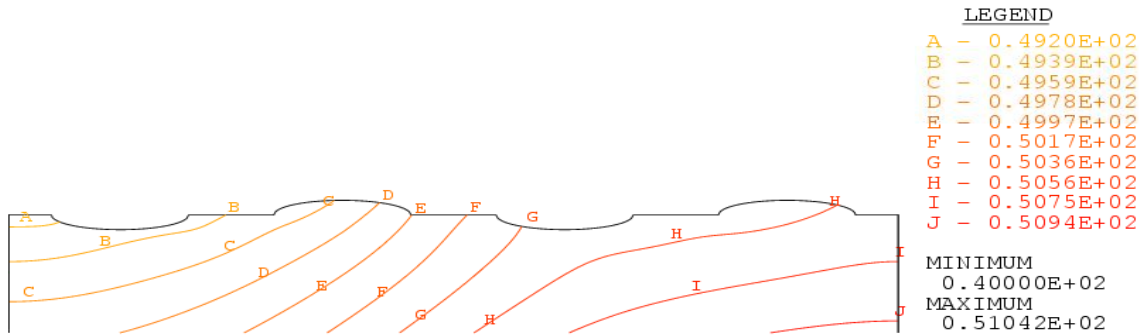


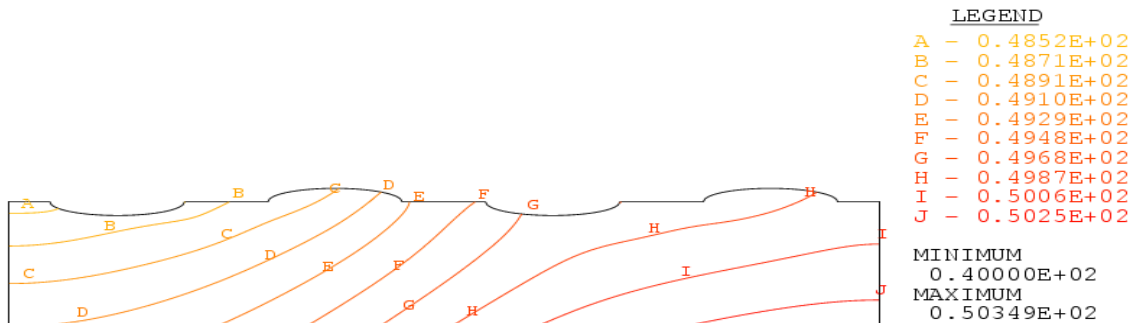
Figure 3.41 Local Nusselt number variation for different surface geometries ($T_j = 313.15$ K, $b = 0.00125$ m, $H_n = 0.0055$ m, Silicon plate, $q = 63$ kW/m², $W = 0.0017$ m)



a) $Re = 500$

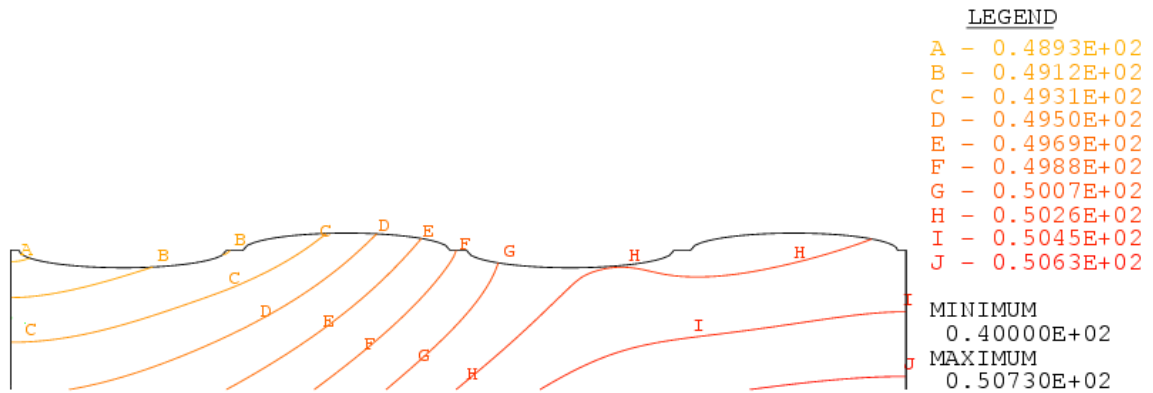


b) $Re = 750$

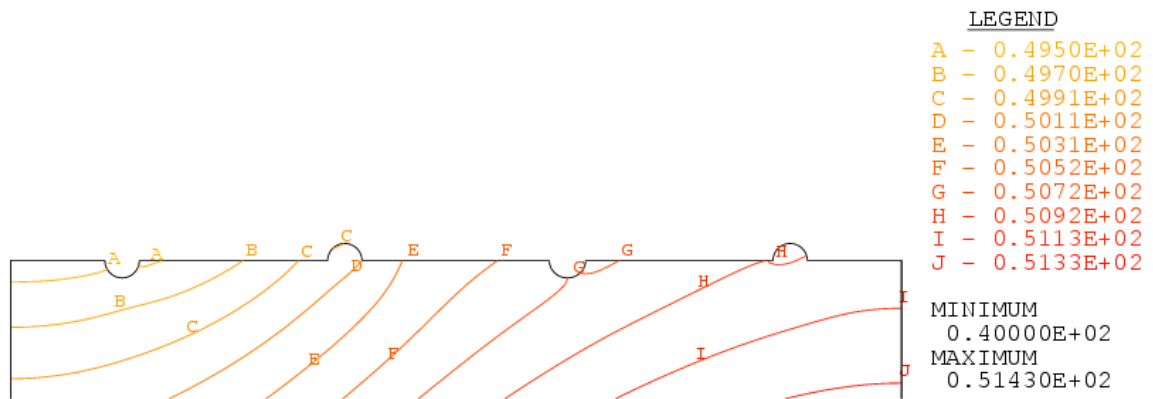


c) $Re = 1000$

Figure 3.42 Isothermal lines (in degrees Celsius) for different Reynolds number
 $(T_j = 313.15 \text{ K}, b = 0.00125 \text{ m}, H_n = 0.0055 \text{ m}, \text{Silicon plate}, q = 63 \text{ kW/m}^2, W = 0.0017 \text{ m})$



a) Case A



b) Case B

Figure 3.43 Isothermal lines (in degrees Celsius) for different plate configurations
($Re = 750$, $T_j = 313.15$ K, $b = 0.00125$ m, $H_n = 0.0055$ m, Silicon plate, $q = 63$ kW/m²,
 $W=0.0017$ m)

Chapter 4

Discussion of Results: Transient Heating

4.1 Slot Jet Impinging on a Uniformly Heated Plate with Rectangular Ridges: Transient Heating

For this investigation three different materials were explored: silicon, copper, and constantan. The working fluids used were water and the refrigerant R134a. The different surface configurations used for these simulations are shown in Figure 3.1. Each case considered 6 steps with the end of the last step coinciding with the outlet. Since the slot jet is positioned exactly half way above the heated plate, the location of $x = 0$ coincided with the mid-point of an indentation. The base case is considered when the step and gaps are of equal length. The velocity vectors for a steady state case are shown in Figure 3.2. The velocity field varies slightly during the transient heating process, but these variations are considered minimal. Figure 3.3 shows the free surface height distribution for varying Reynolds number. This figure is for the steady state condition. However, the free surface height distribution does not change noticeably during the transient heating process.

The variation of interface temperature at different time intervals for the base case is shown in Figure 4.1. At the start of the heating process the temperature is more uniformly distributed, only varying slightly across the length of the plate. During the transient heating process the change of temperature across the interface nearly doubles

from the initial value of 0.82K. The low initial temperature variation is due to the transient thermal storage of the fluid required to develop the thermal boundary layer. The variation in temperature increases as the plate's heat capacity is reached near steady state conditions. Because of the fluid coming into contact with the entire plate there are higher temperatures in the gaps due to fluid stagnation, low peaks caused by the thermal boundary layer being broken up by changes in geometry, and lower plateaus caused by the fluid along the top of the plate. Figure 4.2 displays the development of the local heat-transfer coefficient with time. It can be observed that the heat-transfer coefficient decreases with time until attaining steady state conditions. This is primarily due to the dependence on the solid-liquid interface temperature for the plate. The large drop in heat-transfer coefficient between $t = 0.25 \text{ s}$ and $t = 0.5 \text{ s}$ is due to the rapid increase in interface temperature during the same time. This large temperature increase is possible, in part, due to the thinness of the plate material. The local heat-transfer coefficient is at its peak when the fluid strikes the leading corner of the first rectangular step. This sharp geometry change disrupts the thermal boundary layer, increasing the local heat-transfer coefficient. As the fluid continues downstream the heat-transfer coefficient decreases slightly. Around $\xi/L = 0.3$ the fluid enters another gap, forcing the fluid to slow down and recirculate in the indentation. This low speed recirculation leads to a decrease in convective heat transfer. The free stream fluid above the recirculation continues and encounters the next step at roughly $\xi/L = 0.56$. At this point the heat-transfer coefficient increases due to the sudden geometry change. This trend continues downstream with the local heat-transfer coefficient decreasing. The average heat-transfer coefficient more than halves during the transient process, going from 16.25 to $7.04 \text{ kW/m}^2 \text{ K}$.

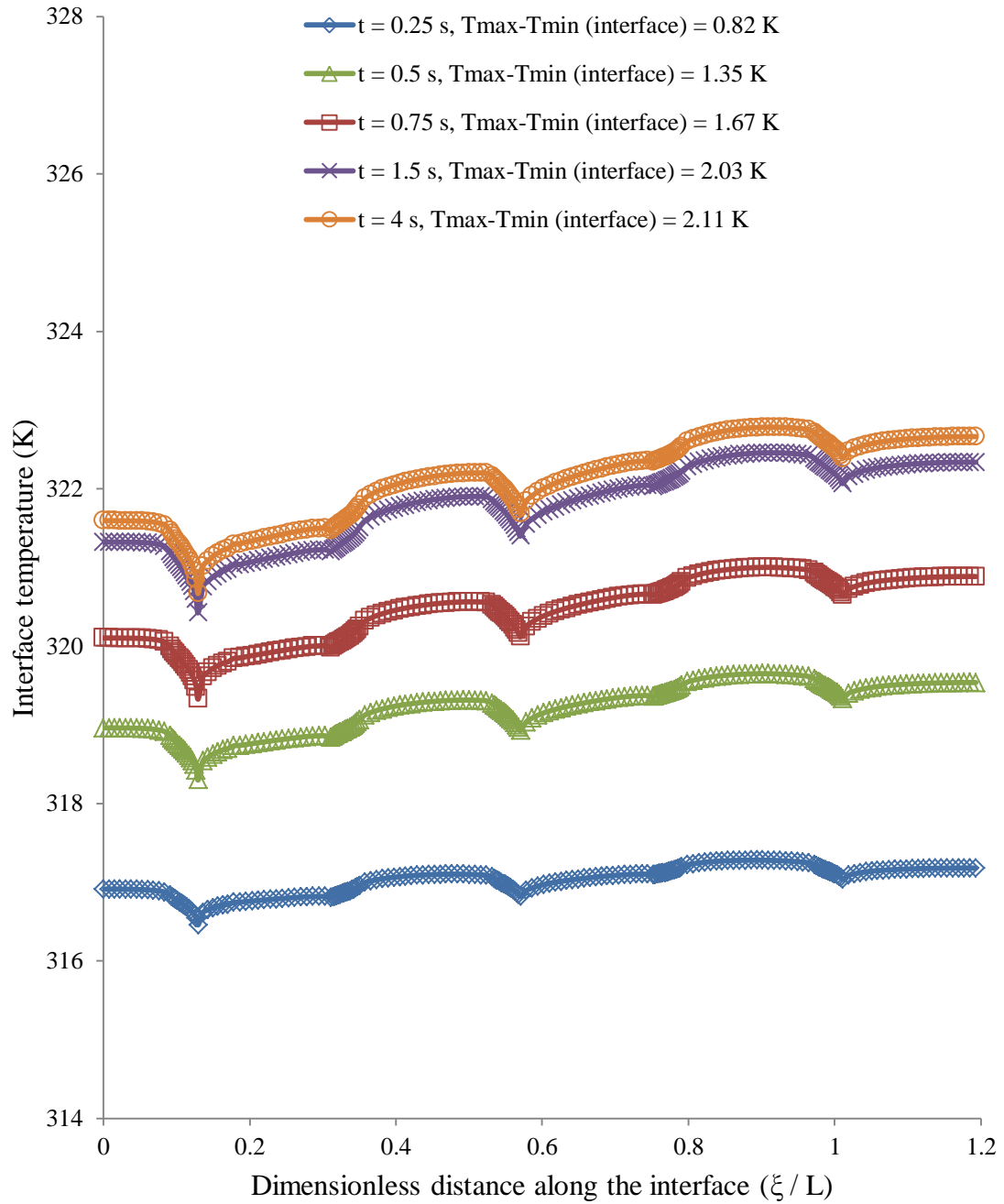


Figure 4.1 Interface temperature for different times
 (Re = 750, $T_j = 313.15$ K, $b = 0.00125$ m, $H_n = 0.0055$ m, Silicon plate base case,
 $q = 63$ kW/m², $W = 0.0017$ m)

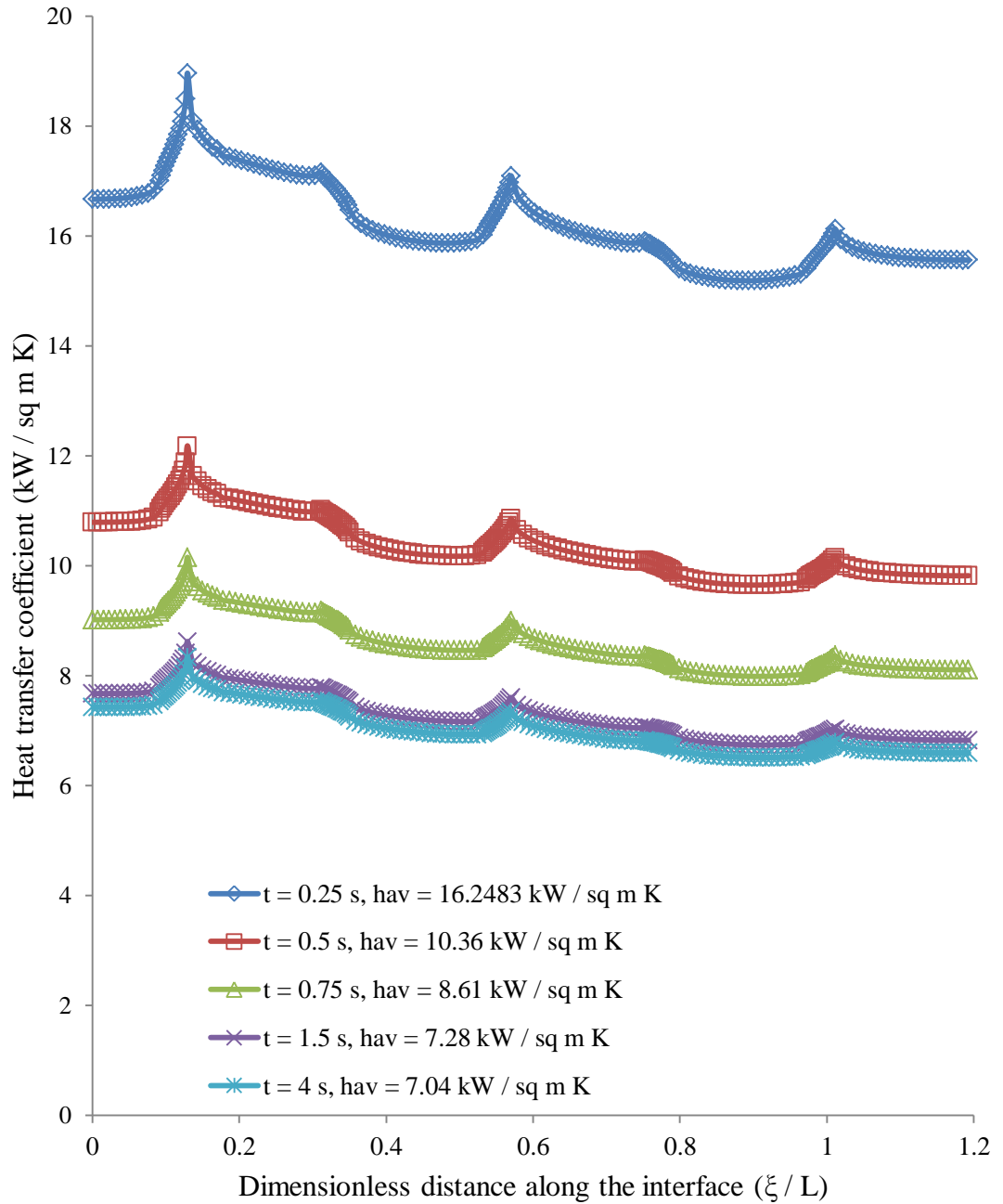


Figure 4.2 Local heat transfer coefficient for different times
 (Re = 750, $T_j = 313.15$ K, $b = 0.00125$ m, $H_n = 0.0055$ m, Silicon plate base case,
 $q = 63$ kW/m², $W = 0.0017$ m)

The development of the Nusselt number with increasing Fourier number is displayed in Figure 4.3. The similarity in the behavior of the local Nusselt number and the local heat-transfer coefficient is due to the dependence on the local heat-transfer coefficient and the use of the nozzle width as the scale factor in the definition of the Nusselt number.

The maximum non-dimensional temperature at the interface, maximum non-dimensional temperature in the solid, and the maximum-to-minimum temperature difference at the interface for three different Reynolds number is shown in Figure 4.4. As previously described, the temperature rapidly increases from the isothermal condition at $t = 0$ s in the early transient process. This is due to the thermal storage capacity of the material. When the storage capacity of the material drops as the system approaches steady state, the temperature increases at a lower rate until reaching the steady state temperature. It is noted that the time required to reach the steady state condition are low for all the cases presented, all falling below 10 seconds. This is due to the low thermal storage capacity of the thin plate used for this study. Increasing Reynolds number leads to a decrease in maximum temperature at both the interface and the solid. The maximum-to-minimum temperature difference along the interface for $Re = 750$ and $Re = 1000$ are observed to be nearly identical for the transient process.

The variation in time for the average heat-transfer coefficient and average Nusselt number is shown in Figure 4.5. Both the average heat-transfer coefficient and average Nusselt number quickly decrease with an exponential decay characteristic until reaching the steady state. There is little difference in the behavior of the average heat-transfer coefficient or Nusselt number for different Reynolds number.

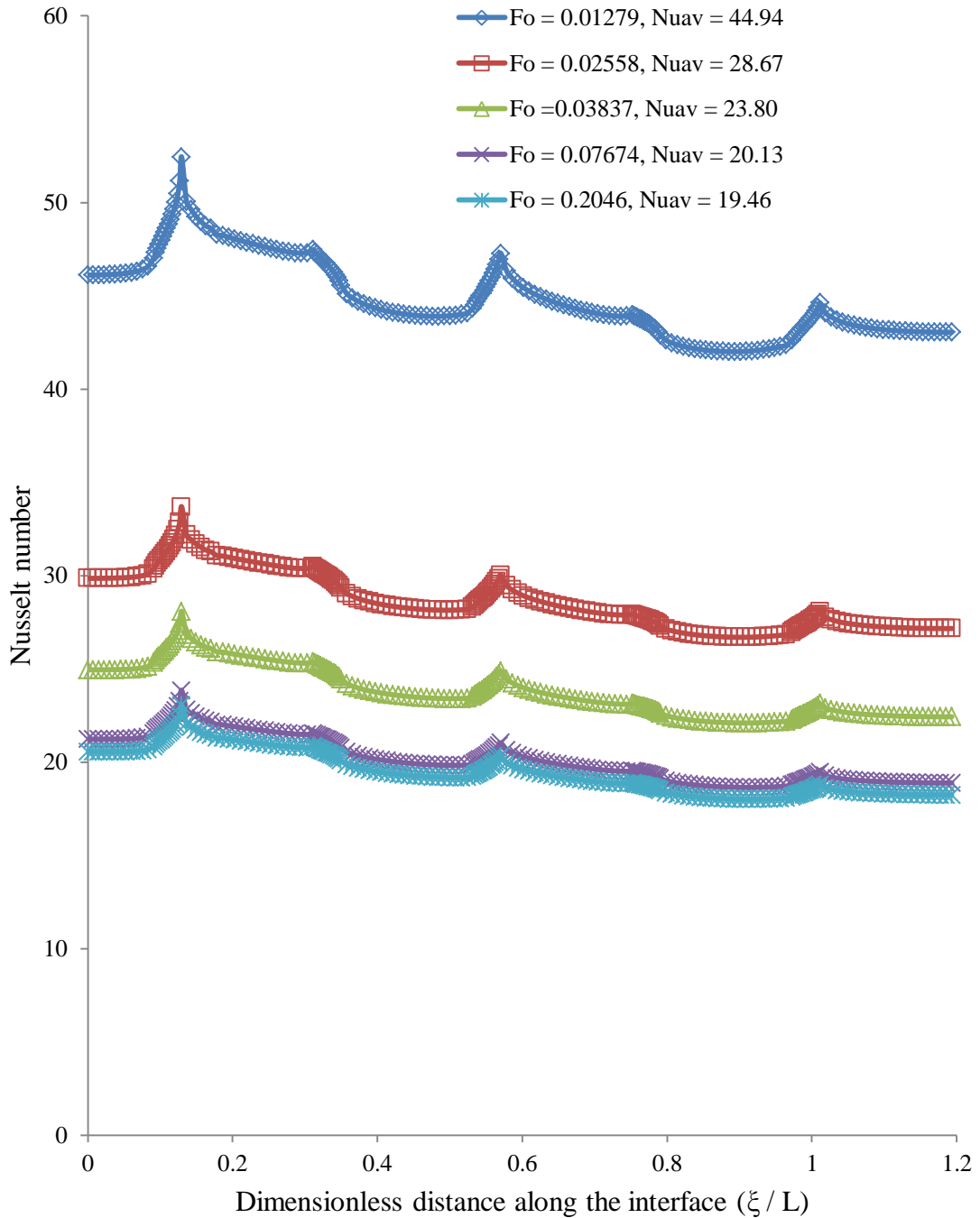


Figure 4.3 Local Nusselt number for different Fourier values
 (Re = 750, $T_j = 313.15$ K, $b = 0.00125$ m, $H_n = 0.0055$ m, Silicon plate base case,
 $q = 63$ kW/m², $W = 0.0017$ m)

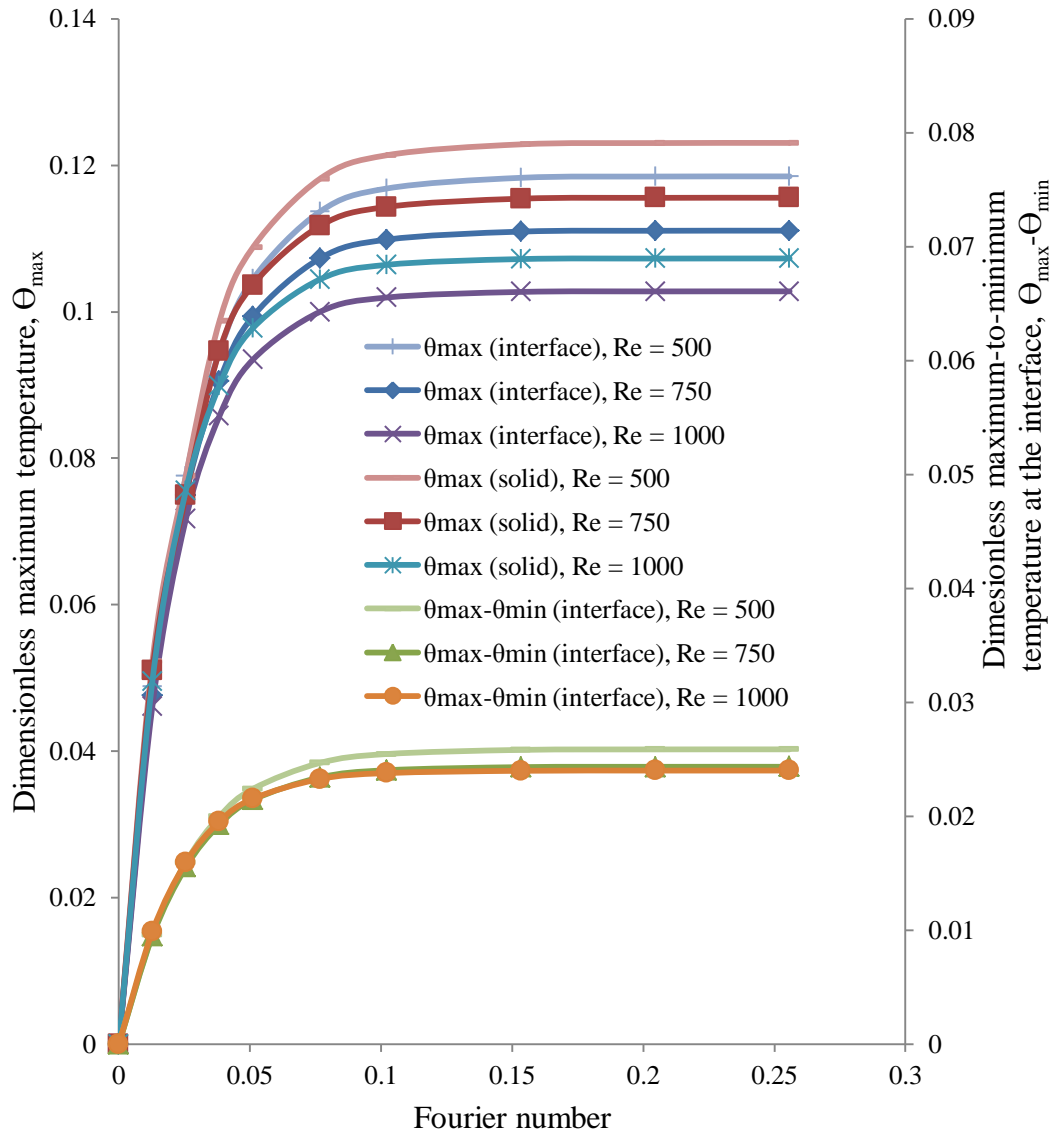


Figure 4.4 Variation in maximum non-dimensional temperature at the interface, maximum non-dimensional temperature within the solid, and the maximum-to-minimum non-dimensional temperature difference at the interface for different Reynolds number ($T_j = 313.15$ K, $b = 0.00125$ m, $H_n = 0.0055$ m, Silicon plate base case, $q = 63$ kW/m², $W=0.0017$ m)

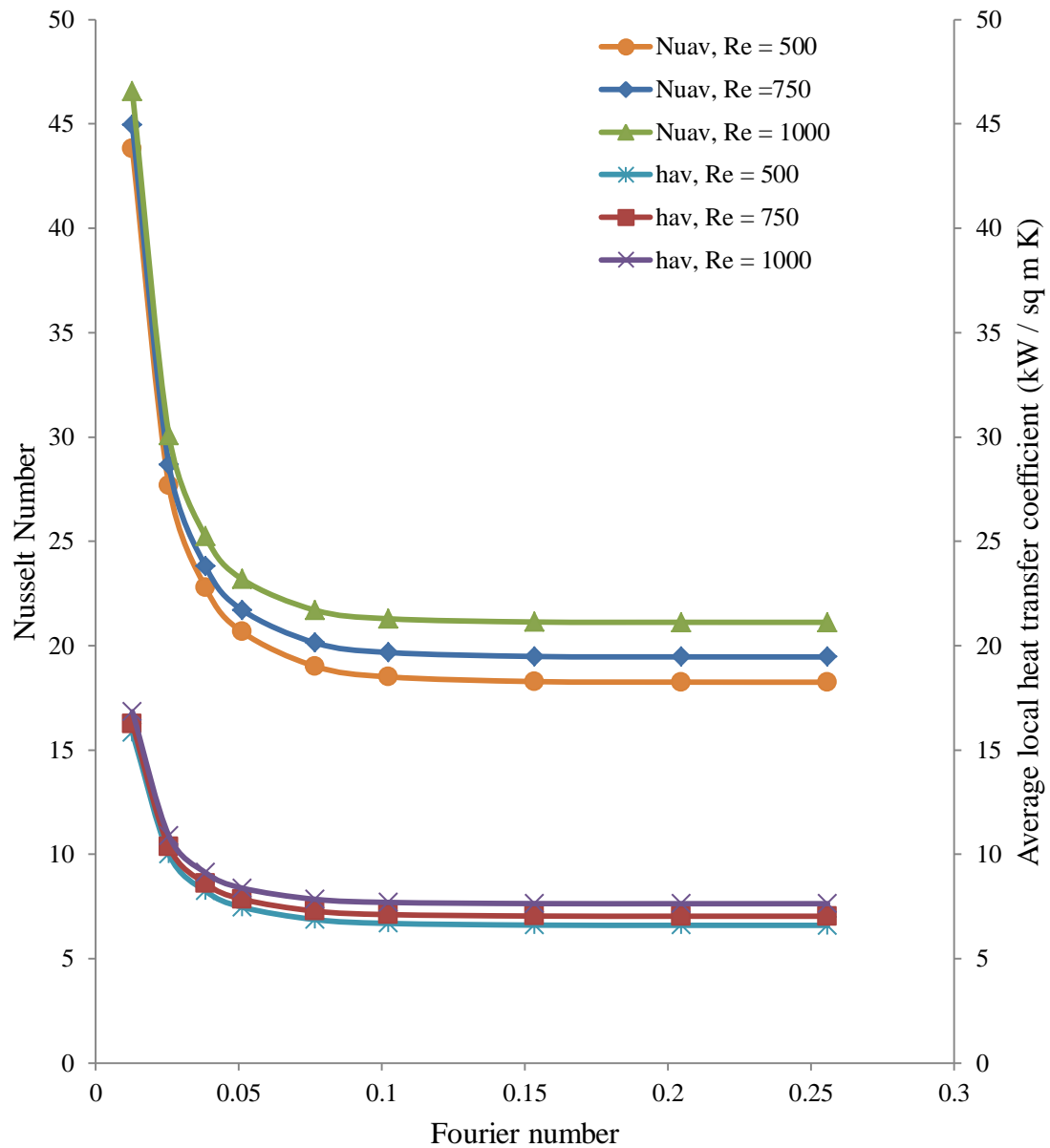


Figure 4.5 Variation of average heat transfer coefficient and average Nusselt number with Fourier number ($T_j = 313.15$ K, $b = 0.00125$ m, $H_n = 0.0055$ m, Silicon plate base case, $q = 63$ kW/m², $W = 0.0017$ m)

The height of the step is another important parameter that affects the transient heating process. Its effect on the maximum non-dimensional temperature at the interface, maximum non-dimensional temperature in the solid, and the maximum-to-minimum temperature difference at the interface is shown in Figure 4.6. The difference in maximum temperature in the solid for different indentation depths is minimal. This is due to the negligible change in thermal storage due to small amount of plate material that is gained or lost from case to case. The relative thinness of the plate also allows for the most of the heat to conduct through the entire plate. Figure 4.7 displays the average heat-transfer coefficient and average Nusselt number variation with time for different indentation depths. It can be observed that the difference in indentation depth has a lesser effect compared to that of the change in Reynolds number observed in Figure 4.5. The values for the average heat-transfer coefficient and Nusselt number are nearly identical across the three indentation depths investigated. This was expected due to the similarity of the average heat-transfer coefficient and average Nusselt number in each case.

Different step configurations also have an effect on the transient heating process. Figure 4.8 shows the maximum non-dimensional temperature at the interface and solid for different indentation depths in case A. The variation in temperature present in this case is greater when compared to the base case. This is due to the shorter lengths of the indentations between each rectangular step, which allows for greater recirculation and flow in and around the edge of the steps. Figure 4.9 displays the average heat-transfer coefficient and average Nusselt number for varying indentation depths in case A. The greater recirculation mentioned above is apparent here as the average heat transfer values are higher than in the base case.

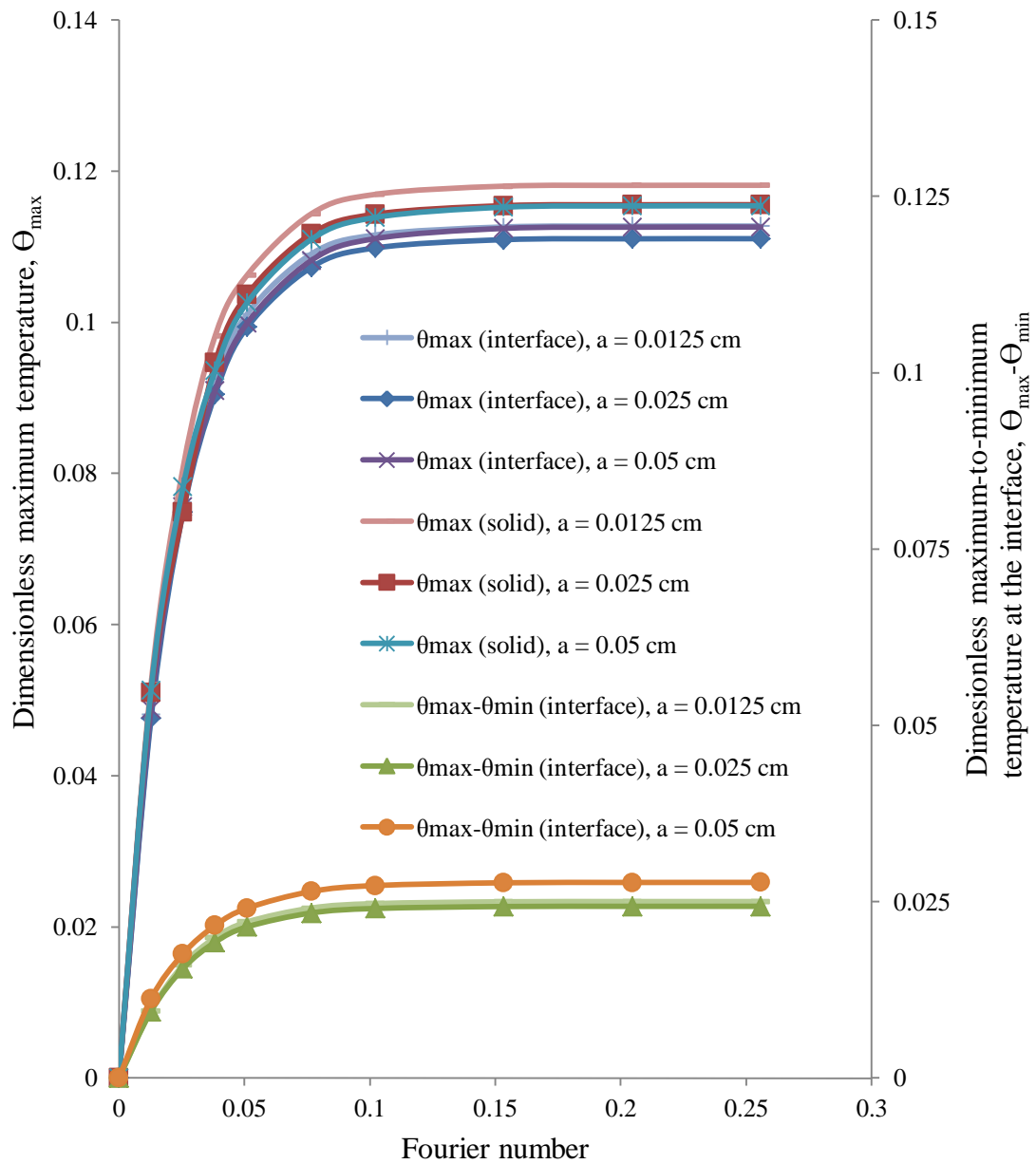


Figure 4.6 Variation in maximum non-dimensional temperature at the interface, maximum non-dimensional temperature within the solid, and the maximum-to-minimum non-dimensional temperature difference at the interface for different indentation depths (Re = 750, $T_j = 313.15$ K, $b = 0.00125$ m, $H_n = 0.0055$ m, Silicon plate base case, $q = 63$ kW/m², $W = 0.0017$ m)

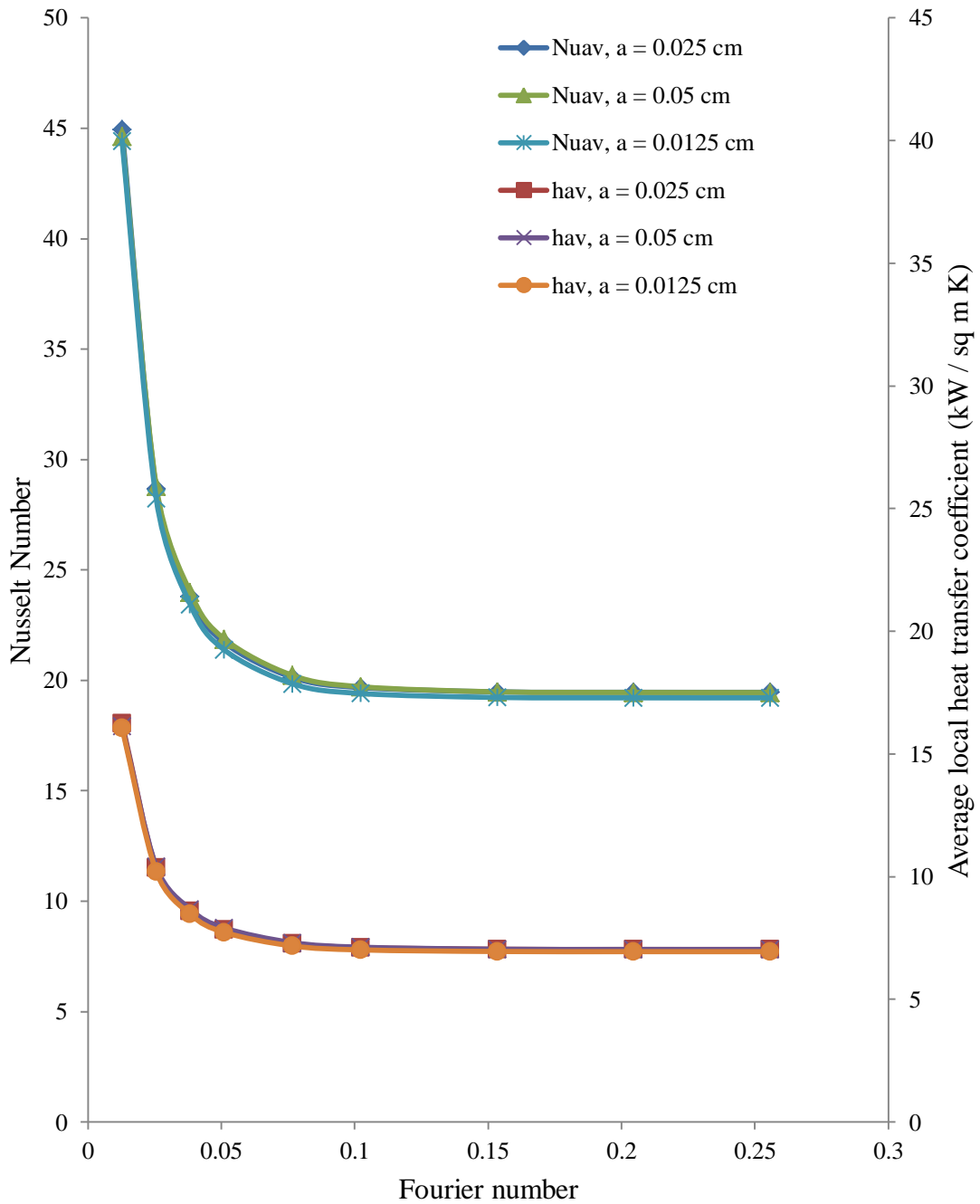


Figure 4.7 Variation of average heat transfer coefficient and average Nusselt number with Fourier number for different indentation depths (Re = 750, $T_j = 313.15$ K, $b = 0.00125$ m, $H_n = 0.0055$ m, Silicon plate base case, $q = 63$ kW/m², $W = 0.0017$ m)

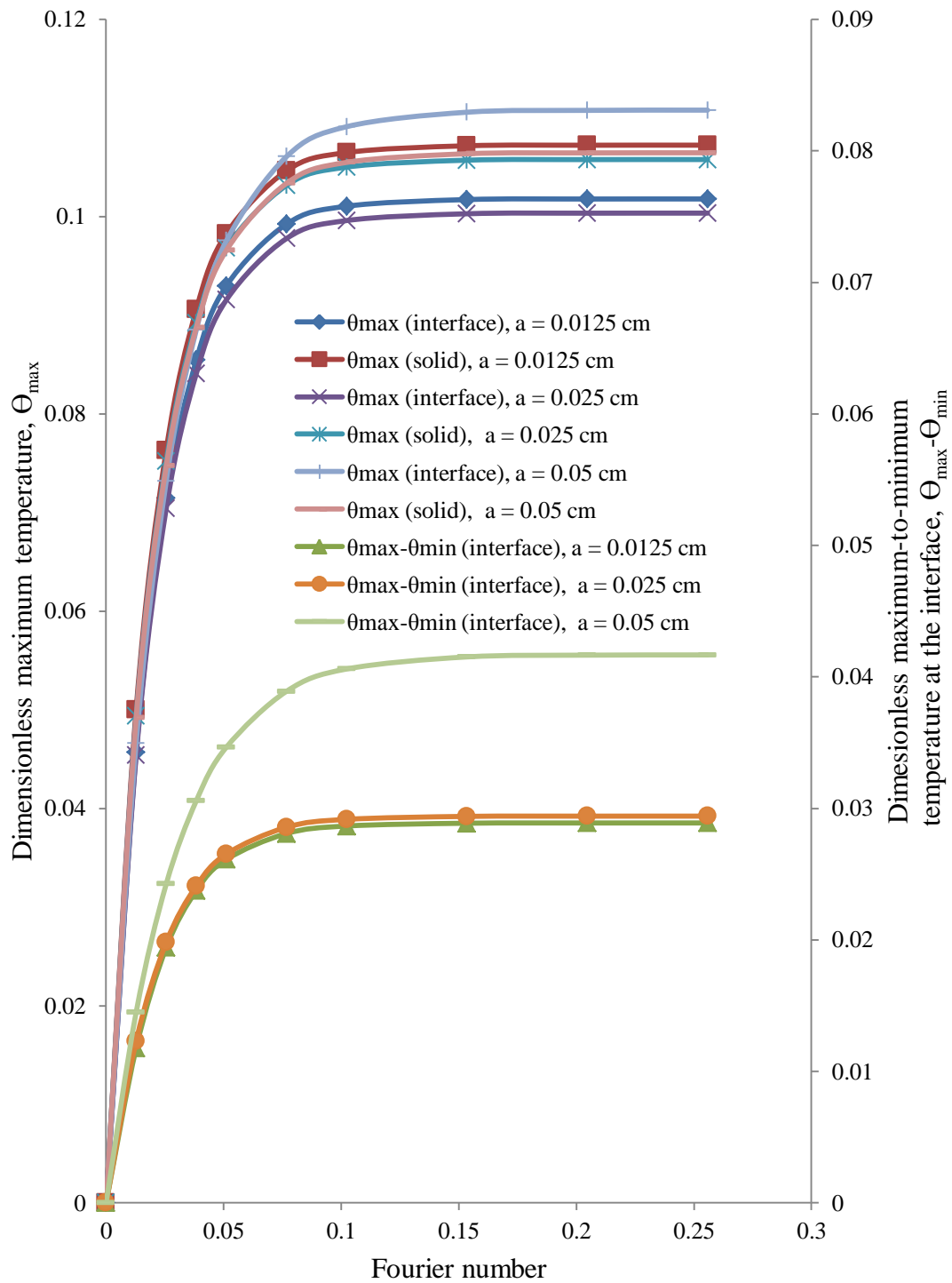


Figure 4.8 Variation in maximum non-dimensional temperature at the interface, maximum non-dimensional temperature within the solid, and the maximum-to-minimum non-dimensional temperature difference at the interface for different indentation depths ($Re = 750$, $T_j = 313.15$ K, $b = 0.00125$ m, $H_n = 0.0055$ m, Silicon plate, Case A, $q = 63$ kW/m², $W = 0.0017$ m)

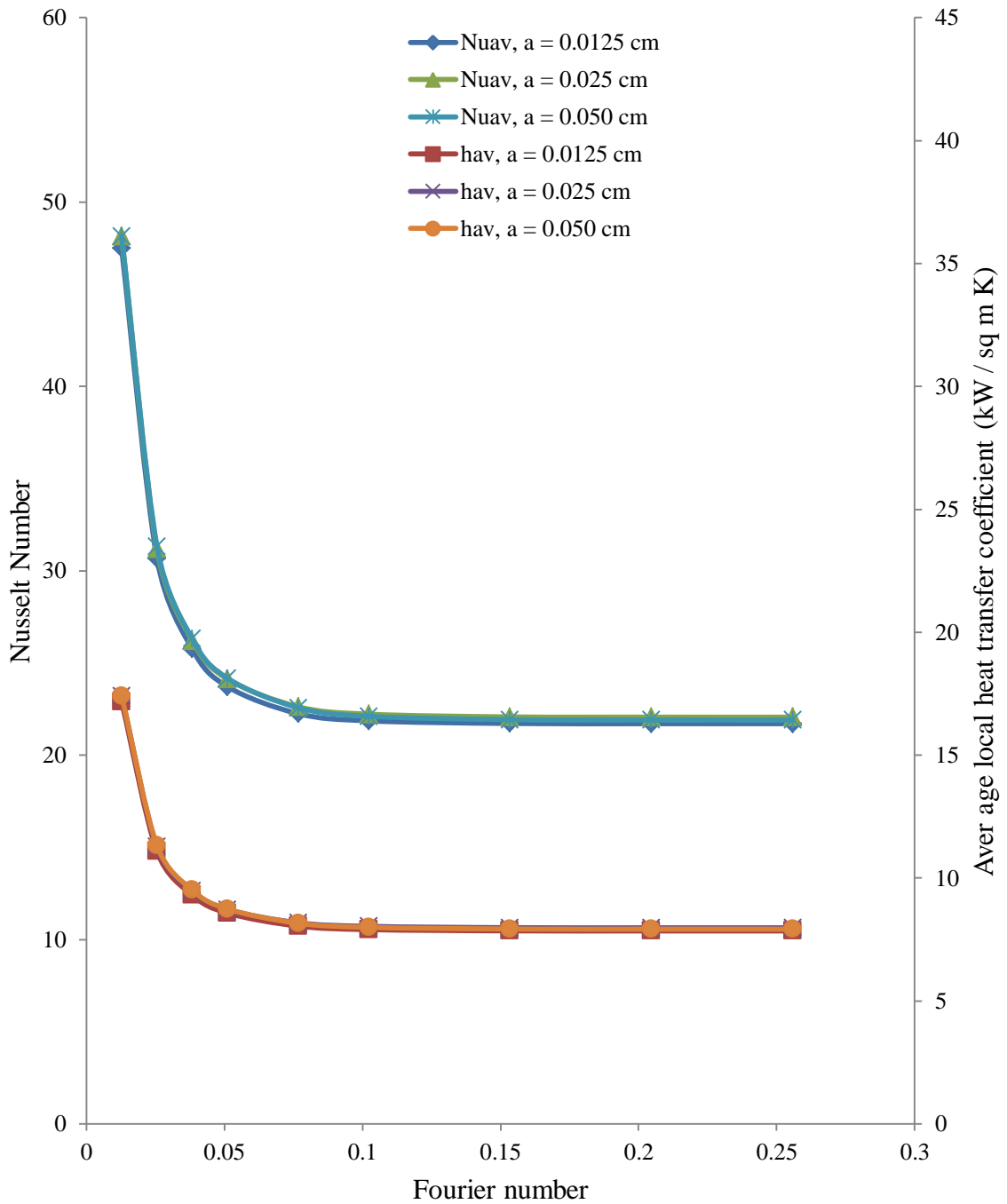


Figure 4.9 Variation of average heat transfer coefficient and average Nusselt number with Fourier number for different indentation depths ($Re = 750$, $T_j = 313.15$ K, $b = 0.00125$ m, $H_n = 0.0055$ m, Silicon plate, Case A, $q = 63$ kW/m², $W=0.0017$ m)

Figure 4.10 shows the maximum non-dimensional temperature at the interface and solid for different indentation depths in case B. The lowest maximum temperature within the solid is for when $a = 0.00025 \text{ m}$, this is consistent with the results for case A. The average heat-transfer coefficient and average Nusselt number for different indentation depths in case B are displayed in Figure 4.11. Compared to case A and the base case, there is a larger variation in the average heat-transfer coefficient and average Nusselt number as time increases. The surprising result from case B is that the average Nusselt number is higher for $a = 0.0005 \text{ m}$ compared to the other two heights. Given the increased depth of the indentation it was assumed that the velocity profile inside the gaps between each of the rectangular steps would be very low, prompting a drop in the average convective heat transfer. This is now the case, however, as the peaks in convective heat transfer caused by the changes of geometry along the plate more than make up for the losses in the indentations. The value at this step is nearly equal to that of case A. Both case A and B yield better heat transfer characteristics than the base case.

Three different materials were used in the simulations for the base case: silicon (the base material), copper, and constantan. Figure 4.12 shows the maximum non-dimensional temperature at the interface and solid for the different materials simulated. An important observation is the difference in time required to reach steady state. In this case the material with the higher thermal diffusivity, silicon with $\alpha = 0.984\text{E-}4 \text{ m}^2/\text{s}$, reaches the steady state most quickly. Constantan has the lowest thermal diffusivity with $\alpha = 6.12\text{E-}6 \text{ m}^2/\text{s}$ and takes the longest time (~33 seconds) to reach steady state. The temperature difference across the interface and the maximum temperature inside the solid for constantan is also highest. This was expected as constantan is a thermal insulator.

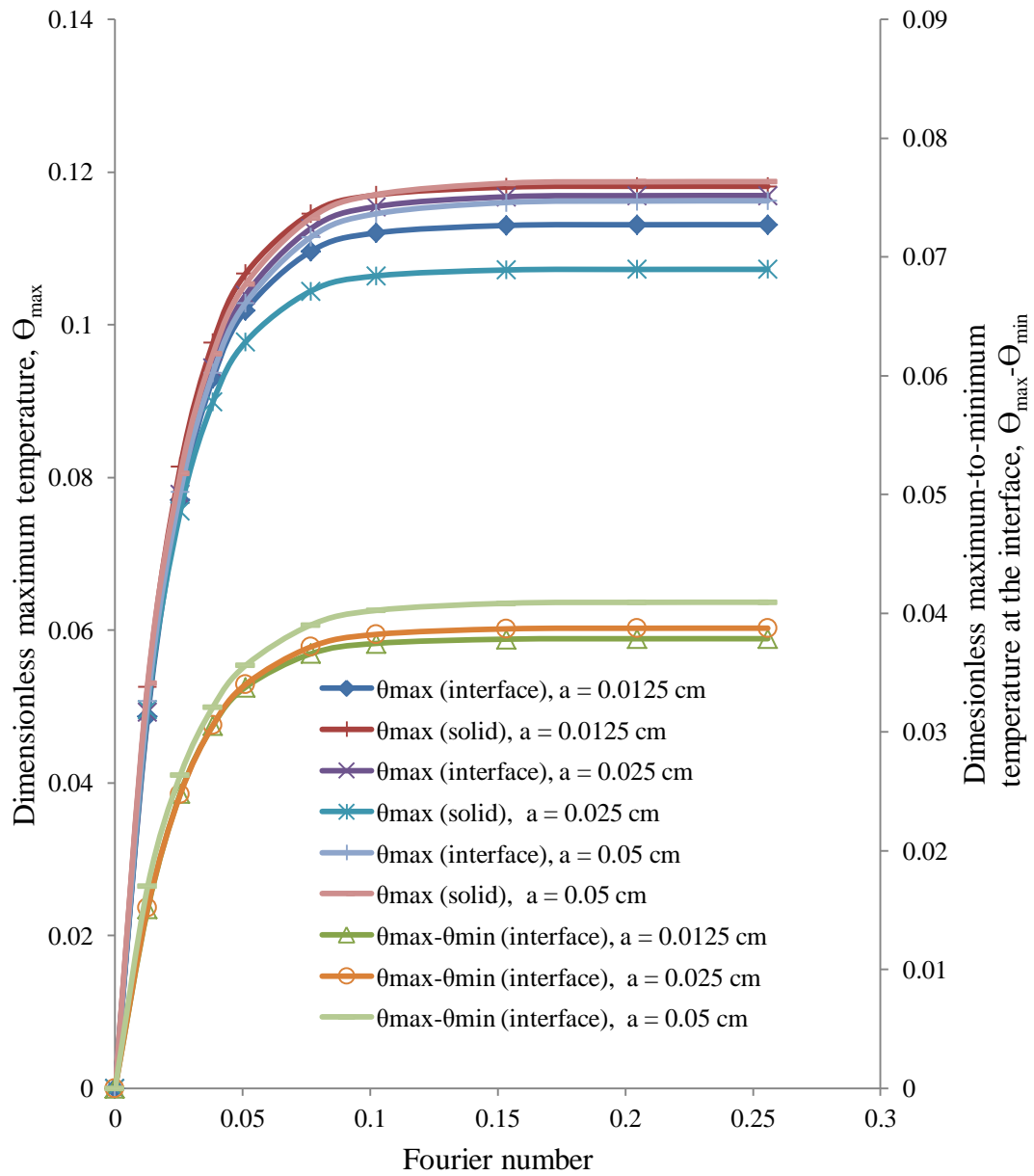


Figure 4.10 Variation in maximum non-dimensional temperature at the interface, maximum non-dimensional temperature within the solid, and the maximum-to-minimum non-dimensional temperature difference at the interface for different indentation depth (Re = 750, $T_j = 313.15$ K, $b = 0.00125$ m, $H_n = 0.0055$ m, Silicon plate, Case B, $q = 63$ kW/m², $W = 0.0017$ m)

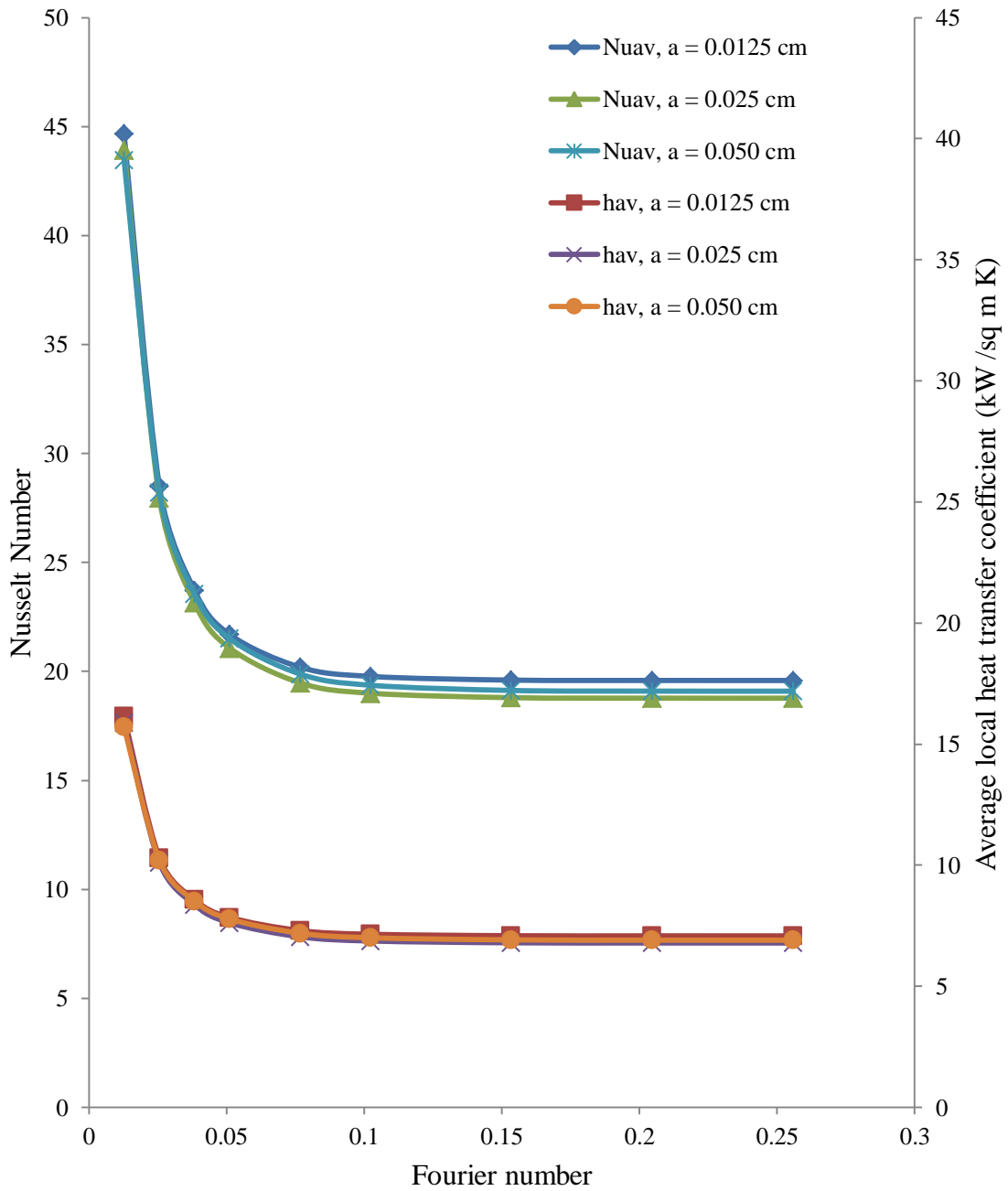


Figure 4.11 Variation of average heat transfer coefficient and average Nusselt number with Fourier number for different indentation depths ($Re = 750$, $T_j = 313.15$ K, $b = 0.00125$ m, $H_n = 0.0055$ m, Silicon plate, Case B, $q = 63$ kW/m², $W=0.0017$ m)

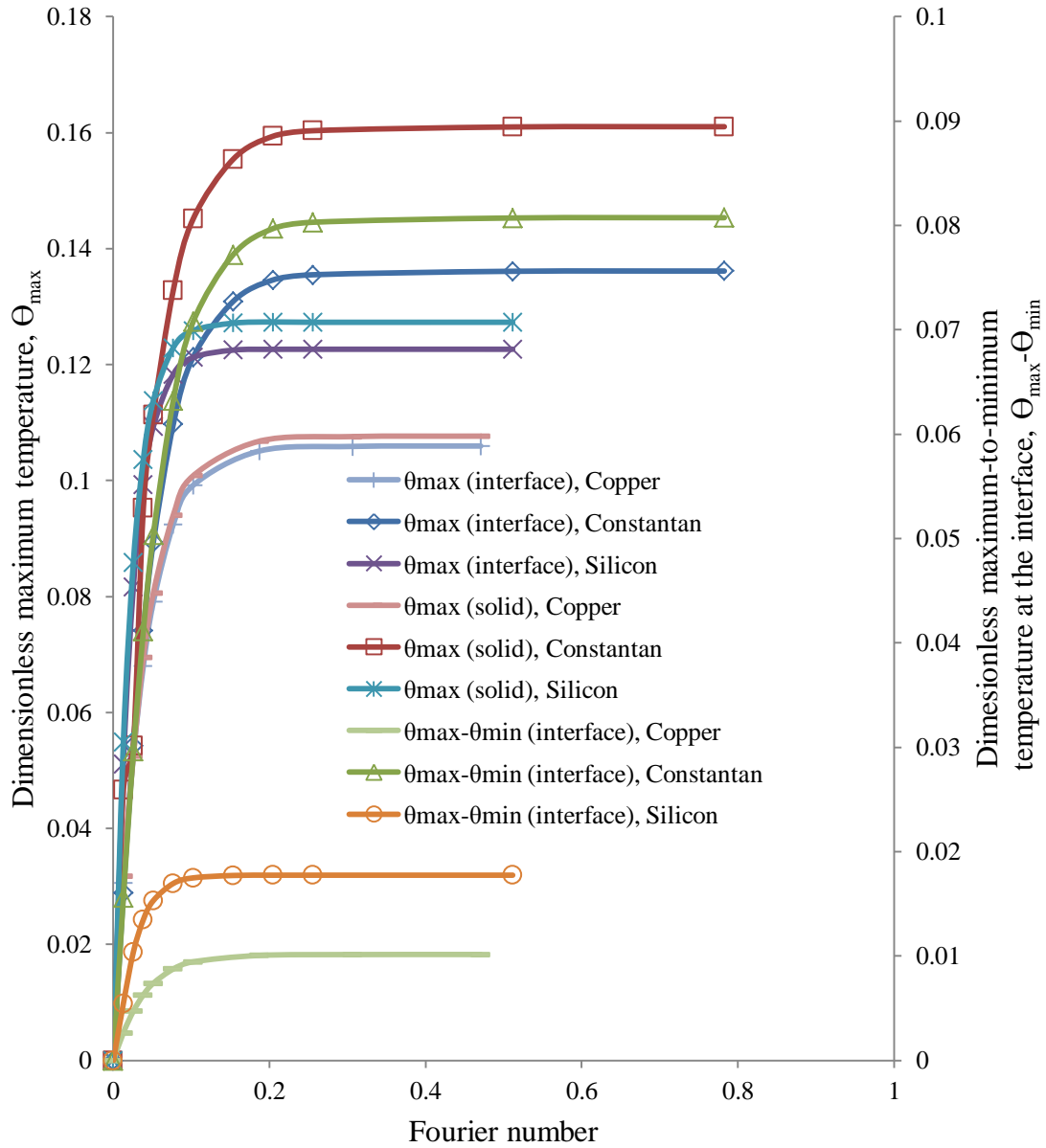


Figure 4.12 Variation in maximum non-dimensional temperature at the interface, maximum non-dimensional temperature within the solid, and the maximum-to-minimum non-dimensional temperature difference at the interface for different materials (Re = 750, $T_j = 313.15$ K, $b = 0.00125$ m, $H_n = 0.0055$ m, base case, $q = 63$ kW/m², $W = 0.0017$ m)

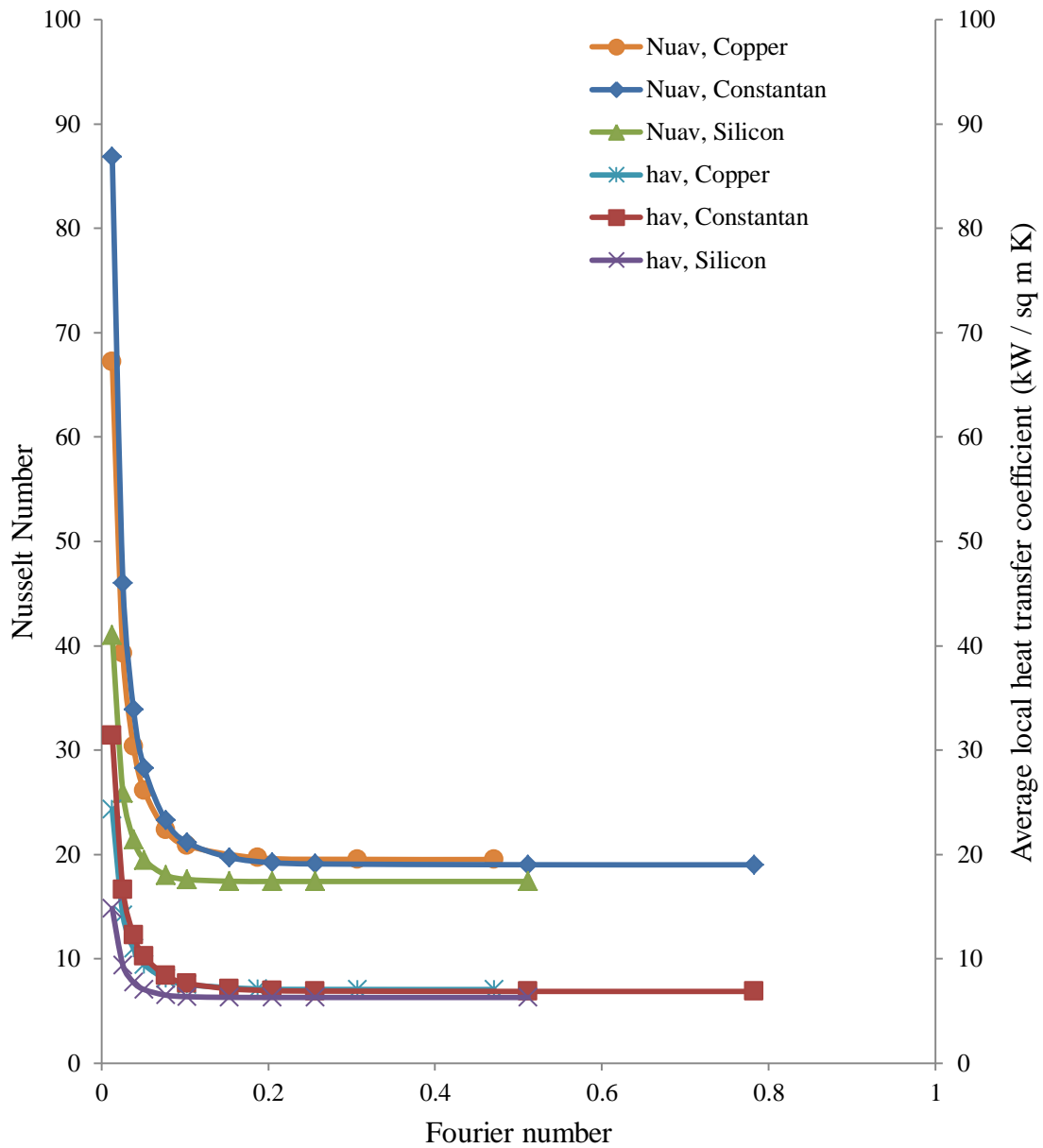


Figure 4.13 Variation of average heat transfer coefficient and average Nusselt number with Fourier number for different materials (Re = 750, $T_j = 313.15$ K, $b = 0.00125$ m, $H_n = 0.0055$ m, base case, $q = 63$ kW/m², $W = 0.0017$ m)

Figure 4.13 displays the development of the average local heat-transfer coefficient and Nusselt number with time. The highest values of the local heat transfer coefficient occur at the beginning of the transient process where the temperature of the plate is very close to the temperature of the jet. This effect is most noticeable in the case of constantan, where the plate is more thermally insulated from the heat flux at the bottom of the plate. As the plate heats for all materials the heat-transfer coefficient and Nusselt number drop until reaching steady state levels.

The refrigerant R-134a was used as an alternate cooling fluid for the base case with variable properties taken into account. Figure 4.14 displays the maximum temperature present on the interface and in the solid. The results show that silicon plate's temperature rises more quickly than the other materials and it reaches steady state at the fastest time. This is in line with the results where water was the working fluid. Again, constantan and copper have the longest times to steady state, an effect of their lower thermal diffusivity and higher thermal storage capacity. Figure 4.15 displays the development of the average heat-transfer coefficient and average Nusselt number with time. It is observed that constantan displays a very large peak of average Nusselt number at the onset of the transient process. This is due to the low amount of conduction taking place within the material, allowing very little heat to reach the solid-fluid interface. The extremely low jet temperature also had a noticeable impact on the peak heat transfer values. As each material approaches steady state the behavior of the heat transfer values falls more in line with those described above when water was the working fluid. Of note are the similar heat transfer characteristics of the materials at steady state conditions.

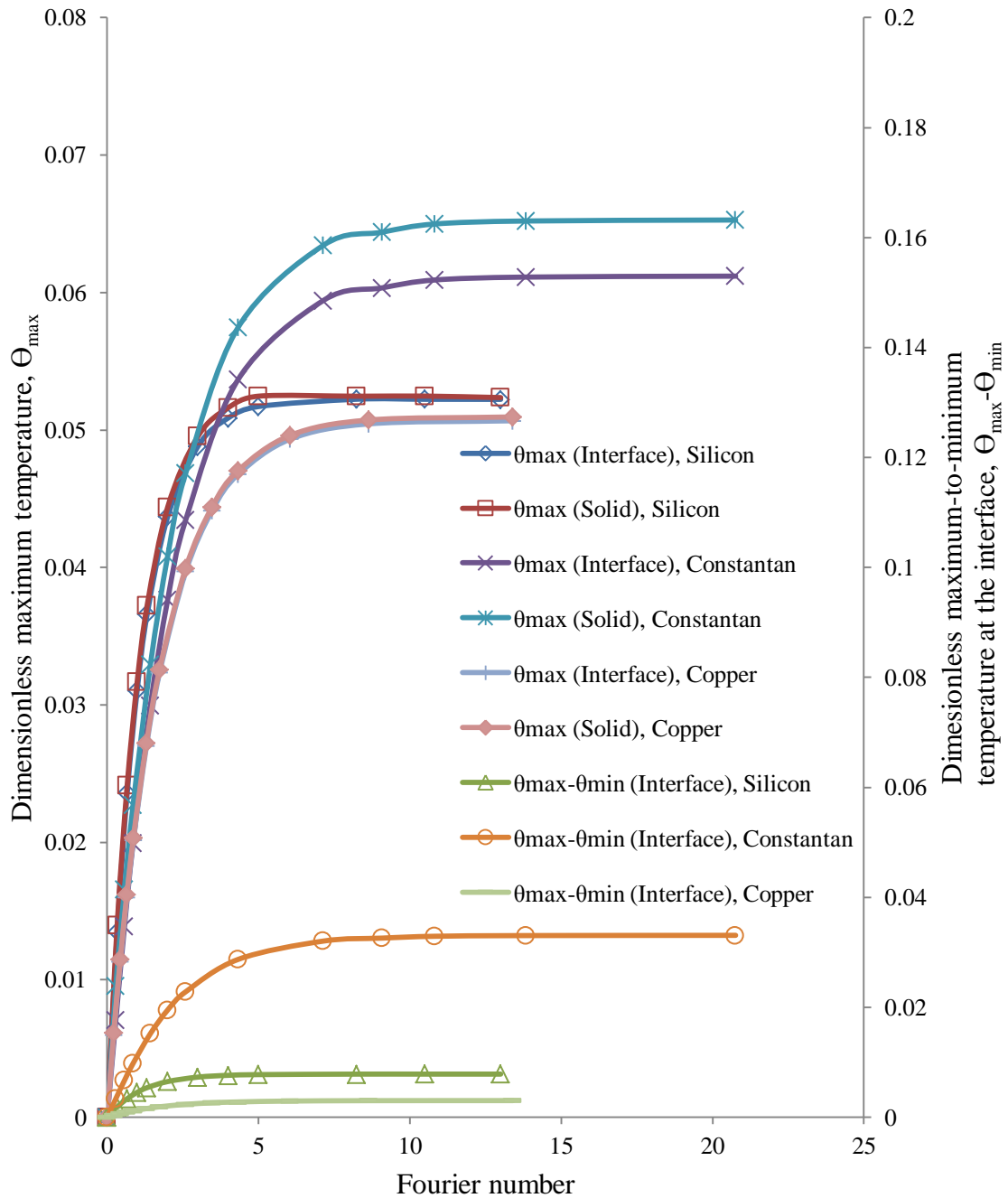


Figure 4.14 Variation in maximum non-dimensional temperature at the interface, maximum non-dimensional temperature within the solid, and the maximum-to-minimum non-dimensional temperature difference at the interface for different materials (R134a) ($Re = 1500$, $T_j = 313.15$ K, $b = 0.00125$ m, $H_n = 0.0055$ m, base case, $q = 63$ kW/m², $W = 0.0017$ m)

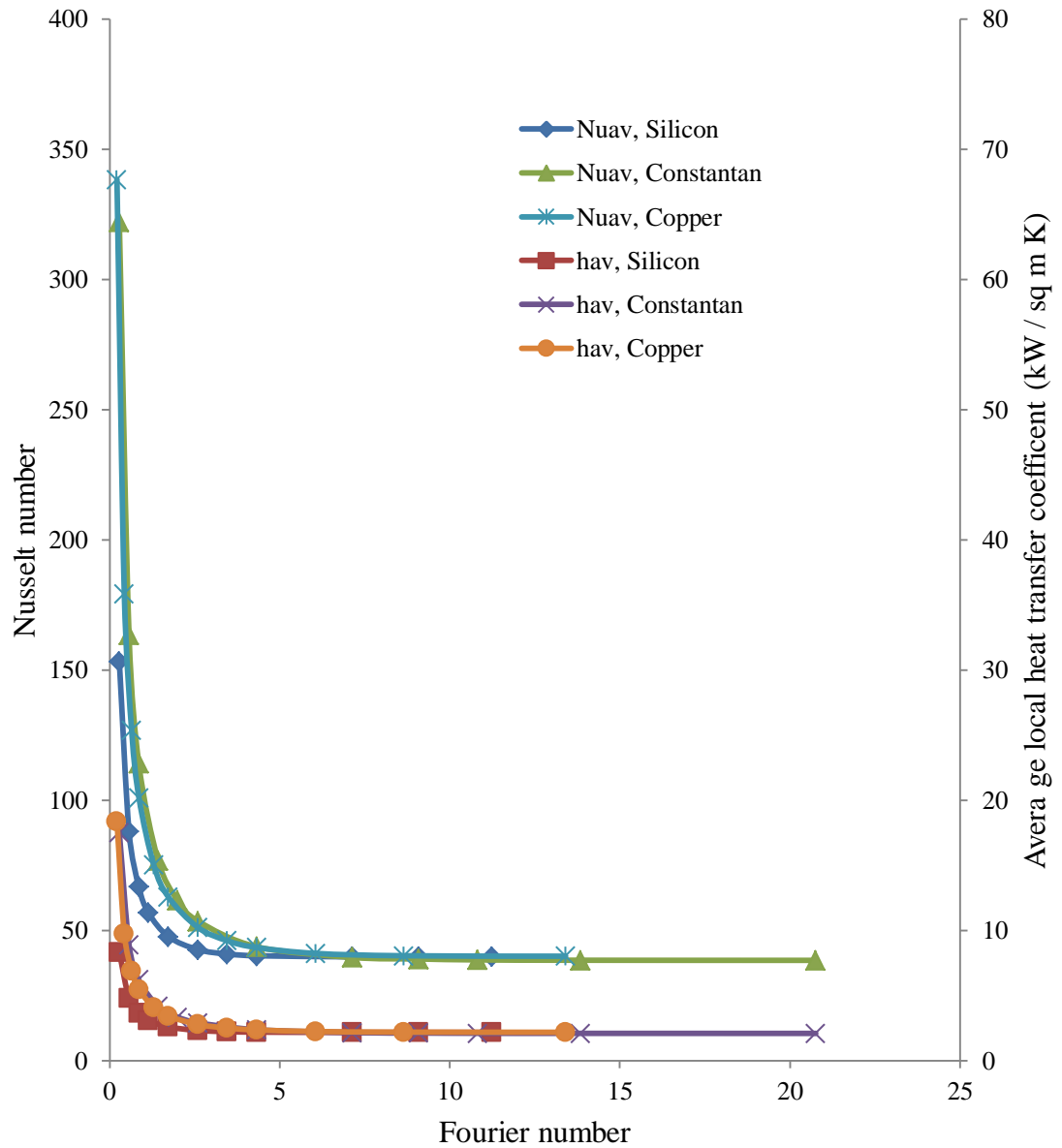


Figure 4.15 Variation of average heat transfer coefficient and average Nusselt number with Fourier number for different materials (R134a)
 (Re = 1500, $T_j = 313.15$ K, $b = 0.00125$ m, $H_n = 0.0055$ m, base case, $q = 63$ kW/m², $W = 0.0017$ m)

4.2 Slot Jet Impinging on a Uniformly Heated Plate with Triangular Ridges:

Transient Heating

For this simulation the working fluid was water and the solid plate was silicon. The different surface configurations used for these simulations are shown in Figure 3.22. The base case is defined as when the angle at the top of each rib is 60 degrees. Case A is defined as when that angle is 90 degrees and case B is defined as when the angle is 30 degrees. Figure 3.23 displays a representation of the velocity field at the steady state condition. The change in free surface height for different Reynolds number in the steady state is shown in Figure 3.24. While the velocity field does vary slightly during the transient process, it does not noticeably or meaningfully change the free surface height.

The development of the interface temperature with time for the base case is shown in Figure 4.16. As expected, the temperature raises as time increases. The greatest increase in temperature occurs in the early part of the transient process from $t = 0$ to $t = 0.5$ s. The difference between the minimum and maximum temperature at the interface also increases with time. At $t = 0.25$ s it is observed that the temperature across the interface shows little variation. This is due to the transient thermal storage of the fluid required to develop a thermal boundary layer. As the layer develops with time it has a larger impact on the temperature profile across the length of the plate, demonstrated by the increase in temperature along the length. As with the rectangular step case, the low peaks in temperature occur when the fluid interacts with the change in geometry. This effect is greatest at the first triangular rib as the fluid is already changing direction and is forced into the sharp peak at $x = 0.06$ cm.

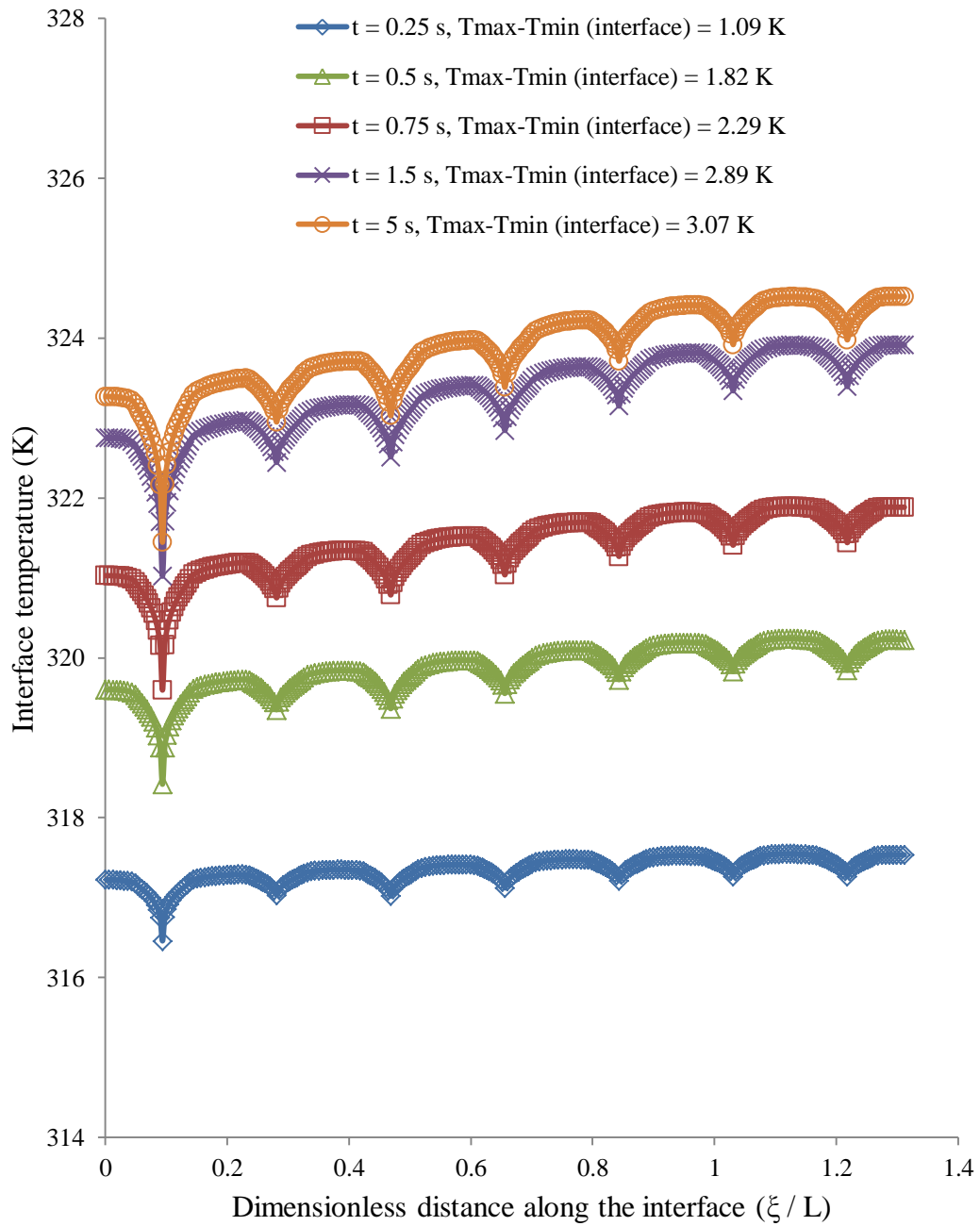


Figure 4.16 Interface temperature for different times
 ($Re = 750$, $T_j = 313.15$ K, $b = 0.00125$ m, $H_n = 0.0055$ m, Silicon plate base case, $q = 63$ kW/m², $W = 0.0017$ m)

Figure 4.17 shows the development of the local heat-transfer coefficient across selected times for the base case. The local heat-transfer coefficient across the entire plate surface is zero at $t = 0$ s as the heat source is not active. The local heat-transfer coefficient peaks at $t = 0.25$ s and decreases as time moves forward. As the magnitude of the local heat-transfer coefficient is calculated as a function of the interface temperature, its behavior changes in a similar fashion. The peaks in local heat-transfer coefficient are due to the fluid stream interacting with the geometry, causing instability that agitates the fluid. The dips along the curve coincide with the gaps between the triangular ribs. In these gaps the fluid speed is greatly reduced, causing a decrease in convective heat transfer. The development of the Nusselt number with non-dimensional time is displayed in Figure 4.18. The maximum value of the Nusselt number occurs at the first triangular rib in each time frame specified. As time continues, the Nusselt number drops in a nearly uniform fashion. The larger variation in minimum to maximum Nusselt number at $Fo = 0.01279$ is due to the larger difference in local heat-transfer coefficient during the earlier stages of the transient process.

The effect of the Reynolds number on the transient process is essential and displayed in Figures 4.19-4.20. The maximum non-dimensional temperature at the interface, maximum non-dimensional temperature in the solid, and the maximum-to-minimum temperature difference at the interface for three different Reynolds number is shown in Figure 4.19. It can be seen that the temperatures rise rapidly from the isothermal condition until the point where the thermal storage capacity of the material is depleted. Due to the thinness of the plate, the system reaches steady state quickly. For the three Reynolds number presented in this investigation the system is within 0.004% of

the steady state interface temperature in less than 7 seconds. The highest maximum temperatures occur when $Re = 500$ due to the lower heat transfer associated with the slower fluid speed. Nearly all of the temperature increase occurs in the first few seconds of the transient process before the rate of increase drops off well before $t = 5$ s.

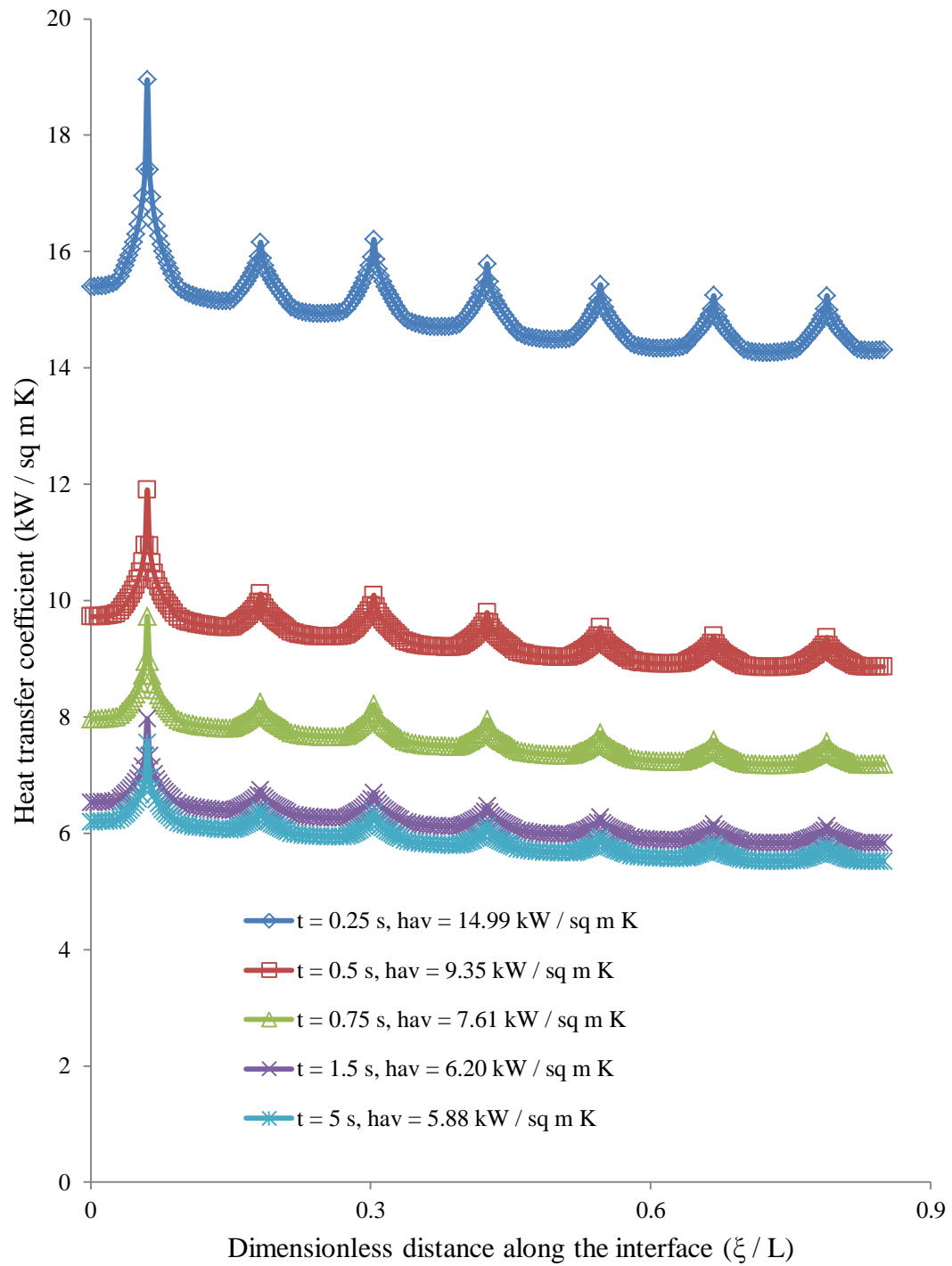


Figure 4.17 Local heat transfer coefficient for different times
 (Re = 750, $T_j = 313.15$ K, $b = 0.00125$ m, $H_n = 0.0055$ m, Silicon plate base case,
 $q = 63$ kW/m², $W = 0.0017$ m)

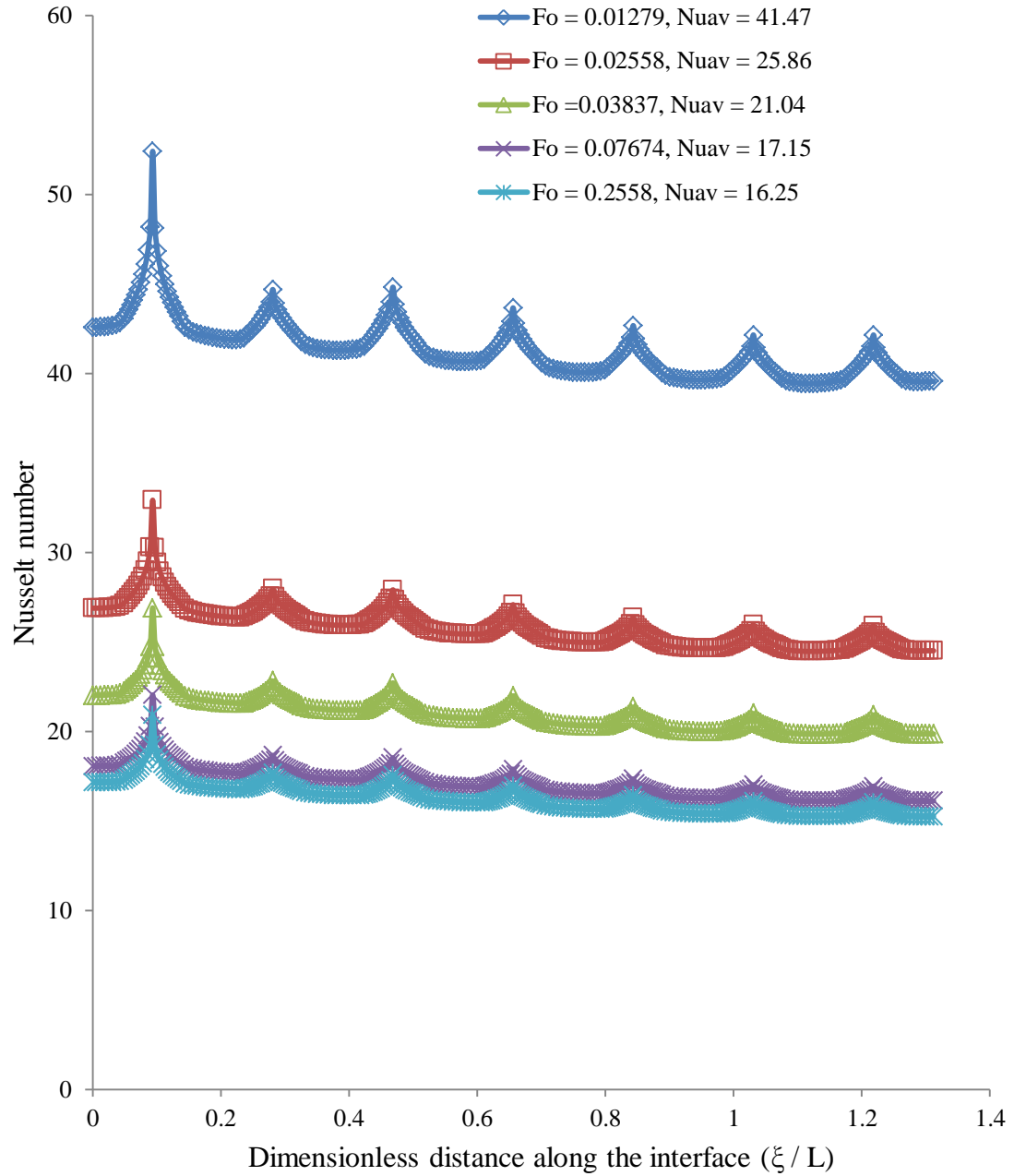


Figure 4.18 Local Nusselt number for different Fourier values
 (Re = 750, $T_j = 313.15$ K, $b = 0.00125$ m, $H_n = 0.0055$ m, Silicon plate base case,
 $q = 63$ kW/m², $W=0.0017$ m)

the steady state interface temperature in less than 7 seconds. The highest maximum temperatures occur when $Re = 500$ due to the lower heat transfer associated with the slower fluid speed. Nearly all of the temperature increase occurs in the first few seconds of the transient process before the rate of increase drops off well before $t = 5$ s. Figure 4.20 displays the effect of the Reynolds number on the average heat-transfer coefficient and Nusselt number with respect to time. The values of both the average heat-transfer coefficient and Nusselt number decrease as time increases. Note the change in Reynolds number does not considerably change the behavior of the decay curves.

The effect of changing the indentation depth for the triangular ribs is shown in Figures 4.21 and 4.22. The maximum non-dimensional temperature at the interface, maximum non-dimensional temperature in the solid, and the maximum-to-minimum temperature difference at the interface for the three different indentation depths is shown in Figure 4.21. The highest maximum temperature for both the interface and the solid occurs for the smallest rib height. This was not entirely due to the known poor heat transfer quality of the smaller ribs. For the triangular rib cases the increase in indentation depth leads to a decrease in temperature along the length of the plate. Figure 4.22 displays the effect of different indentation depths on the average heat-transfer coefficient with respect to time. It can be seen that the larger indentation sizes produce a higher heat-transfer coefficient and Nusselt number. These higher heat transfer values can be explained by the increased disruption that the larger ribs cause to the fluid flow decreased width of the ribs allowing for an increase in conduction through the fin-shaped triangles.

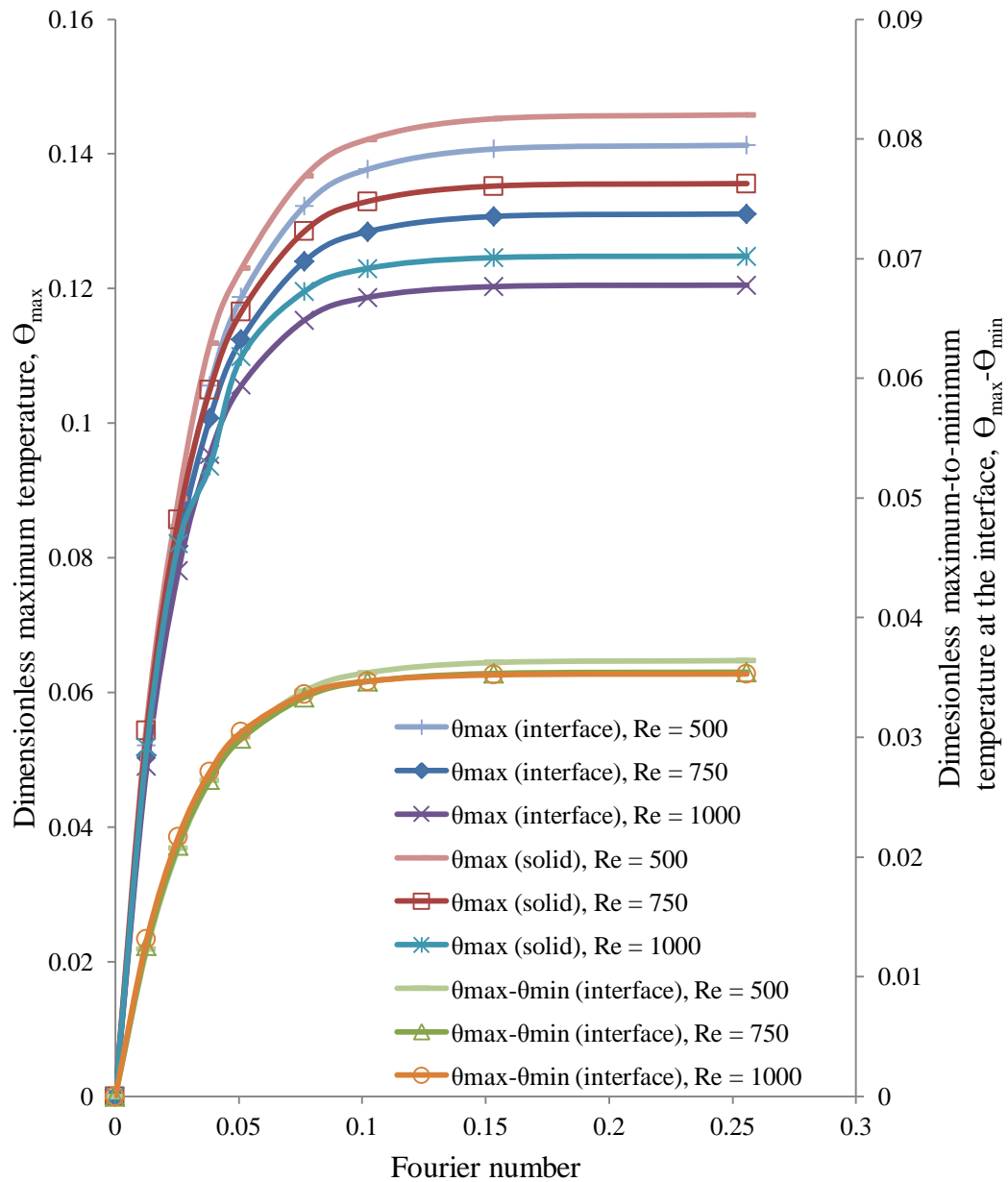


Figure 4.19 Variation in maximum non-dimensional temperature at the interface, maximum non-dimensional temperature within the solid, and the maximum-to-minimum non-dimensional temperature difference at the interface for different Reynolds number ($T_j = 313.15$ K, $b = 0.00125$ m, $H_n = 0.0055$ m, Silicon plate base case, $q = 63$ kW/m², $W = 0.0017$ m)

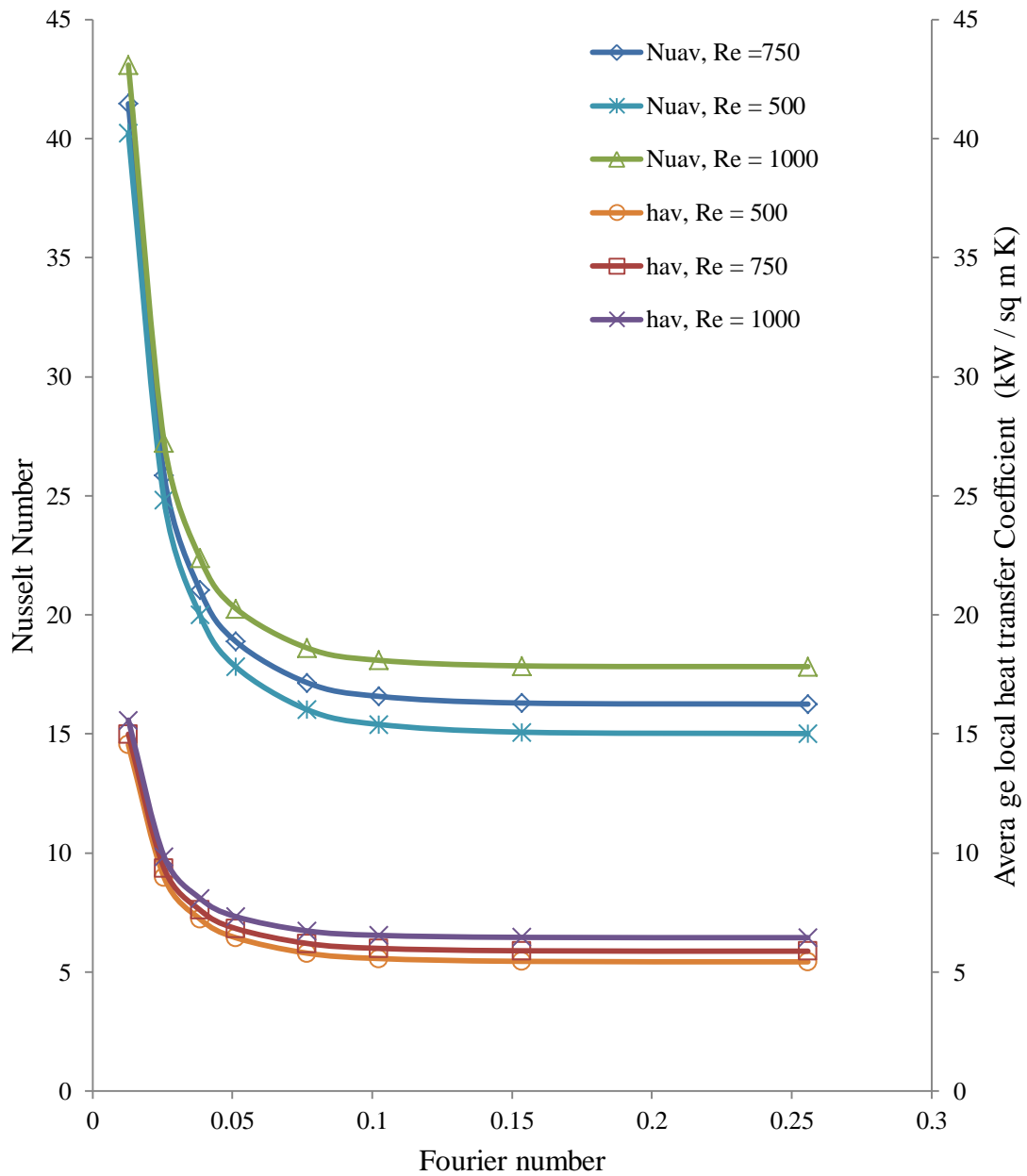


Figure 4.20 Variation of average heat transfer coefficient and average Nusselt number with Fourier number ($T_j = 313.15$ K, $b = 0.00125$ m, $H_n = 0.0055$ m, Silicon plate base case, $q = 63$ kW/m², $W = 0.0017$ m)

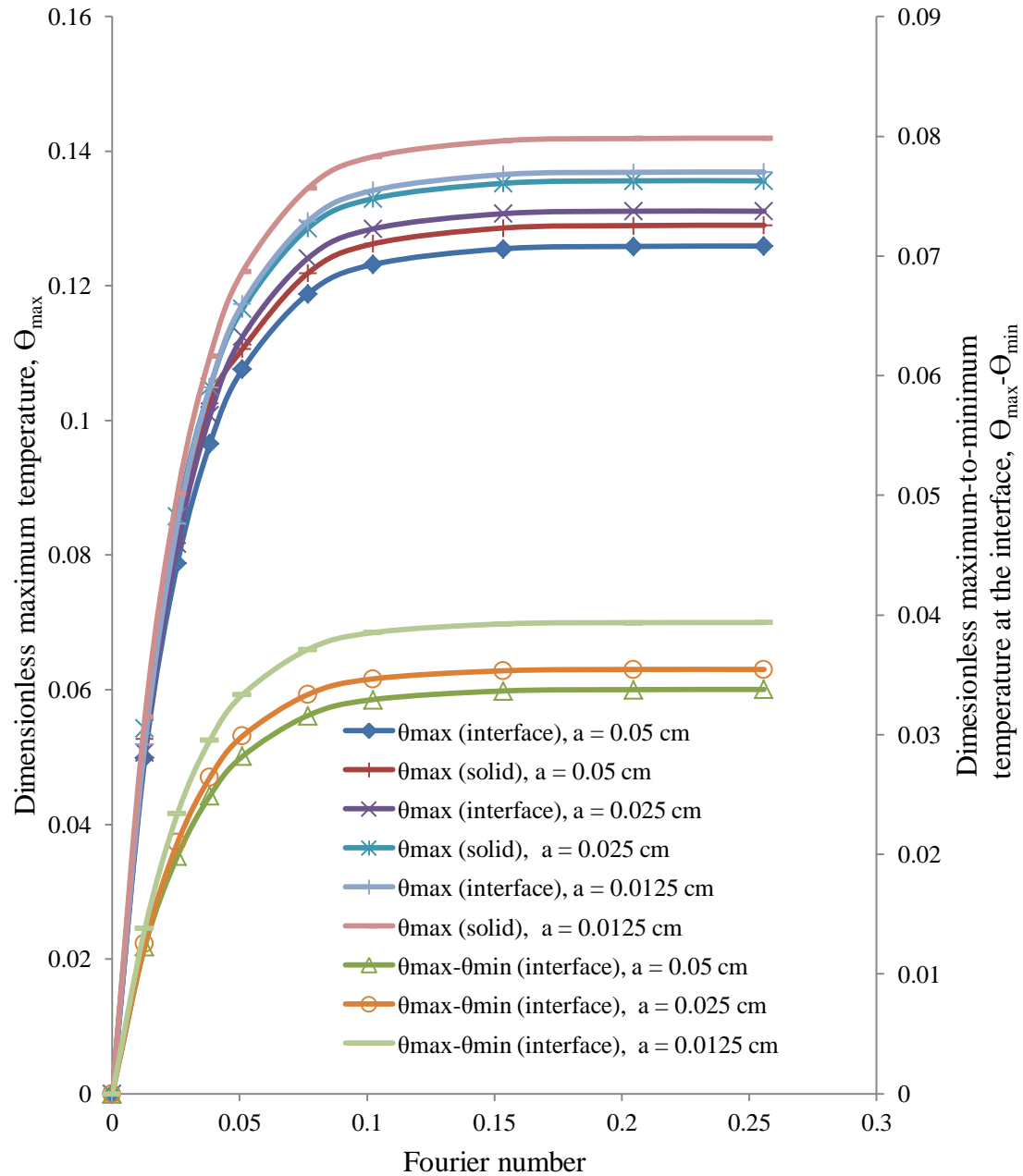


Figure 4.21 Variation in maximum non-dimensional temperature at the interface, maximum non-dimensional temperature within the solid, and the maximum-to-minimum non-dimensional temperature difference at the interface for different indentation depths (Re = 750, $T_j = 313.15$ K, $b = 0.00125$ m, $H_n = 0.0055$ m, Silicon plate base case, $q = 63$ kW/m², $W = 0.0017$ m)

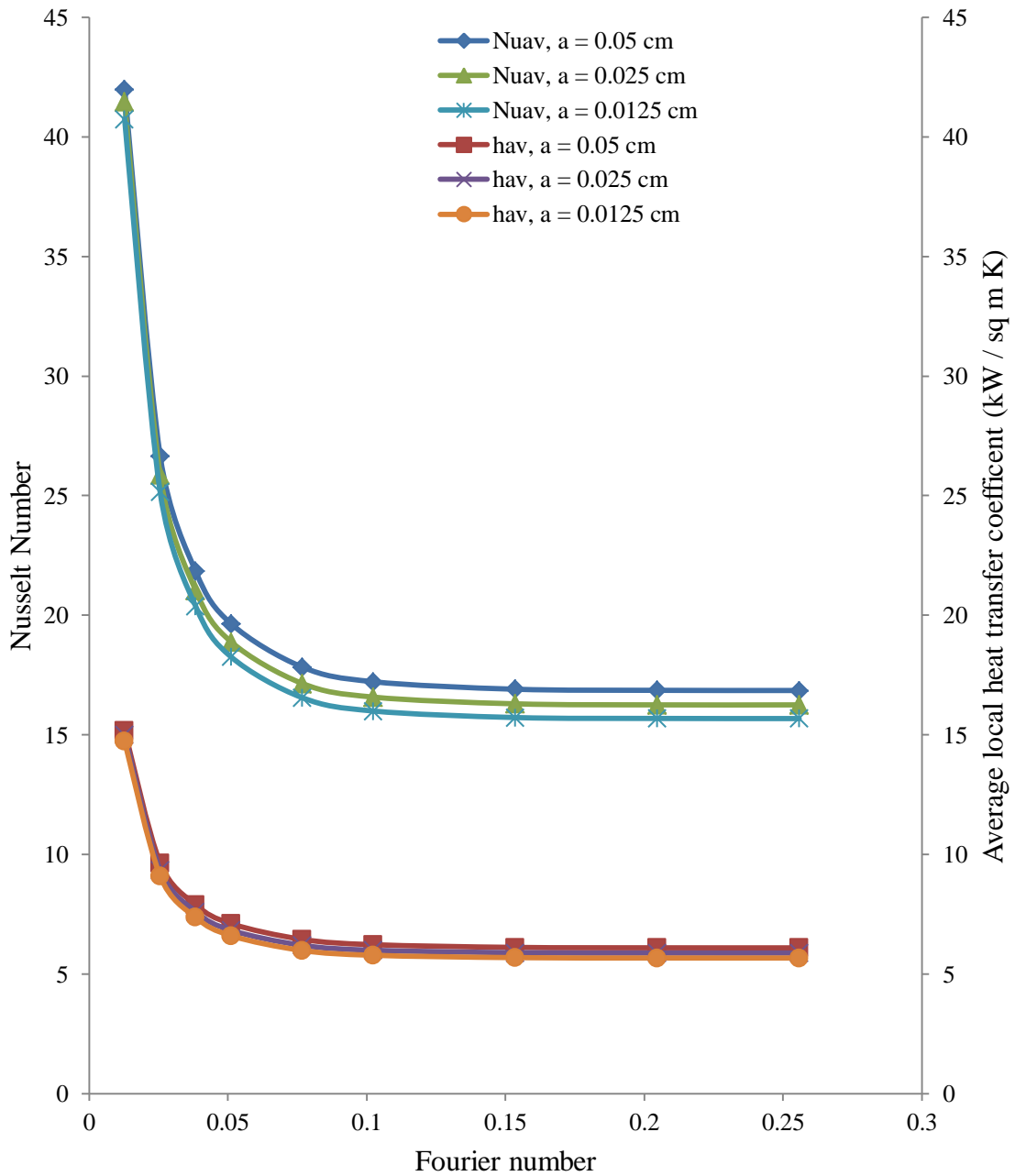


Figure 4.22 Variation of average heat transfer coefficient and average Nusselt number for different indentation depths (Re = 750, $T_j = 313.15$ K, $b = 0.00125$ m, $H_n = 0.0055$ m, Silicon plate base case, $q = 63$ kW/m², $W = 0.0017$ m)

The effect of surface configuration, in this case the pitch angle of the triangular ribs, is also an important parameter to examine. Figure 4.23 displays the maximum interface and surface temperature with changing indentation depth for case A. Interestingly, the maximum temperature of the interface when $a = 0.000125 \text{ m}$ is nearly identical to the maximum temperature of the solid when $a = 0.00025 \text{ m}$. The behavior of the average heat-transfer coefficient and average Nusselt number for case A is described in Figure 4.24. The main conclusion to take from case A is that the change in height of the indentation does very little in the way of changing the average heat-transfer coefficient or Nusselt number as the system goes to steady state. The effect of adding surface area by increasing the height of the surface geometry does not overcome the effect of reducing the velocity profile in the gaps between the ribs.

The maximum non-dimensional temperature of the interface and solid for the different indentation depths in case B is found in Figure 4.25. It is observed that the temperatures profile is nearly identical to the base case and case A. The behavior of the average heat-transfer coefficient and average Nusselt number with time for case B are displayed in Figure 4.26. The effect of indentation depth on the heat transfer characteristics for this case is more evident when compared against case A. As the indentation depth increases both the average heat-transfer coefficient and Nusselt number decreases.

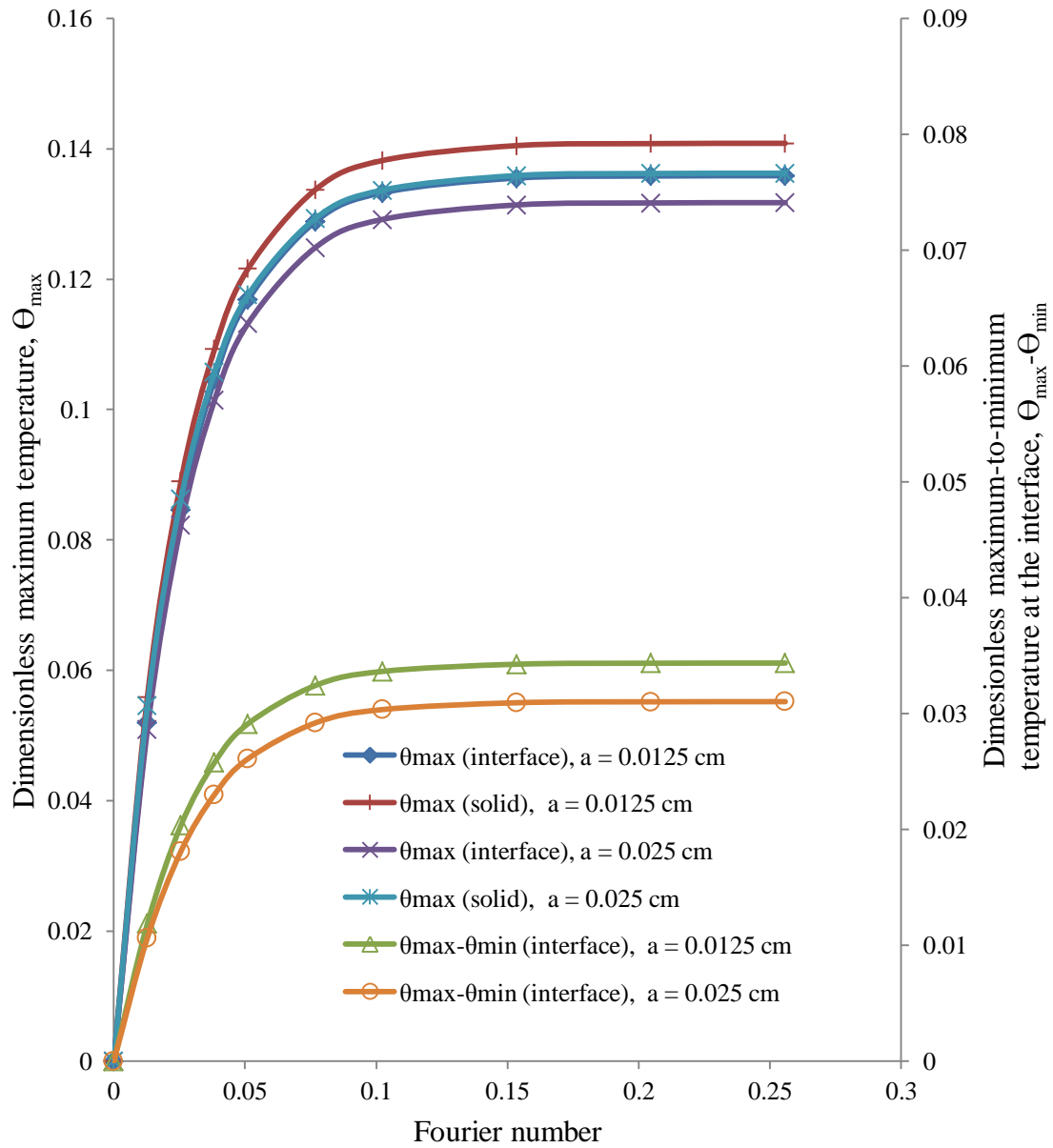


Figure 4.23 Variation in maximum non-dimensional temperature at the interface, maximum non-dimensional temperature within the solid, and the maximum-to-minimum non-dimensional temperature difference at the interface for different indentation depths (Re = 750, $T_j = 313.15$ K, $b = 0.00125$ m, $H_n = 0.0055$ m, Silicon plate, Case A, $q = 63$ kW/m², $W = 0.0017$ m)

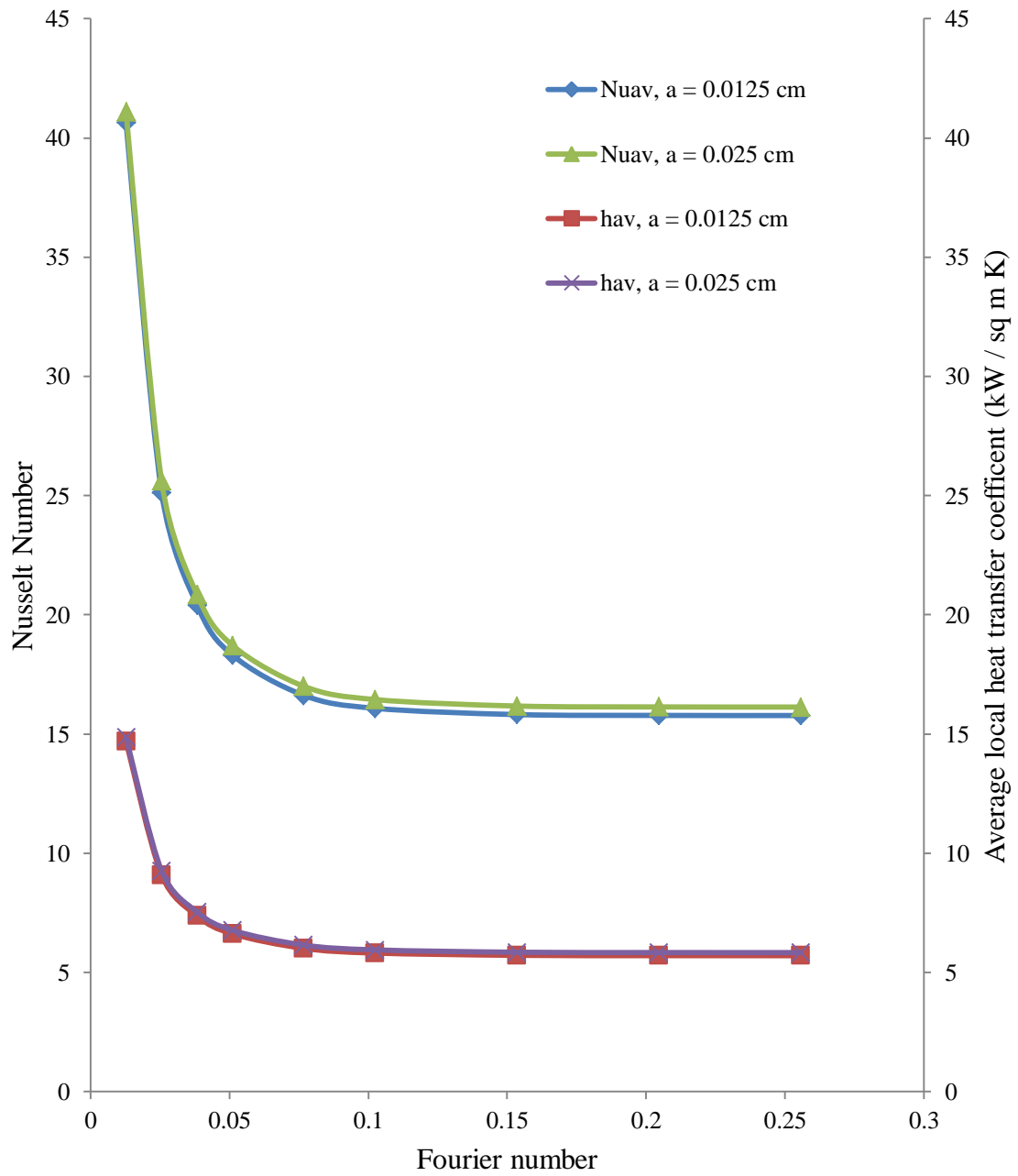


Figure 4.24 Variation of average heat transfer coefficient and average Nusselt number for different indentation depths ($T_j = 313.15 \text{ K}$, $b = 0.00125 \text{ m}$, $H_n = 0.0055 \text{ m}$, Silicon plate, Case A, $q = 63 \text{ kW/m}^2$, $W=0.0017 \text{ m}$)

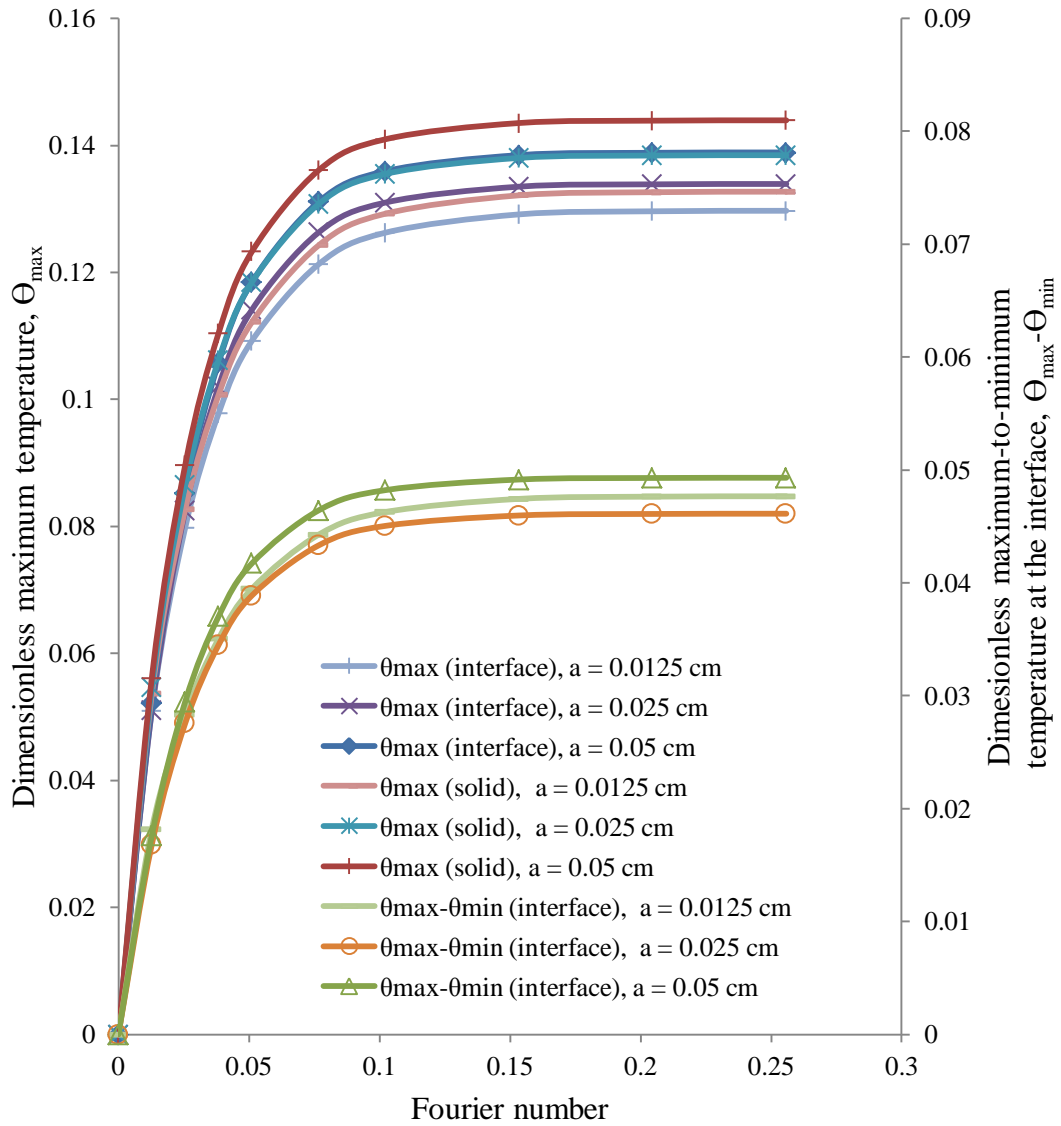


Figure 4.25 Variation in maximum non-dimensional temperature at the interface, maximum non-dimensional temperature within the solid, and the maximum-to-minimum non-dimensional temperature difference at the interface for different indentation depths ($Re = 750$, $T_j = 313.15$ K, $b = 0.00125$ m, $H_n = 0.0055$ m, Silicon plate, Case B, $q = 63$ kW/m², $W = 0.0017$ m)

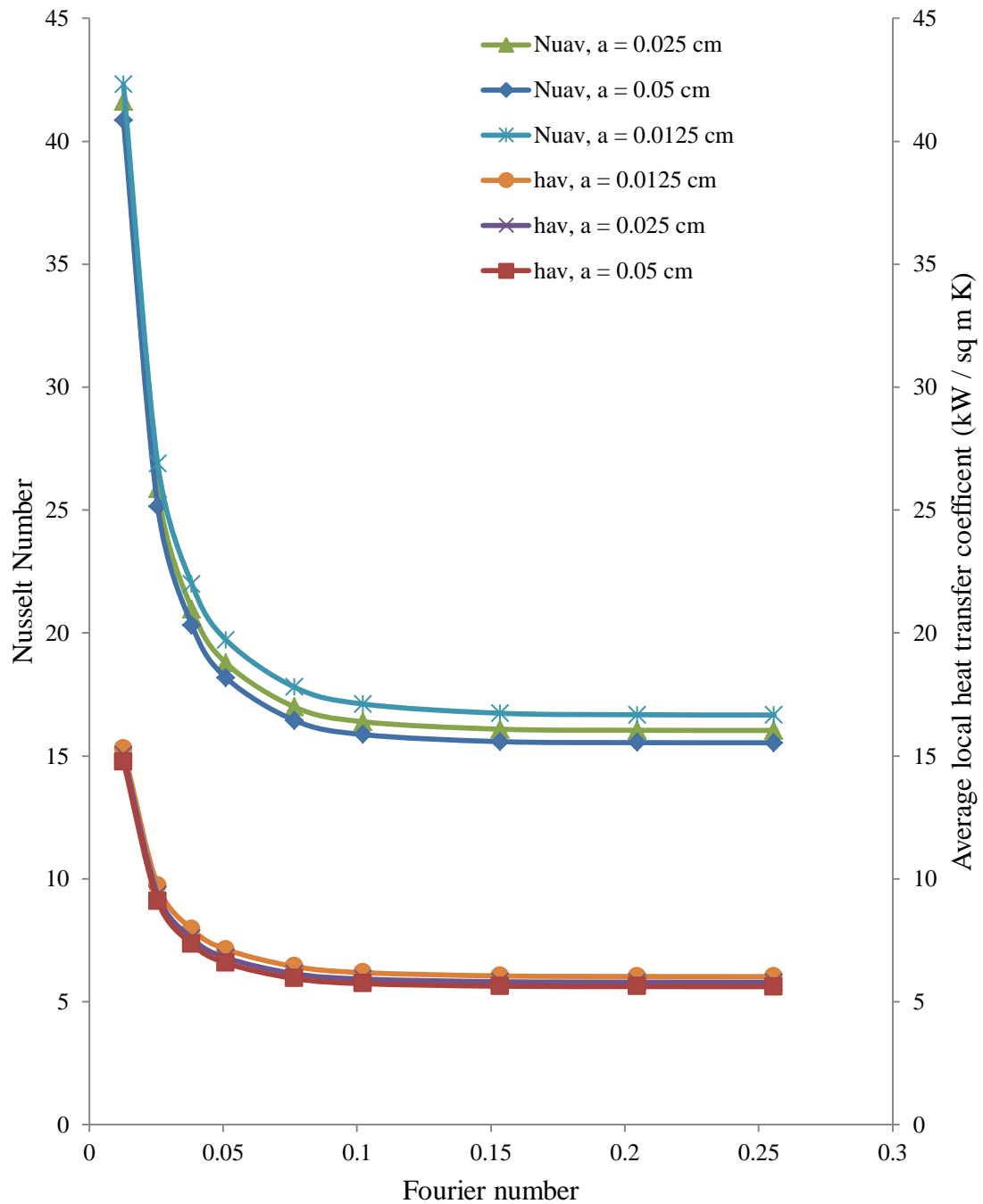


Figure 4.26 Variation of average heat transfer coefficient and average Nusselt number for different indentation depths ($T_j = 313.15$ K, $b = 0.00125$ m, $H_n = 0.0055$ m, Silicon plate, Case B, $q = 63$ kW/m², $W=0.0017$ m)

4.3 Slot Jet Impinging on a Uniformly Heated Plate with Sinusoidal Ridges:

Transient Heating

For this simulation the working fluid was water and the solid plate was silicon. The different surface configurations used for these simulations are shown in Figure 3.33. Unlike the previous geometries, the slot jet impinged in-between two indentations at $x = 0$. The velocity vector distribution at steady state is shown in Figure 3.34. Figure 3.35 shows the free surface height distribution for different Reynolds number. While there will be slight changes in the velocity field when the system is subjected to transient heating, the effect on the free surface height is negligible.

Figure 4.27 shows the development of the interface temperature with time for the base case. At the onset of the transient process the temperature profile is nearly constant across the length of the plate, with a change in temperature of under a half a degree. This is due to the early development of the thermal boundary layer when the thermal storage capacity of the fluid exerts the most influence. As the system approaches the steady state condition, the temperature of the plate begins to vary more, going from a minimum near the beginning of the plate to a maximum at the end. The development of the local heat-transfer coefficient with time is displayed in Figure 4.28. The local heat-transfer coefficient decreases as time increases. The highest value is present in the stagnation zone before the local heat-transfer coefficient drops as the flow enters the first curved indentation. As the fluid continues along the plate there are very slight increases in convective heat transfer when the geometry moves the fluid upward at $\xi/L = 0.22$. These increases are not nearly as drastic when compared to the other geometries due to the smooth sine shaped surface along the interface surface.

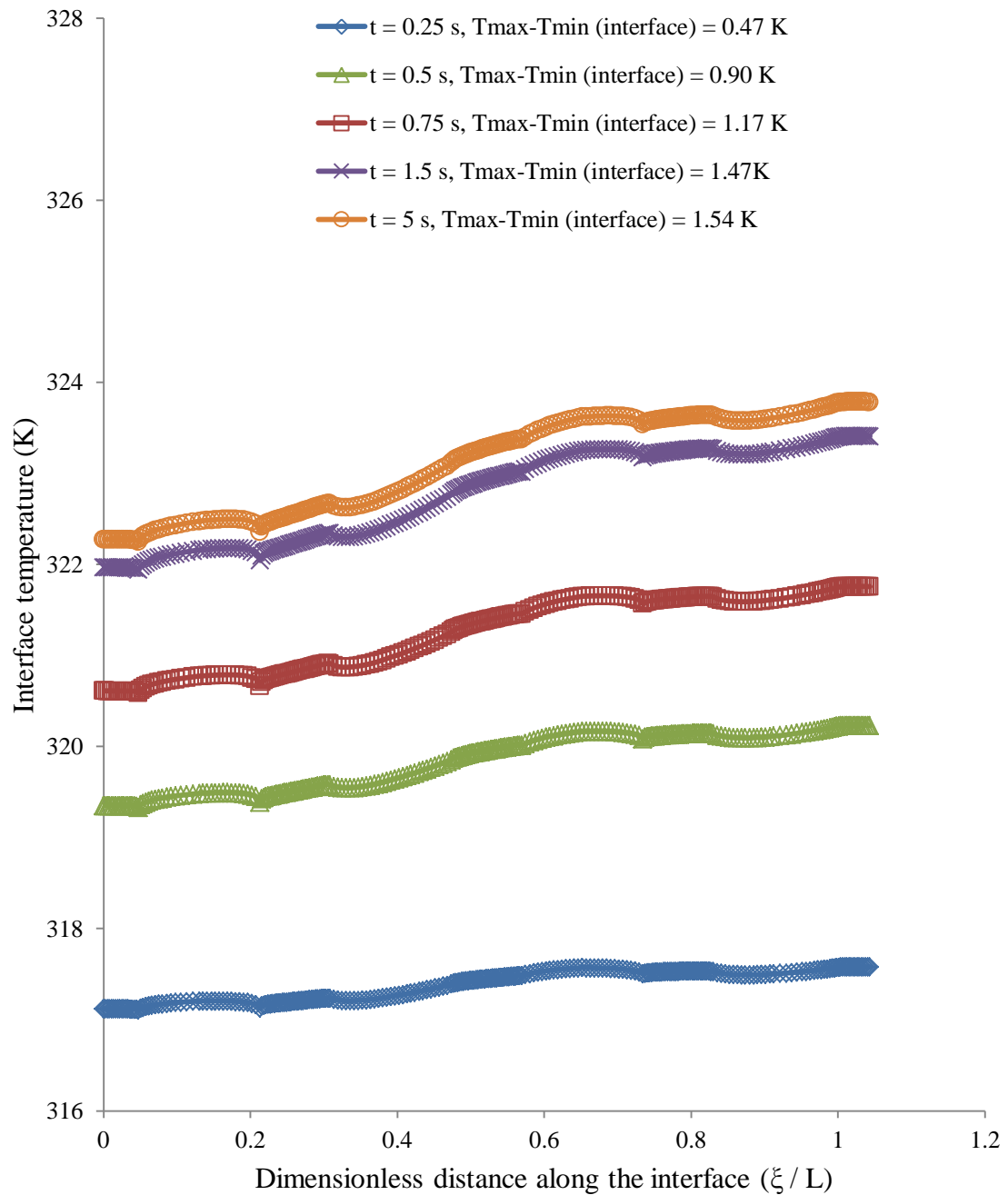


Figure 4.27 Interface temperature for different times
 ($Re = 750$, $T_j = 313.15$ K, $b = 0.00125$ m, $H_n = 0.0055$ m, Silicon plate, sine base case,
 $q = 63$ kW/m², $W = 0.0017$ m)

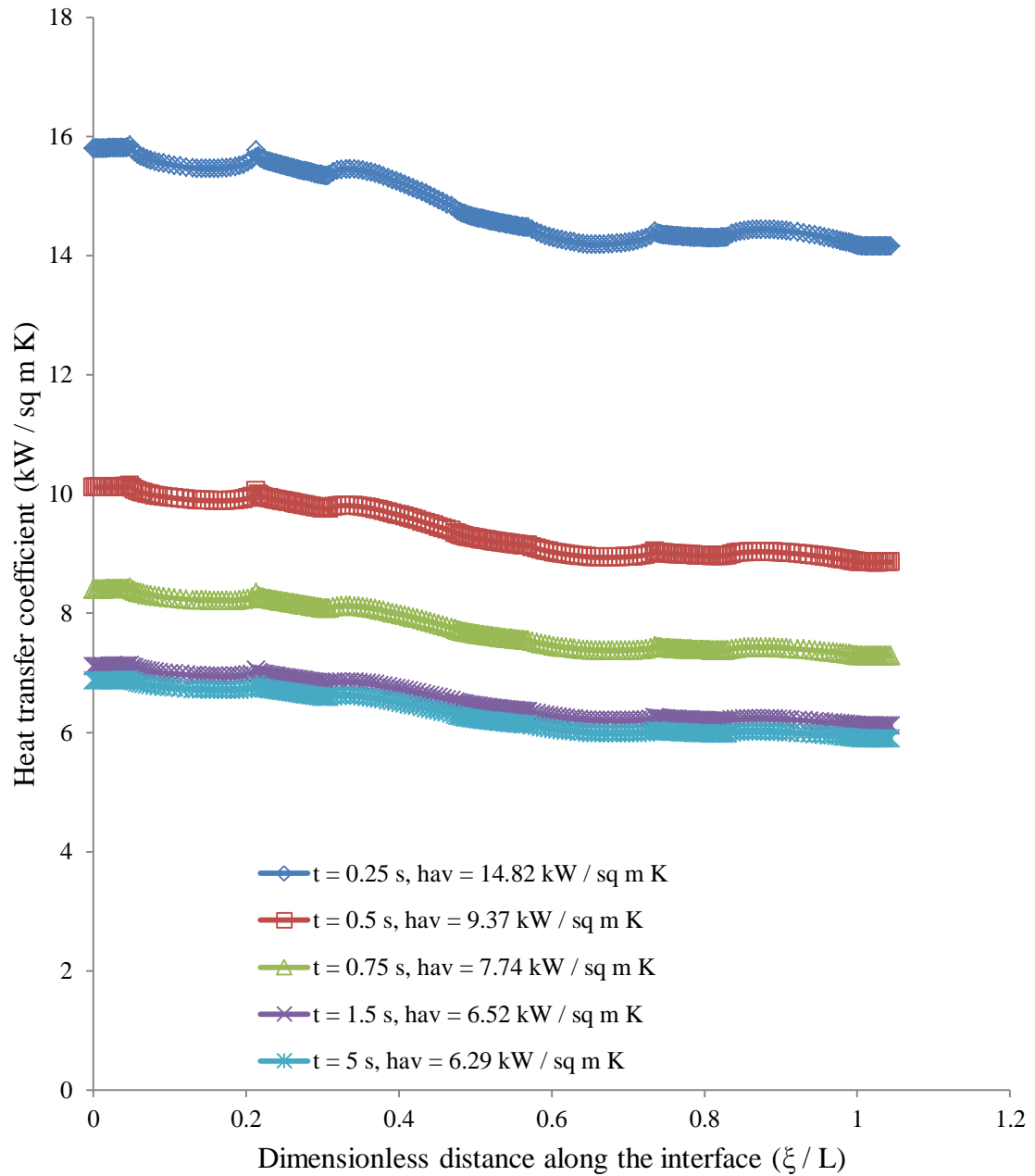


Figure 4.28 Local heat transfer coefficient for different times
 ($Re = 750$, $T_j = 313.15$ K, $b = 0.00125$ m, $H_n = 0.0055$ m, Silicon plate base case,
 $q = 63$ kW/m², $W = 0.0017$ m)

The behavior of the Nusselt number with increasing time for the base case is shown in Figure 4.29. As expected, the highest Nusselt number occurs at the onset of the transient condition. This is due to the dominance of the convective heat transfer at this time. As time continues towards steady state the local Nusselt number drops due to the increase in the conduction within the fluid as it overcomes the resistance due to thermal storage. Note that the behavior of the Nusselt number is strongly coupled to that of the local heat-transfer coefficient.

The effect of the Reynolds number on the maximum non-dimensional interface and solid temperatures is displayed in Figure 4.30. The temperature rises rapidly for the initial stages of the transient process as the plate absorbs heat until its heat capacity is maxed. As the plate is thin this process takes a short amount of time and the plate is at steady state well before $t = 10$ s. The maximum temperature on both the interface and within the plate decreases as the Reynolds number increases. The difference between the maximum and minimum temperature on the interface is essentially equal for each of the three speeds investigated. Figure 4.31 shows the development of the average heat-transfer coefficient and average Nusselt number as a function of time. Soon after the heat source is turned on, both the average heat-transfer coefficient and average Nusselt number are at their highest values. As time continues and the plate heats up, the values of both decay exponentially to the steady state condition. As the Reynolds number increases, so does both the average heat-transfer coefficient and average Nusselt number.

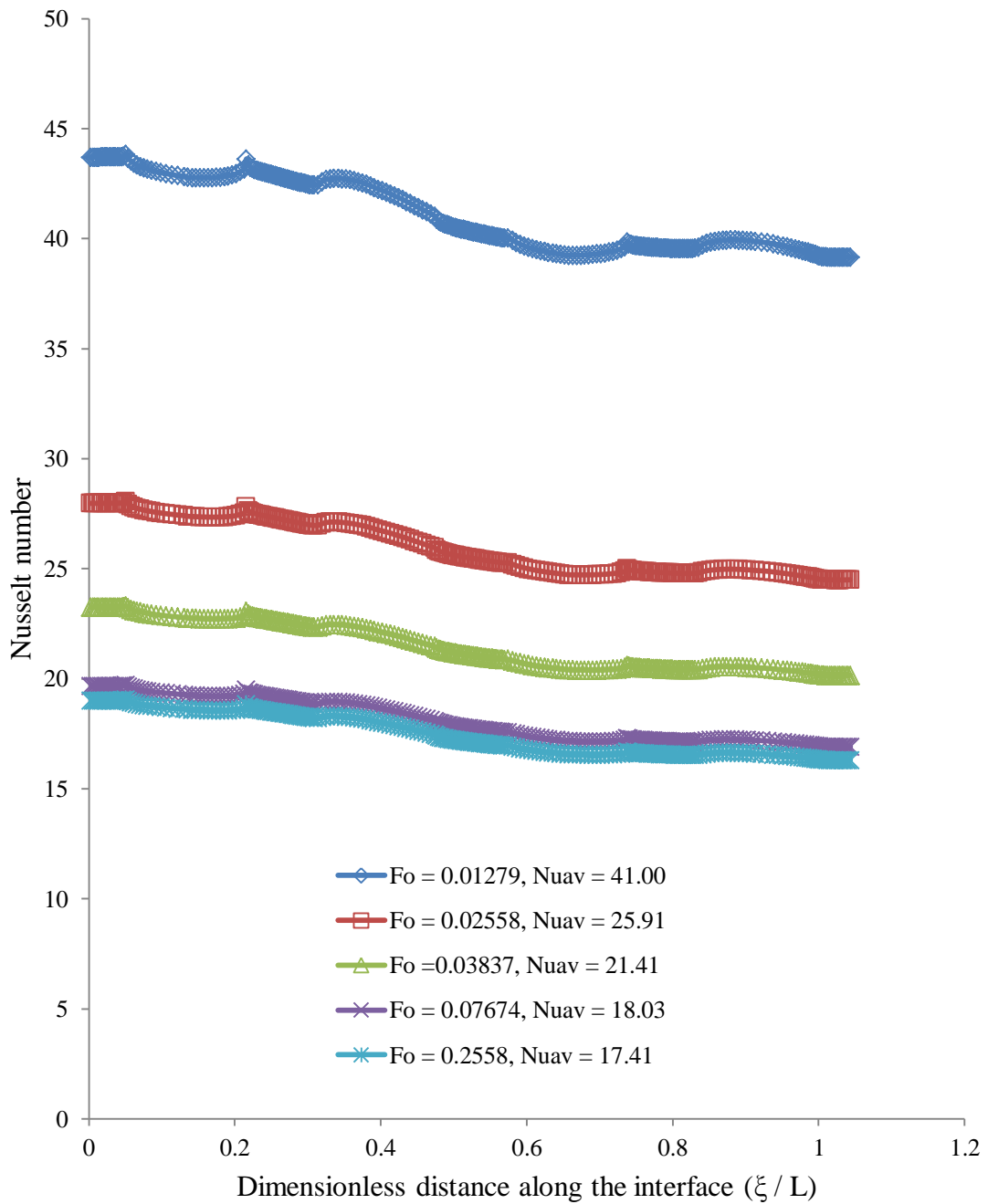


Figure 4.29 Local Nusselt number for different Fourier values
 (Re = 750, $T_j = 313.15$ K, $b = 0.00125$ m, $H_n = 0.0055$ m, Silicon plate base case, $q = 63$ kW/m², $W = 0.0017$ m)

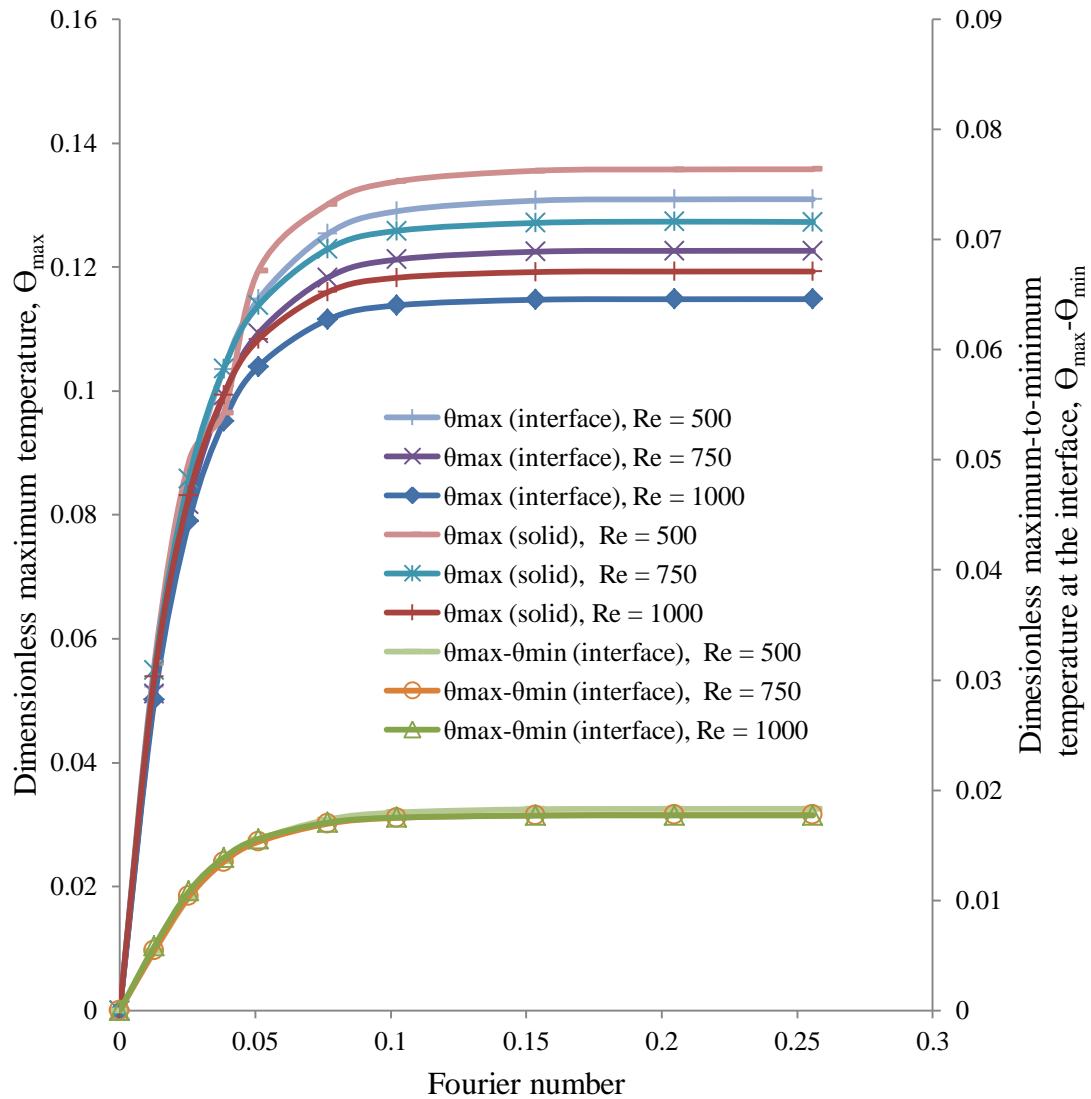


Figure 4.30 Variation in maximum non-dimensional temperature at the interface, maximum non-dimensional temperature within the solid, and the maximum-to-minimum non-dimensional temperature difference at the interface for different Reynolds number ($T_j = 313.15$ K, $b = 0.00125$ m, $H_n = 0.0055$ m, Silicon plate, sine base case, $q = 63$ kW/m², $W = 0.0017$ m)

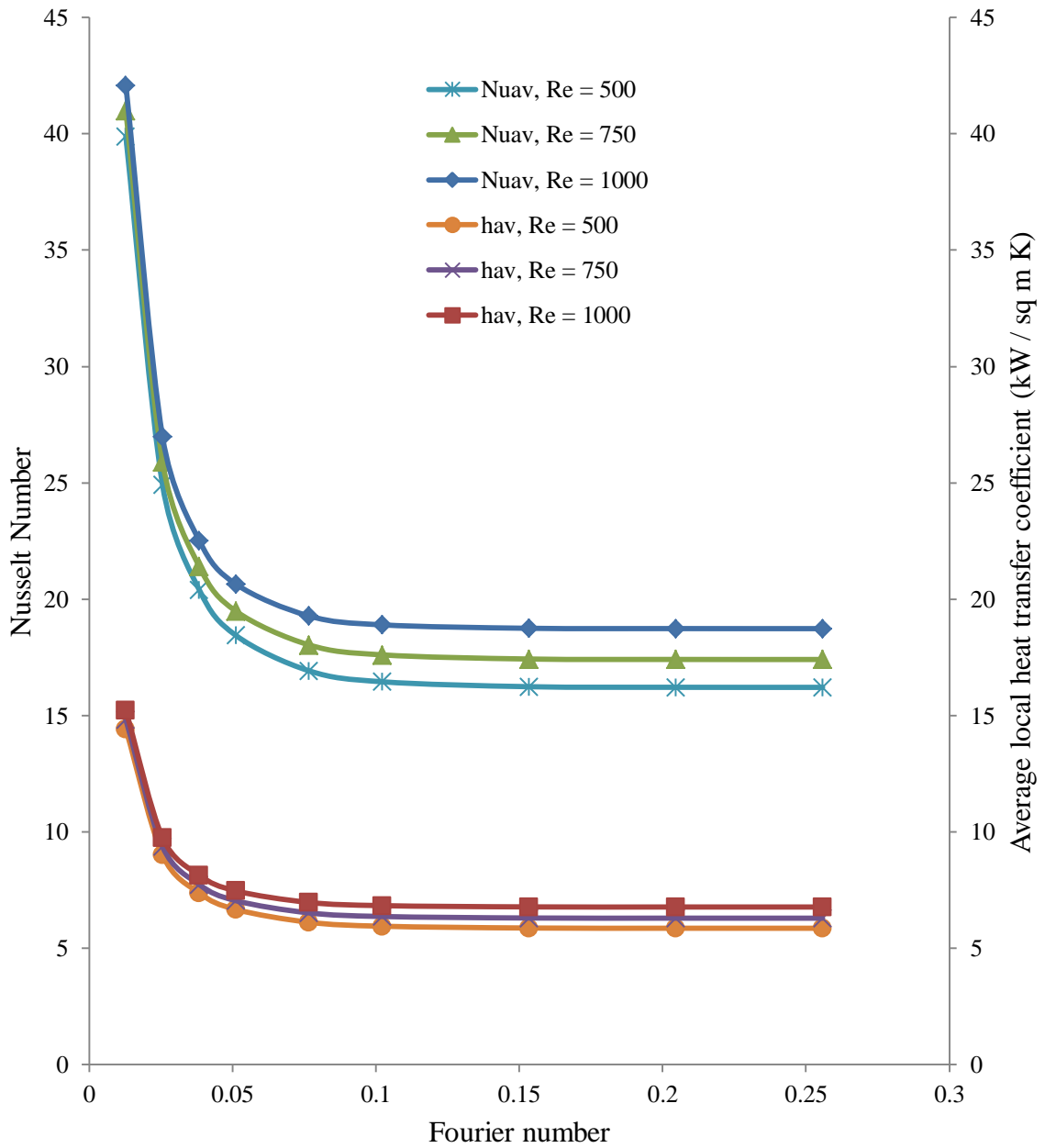


Figure 4.31 Variation of average heat transfer coefficient and average Nusselt number with Fourier number
 ($T_j = 313.15$ K, $b = 0.00125$ m, $H_n = 0.0055$ m, Silicon plate, sine base case, $q = 63$ kW/m², $W = 0.0017$ m)

The effect of the indentation depth is an important parameter for finding the effect of surface geometry on the heat transfer characteristics of the system. Figure 4.32 displays the maximum non-dimensional temperature for the interface and the solid for different indentation depths. It can be seen that increasing the depth of the indentation increases the maximum temperature present at both the interface and inside the material. This was the expected result as Lou et al. [16] had stated that the surface effects would trap fluid in any indentations present along the surface. It is again shown that the maximum to minimum temperature difference is nearly equal across all indentation depths. The effect of the increased indentation depths is again shown in Figure 4.33. The average heat-transfer coefficient and average Nusselt number decreases with time and is lowest for the largest indentation depth. This further reinforces the notion that the fluid trapped below the free stream decreases heat transfer for the system and this effect is magnified for larger indentation depths.

The effect of the different surface geometries for this case, described in Figure 3.33, is described by Figures 4.34-4.36. Figure 4.34 shows the maximum dimensionless temperature for the interface and the solid in case A. The increase in temperature with time remains consistent with the previous results from the base case. It is observed that the difference between the maximum and minimum interface temperature is more varied compared to the base case. The development of the average local heat-transfer coefficient and Nusselt number with time for various indentation depths in case A is shown in Figure 4.35. As expected, as the step depth increases the average local heat-transfer coefficient and Nusselt number decrease.

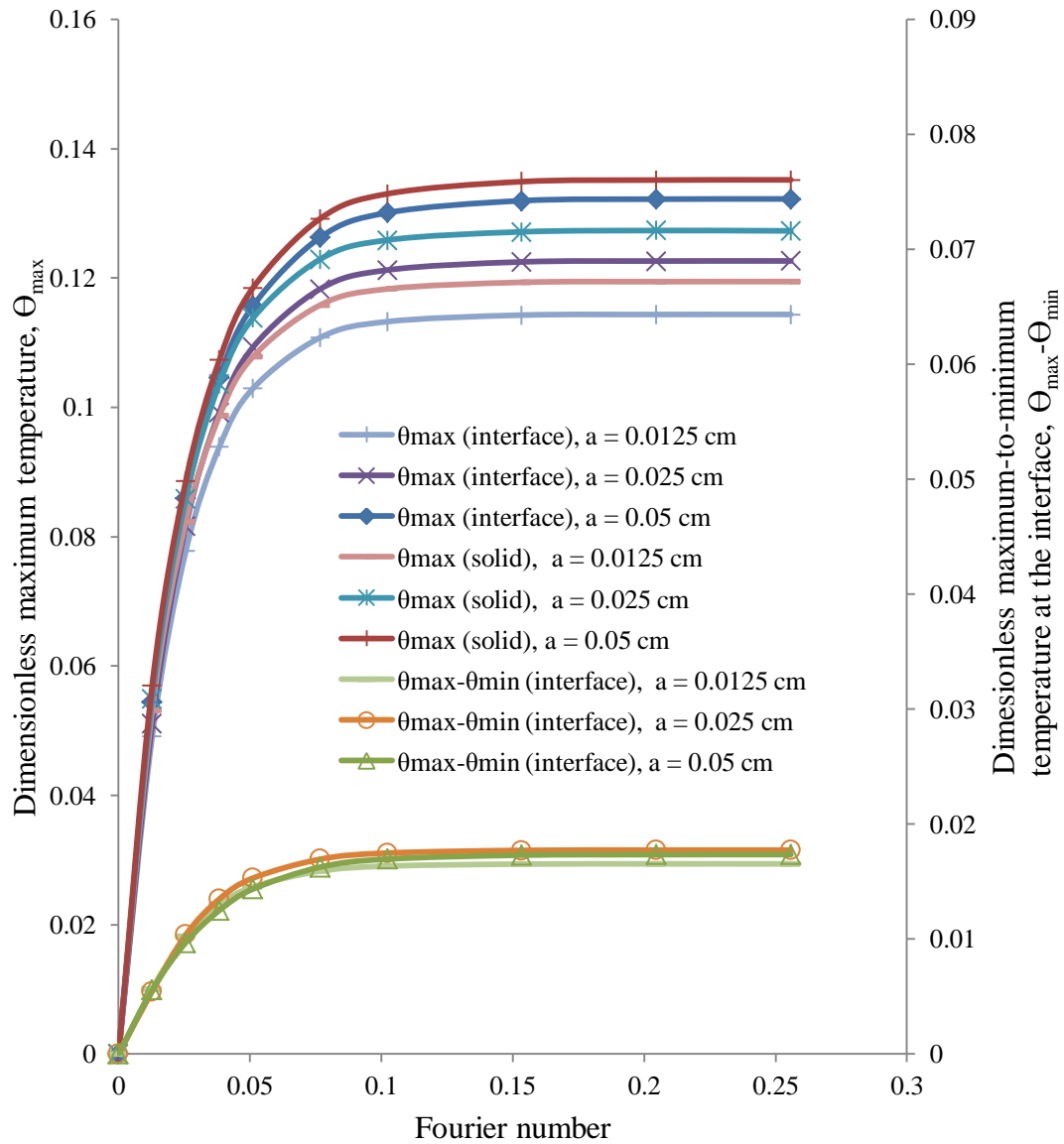


Figure 4.32 Variation in maximum non-dimensional temperature at the interface, maximum non-dimensional temperature within the solid, and the maximum-to-minimum non-dimensional temperature difference at the interface for different indentation depths ($Re = 750$, $T_j = 313.15$ K, $b = 0.00125$ m, $H_n = 0.0055$ m, Silicon plate, sine base case, $q = 63$ kW/m², $W = 0.0017$ m)

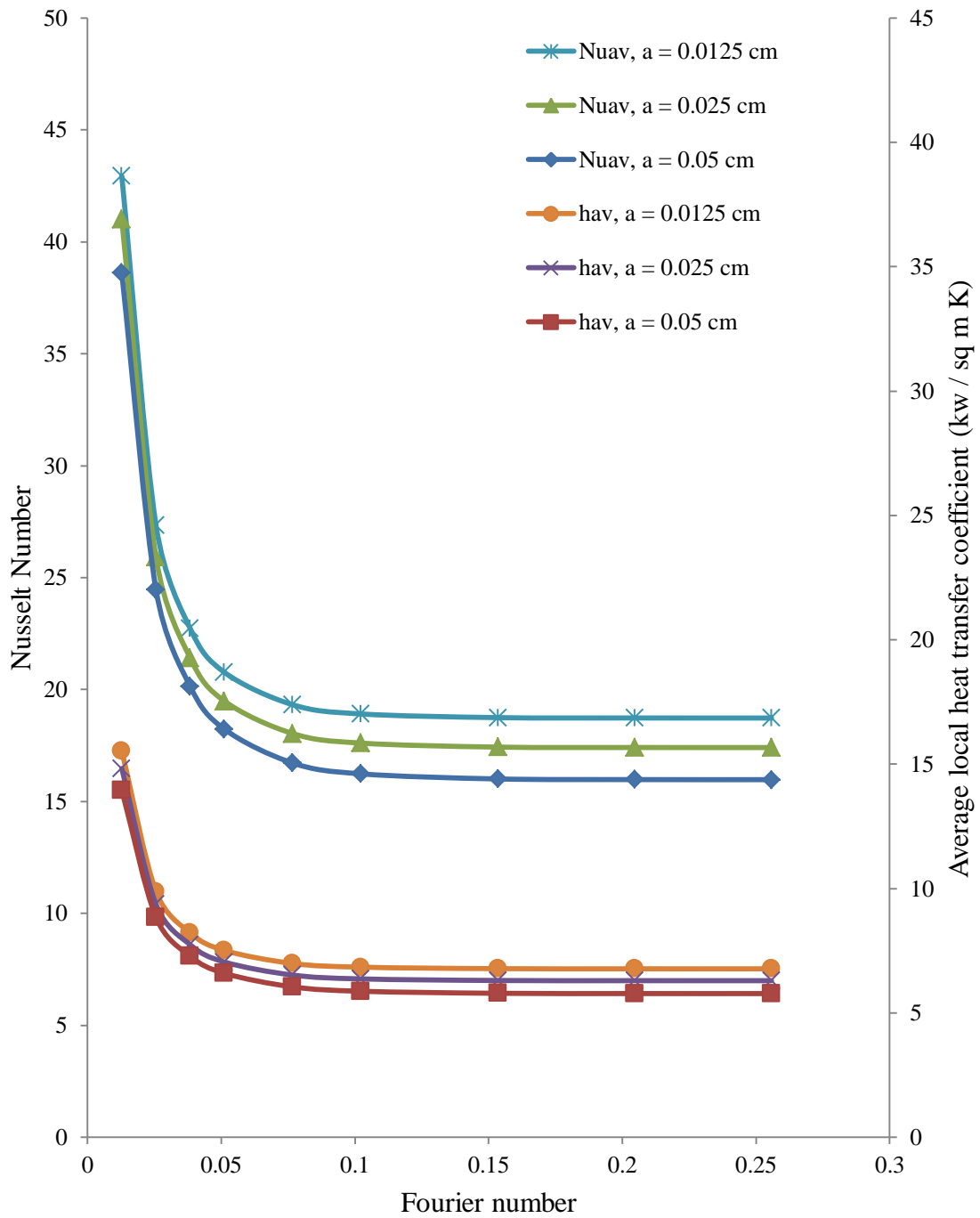


Figure 4.33 Variation of average heat transfer coefficient and average Nusselt number with Fourier number for different indentation depths ($T_j = 313.15$ K, $b = 0.00125$ m, $H_n = 0.0055$ m, Silicon plate, sine base case, $q = 63$ kW/m², $W = 0.0017$ m)

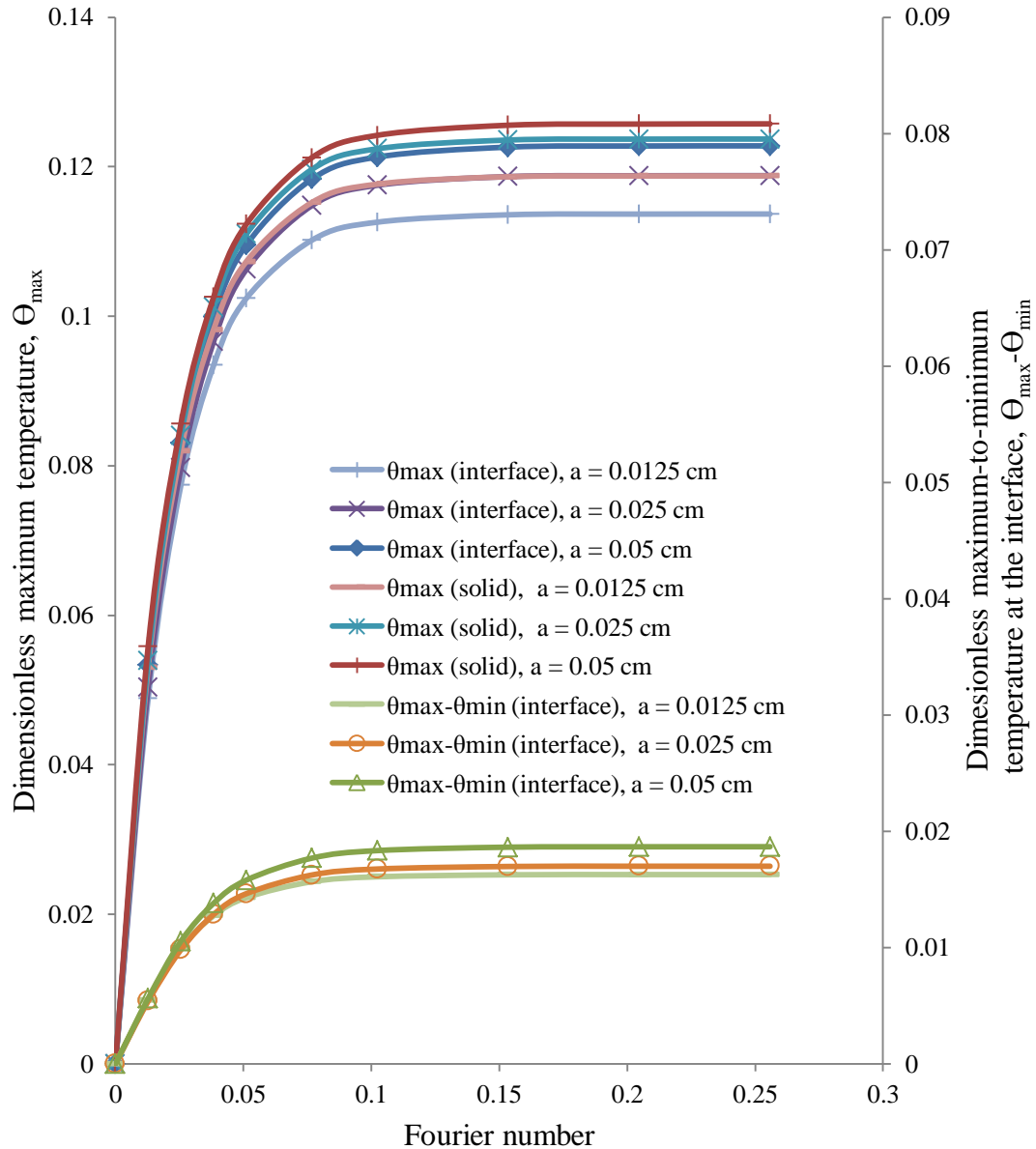


Figure 4.34 Variation in maximum non-dimensional temperature at the interface, maximum non-dimensional temperature within the solid, and the maximum-to-minimum non-dimensional temperature difference at the interface for different indentation depths (Re = 750, $T_j = 313.15$ K, $b = 0.00125$ m, $H_n = 0.0055$ m, Silicon plate, sine case A, $q = 63$ kW/m², $W = 0.0017$ m)

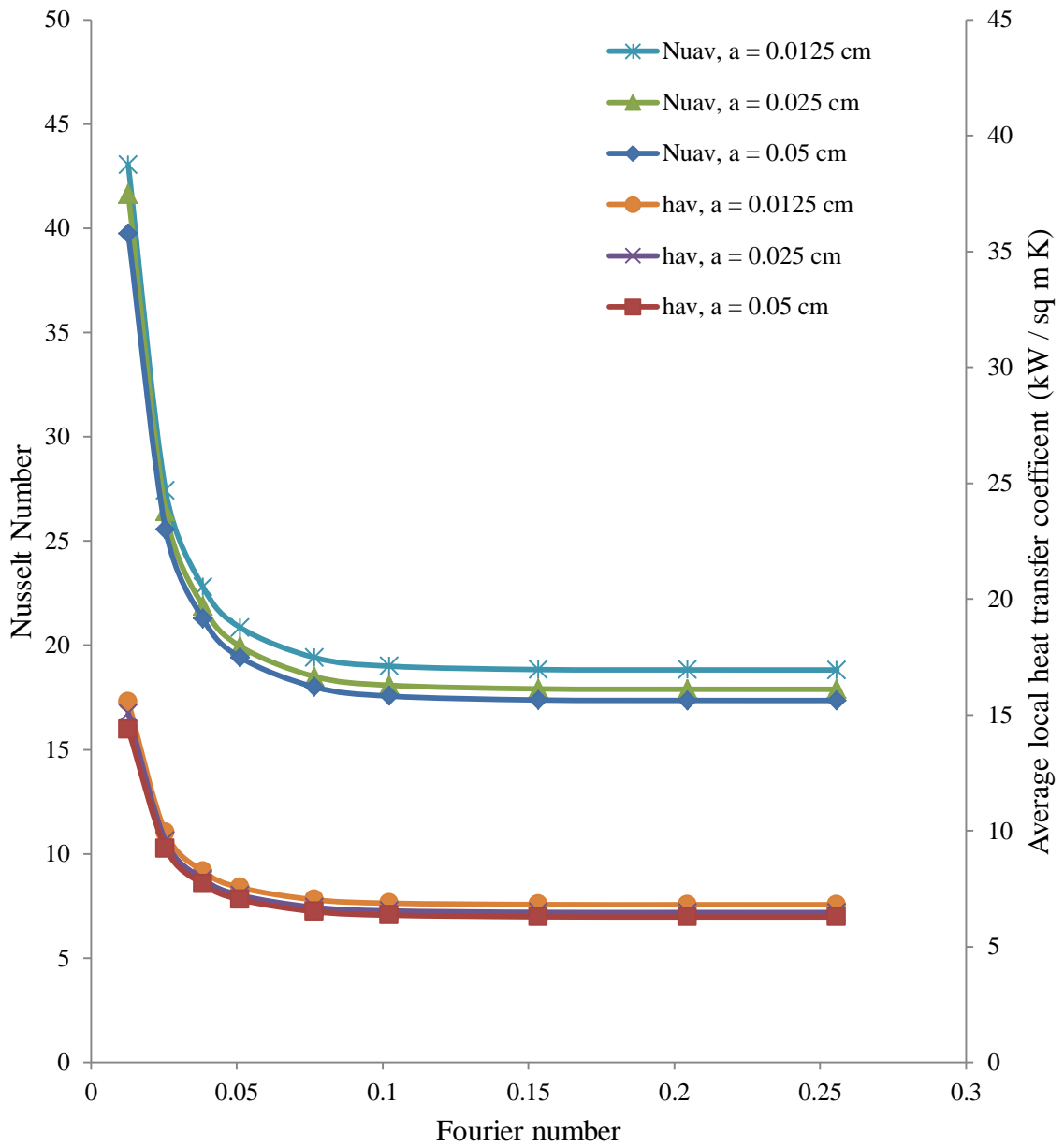


Figure 4.35 Variation of average heat transfer coefficient and average Nusselt number for different indentation depths ($T_j = 313.15 \text{ K}$, $b = 0.00125 \text{ m}$, $H_n = 0.0055 \text{ m}$, Silicon plate, sine case A, $q = 63 \text{ kW/m}^2$, $W = 0.0017 \text{ m}$)

The maximum dimensionless temperature at the interface and in the solid for varying step heights in case B is plotted in Figure 3.36. The time required for this configuration to reach steady state was considerably higher than the previous cases. This is especially true when $a = 0.0005 \text{ m}$ due to the semicircular pattern on the plate. As the fluid impacts the first semicircle shaped step near $\xi/L = 0.22$, it is forced over the surface geometry. This results in the fluid pushing upward, with the free stream essentially jumping over the indentation near $\xi/L = 0.73$. This behavior is not encountered with any of the other geometries. As a result of this, the maximum temperatures for both the interface and the solid when $a = 0.0005 \text{ m}$ are higher than the other two indentation depths explored. The lowest temperatures are present on the plate with the smallest indentation size. This was expected as the plate is nearly flat, with only extremely small areas for the fluid to become trapped. Figure 3.37 displays the development of the average heat-transfer coefficient and Nusselt number with time. As with the previous cases, the heat-transfer coefficient and Nusselt number decrease with time until reaching the steady state condition. The heat transfer values also decrease with increasing indentation size.

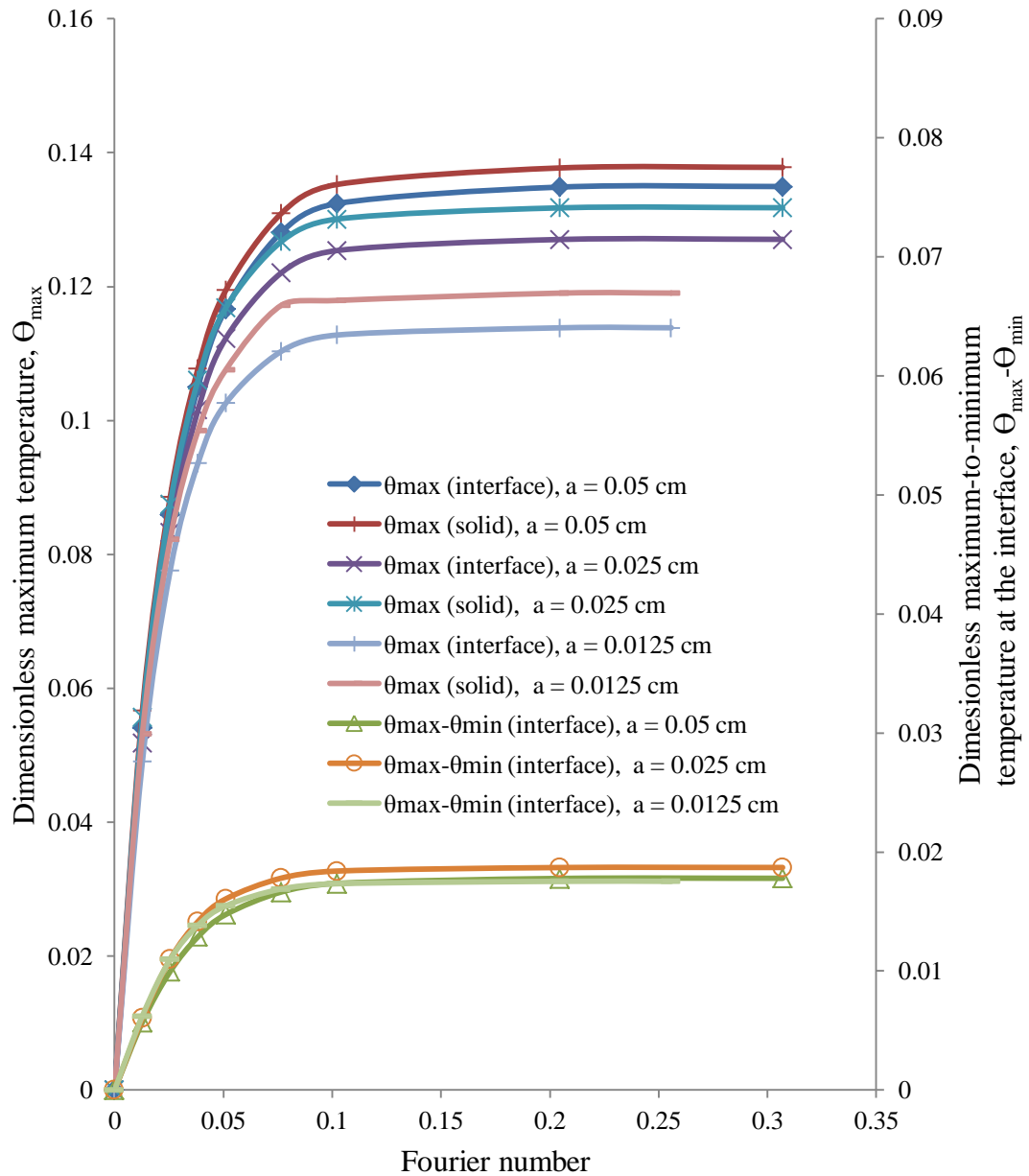


Figure 4.36 Variation in maximum non-dimensional temperature at the interface, maximum non-dimensional temperature within the solid, and the maximum-to-minimum non-dimensional temperature difference at the interface for different indentation depths (Re = 750, $T_j = 313.15$ K, $b = 0.00125$ m, $H_n = 0.0055$ m, Silicon plate, sine case B, $q = 63$ kW/m², $W = 0.0017$ m)

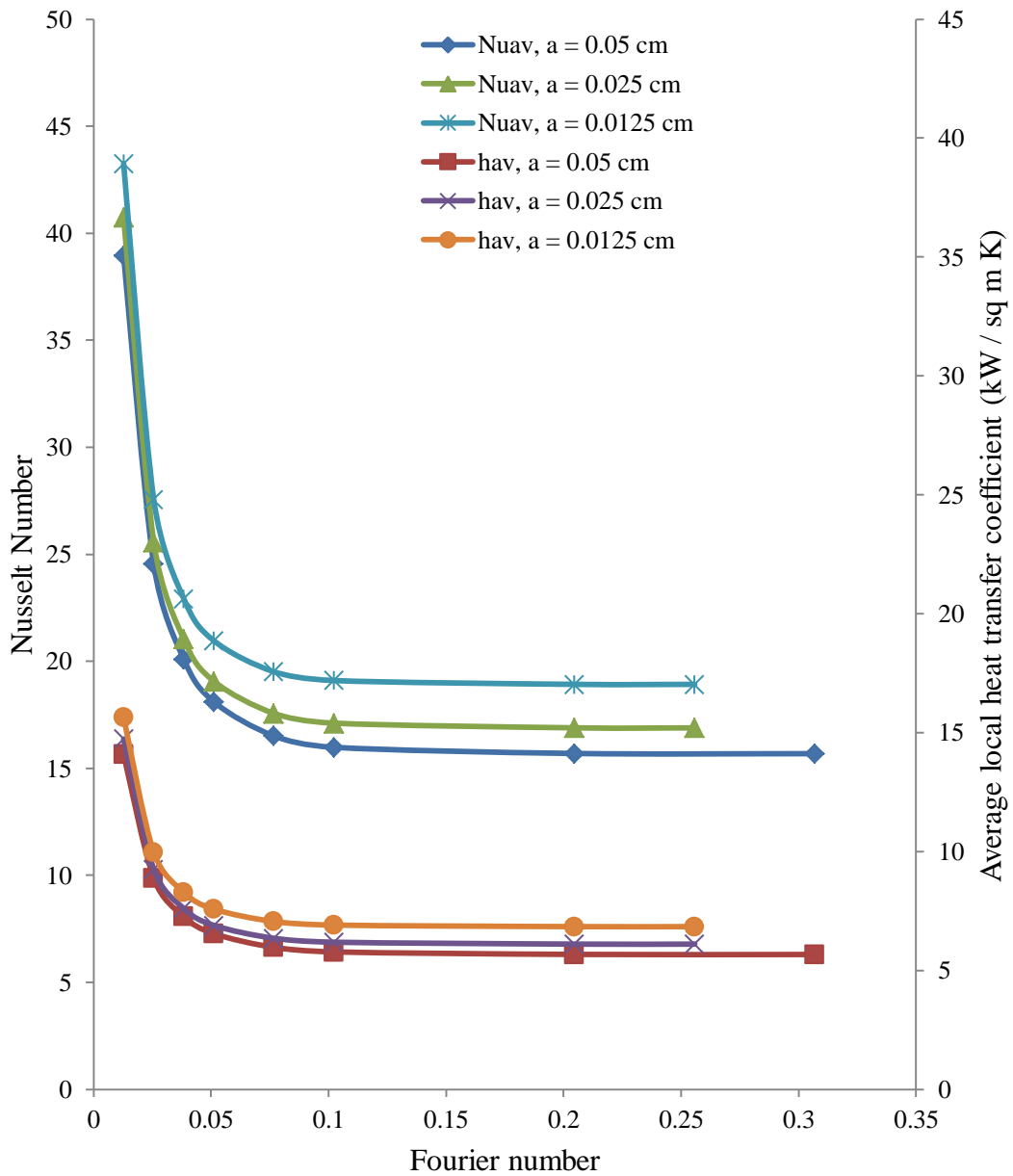


Figure 4.37 Variation of average heat transfer coefficient and average Nusselt number for different indentation depths ($T_j = 313.15$ K, $b = 0.00125$ m, $H_n = 0.0055$ m, Silicon plate, sine case B, $q = 63$ kW/m², $W = 0.0017$ m)

Chapter 5

Conclusions and Recommendations for Future Research

5.1 Steady State Conclusions

A numerical study was conducted to determine the effect of surface geometry on the heat transfer of a uniformly heated plate undergoing liquid-free jet impingement. The following conclusions have been made:

1. The Reynolds number of the jet has a large impact on the heat transfer the plate undergoes. Increasing the jet velocity results in an increase in local heat-transfer coefficient and an increase in local Nusselt number. For all cases, increasing jet velocity also decreased the maximum interface temperature and maximum solid temperature.
2. The fluid typically showed spikes in heat-transfer coefficient and Nusselt number when interacting with abrupt changes in geometry. This is caused by the disruption of any thermal boundary layer that has formed before the interaction.
3. While there were spikes in heat transfer values at geometry changes, there was a strong drop in these values when the fluid was forced to recirculate in the indentations between surface features. This was especially true of the rectangular and sinusoidal geometries.
4. For the rectangular and sinusoidal geometries, increasing the depth of the indentations had a negative effect on the heat-transfer coefficient and Nusselt

number. As the fluid enters these deeper steps it is forced to recirculate more slowly, thus allowing for less convective heat transfer.

5. In the case of the triangular ribs, increasing the indentation depth allows for a slight increase in heat-transfer coefficient. This effect is not unexpected as the taller thinner ribs act as fins, allowing for the heat from the plate to conduct upward through the ribs towards the cooler jet. The shape of the gaps between each rib also aids in fluid flow, allowing for slightly better recirculation.
6. Increasing the length of the rectangular step, as in case A, showed a considerable increase in heat-transfer coefficient and Nusselt number. The smaller channels clearly allow for better recirculation for this case.
7. Increasing the height of the geometric features in case B for the sinusoidal surface had the interesting effect of causing the free stream to essentially jump over the semicircular channel after the first step. The semicircular shape of the surface had this effect, causing the temperature at the center of the plate to be far higher than the other cases.
8. The inclusion of surface geometry has a negative impact on the Nusselt number for the triangular rib and sinusoidal wave patterned surfaces, whereas rectangular steps had either a neutral or a positive impact when compared to the flat plate. The only advantageous configuration was case A of the rectangular step.
8. The thermal conductivity of the material has a large impact on the temperature of the plate. But the thinness of the plate did not allow for thermal conductivity to play a large role in the isotherm distribution from material to material. Radial conduction was prevalent due to the thinness of the plate.

5.2 Transient Conclusions

1. The temperature of the fluid and the solid at the interface increase with time until the steady state condition is reached.
2. For the plate thickness selected the Reynolds number had very little impact on the time required for the system to reach steady state. All cases using silicon were within 0.5% of steady state in less than 15 seconds.
3. Selection of material played a much larger part in the time required to reach steady state. It was shown that the materials with the highest thermal diffusivity reached steady state first.
4. For all geometries, the average heat-transfer coefficient and Nusselt number decrease with time until the steady state is reached.
5. Increasing indentation depth leads to a higher temperature in the solid and at the interface for all cases except the triangular rib.

5.3 Recommendations for Future Research

While a large amount of data can be obtained from the present work, there are several areas of study that remain untouched. A more detailed study of the effect of plate thickness could lead to the best configuration for these different geometries. The use of other working fluids, such as lubricants and other coolants would be advised. A more thorough examination of the effect of turbulence within the system could also provide valuable information to the field.

List of References

- 1 M. B. Glauert, The Wall Jet, *Journal of Fluid Mechanics*, vol. 1, no. 6, pp. 625-643, 1956
- 2 S. Inada, Y. Miyasaka, and R. Izumi, A Study on the Laminar Flow Between a Two-dimensional Water Jet and a Flat Surface with Constant Heat Flux, *Bulletin of the JSME*, vol. 24, no. 196, pp. 1803-1810, 1981.
- 3 X. S. Wang, Z. Dagan, and L. M. Jiji, Conjugate Heat Transfer between a Laminar Impinging Liquid Jet and a Solid Disk, *International Journal of Heat and Mass Transfer*, vol. 32, no. 11, pp. 2189-2197, 1989.
- 4 D. T. Vader, F.P. Incropera, and R. Viskanta, Local Convective Heat Transfer from a Heated Surface to an Impinging, Planar Jet of Water, *International Journal of Heat and Mass Transfer*, vol. 34, no. 3, pp. 611-623, 1991.
- 5 B. W. Webb and C. Ma, *Advances in Heat Transfer*, Elsevier, pp. 105-217, 1995.
- 6 A. J. Bula, Numerical Modeling of Conjugate Heat Transfer During Impingement of Free Liquid Jet Issuing from a Slot Nozzle, *Numerical Heat Transfer, Part A: Applications*, vol. 38, no. 1, pp. 45-66, 2000.
- 7 F. Sarghini, and G. Ruocco, Enhancement and Reversal Heat Transfer by Competing Modes in Jet Impingement, *International Journal of Heat and Mass Transfer*, vol. 47, no. 8-9, pp. 1711-1718, 2004.
- 8 D. H. Lee, J. Song, and M. C. Jo, The Effects of Nozzle Diameter on Impinging Jet Heat Transfer and Fluid Flow, *Journal of Heat Transfer*, vol. 126, no. 4, pp. 554-557, 2004.
- 9 V. Narayanan, J. Seyed-Yagoobi, and R. H. Page, An Experimental Study of Fluid Mechanics and Heat Transfer in an Impinging Slot Jet Flow, *International Journal of Heat and Mass Transfer*, vol. 47, no. 8-9, pp. 1827-1845, 2004.
- 10 N. Gao, and D. Ewing, D., Investigation of the Effect of Confinement on the Heat Transfer to Round Impinging Jets Exiting a Long Pipe, *International Journal of Heat and Fluid Flow*, vol. 27, no. 1, pp. 33-41, 2004.

- 11 Y. C. Chen, C. F. Ma, and M. Qin, Theoretical Study on Impingement Heat Transfer with Single-Phase Free-Surface Slot Jets, *International Journal of Heat and Mass Transfer*, vol. 48. no. 16, pp. 3381-3386, 2005.
- 12 K. Ibuki, T. Umeda, and H. Fujimoto, Heat Transfer Characteristics of a Planar Water Jet Impinging Normally Or Obliquely on a Flat Surface at Relatively Low Reynolds Numbers, *Experimental Thermal and Fluid Science*, vol. 33, no. 8, pp. 1226-1234, 2009.
- 13 N. Zuckerman, and N. Lior, Jet Impingement Heat Transfer: Physics, Correlations, and Numerical Modeling, *Advances in Heat Transfer*, vol. 39, pp. 565-631, 2006.
- 14 C. Gau, and I. C. Lee, Flow and Impingement Cooling Heat Transfer Along Triangular Rib-Roughened Walls, *International Journal of Heat and Mass Transfer*, vol. 43, no. 24, pp. 4405-4418, 2000.
- 15 S. V. Ekkad and D. Kontrovitz, Jet Impingement Heat Transfer on Dimpled Target Surfaces, *International Journal of Heat and Fluid Flow*, vol. 23, no. 1, pp. 22-28, 2000.
- 16 Z. W. Lou, A. S. Mujumdar, and C. Yap, Effects of Geometric Parameters on Confined Impinging Jet Heat Transfer, *Applied Thermal Engineering*, vol. 25, no. 17-18, pp. 2687-2697, 2005.
- 17 Y. Xing, S. Spring, and B. Weigand, Experimental and Numerical Investigation of Impingement Heat Transfer on a Flat and Micro-Rib Roughened Plate with Different Crossflow Schemes, *International Journal of Thermal Sciences*, vol. 50, no. 7, pp. 1293-1307, 2011.
- 18 S. Kumagai, S. Suzuki, R. Kubo, and M. Kawazoe, Transient Cooling of a Hot Metal Plate With an Impinging Water Jet, *Heat Transfer–Japanese Research*, vol.24, no.6, pp.538–550, 1995.
- 19 H. Fujimoto, H. Takuda, N. Hatta, and R. Viskanta, Numerical Simulation of Transient Cooling of a Hot Solid by an Impinging Free Surface Jet, *Numerical Heat Transfer, Part A*, vol.36, no.8, pp.767–780, 1999.
- 20 N. Saniei and X. Yan, Experimental study of heat transfer from a disk rotating in an infinite environment including heat transfer enhancement by jet impingement cooling, *Journal of Enhanced Heat Transfer*, vol. 7, no. 4, pp. 231-245, 2000.
- 21 S. Hsieh, H. Tsai, and S. Chan, Local heat transfer in rotation square-rib-roughened and south channels with jet impingement, *International Journal of Heat and Mass Transfer*, vol. 47, no. 12-13, pp. 2769-2784, 2004.

- 22 M.M. Rahman, A.J. Bula, Analysis of transient conjugate heat transfer to a free impinging jet, *Journal of Thermophysics and Heat Transfer*, vol. 14, no. 2, pp. 1-10, 2004.
- 23 F. Sarghini and G. Ruocco, Enhancement and reversal heat transfer by competing modes in jet impingement, *International Journal of Heat and Mass Transfer*, vol. 47, no 8-9, pp. 1711-1718, 2004.
- 24 W. M. Yan, H. C. Liu, C. Y. Soong, and W. J. Wang, Experimental study of impinging heat transfer along rib-roughened walls by using transient liquid crystal technique, *International Journal of Heat and Mass Transfer*, vol. 48, no. 12, pp. 2420-2428, 2005.
- 25 T. Lin, M. Wu, L. Liu, C. Fang, and Y. Hung, Cooling performance of using a confined slot impinging onto heated heat sinks, *Journal of Electronic Packaging*, vol. 128, no. 1, pp. 82-91, 2006.
- 26 J. C. Lallave and M. M. Rahman, Transient Thermal Transport on a Rotating Disk Under Partially Confined Laminar Liquid Jet Impingement, *Journal of Heat Transfer*, vol. 132, no. 5, pp. 2201-2209.
- 27 F.M. White, Fluid mechanics, fifth ed., McGraw-Hill, New York, USA, 2003.
- 28 A. Bejan, Convection heat transfer, second ed., John Wiley & Sons, New York, USA, 1995
- 29 M.N. Özisik, Heat conduction, second ed., John Wiley & Sons, New York, USA, 1993.
- 30 R. Tillner-Roth and H. D. Baehr, An international standard formulation of the thermodynamic properties of 1,1,1,2-tetrafluoroethane (HFC-134a) covering temperatures from 170 K to 455 K at pressures up to 70 MPa, *J. Phys. Chem. Ref. Data*, , vol. 23, pp. 657-729, 1994.

Appendices

Appendix A: Rectangular Ridge FIDAP Code

//This is the FIDAP code for the base rectangular step case

```
Title( )
Step Plate
Fi-Gen(Elem = 1, POIN = 1, CURV = 1, SURF = 1, NODE = 0, MEDG= 1, MLOO = 1,
MFAC = 1, BEDG = 1, SPAV = 1, MSHE = 1, MSOL = 1, COOR = 1, TOLE =
0.0000001)
```

```
//Specifications
//Plate Thickness
$PlateT = 0.125
//Plate Length
$PlateL = 0.6475
//Nozzle width
$NozzleW = 0.085
//Nozzle height
$NozzleH = 0.55
//Length of step
$a = 0.1177273
//Length of gap
$b = 0.1177273
//Depth of step
$Step = 0.025
```

```
//Creating basic geometry
//Points 1-8
POINT( ADD, COOR )
0 0
-$NozzleH 0
-$NozzleH $NozzleW
-0.25 0.20
-0.15 $PlateL
0 $PlateL
$PlateT $PlateL
$PlateT 0
```

```
//Lines 1-9
POINT( SELE, ID)
1
2
CURVE( ADD, LINE)
```

Appendix A (continued)

POINT(SELE, ID)

2

3

CURVE(ADD, LINE)

POINT(SELE, ID)

3

4

CURVE(ADD,LINE)

POINT(SELE, ID)

4

5

CURVE(ADD,LINE)

POINT(SELE, ID)

5

6

CURVE(ADD,LINE)

POINT(SELE, ID)

6

7

CURVE(ADD,LINE)

POINT(SELE, ID)

7

8

CURVE(ADD,LINE)

POINT(SELE, ID)

8

1

CURVE(ADD,LINE)

CURVE(SELE, ID)

3

4

CURVE(ADD, FILL, RADI=0.2)

//Interface Geometry

//Points 9-19

POINT(ADD, COOR)

\$Step 0

Appendix A (continued)

\$Step 0.0588637
0 0.0588637
0 0.176591
\$Step 0.176591
\$Step 0.2943183
0 0.2943183
0 0.4120456
\$Step 0.4120456
\$Step 0.5297729
0 0.5297729

POINT(SELE,ID)
11
12
CURVE(ADD,LINE)

POINT(SELE,ID)
12
13
CURVE(ADD,LINE)

POINT(SELE,ID)
13
14
CURVE(ADD,LINE)

POINT(SELE,ID)
14
15
CURVE(ADD,LINE)

POINT(SELE,ID)
15
16
CURVE(ADD,LINE)

POINT(SELE,ID)
16
17
CURVE(ADD,LINE)

POINT(SELE,ID)
17
18

Appendix A (continued)

CURVE(ADD,LINE)

POINT(SELE,ID)

18

19

CURVE(ADD,LINE)

POINT(SELE,ID)

19

20

CURVE(ADD,LINE)

POINT(SELE,ID)

20

21

CURVE(ADD,LINE)

POINT(SELE,ID)

21

6

CURVE(ADD,LINE)

POINT(ADD, COOR)

-0.183411 0.536687

-0.218556 0.420121

-0.350197 0.000000

\$step \$PlateL

\$PlateT 0.058864

0 \$NozzleW

-0.315307 0.179040

\$Step \$NozzleW

\$PlateT \$NozzleW

\$PlateT 0.176591

POINT(SELE,ID)

1

13

CURVE(ADD, LINE)

POINT(SELE,ID)

14

17

CURVE(ADD, LINE)

Appendix A (continued)

POINT(SELE, ID)

18

21

CURVE(ADD, LINE)

POINT(SELE, ID)

12

15

CURVE(ADD, LINE)

POINT(SELE, ID)

16

19

CURVE(ADD, LINE)

POINT(SELE, ID)

20

25

CURVE(ADD, LINE)

CURVE(SELE, ID=9)

POINT(SELE, ID=28)

CURVE(SPLIT)

CURVE(SELE, ID=4)

POINT(SELE, ID=23)

CURVE(SPLIT)

CURVE(SELE, ID=30)

POINT(SELE, ID=22)

CURVE(SPLIT)

CURVE(SELE, ID=8)

POINT(SELE, ID=11)

CURVE(SPLIT)

CURVE(SELE, ID=6)

POINT(SELE, ID=25)

CURVE(SPLIT)

CURVE(SELE, ID=7)

POINT(SELE, ID=26)

CURVE(SPLIT)

Appendix A (continued)

CURVE(SELE, ID=12)
POINT(SELE, ID=27)
CURVE(SPLIT)

CURVE(SELE, ID)
3
27
CURVE(JOIN)

CURVE(SELE, ID=24)
POINT(SELE, ID=29)
CURVE(SPLIT)

CURVE(SELE, ID=37)
POINT(SELE, ID=30)
CURVE(SPLIT)

CURVE(SELE, ID=44)
POINT(SELE, ID=31)
CURVE(SPLIT)

//surface
POINT(ADD,COOR)
-\$NozzleH \$PlateL
POINT(SELE,ID)
32
7
2
8
SURFACE(ADD,POINTS, ROWW=2, NOAD)

//mesh edges
CURVE(SELE,ID)
32
20
26
31
23
18
29
16
25
28
22

Appendix A (continued)

14

MEDGE(ADD, SUCC, INTE=23, RATI=0, 2RAT=0, PCEN=0)

CURVE(SELE, ID)

43

MEDGE(ADD, SUCC, INTE=17, RATI=0, 2RAT=0, PCEN=0)

CURVE(SELE, ID)

2

MEDGE(ADD, SUCC, INTE=18, RATI=0, 2RAT=0, PCEN=0)

CURVE(SELE, ID)

1

MEDGE(ADD, FRSTLAST, INTE=30, RATI=0.4, 2RAT=0, PCEN=0)

CURVE(SELE, ID)

5

MEDGE(ADD, LSTFIRST, INTE=30, RATI=0.8, 2RAT=0, PCEN=0)

CURVE(SELE, ID)

41

40

MEDGE(ADD, SUCC, INTE=17, RATI=0, 2RAT=0, PCEN=0)

CURVE(SELE, ID)

10

21

38

MEDGE(ADD, SUCC, INTE=12, RATI=0, 2RAT=0, PCEN=0)

CURVE(SELE, ID)

34

11

13

15

17

19

35

MEDGE(ADD, SUCC, INTE=15, RATI=0, 2RAT=0, PCEN=0)

CURVE(SELE, ID)

36

33

Appendix A (continued)

MEDGE(ADD, SUCC, INTE=25, RATI=0, 2RAT=0, PCEN=0)

CURVE(SELE,ID)

46

MEDGE(ADD, SUCC, INTE=92, RATI=0, 2RAT=0, PCEN=0)

CURVE(SELE,ID)

39

42

45

MEDGE(ADD, SUCC, INTE=6, RATI=0, 2RAT=0, PCEN=0)

CURVE(SELE,ID)

47

MEDGE(ADD, SUCC, INTE=17, RATI=0, 2RAT=0, PCEN=0)

//mesh loops

CURVE(SELE,ID)

1

21

39

40

22

16

23

20

5

32

31

29

28

41

2

MLOOP(ADD, MAP, VISI, NOSH, EDG1=1, EDG2=7, EDG3=1, EDG4=6)

CURVE(SELE,ID)

34

10

11

21

MLOOP(ADD, MAP, VISI, NOSH, EDG1=1, EDG2=1, EDG3=1, EDG4=1)

Appendix A (continued)

CURVE(SELE,ID)

11

42

43

13

40

39

MLOOP(ADD, MAP, VISI, NOSH, EDG1=1, EDG2=2, EDG3=1, EDG4=2)

CURVE(SELE,ID)

13

14

15

22

MLOOP(ADD, MAP, VISI, NOSH, EDG1=1, EDG2=1, EDG3=1, EDG4=1)

CURVE(SELE,ID)

15

25

17

16

MLOOP(ADD, MAP, VISI, NOSH, EDG1=1, EDG2=1, EDG3=1, EDG4=1)

CURVE(SELE,ID)

17

18

19

23

MLOOP(ADD, MAP, VISI, NOSH, EDG1=1, EDG2=1, EDG3=1, EDG4=1)

CURVE(SELE,ID)

19

26

35

20

MLOOP(ADD, MAP, VISI, NOSH, EDG1=1, EDG2=1, EDG3=1, EDG4=1)

CURVE(SELE,ID)

33

38

45

47

46

36

Appendix A (continued)

26

18

25

14

43

42

10

MLOOP(ADD, MAP, VISI, NOSH, EDG1=1, EDG2=4, EDG3=1, EDG4=7)

//mesh faces

SURFACE(SELE,ID=1)

MLOOP(SELE,ID=1)

MFACE(ADD)

SURFACE(SELE,ID=1)

MLOOP(SELE,ID=2)

MFACE(ADD)

SURFACE(SELE,ID=1)

MLOOP(SELE,ID=3)

MFACE(ADD)

SURFACE(SELE,ID=1)

MLOOP(SELE,ID=4)

MFACE(ADD)

SURFACE(SELE,ID=1)

MLOOP(SELE,ID=5)

MFACE(ADD)

SURFACE(SELE,ID=1)

MLOOP(SELE,ID=6)

MFACE(ADD)

SURFACE(SELE,ID=1)

MLOOP(SELE,ID=7)

MFACE(ADD)

SURFACE(SELE,ID=1)

MLOOP(SELE,ID=8)

MFACE(ADD)

//meshing

MFACE(SELE,ID)

Appendix A (continued)

1
2
4
6
ELEMENT(SETD, QUAD, NODE=4)
MFACE(MESH, MAP, ENTI="fluid")

MFACE(SELE, ID)
3
5
7
8
ELEMENT(SETD, QUAD, NODE=4)
MFACE(MESH, MAP, ENTI="solid")

ELEMENT(SETD, EDGE, NODE=2)
MEDGE(SELE, ID)
14
MEDGE(MESH, MAP, ENTI="inlet")

MEDGE(SELE, ID)
16
MEDGE(MESH, MAP, ENTI="outlet")

MEDGE(SELE, ID)
15
22
MEDGE(MESH, MAP, ENTI="axis")

MEDGE(SELE, ID)
17
10
7
4
1
MEDGE(MESH, MAP, ENTI="freesurf")

MEDGE(SELE, ID)
19
23
32
18
24

Appendix A (continued)

```
12
8
25
26
6
27
2
MEDGE(MESH,MAP,ENTI="interface")

MEDGE(SELE,ID)
29
28
MEDGE(MESH,MAP,ENTI="edge")

MEDGE(SELE,ID)
31
21
35
34
MEDGE(MESH,MAP,ENTI="bottom")

MEDGE(SELE,ID)
30
MEDGE(MESH,MAP,ENTI="axiss")

END( )
FIPREP( )

//To change the fluid or plate material change the following fields
//PROPERTIES
DENSITY( ADD, SET = "water", CONS = 0.992 )
CONDUCTIVITY( ADD, SET = "water", CONS = 0.0014699 )
VISCOSITY( ADD, SET = "water", CONS = 0.00657 )
SPECIFICHEAT( ADD, SET = "water", CONS = 0.998137 )
SURFACETENSION( ADD, SET = "water", CONS = 68 )

DENSITY( ADD, SET = "silicon", CONS = 2.33 )
CONDUCTIVITY( ADD, SET = "silicon", CONS = 0.334608 )
SPECIFICHEAT( ADD, SET = "silicon", CONS = 0.17006 )

//ENTITIES
ENTITY(ADD, NAME="fluid", FLUI, PROP="water")
ENTITY( ADD, NAME = "solid", SOLI, PROP = "silicon" )
ENTITY(ADD, NAME="outlet", PLOT)
```

Appendix A (continued)

```
ENTITY(ADD, NAME="inlet", PLOT)
ENTITY(ADD, NAME="axis", PLOT)
ENTITY(ADD, NAME="freesurf", SURF, DEPT = 31, SPIN, STRA, ANG1=10,
ANG2=180)
ENTITY(ADD, NAME="axiss", PLOT)
ENTITY(ADD, NAME="edge", PLOT)
ENTITY(ADD, NAME="bottom", PLOT)
ENTITY( ADD, NAME = "interface", PLOT, ATTA = "solid", NATT = "fluid" )
BODYFORCE(ADD, CONS, FX=981, FY=0, FZ=0)
PRESSURE(ADD, MIXE=1.0E-11, DISC)

OPTIONS(ADD, UPWINDING)
UPWINDING(ADD, STRE)
RELAXATION( )
    0.3, 0.3, 0.3, 0, 0.5, 0.25

//BC
BCNODE(ADD, COOR, NODE=298)
BCNODE(ADD, SURF, NODE=298, ZERO)
BCNODE(ADD, VELO, NODE=298, ZERO)
BCNODE(ADD, UT, NODE=298, ZERO)
BCNODE(ADD, UZC, ENTI="inlet", CONS=29.05)
BCNODE(ADD, URC, ENTI="inlet", ZERO)
BCNODE(ADD, URC, ENTI="axis", ZERO)
BCNODE(ADD, VELO, ENTI="interface", ZERO)
BCNODE(ADD, VELO, ENTI="bottom", ZERO)
BCNODE(ADD, VELO, ENTI="edge", ZERO)
BCNODE(ADD, VELO, ENTI="axiss", ZERO)
BCNODE( ADD, VELO, ENTI = "solid", ZERO )
BCNODE( ADD, TEMP, ENTI = "inlet", CONS = 40 )
/BCNODE( ADD, TEMP, ENTI = "bottom", CONS = 100 )
BCFLUX( ADD, HEAT, ENTI = "bottom", CONS = 1.5 )
PROBLEM( ADD, AXI-, INCOMP, TRAN, LAMI, NONL, NEWT, MOME, ENERGY,
FREE, SING )
SOLUTION( ADD, N.R. = 50, KINE = 25, VELC = 1e-4, RESC = 1e-4, SURF = 1e-3 )
TIMEINTEGRATION( ADD, BACK, NSTE = 501, TSTA = 0, DT = 0.0001, VARI,
WIND = 9, NOFI = 12 )
POSTPROCESS( NBLO = 2 )
    1, 101, 1
    101, 501, 2
CLIPPING( ADD, MINI )
    0, 0, 0, 0, 40, 0
ICNODE( ADD, URC, ENTI = "fluid", CONS = 29.05 )
EXECUTION(ADD, NEWJ)
```

Appendix A (continued)

PRINTOUT(ADD, NONE, BOUN)
DATAPRINT(ADD, CONT)

END()

CREATE(FISO)

RUN(FISOLV, BACK, AT="", TIME="NOW", COMP)

Appendix B: Triangular Rib FIDAP Code

```
Title( )
Rib plate 60 angle 0.0125 step
Fi-Gen(Elem = 1, POIN = 1, CURV = 1, SURF = 1, NODE = 0, MEDG= 1, MLOO = 1,
MFAC = 1, BEDG = 1, SPAV = 1, MSHE = 1, MSOL = 1, COOR = 1, TOLE = 0.00)

//Specifications
//Plate Thickness
$PlateT = 0.125
//Plate Length
$PlateL = 0.6475
//Nozzle width
$NozzleW = 0.085
//Nozzle height
$NozzleH = 0.55
//Length of step
$a = 0.1177273
//Length of gap
$b = 0.1177273
//Depth of step
$Step = 0.025
//double step
$Step2 = 0.050

//Creating basic geometry
//Points 1-8
POINT( ADD, COOR )
0 0
-$NozzleH 0
-$NozzleH $NozzleW
-0.18 0.17
-0.15 $PlateL
0 $PlateL
$PlateT $PlateL
$PlateT 0

//Lines 1-9
POINT( SELE, ID)
1
2
CURVE( ADD, LINE)

POINT( SELE, ID )
2
```

Appendix B (continued)

3

CURVE(ADD, LINE)

POINT(SELE, ID)

3

4

CURVE(ADD,LINE)

POINT(SELE, ID)

4

5

CURVE(ADD,LINE)

POINT(SELE, ID)

5

6

CURVE(ADD,LINE)

POINT(SELE, ID)

6

7

CURVE(ADD,LINE)

POINT(SELE, ID)

7

8

CURVE(ADD,LINE)

POINT(SELE, ID)

8

1

CURVE(ADD,LINE)

CURVE(SELE, ID)

3

4

CURVE(ADD, FILL, RADI=0.205)

POINT(ADD, COOR)

0 0.04625

0 0.13875

0 0.23125

Appendix B (continued)

0 0.32375
0 0.41625
0 0.50875
0 0.60125
\$Step 0.031815
\$Step 0.060685
\$Step 0.124315
\$Step 0.153185
\$Step 0.216815
\$Step 0.245685
\$Step 0.309315
\$Step 0.338185
\$Step 0.401815
\$Step 0.430685
\$Step 0.494315
\$Step 0.523185
\$Step 0.586815
\$Step 0.615685
\$Step2 0.04625
\$Step2 0.13875
\$Step2 0.23125
\$Step2 0.32375
\$Step2 0.41625
\$Step2 0.50875
\$Step2 0.60125
\$Step 0
\$Step \$PlateL
\$Step2 0
\$Step2 \$PlateL
-0.153297 0.60125
-0.158803 0.50875
-0.164769 0.41625
0 \$NozzleW
\$Step2 \$NozzleW
\$PlateT \$NozzleW
\$PlateT 0.04625
\$PlateT 0.13875
-\$NozzleH \$PlateL
-\$NozzleH 0.04625

POINT(SELE,ID)
1
11
12

Appendix B (continued)

13
14
15
16
17
6
CURVE(ADD,LINE)

POINT(SELE,ID)
41
32
33
34
35
36
37
38
42
CURVE(ADD,LINE)

POINT(SELE,ID)
39
18
CURVE(ADD,LINE)

POINT(SELE,ID)
19
20
CURVE(ADD,LINE)

POINT(SELE,ID)
21
22
CURVE(ADD,LINE)

POINT(SELE,ID)
23
24
CURVE(ADD,LINE)

POINT(SELE,ID)
25
26
CURVE(ADD,LINE)

Appendix B (continued)

POINT(SELE,ID)

27

28

CURVE(ADD,LINE)

POINT(SELE,ID)

29

30

CURVE(ADD,LINE)

POINT(SELE,ID)

31

40

CURVE(ADD,LINE)

POINT(SELE,ID)

1

39

41

CURVE(ADD,LINE)

POINT(SELE,ID)

6

40

42

CURVE(ADD,LINE)

POINT(SELE,ID)

18

11

19

32

18

CURVE(ADD,LINE)

POINT(SELE,ID)

20

12

21

33

20

CURVE(ADD,LINE)

POINT(SELE,ID)

Appendix B (continued)

22
13
23
34
22
CURVE(ADD,LINE)

POINT(SELE,ID)
24
14
25
35
24
CURVE(ADD,LINE)

POINT(SELE,ID)
26
15
27
36
26
CURVE(ADD,LINE)

POINT(SELE,ID)
28
16
29
37
28
CURVE(ADD,LINE)

POINT(SELE,ID)
30
17
31
38
30
CURVE(ADD,LINE)

CURVE(SELE,ID)
6
8
CURVE(DELETE)

Appendix B (continued)

POINT(SELE,ID)

41

8

CURVE(ADD,LINE)

POINT(SELE,ID)

42

7

CURVE(ADD,LINE)

CURVE(SELE,ID=4)

POINT(SELE,ID=45)

CURVE(SPLIT)

CURVE(SELE,ID=69)

POINT(SELE,ID=44)

CURVE(SPLIT)

CURVE(SELE,ID=71)

POINT(SELE,ID=43)

CURVE(SPLIT)

CURVE(SELE,ID=11)

POINT(SELE,ID=46)

CURVE(SPLIT)

CURVE(SELE,ID=19)

POINT(SELE,ID=47)

CURVE(SPLIT)

CURVE(SELE,ID=7)

POINT(SELE,ID=48)

CURVE(SPLIT)

CURVE(SELE,ID=79)

POINT(SELE,ID=49)

CURVE(SPLIT)

CURVE(SELE,ID=78)

POINT(SELE,ID=50)

CURVE(SPLIT)

CURVE(SELE,ID=2)

POINT(SELE,ID=52)

Appendix B (continued)

CURVE(SPLIT)

//Surface

POINT(SELE,ID)

51

7

2

8

SURFACE(ADD,POINTS, ROWW=2, NOAD)

//Medges

//AXIS

CURVE(SELE,ID)

1

MEDGE(ADD, FRSTLAST, INTE=20, RATI=0.4, 2RAT=0, PCEN=0)

//OUTLET

CURVE(SELE,ID)

5

MEDGE(ADD, LSTFIRST, INTE=20, RATI=0.7, 2RAT=0, PCEN=0)

//INLET1

CURVE(SELE,ID)

84

MEDGE(ADD, SUCC, INTE=8, RATI=0, 2RAT=0, PCEN=0)

//MIDDLE SQUARES

CURVE(SELE,ID)

34

35

38

39

40

41

42

43

44

45

46

47

48

49

50

Appendix B (continued)

51
52
53
54
55
56
57
58
59
60
61
62
63
64
65
36
37
MEDGE(ADD, SUCC, INTE=12, RATI=0, 2RAT=0, PCEN=0)

//TRAP BASES
CURVE(SELE,ID)
12
13
14
15
16
20
21
22
23
24
27
28
29
30
31
32
MEDGE(ADD, SUCC, INTE=16, RATI=0, 2RAT=0, PCEN=0)

//HALF TRAPS
CURVE(SELE,ID)
10
18
26

Appendix B (continued)

```
17
25
33
MEDGE(ADD, SUCC, INTE=8, RATI=0, 2RAT=0, PCEN=0)

//REST OF INTERFACE
CURVE(SELE,ID)
74
76
80
MEDGE(ADD, SUCC, INTE=7, RATI=0, 2RAT=0, PCEN=0)

CURVE(SELE,ID)
75
77
83
MEDGE(ADD, SUCC, INTE=9, RATI=0, 2RAT=0, PCEN=0)

//BOTTOM
CURVE(SELE,ID)
82
MEDGE(ADD, SUCC, INTE=88, RATI=0, 2RAT=0, PCEN=0)

CURVE(SELE,ID)
81
MEDGE(ADD, SUCC, INTE=8, RATI=0, 2RAT=0, PCEN=0)

//FREESURFACE
CURVE(SELE,ID)
73
MEDGE(ADD, SUCC, INTE=9, RATI=0, 2RAT=0, PCEN=0)

CURVE(SELE,ID)
68
70
72
MEDGE(ADD, SUCC, INTE=16, RATI=0, 2RAT=0, PCEN=0)

CURVE(SELE,ID)
9
MEDGE(ADD, LSTFIRST, INTE=32, RATI=0.4, 2RAT=0, PCEN=0)

CURVE(SELE,ID)
```


Appendix B (continued)

```
3
MEDGE(ADD, SUCC, INTE=8, RATI=0, 2RAT=0, PCEN=0)

//SIDES
CURVE(SELE,ID)
66
67
MEDGE(ADD, SUCC, INTE=20, RATI=0, 2RAT=0, PCEN=0)

//INLET2
CURVE(SELE,ID)
85
MEDGE(ADD, SUCC, INTE=7, RATI=0, 2RAT=0, PCEN=0)

//Mesh loops
//Liquid
CURVE(SELE,ID)
1
10
74
75
12
13
14
15
16
17
5
73
72
70
68
9
3
85
84
MLOOP(ADD, MAP, VISI, NOSH, EDG1=1, EDG2=9, EDG3=1, EDG4=8)

CURVE(SELE,ID)
34
26
38
10
```

Appendix B (continued)

MLOOP(ADD, MAP, VISI, NOSH, EDG1=1, EDG2=1, EDG3=1, EDG4=1)

CURVE(SELE, ID)

39

27

42

75

74

MLOOP(ADD, MAP, VISI, NOSH, EDG1=1, EDG2=1, EDG3=1, EDG4=2)

CURVE(SELE, ID)

43

28

46

12

MLOOP(ADD, MAP, VISI, NOSH, EDG1=1, EDG2=1, EDG3=1, EDG4=1)

CURVE(SELE, ID)

47

29

50

13

MLOOP(ADD, MAP, VISI, NOSH, EDG1=1, EDG2=1, EDG3=1, EDG4=1)

CURVE(SELE, ID)

51

30

54

14

MLOOP(ADD, MAP, VISI, NOSH, EDG1=1, EDG2=1, EDG3=1, EDG4=1)

CURVE(SELE, ID)

55

31

58

15

MLOOP(ADD, MAP, VISI, NOSH, EDG1=1, EDG2=1, EDG3=1, EDG4=1)

CURVE(SELE, ID)

59

32

62

16

MLOOP(ADD, MAP, VISI, NOSH, EDG1=1, EDG2=1, EDG3=1, EDG4=1)

Appendix B (continued)

CURVE(SELE,ID)

63

33

36

17

MLOOP(ADD, MAP, VISI, NOSH, EDG1=1, EDG2=1, EDG3=1, EDG4=1)

//Solid

CURVE(SELE,ID)

35

18

41

26

MLOOP(ADD, MAP, VISI, NOSH, EDG1=1, EDG2=1, EDG3=1, EDG4=1)

CURVE(SELE,ID)

38

39

40

41

MLOOP(ADD, MAP, VISI, NOSH, EDG1=1, EDG2=1, EDG3=1, EDG4=1)

CURVE(SELE,ID)

40

76

77

45

27

MLOOP(ADD, MAP, VISI, NOSH, EDG1=1, EDG2=2, EDG3=1, EDG4=1)

CURVE(SELE,ID)

42

43

44

45

MLOOP(ADD, MAP, VISI, NOSH, EDG1=1, EDG2=1, EDG3=1, EDG4=1)

CURVE(SELE,ID)

44

20

49

28

MLOOP(ADD, MAP, VISI, NOSH, EDG1=1, EDG2=1, EDG3=1, EDG4=1)

Appendix B (continued)

CURVE(SELE,ID)

46

47

48

49

MLOOP(ADD, MAP, VISI, NOSH, EDG1=1, EDG2=1, EDG3=1, EDG4=1)

CURVE(SELE,ID)

48

21

53

29

MLOOP(ADD, MAP, VISI, NOSH, EDG1=1, EDG2=1, EDG3=1, EDG4=1)

CURVE(SELE,ID)

50

51

52

53

MLOOP(ADD, MAP, VISI, NOSH, EDG1=1, EDG2=1, EDG3=1, EDG4=1)

CURVE(SELE,ID)

52

22

57

30

MLOOP(ADD, MAP, VISI, NOSH, EDG1=1, EDG2=1, EDG3=1, EDG4=1)

CURVE(SELE,ID)

54

55

56

57

MLOOP(ADD, MAP, VISI, NOSH, EDG1=1, EDG2=1, EDG3=1, EDG4=1)

CURVE(SELE,ID)

56

23

61

31

MLOOP(ADD, MAP, VISI, NOSH, EDG1=1, EDG2=1, EDG3=1, EDG4=1)

CURVE(SELE,ID)

58

Appendix B (continued)

59

60

61

MLOOP(ADD, MAP, VISI, NOSH, EDG1=1, EDG2=1, EDG3=1, EDG4=1)

CURVE(SELE,ID)

60

24

65

32

MLOOP(ADD, MAP, VISI, NOSH, EDG1=1, EDG2=1, EDG3=1, EDG4=1)

CURVE(SELE,ID)

62

63

64

65

MLOOP(ADD, MAP, VISI, NOSH, EDG1=1, EDG2=1, EDG3=1, EDG4=1)

CURVE(SELE,ID)

64

25

37

33

MLOOP(ADD, MAP, VISI, NOSH, EDG1=1, EDG2=1, EDG3=1, EDG4=1)

CURVE(SELE,ID)

66

81

80

83

82

67

25

24

23

22

21

20

77

76

18

MLOOP(ADD, MAP, VISI, NOSH, EDG1=1, EDG2=4, EDG3=1, EDG4=9)

Appendix B (continued)

//Mesh faces

SURFACE(SELE,ID=1)
MLOOP(SELE,ID=1)
MFACE(ADD)

SURFACE(SELE,ID=1)
MLOOP(SELE,ID=2)
MFACE(ADD)

SURFACE(SELE,ID=1)
MLOOP(SELE,ID=3)
MFACE(ADD)

SURFACE(SELE,ID=1)
MLOOP(SELE,ID=4)
MFACE(ADD)

SURFACE(SELE,ID=1)
MLOOP(SELE,ID=5)
MFACE(ADD)

SURFACE(SELE,ID=1)
MLOOP(SELE,ID=6)
MFACE(ADD)

SURFACE(SELE,ID=1)
MLOOP(SELE,ID=7)
MFACE(ADD)

SURFACE(SELE,ID=1)
MLOOP(SELE,ID=8)
MFACE(ADD)

SURFACE(SELE,ID=1)
MLOOP(SELE,ID=9)
MFACE(ADD)

SURFACE(SELE,ID=1)
MLOOP(SELE,ID=10)
MFACE(ADD)

SURFACE(SELE,ID=1)
MLOOP(SELE,ID=11)
MFACE(ADD)

Appendix B (continued)

SURFACE(SELE,ID=1)
MLOOP(SELE,ID=12)
MFACE(ADD)

SURFACE(SELE,ID=1)
MLOOP(SELE,ID=13)
MFACE(ADD)

SURFACE(SELE,ID=1)
MLOOP(SELE,ID=14)
MFACE(ADD)

SURFACE(SELE,ID=1)
MLOOP(SELE,ID=15)
MFACE(ADD)

SURFACE(SELE,ID=1)
MLOOP(SELE,ID=16)
MFACE(ADD)

SURFACE(SELE,ID=1)
MLOOP(SELE,ID=17)
MFACE(ADD)

SURFACE(SELE,ID=1)
MLOOP(SELE,ID=18)
MFACE(ADD)

SURFACE(SELE,ID=1)
MLOOP(SELE,ID=19)
MFACE(ADD)

SURFACE(SELE,ID=1)
MLOOP(SELE,ID=20)
MFACE(ADD)

SURFACE(SELE,ID=1)
MLOOP(SELE,ID=21)
MFACE(ADD)

SURFACE(SELE,ID=1)
MLOOP(SELE,ID=22)
MFACE(ADD)

Appendix B (continued)

```
SURFACE(SELE,ID=1)  
MLOOP(SELE,ID=23)  
MFACE(ADD)
```

```
SURFACE(SELE,ID=1)  
MLOOP(SELE,ID=24)  
MFACE(ADD)
```

```
SURFACE(SELE,ID=1)  
MLOOP(SELE,ID=25)  
MFACE(ADD)
```

```
//meshing  
MFACE(SELE,ID)  
1  
2  
3  
4  
5  
6  
7  
8  
9  
ELEMENT(SETD, QUAD, NODE=4)  
MFACE(MESH, MAP, ENTI="fluid")
```

```
MFACE(SELE,ID)  
10  
11  
12  
13  
14  
15  
16  
17  
18  
19  
20  
21  
22  
23  
24  
25  
ELEMENT(SETD,QUAD,NODE=4)
```


Appendix B (continued)

MFACE(MESH,MAP,ENTI="solid")

ELEMENT(SETD, EDGE, NODE=2)

MEDGE(SELE,ID)

3

74

MEDGE(MESH,MAP,ENTI="inlet")

MEDGE(SELE,ID)

2

34

MEDGE(MESH,MAP,ENTI="outlet")

MEDGE(SELE,ID)

1

4

MEDGE(MESH,MAP,ENTI="axis")

MEDGE(SELE,ID)

71

70

67

68

69

66

MEDGE(MESH,MAP,ENTI="freesurf")

MEDGE(SELE,ID)

54

6

7

46

10

11

47

14

15

48

18

19

49

22

23

Appendix B (continued)

```
50
26
27
51
30
31
57
MEDGE(MESH,MAP,ENTI="interface")

MEDGE(SELE,ID)
35
73
MEDGE(MESH,MAP,ENTI="edge")

MEDGE(SELE,ID)
65
60
63
64
MEDGE(MESH,MAP,ENTI="bottom")

MEDGE(SELE,ID)
5
72
MEDGE(MESH,MAP,ENTI="axiss")

END( )

FIPREP( )
//PROPERTIES
DENSITY( ADD, SET = "water", CONS = 0.992 )
CONDUCTIVITY( ADD, SET = "water", CONS = 0.0014699 )
VISCOSITY( ADD, SET = "water", CONS = 0.00657 )
SPECIFICHEAT( ADD, SET = "water", CONS = 0.998137 )
SURFACETENSION( ADD, SET = "water", CONS = 68 )

DENSITY( ADD, SET = "silicon", CONS = 2.33 )
CONDUCTIVITY( ADD, SET = "silicon", CONS = 0.334608 )
SPECIFICHEAT( ADD, SET = "silicon", CONS = 0.17006 )

//ENTITIES
ENTITY(ADD, NAME="fluid", FLUI, PROP="water")
ENTITY( ADD, NAME = "solid", SOLI, PROP = "silicon" )
ENTITY(ADD, NAME="outlet", PLOT)
```

Appendix B (continued)

```
ENTITY(ADD, NAME="inlet", PLOT)
ENTITY(ADD, NAME="axis", PLOT)
ENTITY(ADD, NAME="freesurf", SURF, DEPT = 21, SPIN, STRA, ANG1=10,
ANG2=180)
ENTITY(ADD, NAME="axiss", PLOT)
ENTITY(ADD, NAME="edge", PLOT)
ENTITY(ADD, NAME="bottom", PLOT)
ENTITY( ADD, NAME = "interface", PLOT, ATTA = "solid", NATT = "fluid" )
BODYFORCE(ADD, CONS, FX=981, FY=0, FZ=0)
PRESSURE(ADD, MIXE=1.0E-11, DISC)

OPTIONS(ADD, UPWINDING)
UPWINDING(ADD, STRE)
RELAXATION( )
    0.3, 0.3, 0.3, 0, 0.25, 0.25

//BC
BCNODE(ADD, COOR, NODE=949)
BCNODE(ADD, SURF, NODE=949, ZERO)
BCNODE(ADD, VELO, NODE=949, ZERO)
BCNODE(ADD, UT, NODE=949, ZERO)
BCNODE(ADD, UX, ENTI="inlet", CONS=29.05)
BCNODE(ADD, UY, ENTI="inlet", ZERO)
BCNODE(ADD, UY, ENTI="axis", ZERO)
BCNODE(ADD, VELO, ENTI="interface", ZERO)
BCNODE(ADD, VELO, ENTI="bottom", ZERO)
BCNODE(ADD, VELO, ENTI="edge", ZERO)
BCNODE(ADD, VELO, ENTI="axiss", ZERO)
BCNODE( ADD, VELO, ENTI = "solid", ZERO )
BCNODE( ADD, TEMP, ENTI = "inlet", CONS = 40 )
/BCNODE( ADD, TEMP, ENTI = "bottom", CONS = 100 )
BCFLUX( ADD, HEAT, ENTI = "bottom", CONS = 1.5 )
PROBLEM( ADD, 2-d, INCOMP, TRAN, LAMI, NONL, NEWT, MOME, ENERGY,
FREE, SING )
SOLUTION( ADD, N.R. = 50, KINE = 25, VELC = 1e-4, RESC = 1e-4, SURF = 1e-3 )
TIMEINTEGRATION( ADD, BACK, NSTE = 501, TSTA = 0, DT = 0.0001, VARI,
WIND = 9, NOFI = 12 )
POSTPROCESS( NBLO = 2 )
    1, 101, 1
    101, 501, 2
CLIPPING( ADD, MINI )
    0, 0, 0, 0, 40, 0
ICNODE( ADD, UX, ENTI = "fluid", CONS = 29.05 )
EXECUTION(ADD, NEWJ)
```

Appendix B (continued)

PRINTOUT(ADD, NONE, BOUN)
DATAPRINT(ADD, CONT)

END()

CREATE(FISO)

RUN(FISOLV, BACK, AT="", TIME="NOW", COMP)

Appendix C: Sine Shaped Surface FIDAP Code

```
Title( )
Sine Plate Base Case
Fi-Gen(Elem = 1, POIN = 1, CURV = 1, SURF = 1, NODE = 0, MEDG= 1, MLOO = 1,
MFAC = 1, BEDG = 1, SPAV = 1, MSHE = 1, MSOL = 1, COOR = 1, TOLE = 0.000)

//Specifications
//Plate Thickness
$PlateT = 0.125
//Plate Length
$PlateL = 0.6475
//Nozzle width
$NozzleW = 0.085
//Nozzle height
$NozzleH = 0.55
//Length of step
$a = 0.1177273
//Length of gap
$b = 0.1177273
//Depth of step
$Step = 0.025
$HalfS = 0.0125

//Creating Basic Geometry
//Points 1-12
POINT( ADD, COOR )
0 0
-$NozzleH 0
-$NozzleH $NozzleW
-0.18 0.17
-0.15 $PlateL
0 $PlateL
$PlateT $PlateL
$PlateT 0
-0.165370 0.406875
-0.155146 0.5665625
$HalfS 0
$HalfS $PlateL
-$NozzleH $PlateL

//Interface Points
//Points 13-
$HalfS 0.030937
$HalfS 0.080937
```

Appendix C (continued)

\$HalfS 0.130937
\$HalfS 0.192812
\$HalfS 0.242812
\$HalfS 0.292812
\$HalfS 0.354687
\$HalfS 0.404687
\$HalfS 0.454688
\$HalfS 0.516563
\$HalfS 0.566563
\$HalfS 0.616563
0 0.0809375
0 0.2428125
0 0.4046875
0 0.5665625
\$Step 0.0809375
\$Step 0.2428125
\$Step 0.4046875
\$Step 0.5665625
\$Step 0
\$Step \$PlateL

//Lines 1-9

POINT(SELE, ID)

1

2

CURVE(ADD, LINE)

POINT(SELE, ID)

2

3

CURVE(ADD, LINE)

POINT(SELE, ID)

3

4

CURVE(ADD,LINE)

POINT(SELE, ID)

4

5

CURVE(ADD,LINE)

POINT(SELE, ID)

5

Appendix C (continued)

```
6
CURVE(ADD,LINE)

POINT(SELE,ID)
6
7
CURVE(ADD,LINE)

POINT(SELE,ID)
7
8
CURVE(ADD,LINE)

POINT(SELE,ID)
8
1
CURVE(ADD,LINE)

CURVE(SELE,ID)
3
4
CURVE(ADD, FILL, RADI=0.2)

CURVE(SELE,ID=4)
CURVE(DELETE)

POINT(SELE,ID)
37
9
10
5
CURVE(ADD,LINE)

CURVE(SELE,ID=8)
POINT(SELE,ID=11)
CURVE(SPLIT)

CURVE(SELE,ID=6)
POINT(SELE,ID=12)
CURVE(SPLIT)

//Geometry
POINT(SELE,ID)
1
```

Appendix C (continued)

26

27

28

29

6

CURVE(ADD,LINE)

POINT(SELE,ID)

34

30

31

32

33

35

CURVE(ADD,LINE)

POINT(SELE,ID)

11

14

CURVE(ADD,LINE)

POINT(SELE,ID)

16

17

CURVE(ADD,LINE)

POINT(SELE,ID)

19

20

CURVE(ADD,LINE)

POINT(SELE,ID)

22

23

CURVE(ADD,LINE)

POINT(SELE,ID)

25

12

CURVE(ADD,LINE)

POINT(SELE,ID)

15

16

Appendix C (continued)

30
CURVE(ADD,ELLIPSE)

POINT(SELE,ID)

18

19

31

CURVE(ADD,ELLIPSE)

POINT(SELE,ID)

21

22

32

CURVE(ADD,ELLIPSE)

POINT(SELE,ID)

24

25

33

CURVE(ADD,ELLIPSE)

CURVE(SELE,ID=16)

POINT(SELE,ID=35)

CURVE(SPLIT)

CURVE(SELE,ID=13)

POINT(SELE,ID=34)

CURVE(SPLIT)

CURVE(SELE,ID=32)

POINT(SELE,ID=14)

CURVE(SPLIT)

CURVE(SELE,ID=40)

POINT(SELE,ID=30)

CURVE(SPLIT)

CURVE(SELE,ID=41)

POINT(SELE,ID=26)

CURVE(SPLIT)

CURVE(SELE,ID=33)

POINT(SELE,ID=17)

CURVE(SPLIT)

Appendix C (continued)

CURVE(SELE,ID=47)
POINT(SELE,ID=27)
CURVE(SPLIT)

CURVE(SELE,ID=46)
POINT(SELE,ID=31)
CURVE(SPLIT)

CURVE(SELE,ID=34)
POINT(SELE,ID=20)
CURVE(SPLIT)

CURVE(SELE,ID=53)
POINT(SELE,ID=28)
CURVE(SPLIT)

CURVE(SELE,ID=52)
POINT(SELE,ID=32)
CURVE(SPLIT)

CURVE(SELE,ID=35)
POINT(SELE,ID=23)
CURVE(SPLIT)

CURVE(SELE,ID=58)
POINT(SELE,ID=33)
CURVE(SPLIT)

CURVE(SELE,ID=59)
POINT(SELE,ID=29)
CURVE(SPLIT)

//Mods to help with meshing
POINT(ADD, COOR)
-\$NozzleH 0.080937
0 0.136582
0 \$NozzleW

CURVE(SELE,ID=2)
POINT(SELE,ID=38)
CURVE(SPLIT)

CURVE(SELE,ID=18)
POINT(SELE,ID=39)

Appendix C (continued)

CURVE(SPLIT)

CURVE(SELE,ID=66)
POINT(SELE,ID=40)
CURVE(SPLIT)

//Surface
POINT(SELE,ID)
13
7
2
8
SURFACE(ADD,POINTS, ROWW=2, NOAD)

//Medges
CURVE(SELE,ID)
43
MEDGE(ADD, LSTFIRST, INTE=15, RATI=0.35, 2RAT=0, PCEN=0)

CURVE(SELE,ID)
42
45
MEDGE(ADD, SUCC, INTE=15, RATI=0, 2RAT=0, PCEN=0)

CURVE(SELE,ID)
44
MEDGE(ADD, FRSTLAST, INTE=15, RATI=0.35, 2RAT=0, PCEN=0)

CURVE(SELE,ID)
51
50
49
48
57
56
55
54
61
MEDGE(ADD, SUCC, INTE=15, RATI=0, 2RAT=0, PCEN=0)

CURVE(SELE,ID)
60
MEDGE(ADD, FRSTLAST, INTE=15, RATI=0.35, 2RAT=0, PCEN=0)

Appendix C (continued)

CURVE(SELE,ID)

63

MEDGE(ADD, LSTFIRST, INTE=15, RATI=0.35, 2RAT=0, PCEN=0)

CURVE(SELE,ID)

62

14

39

15

36

MEDGE(ADD, SUCC, INTE=15, RATI=0, 2RAT=0, PCEN=0)

CURVE(SELE,ID)

27

17

22

31

21

26

MEDGE(ADD, SUCC, INTE=17, RATI=0, 2RAT=0, PCEN=0)

CURVE(SELE,ID)

19

20

23

24

25

30

29

28

MEDGE(ADD, SUCC, INTE=34, RATI=0, 2RAT=0, PCEN=0)

CURVE(SELE,ID)

1

5

MEDGE(ADD, SUCC, INTE=30, RATI=0, 2RAT=0, PCEN=0)

CURVE(SELE,ID)

12

MEDGE(ADD, SUCC, INTE=17, RATI=0, 2RAT=0, PCEN=0)

CURVE(SELE,ID)

10

Appendix C (continued)

MEDGE(ADD, SUCC, INTE=18, RATI=0, 2RAT=0, PCEN=0)

CURVE(SELE, ID)

11

MEDGE(ADD, SUCC, INTE=34, RATI=0, 2RAT=0, PCEN=0)

CURVE(SELE, ID)

67

MEDGE(ADD, SUCC, INTE=22, RATI=0, 2RAT=0, PCEN=0)

CURVE(SELE, ID)

69

MEDGE(ADD, SUCC, INTE=11, RATI=0, 2RAT=0, PCEN=0)

CURVE(SELE, ID)

68

65

MEDGE(ADD, SUCC, INTE=1, RATI=0, 2RAT=0, PCEN=0)

CURVE(SELE, ID)

64

MEDGE(ADD, SUCC, INTE=17, RATI=0, 2RAT=0, PCEN=0)

CURVE(SELE, ID)

3

MEDGE(ADD, SUCC, INTE=11, RATI=0, 2RAT=0, PCEN=0)

CURVE(SELE, ID)

9

MEDGE(ADD, LSTFIRST, INTE=38, RATI=0.4, 2RAT=0, PCEN=0)

CURVE(SELE, ID)

37

38

MEDGE(ADD, SUCC, INTE=20, RATI=0, 2RAT=0, PCEN=0)

CURVE(SELE, ID)

7

MEDGE(ADD, SUCC, INTE=136, RATI=0, 2RAT=0, PCEN=0)

//Mloops

CURVE(SELE, ID)

1

Appendix C (continued)

17

68

69

67

19

20

21

5

12

11

10

9

3

65

64

MLOOP(ADD, MAP, VISI, NOSH, EDG1=1, EDG2=7, EDG3=1, EDG4=7)

CURVE(SELE, ID)

14

27

44

17

MLOOP(ADD, MAP, VISI, NOSH, EDG1=1, EDG2=1, EDG3=1, EDG4=1)

CURVE(SELE, ID)

45

28

48

67

69

68

MLOOP(ADD, MAP, VISI, NOSH, EDG1=1, EDG2=1, EDG3=1, EDG4=3)

CURVE(SELE, ID)

49

29

54

19

MLOOP(ADD, MAP, VISI, NOSH, EDG1=1, EDG2=1, EDG3=1, EDG4=1)

CURVE(SELE, ID)

55

30

62

Appendix C (continued)

20

MLOOP(ADD, MAP, VISI, NOSH, EDG1=1, EDG2=1, EDG3=1, EDG4=1)

CURVE(SELE,ID)

63

31

15

21

MLOOP(ADD, MAP, VISI, NOSH, EDG1=1, EDG2=1, EDG3=1, EDG4=1)

CURVE(SELE,ID)

43

42

45

44

MLOOP(ADD, MAP, VISI, NOSH, EDG1=1, EDG2=1, EDG3=1, EDG4=1)

CURVE(SELE,ID)

51

50

49

48

MLOOP(ADD, MAP, VISI, NOSH, EDG1=1, EDG2=1, EDG3=1, EDG4=1)

CURVE(SELE,ID)

57

56

55

54

MLOOP(ADD, MAP, VISI, NOSH, EDG1=1, EDG2=1, EDG3=1, EDG4=1)

CURVE(SELE,ID)

61

60

63

62

MLOOP(ADD, MAP, VISI, NOSH, EDG1=1, EDG2=1, EDG3=1, EDG4=1)

CURVE(SELE,ID)

39

22

43

27

Appendix C (continued)

MLOOP(ADD, MAP, VISI, NOSH, EDG1=1, EDG2=1, EDG3=1, EDG4=1)

CURVE(SELE,ID)

42

23

51

28

MLOOP(ADD, MAP, VISI, NOSH, EDG1=1, EDG2=1, EDG3=1, EDG4=1)

CURVE(SELE,ID)

50

24

57

29

MLOOP(ADD, MAP, VISI, NOSH, EDG1=1, EDG2=1, EDG3=1, EDG4=1)

CURVE(SELE,ID)

56

25

61

30

MLOOP(ADD, MAP, VISI, NOSH, EDG1=1, EDG2=1, EDG3=1, EDG4=1)

CURVE(SELE,ID)

60

26

36

31

MLOOP(ADD, MAP, VISI, NOSH, EDG1=1, EDG2=1, EDG3=1, EDG4=1)

CURVE(SELE,ID)

38

7

37

26

25

24

23

22

MLOOP(ADD, MAP, VISI, NOSH, EDG1=1, EDG2=1, EDG3=1, EDG4=5)

Appendix C (continued)

```
//mesh faces  
SURFACE(SELE,ID=1)  
MLOOP(SELE,ID=1)  
MFACE(ADD)
```

```
SURFACE(SELE,ID=1)  
MLOOP(SELE,ID=2)  
MFACE(ADD)
```

```
SURFACE(SELE,ID=1)  
MLOOP(SELE,ID=3)  
MFACE(ADD)
```

```
SURFACE(SELE,ID=1)  
MLOOP(SELE,ID=4)  
MFACE(ADD)
```

```
SURFACE(SELE,ID=1)  
MLOOP(SELE,ID=5)  
MFACE(ADD)
```

```
SURFACE(SELE,ID=1)  
MLOOP(SELE,ID=6)  
MFACE(ADD)
```

```
SURFACE(SELE,ID=1)  
MLOOP(SELE,ID=7)  
MFACE(ADD)
```

```
SURFACE(SELE,ID=1)  
MLOOP(SELE,ID=8)  
MFACE(ADD)
```

```
//mesh faces  
SURFACE(SELE,ID=1)  
MLOOP(SELE,ID=9)  
MFACE(ADD)
```

```
SURFACE(SELE,ID=1)  
MLOOP(SELE,ID=10)  
MFACE(ADD)
```

```
SURFACE(SELE,ID=1)  
MLOOP(SELE,ID=11)
```

Appendix C (continued)

MFACE(ADD)

SURFACE(SELE,ID=1)
MLOOP(SELE,ID=12)
MFACE(ADD)

SURFACE(SELE,ID=1)
MLOOP(SELE,ID=13)
MFACE(ADD)

SURFACE(SELE,ID=1)
MLOOP(SELE,ID=14)
MFACE(ADD)

SURFACE(SELE,ID=1)
MLOOP(SELE,ID=15)
MFACE(ADD)

SURFACE(SELE,ID=1)
MLOOP(SELE,ID=16)
MFACE(ADD)

//meshing

MFACE(SELE,ID)

1
2
3
4
5
6
7
9

ELEMENT(SETD, QUAD, NODE=4)
MFACE(MESH, MAP, ENTI="fluid")

MFACE(SELE,ID)

8
10
11
12
13
14
15
16

Appendix C (continued)

ELEMENT(SETD,QUAD,NODE=4)
MFACE(MESH,MAP,ENTI="solid")

ELEMENT(SETD, EDGE, NODE=2)
MEDGE(SELE,ID)

44

43

MEDGE(MESH,MAP,ENTI="inlet")

MEDGE(SELE,ID)

36

19

MEDGE(MESH,MAP,ENTI="outlet")

MEDGE(SELE,ID)

35

17

MEDGE(MESH,MAP,ENTI="axis")

MEDGE(SELE,ID)

45

46

38

39

37

MEDGE(MESH,MAP,ENTI="freesurf")

MEDGE(SELE,ID)

21

1

2

34

8

7

33

9

10

32

16

15

24

MEDGE(MESH,MAP,ENTI="interface")

Appendix C (continued)

MEDGE(SELE,ID)

20

47

MEDGE(MESH,MAP,ENTI="edge")

MEDGE(SELE,ID)

49

MEDGE(MESH,MAP,ENTI="bottom")

MEDGE(SELE,ID)

18

48

MEDGE(MESH,MAP,ENTI="axiss")

END()

FIPREP()

//PROPERTIES

DENSITY(ADD, SET = "water", CONS = 0.992)

CONDUCTIVITY(ADD, SET = "water", CONS = 0.0014699)

VISCOSITY(ADD, SET = "water", CONS = 0.00657)

SPECIFICHEAT(ADD, SET = "water", CONS = 0.998137)

SURFACETENSION(ADD, SET = "water", CONS = 68)

DENSITY(ADD, SET = "silicon", CONS = 2.33)

CONDUCTIVITY(ADD, SET = "silicon", CONS = 0.334608)

SPECIFICHEAT(ADD, SET = "silicon", CONS = 0.17006)

//ENTITIES

ENTITY(ADD, NAME="fluid", FLUI, PROP="water")

ENTITY(ADD, NAME = "solid", SOLI, PROP = "silicon")

ENTITY(ADD, NAME="outlet", PLOT)

ENTITY(ADD, NAME="inlet", PLOT)

ENTITY(ADD, NAME="axis", PLOT)

ENTITY(ADD, NAME="freesurf", SURF, DEPT = 31, SPIN, STRA, ANG1=10,
ANG2=180)

ENTITY(ADD, NAME="axiss", PLOT)

ENTITY(ADD, NAME="edge", PLOT)

ENTITY(ADD, NAME="bottom", PLOT)

ENTITY(ADD, NAME = "interface", PLOT, ATTA = "solid", NATT = "fluid")

BODYFORCE(ADD, CONS, FX=981, FY=0, FZ=0)

PRESSURE(ADD, MIXE=1.0E-11, DISC)

OPTIONS(ADD, UPWINDING)

Appendix C (continued)

```
UPWINDING(ADD, STRE)
RELAXATION( )
  0.3, 0.3, 0.3, 0, 0.5, 0.25

//BC
BCNODE(ADD, COOR, NODE=826)
BCNODE(ADD, SURF, NODE=826, ZERO)
BCNODE(ADD, VELO, NODE=826, ZERO)
BCNODE(ADD, UT, NODE=826, ZERO)
BCNODE(ADD, UX, ENTI="inlet", CONS=29.05)
BCNODE(ADD, UY, ENTI="inlet", ZERO)
BCNODE(ADD, UY, ENTI="axis", ZERO)
BCNODE(ADD, VELO, ENTI="interface", ZERO)
BCNODE(ADD, VELO, ENTI="bottom", ZERO)
BCNODE(ADD, VELO, ENTI="edge", ZERO)
BCNODE(ADD, VELO, ENTI="axiss", ZERO)
BCNODE( ADD, VELO, ENTI = "solid", ZERO )
BCNODE( ADD, TEMP, ENTI = "inlet", CONS = 40 )
/BCNODE( ADD, TEMP, ENTI = "bottom", CONS = 100 )
BCFLUX( ADD, HEAT, ENTI = "bottom", CONS = 1.5 )
PROBLEM( ADD, 2-d, INCOMP, TRAN, LAMI, NONL, NEWT, MOME, ENERGY,
FREE, SING )
SOLUTION( ADD, N.R. = 50, KINE = 25, VELC = 1e-4, RESC = 1e-4, SURF = 1e-3 )
TIMEINTEGRATION( ADD, BACK, NSTE = 501, TSTA = 0, DT = 0.0001, VARI,
WIND = 9, NOFI = 12 )
POSTPROCESS( NBLO = 2 )
  1, 101, 1
  101, 501, 2
CLIPPING( ADD, MINI )
  0, 0, 0, 0, 40, 0
ICNODE( ADD, UX, ENTI = "fluid", CONS = 29.05 )
EXECUTION(ADD, NEWJ)
PRINTOUT(ADD, NONE, BOUN)
DATAPRINT(ADD, CONT)

END( )

CREATE(FISO)

RUN(FISOLV, BACK, AT="", TIME="NOW", COMP)
```